Reliability Assessment and Energy Loss Evaluation for Modern Wind Turbine Systems

Zhou, Dao

Publication date:
2014

Document Version
Publisher's PDF, also known as Version of record

RELIABILITY ASSESSMENT AND ENERGY LOSS EVALUATION OF MODERN WIND TURBINE SYSTEMS

DAO ZHOU

AALBORG UNIVERSITY
DENMARK

Reliability Assessment and Energy Loss Evaluation of Modern Wind Turbine Systems

Dao Zhou

DEPARTMENT OF ENERGY TECHNOLOGY
AALBORG UNIVERSITY

Reliability Assessment and Energy Loss Evaluation of Modern Wind Turbine Systems

by

Dao Zhou

Dissertation submitted to Faculty of Engineering, Science

Aalborg University

Department of Energy Technology

Aalborg University, Denmark

October 2014

Department of Energy Technology
Aalborg University
Pontopidanstræde 101
Aalborg, DK-9220, Denmark
http:// www.et.aau.dk
Email: zda@et.aau.dk

Printed in Denmark by Uniprint

ISBN: 978-87-92846-50-1

Preface

This thesis is a summary of industrial PhD project “Reliability Assessment and Energy Loss Evaluation of Modern Wind Turbine Systems”, and the research work is supported by Danfoss Silicon Power GmbH and Department of Energy Technology at Aalborg University. Acknowledgements are given to the above mentioned institutions, as well as the Center of Reliable Power Electronics (CORPE) and Danish Ministry of Higher Education and Science, who financially support me for several conference participations and stays at the company.

This project was supervised by Prof. Frede Blaabjerg from Department of Energy Technology in Aalborg University, Dr. Michael Tønnes, Dr. Toke Franke from Danfoss Silicon Power GmbH, and Mogens Lau from Siemens Wind Power A/S. First and foremost, I would like to express my deepest gratitude to my supervisor, Prof. Frede Blaabjerg, for his inspired proposals, constructive discussions, patient guidance and consistent encouragements. Besides, I sincerely thank Michael, Toke and Mogens for their useful suggestions and comments in the viewpoint of the industry. I do believe that their earnestness and dedication will have an important impact on my future career.

My gratitude also goes to Prof. Dehong Xu from Zhejiang University and Zhongping (David) Lu from Holip, Chinese division of Danfoss, for their initiation of this project. Many thanks go to Klaus Olesen, Ruimin Tan for their useful discussions during my stays at Danfoss.

I also want to thank my colleagues from the Department of Energy Technology for the friendly environment and enthusiastic help. I would like to send my best wishes to my friends - Xiongfei Wang, Ke Ma, Huai Wang, Xiao Liu, Chi Su, Yongheng Yang, Ge Xie, Ning He and Wenli Yao. Moreover, my special appreciations are extended to Prof. Poh Chiang Loh, Assoc. Prof. Kaiyuan Lu, John K. Pedersen, Tina Larsen, Mette Skov Jensen, Corina Busk Gregersen, Casper Jørgensen and Mads Lund for their assistance in many different ways.

The sincerest gratitude goes to my parents for their endless love and support. Finally and most importantly, I would like to acknowledge my wife Chenjing Jiang for her support, concern and understanding.

Dao Zhou
October, 2014
Aalborg

Abstract

With a steady increase of the wind power penetration, the demands to the wind power technology are becoming the same as those to the conventional energy sources. In order to fulfill the requirements, power electronics technology is the key for the modern wind turbine systems – both the Doubly-Fed Induction Generator (DFIG) based partial-scale wind power converter and the Permanent Magnet Synchronous Generator (PMSG) based full-scale wind power converter. Since lower cost per kWh, higher power density and longer lifetime are the main concern of power electronics, this project has been aimed to explore the reliability and cost of energy in the modern wind turbine systems. Moreover, advanced control strategies have been proposed and developed for an efficient and reliable operation during the normal condition as well as under grid faults.

The documented thesis starts with the descriptions of the DFIG system and the PMSG system. The design of the back-to-back power converters and the loss model of the power semiconductor device are discussed and established in Chapter 2. Then, Chapter 3 and Chapter 4 are dedicated to the assessment of the wind power converter in terms of reliability. Specifically, Chapter 4 estimates and compares the lifespan of the back-to-back power converters based on the thermal stress analyzed in Chapter 3. In accordance with the grid codes, Chapter 4 further evaluates the cost on reliability with various types of reactive power injection for both the configurations. The cost of energy in wind turbine system is then addressed in Chapter 5, where different wind classes and operation modes of the reactive power injection are taken into account. Finally, the internal and external challenges for power converters in the DFIG systems to ride through balanced grid faults are explored in Chapter 6.

The main contribution of this project is in developing a universal approach to evaluate and estimate the reliability and the cost of energy for modern wind turbine systems. Furthermore, simulation and experimental results validates the feasibility of an enhanced lifespan of the power electronic converters and reduced cost of energy in the DFIG system, employing a proper reactive power control method between the

back-to-back power converters. In the case of grid disturbances, an optimized demagnetizing current control strategy has been proposed in order to keep the minimum thermal stress of the DFIG power converter, and thus improve its reliability.

Dansk Abstrakt

Med den hastige stigning i installeret vindkraft, bliver kravene til vindkraft teknologien de samme som dem, der er til de konventionelle energikilder. For at opfylde disse krav, er effektelektronikken nøglen til moderne vindmølle-systemer - både til den Dobbelt Fødede Induktions Generator (DFIG), som er baseret en effektkonverter, der har en størrelse, som er en tredje-del af generatorens størrelse og Permanent Magnet Synkron Generator (PMSG), som er baseret på en effekt-konverter, der har samme størrelse som generatoren. Da lavere pris pr produceret kWh, højere effekttæthed og længere levetid er nøgle parametre i moderne vindmøller har dette projekt fokuseret på pålideligheden og prisen på energi. Desuden er avancerede kontrolstrategier blevet foreslået til at understøtte de forskellige krav og de er udviklet til en effektiv og pålidelig drift under både normal drift samt under netfejl.

Afhandlingen indleder med beskrivelser af DFIG systemet og PMSG systemet. De tilhørende effektomformere er beskrevet og tabs modeller for effekthalvlederne er etableret i kapitel 2. Derefter, er kapitel 3 og kapitel 4 dedikeret til at undersøge og vurdere effektkonverterne med hensyn til pålidelighed. Særligt i kapitel 4 estimeres og sammenlignes levetiden for effektomformerne baseret på den termiske stress, som er analyseret i kapitel 3. I overensstemmelse med de gældende netkrav, vurderer kapitel 4 endvidere omkostningerne på pålideligheden for begge konfigurationer, når forskellige typer af reaktiv effekt sendes ind på nettet under forskellige driftsforhold. Omkostningerne ved disse driftsformer i vindmølle-systemerne bliver derefter behandlet i kapitel 5, hvor der også tages hensyn til forskellige vind- klasser, hvori vindmøllerne er, samt forskellige driftstilstande omkring den reaktive effekt som tilføres nettet. Endelig er DFIG systemet i kapitel 6 undersøgt, når der opstår netfejl med henblik på at få en tilstrækkelig robusthed af vindmøllesystemet.

Det vigtigste bidrag til dette projekt er, at der er udviklet en universel tilgang til at evaluere og vurdere pålideligheden, samt omkostningerne i den forbindelse ved energi-produktionen fra moderne vindmølle-systemer. Endvidere viser simuleringer og eksperimentelle resultater, at der er muligheder for en forbedret levetid af de

effektelektroniske omformere og dermed reducerede omkostninger i forbindelse med energi-produktionen i DFIG systemet når der anvendes en ny reaktiv effektstyrings metode. I tilfælde af netforstyrrelser, er der blevet foreslået en ny optimeret afmagnetiserings kontrol strategi for DFIG systemet for at holde en minimal termiske belastning af effekt-omformer, og dermed forbedre dens pålidelighed.

Table of Contents

Preface i
Abstract iii
Dansk Abstrakt v
Table of Contents vii
Copyright Statement x
Part I Report 0
Chapter 1 Introduction 1
1.1 Status and development of wind power generation 1
1.2 Currently used wind turbine systems 2
1.3 Emerging challenges in wind turbine system 4
1.3.1 Reliability issues 5
1.3.2 Grid supports 7
1.3.3 Control strategies 9
1.4 Thesis hypothesis and objectives 11
1.5 Thesis outline 11
References 14
Chapter 2 Power device loadings in mainstream wind power converter 17
2.1 Basic design for typical configurations 17
2.1.1 DFIG configuration 19
2.1.2 PMSG configuration 19
2.2 Loss breakdown of power device 20
2.2.1 Power loss model 20
2.2.2 Grid-side converter 21
2.2.3 Rotor-side converter/Generator-side converter 24
2.3 Efficiency comparison 26
2.4 Summary 27
Relevant attached papers 28
References 28
Chapter 3 Thermal stress of wind power converter 30

3.1 Thermal model of power device 30
3.2 Thermal profile of wind power converter 35
3.2.1 Without reactive power injection 35
3.2.2 With reactive power injection 37
3.3 Thermal behavior optimization in DFIG system 38
3.3.1 Allowable range of reactive power 39
3.3.2 Thermal performance during a wind gust 43
3.4 Summary 44
Relevant attached papers 45
References 45
Chapter 4 Reliability assessment of wind power converter 47
4.1 Methods for reliability analysis 47
4.2 Lifetime estimation for wind power converter 50
4.3 Mission profile effect on lifetime 53
4.3.1 Grid codes 54
4.3.2 Wind profile influence 55
4.4 DFIG optimized reactive power flow 56
4.5 Summary 60
Relevant attached papers 60
References 60
Chapter 5 Energy loss evaluation of wind turbine systems 62
5.1 Important concepts of energy loss 62
5.2 Mission profile effects on PMSG system 63
5.2.1 Various wind classes 66
5.2.2 Various operation modes of reactive power injection 67
5.3 Reduced cost of reactive power in DFIG system 68
5.3.1 Loss model of DFIG itself 68
5.3.2 Optimized design of grid filter 71
5.3.3 Cost of energy in DFIG system 74
5.3.4 Experimental verification of loss dissipation 77
5.4 Summary 81
Relevant attached papers 81

References 81
Chapter 6 Reliability-oriented control strategies during grid fault 84
6.1 Existing issues for DFIG during grid fault 84
6.2 LVRT challenge from DFIG itself 85
6.2.1 DFIG model during balanced grid fault 85
6.2.2 Demagnetizing current control 87
6.2.3 DFIG ride through capability 89
6.3 LVRT challenge from grid codes 90
6.3.1 Effects of reactive current injection 90
6.3.2 Effects of natural flux decaying 91
6.4 Optimum control scheme 92
6.4.1 Design criteria of demagnetizing coefficient 92
6.4.2 Simulation validation 94
6.5 Summary 95
Relevant attached papers 95
References 96
Chapter 7 Conclusions 97
7.1 Summary 97
7.2 Contributions 99
7.3 Future work 100
Part II Publications 102

Copyright Statement

Thesis title: Reliability Assessment and Energy Loss Evaluation of Modern Wind Turbine Systems

Name of the PhD student: Dao Zhou

Name of supervisors: Prof. Frede Blaabjerg, Dr. Michael Tønnes, Mogens Lau, Dr. Toke Franke

List of publication: Listed in § 1.5

This present report combined with scientific papers which are listed in § 1.5 has been submitted to the Faculty of Engineering and Science at Aalborg University for assessment in partial fulfillment for the Degree of Doctor of Philosophy (Ph.D.) in Electrical Engineering. The scientific papers are not included in this version due to copyright issues. Detailed publication information is provided in § 1.5 and the interested reader is referred to the original published papers. As part of the assessment, co-author statements have been made available to the assessment committee and are also available at the Faculty of Engineering and Science, Aalborg University.

Part I Report

Chapter 1

Introduction

This chapter presents the background and the motivation of the thesis, followed by the state-of-the-art of the project. Then the targets and the structure of this thesis are described and listed.

1.1 Status and development of wind power generation

Wind power is a main pillar of renewable energy supply, as it generates clean and climate-friendly electricity. Over the last decade, the wind power industry has expanded greatly with governmental support all around the world. According to the statistics provided by Global Wind Energy Council (GWEC), the cumulative wind power has increased from 17.4 GW in 2000 to 318.1 GW at the end of 2013 as shown in Fig. 1.1, almost 18.2 times higher [1]. Although more than 35 GW of the new wind power capacity was brought online in 2013, the annual installed wind power capacity get the first decline over the last decade, mainly due to the dramatic drop in the US market after a record installation in 2012 [1], [2]. However, the wind power is still under a steady development due to the ambitious renewable energy strategies of the European Union and China, and in 2014 more than 50 GW is expected to be installed [3], [4].

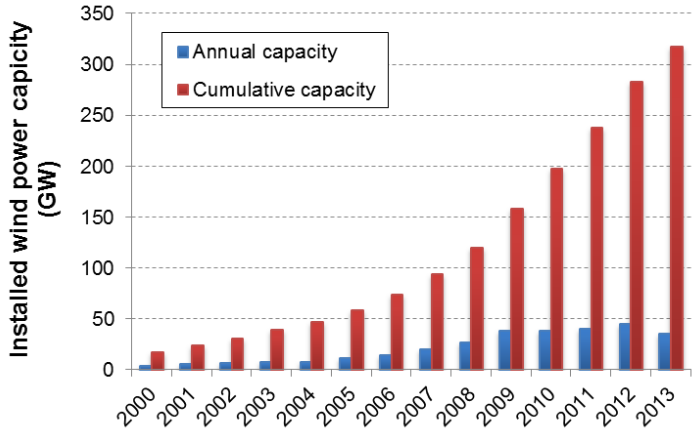

Fig. 1.1. Global annual and cumulative installed wind power capacity [1].

In contrast to the tendency of increasing energy prices for fossil and nuclear power sources, the Levelized Cost Of Electricity (LCOE) of all renewable energy technologies have been falling continuously for decades due to the technological innovations such as the use of less expensive and better performing materials, more-efficient production processes as well as the automated mass production of components. Based on a survey of the LCOE about the German renewable energy as shown in Fig. 1.2 [5], it can be seen that the wind power, especially the offshore wind power has significant potential to reduce the cost, it is expected even to be below the cost of the fossil resource by the end of 2030.

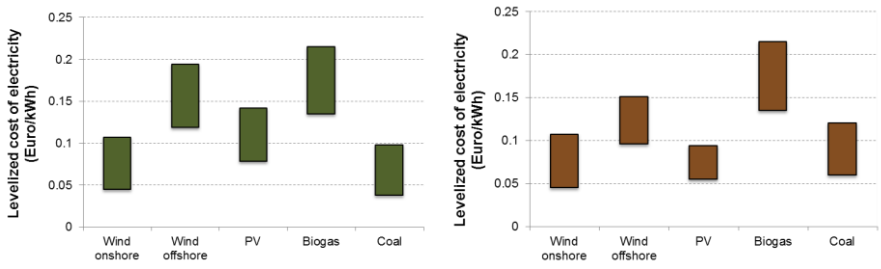

(a) (b)

Fig. 1.2. LCOE of renewable energy technologies and conventional power plant in Germany [5]. (a) Cost situation in 2013; (b) Cost forecast in 2030.

1.2 Currently used wind turbine systems

The steady growth of wind power capacity has a consequence to the wind turbine system - lower cost per kWh, increased power density and higher reliability [6]-[8]. Table 1-1 lists the top 10 wind turbine manufacturers in 2013, including the generator systems and the power levels of their products [9], [10]. It is clear that the constant speed system is fading out pushed by stricter grid connection requirements, and variable speed system in the wind turbine becomes the most popular system. Although the wind turbine system can be categorized into several concepts in terms of the generator type, with and without gearbox, or the rating of power electronics converter, it is common to divide the wind turbine system into a partial-scale power converter equipped with a Doubly-Fed Induction Generator (DFIG) and a full-scale power converter with either a Synchronous Generator (SG) or an Induction Generator (IG).

Table 1-1 Top 10 wind turbine manufacturers in 2013 [9], [10]

Manufacturer	Concept	Rotor diameter	Power range
Vestas (Denmark)	DFIG GFC PMSG	80 - 110 m 105- 164 m	1.8 – 2 MW 3.3 – 8 MW
Goldwind (China)	DD PMSG GFC IG	70 – 109 m 110 m	1.5 – 2.5 MW 3 MW
Enercon (Germany)	DD SG	44 – 126 m	0.8 – 7.5 MW
Siemens (Germany/Denmark)	GFC IG DD PMSG	82- 120 m 101 - 154 m	2.3 – 3.6 MW 3 – 6 MW
Sulzon (India)	CS DFIG	52 - 88 m 95 - 97 m	0.6 – 2.1 MW 2.1 MW
General Electric (US)	DFIG DD PMSG	77 - 120 m 113 m	1.5 – 2.75 MW 4.1 MW
Gamesa (Spain)	DFIG GFC PMSG	52 – 114 m 128 m	0.85 – 2 MW 4.5 MW
Guodian United Power (China)	DFIG DD PMSG	77 – 100 m 136 m	1.5 – 3 MW 6 MW
Ming Yang (China)	DFIG GFC PMSG	77 -83 m 92 – 108 m	1.5 – 2 MW 2.5 – 3 MW
Nordex (Germany)	DFIG	90 – 131 m	2.4 – 3.3 MW

CS: constant speed with gearbox and induction generator
DFIG: variable speed with gearbox, doubly-fed induction generator and partial converter
GFC PMSG: variable speed with gearbox, permanent magnet synchronous generator and full converter
GFC IG: variable speed with gearbox, induction generator and full converter
DD SG: variable speed direct-drive synchronous generator with electrical excitation and full converter
DD PMSG: variable speed direct-drive permanent magnet synchronous generator and full converter

The first concept of wind turbine configuration, which is based on the DFIG, employs a power converter rated to approximately 30% of the nominal generator power and it is shown in Fig. 1.3. The power converter is connected to the rotor through slip-rings and controls the rotor current as well as rotor speed, while the stator is linked to the grid without any decoupling. The fraction of slip power through the converter makes this concept attractive from an economical point of view. However, the main

drawbacks lie in the use of slip rings, and also an additional crowbar might be needed to protect the rotor-side converter under grid faults [9], [11].

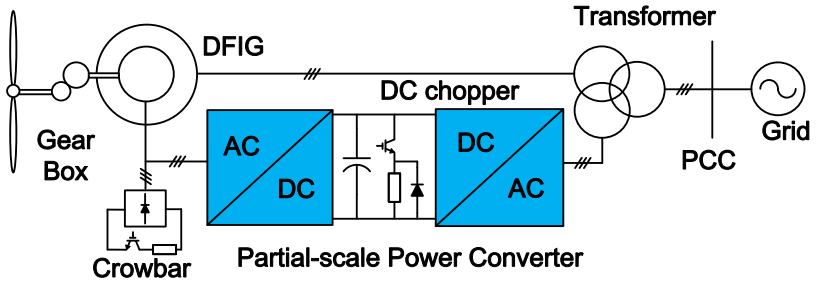

Fig. 1.3. Wind turbine system with partial-scale power converter.

As shown in Fig. 1.4, a full-scale power converter configuration is considered as an alternative promising technology for multi-MW wind turbine system. The generator stator winding is connected to the grid through the full-scale power converter, which performs the reactive power compensation and a smooth grid connection for the entire speed range of the generator. Some variable speed wind turbine systems are gearless by introducing a multi-pole generator. The elimination of the slip rings, a simpler gearbox and full power controllability during the grid faults are the main advantages of such topologies [9]-[12]. However, in order to satisfy the full power rating, a common used approach is to use several converter modules or power devices in parallel.

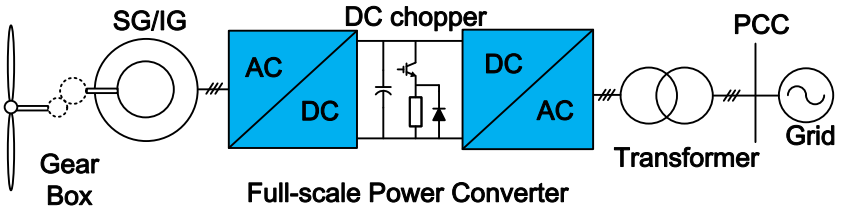

Fig. 1.4. Wind turbine system with full-scale power converter.

1.3 Emerging challenges in wind turbine system

With the increase of the wind power penetration, some new challenges (reliability issues, more grid support functions and control strategies) are imposed to the wind turbine system, and they will be addressed in this section.

1.3.1 Reliability issues

Due to the land limitations and also rich ocean wind energy resource, the location of wind farms with multi-MW wind turbine is moving from onshore to offshore. Because of the higher cost of the maintenance, the lifetime of wind turbine system is in turn prolonged to 20-25 years, which asks for a more reliable and durable technology [13]-[17].

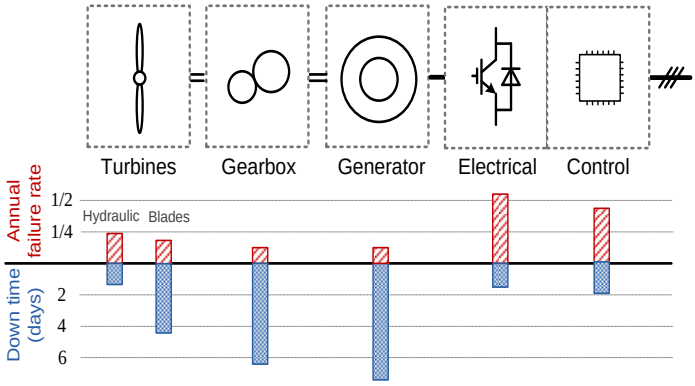

Fig. 1.5. Distribution of failure rate and downtime for different parts in a wind turbine system [14].

Investigations of the wind turbines in the north Germany in time period from 1993-2006 indicate that an increasing power rating could have a higher risk of failure [13]. Moreover, according to a survey regarding the failure rate and downtime distribution of a wind turbine system as shown in Fig. 1.5, it is the power electronics converter that dominates the failure rate [14], although the gearbox and the generator may have the longest downtime in the case of a failure.

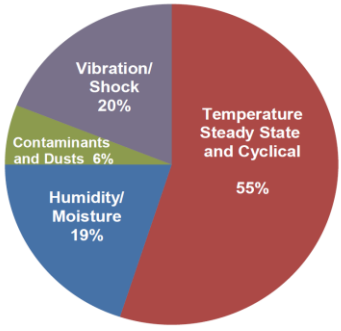

Fig. 1.6. Stressors distribution in a power electronics system [18].

Power semiconductor devices are playing a key role in a power electronic system, and more and more efforts are devoted to the reliability characteristic. The different stressors distribution in power electronic equipment is shown in Fig. 1.6, and it is seen that the temperature cycling has the most significant impact [18]. Besides, it is widely accepted that the thermal profile of the power semiconductor is an important indicator of the lifetime estimation [19]-[27]. As claimed in [28], Semikron proposed the state-of-the-art lifetime model,

$$N_f = A \cdot dT_j^{\alpha} \cdot \exp\left(\frac{E_a}{k_B \cdot T_{jm}}\right) \cdot \left(\frac{C + t_{on}^{\gamma}}{C + 1}\right) \cdot ar^{\beta_1 \cdot dT_j + \beta_0} \cdot f_{Diode} \tag{1.1}$$

The first factor A is a general scaling factor. The second factor represents the Coffin-Manson law, which relevant to the junction temperature fluctuation dT_j [29]. The third factor is an Arrhenius term [29], which describes the impact of the mean junction temperature T_{jm}, where E_a, k_B are the activation energy and Boltzmann constant, respectively. The forth factor expresses the dependence on the load pulse duration t_{on}. Besides, the fifth and sixth factor reflects the influence of the aspect ratio ar and chip thickness. It should be noted that A, α, C, γ, β_1, β_0, f_{Diode} are certain values determined by test results.

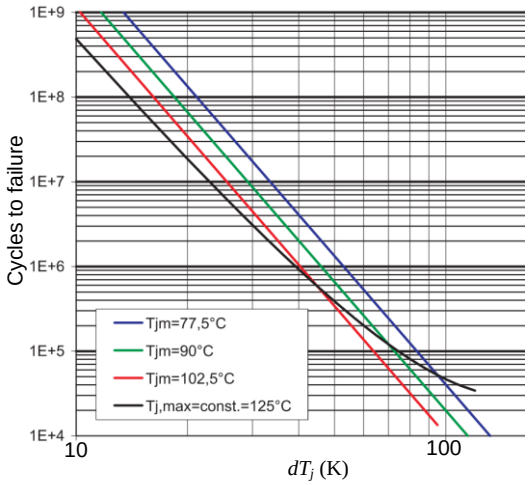

Fig. 1.7. Typical example of cycles to failure vs. mean junction temperature and junction temperature fluctuation of IGBT module [30].

Since the parameters for lifetime model can be different due to various failure mechanisms of the power device and various manufacturers. For simplicity, this study only focuses on the factors of the junction temperature fluctuation, mean junction temperature and the load pulse duration. An example of power cycles to failure is shown in Fig. 1.7 for an IGBT module.

1.3.2 Grid supports

Compared to the conventional power plants, which are composed of synchronous generators, the wind turbine generators consists mainly of the variable speed DFIGs or the synchronous generators with back-to-back power converters as the power controller. Recent grid codes [31]-[34] demand the wind power plants to behave as much as similar to the conventional power plant in order to maintain power system reliability and stability. Although different countries have issued and revised their own grid codes, they have some requirements in common, which includes the normal operation and performance during grid disturbance operation.

A. Normal operation

For normal grid condition, the active power control requirement is defined as an ability to adjust the active power output with respect to either frequency deviations or the commands from the Transmission System Operator (TSO). According to the Danish grid code, a typical relationship between the active power and frequency is graphically represented in Fig. 1.8(a). Due to the power curtailment capability to limit a wind turbine production to any power set-point in the range of 20-100% of its rated power, two examples, one without reduction (black curve) and one with 50% reduction (red curve) of allowed maximum production, are shown in respect to the lower frequency limit (48.7 Hz) and upper frequency limit (51.3 Hz), in which the frequency range from 49.85 Hz to 50.15 Hz is a dead-band to avoid oscillations in normal operation.

Reactive power support during normal operation is the reactive power regulation in response to the voltage variation of the Point of Common Coupling (PCC). Fig. 1.8(b) shows the reactive power and active power curve stated in German grid code [34]. Either the over-excited or the under-excited reactive power might be provided in the

case of a decrease or increase of the PCC voltage. Moreover, the support can be realized as a reactive power requirement or as a power factor requirement [31].

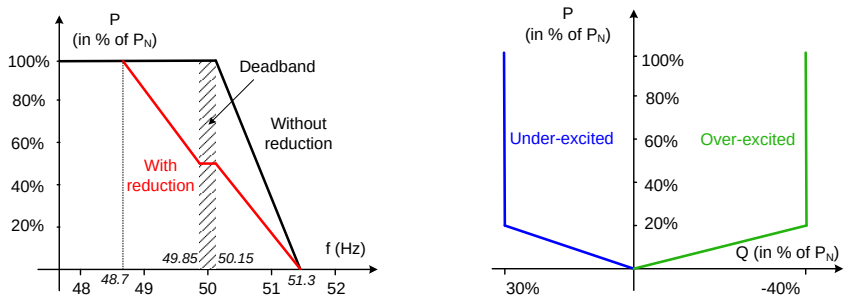

Fig. 1.8. Grid support during normal operation. (a) Active power and frequency curve stated in Danish grid code [33], (b) Reactive power and active power curve stated in German grid code [34].

B. Grid disturbances

Grid disturbances in form of voltage dips or swells can typically lead to disconnection of the wind turbines, which may cause power system instability and even blackout. In order to avoid this phenomenon, the grid code requires the wind power plant to operate uninterrupted, and even to support the voltage recovery during the grid disturbance. These common features are generally defined in grid codes as Voltage Ride Through (VRT) and Reactive Current Injection (RCI) capabilities.

VRT covers terms of Low Voltage Ride-Through (LVRT) and High Voltage Ride-Through (HVRT), and make it possible to withstand symmetrical and asymmetrical faults without disconnection from the grid. For instance, the LVRT and HVRT capabilities stated in the German grid code are shown in Fig. 1.9(a). In respect to LVRT capability, the wind turbine system is only allowed to disconnect below the red line, which implies that the wind power plant is forced to overcome zero voltage for at least 150 ms. Similarly, according to the HVRT requirement, the wind turbine system may be disconnected from the grid if the case is located above the blue line, in which the 120% grid voltage is affordable during 100 ms.

Simultaneously, during the grid fault, RCI is needed to further support the voltage recovery, and the active current can be reduced in order to fulfill the reactive power requirement. As described in Fig. 1.9(b), 100% reactive current is injected if the grid

voltage is below 0.5 pu. On the contrary, the under-excited reactive current is preferred in case of the voltage swell in order to support the grid voltage. Meanwhile, for the offshore wind farms, the grid voltage between 0.95 and 1.05 pu is regarded as the dead-band boundary for the RCI [34].

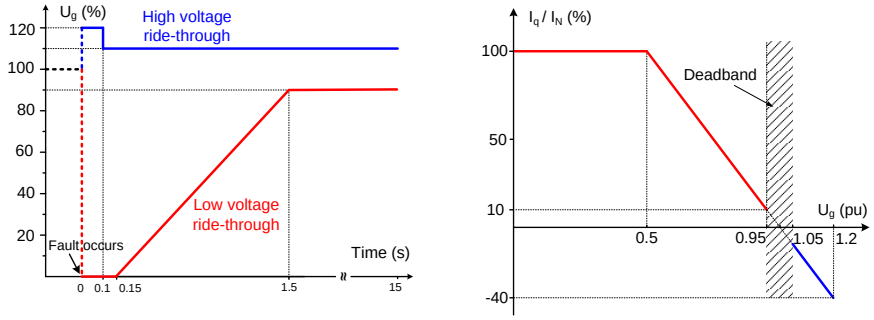

(a) (b)

Fig. 1.9. Grid support under grid disturbance stated in German grid code [34]. (a) Voltage ride through requirement, (b) Reactive current injection.

1.3.3 Control strategies

As listed in Table 1-1, although different wind turbine manufacturers may have their own favorite generators – DFIG, Permanent-Magnet Synchronous Generator (PMSG), electrically excited SG/IG, the control structure for the wind turbine system is almost the same. As shown in Fig. 1.10, the general control scheme for modern wind turbine system includes typical three control units [7], [12], [35] – power converter control strategy (Level I), wind turbine control strategy (Level II) and grid integration control strategy (Level III).

The target of the control strategies are – Level I is to handle the electrical energy transfer from the generator to the grid and to provide grid support in terms of relevant voltage and current control. The active and reactive power command actually comes from the upper control unit – Level II. At this control unit, the tracking of the active power and reactive power reference is realized by the control of the generator stator current and grid-side converter current. Moreover, in order to decouple the generator-side converter and the grid-side converter, the dc-link voltage is required to become constant. For the traditional vector control, the grid synchronization, such as Phase-

Lock Loop (PLL) technology, is also implemented to provide accurate phase information.

Level II control unit is generally designed to obtain the maximum electrical power at normal operation and limit the active power during the grid fault by the response of the mechanical part. Normally, with the help of the Maximum Power Point Tracking (MPPT), the active power reference can be predicted by the generator speed. If the wind speed is higher than the rated wind speed or the fault ride-through operation is enabled, the obtained mechanical power is actively reduced by means of the pitch control. Moreover, providing reactive power is at the expense of the losses and more power rating.

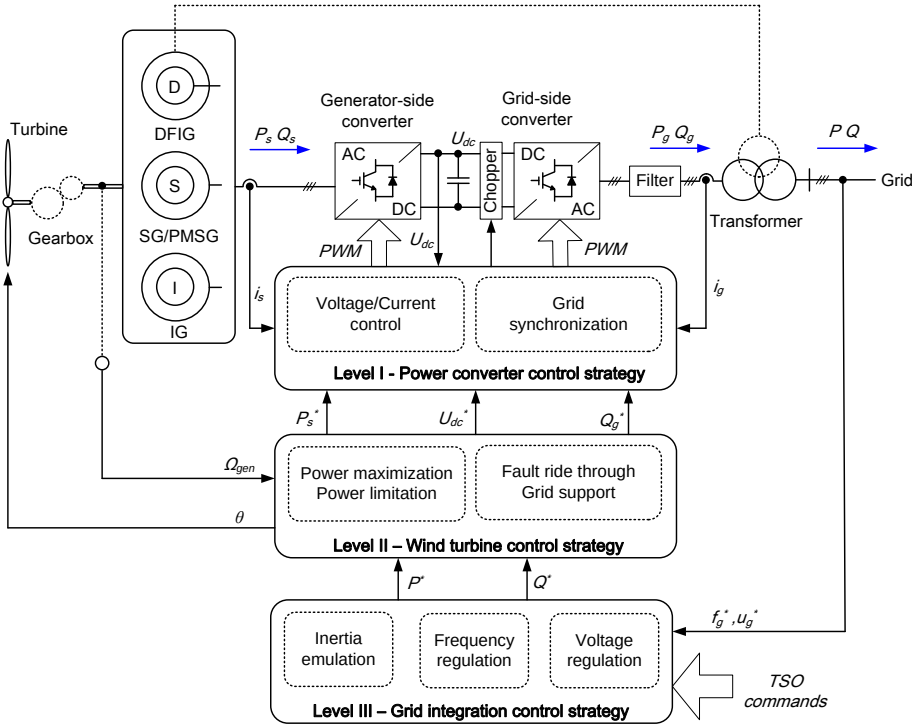

Fig. 1.10. General control strategy for modern wind turbine systems.

Level III control unit is dedicated to the grid integration of the wind turbine, including the inertia emulation, frequency regulation (droop characteristics) and voltage regulation [36]. Based on the commands from the TSO, the wind power plant

can participate in the grid regulation in order to provide ancillary services for the power system and perform like a conventional synchronous generator based power plant.

1.4 Thesis hypothesis and objectives

As the multi-MW wind turbine system is still the best-seller of the wind power market, the reliability and cost of the wind power is of more and more importance. Correspondingly, the objectives of this project are,

1. How to generate a universal approach to assess the reliability and cost of the wind turbine system? How can they take into account the mission profiles and grid codes?
2. In the case of the grid fault, how does the stress look like seen from the reliability perspective? Are there any control strategies to improve the power converter performance from a reliability point of view?

Based on the above mentioned research problems, the scope of this study is to design and analyze the traditional and commonly-used two-level power converter for both the partial-scale power converter and the full-scale power converter, in respect to their efficiency, thermal stress, reliability and energy cost. Low voltage 2 MW wind turbine systems are used for case studies. In order to enable the equal sharing of the current in the paralleled devices at the rated loading, different numbers of Danfoss P3 power modules are selected for both topologies to do the assessment. Considerable analytical and new simulation tools will be developed to evaluate the loss profile, thermal profile, lifetime estimation and cost of energy for use at Danfoss Silicon Power GmbH.

1.5 Thesis outline

This thesis is presented in the form of a collection of papers, and consists of two parts: Part I – Report and Part II – Publications. Part I is a brief summary done throughout the research and it contains 7 chapters. The basic frame of the research work is shown in Fig. 1.11, and is organized as follows:

Chapter 1 gives the background and motivation of this research, and investigates the state-of-the-art wind power technologies. Then, the objectives and outline of thesis are addressed and listed.

Chapter 2 addresses the loading stress of the wind power converter. Two typical 2 MW configurations – partial-scale power converter based DFIG system and full-scale power converter based direct-drive PMSG system are designed and modeled. Afterwards, according to the loss breakdown of each power device, the total efficiency curves between the two configurations are studied and compared.

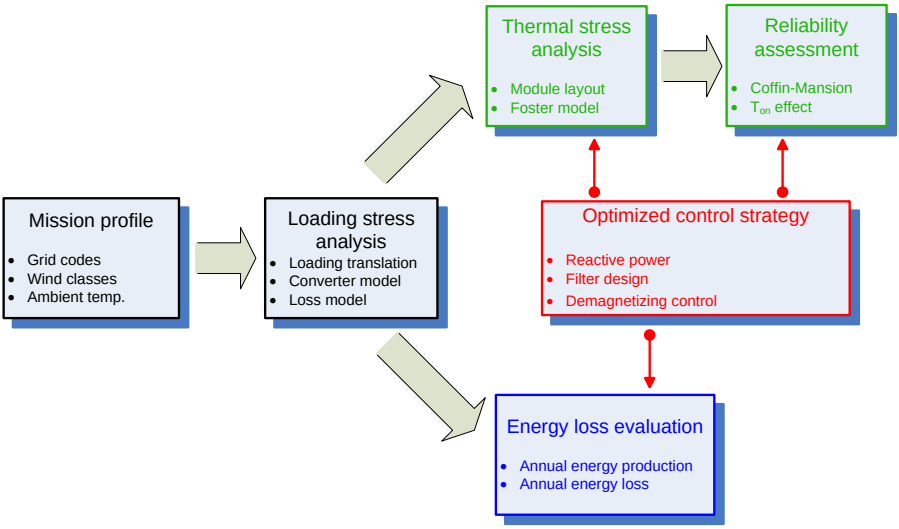

Fig. 1.11. Framework of the research topics in this thesis.

Chapter 3 evaluates the thermal stress of the mainstream wind power converter based on the power loss calculated in Chapter 2. Due to the additional amount of the reactive power required by the modern grid codes, the effects of the reactive power on the thermal behavior of the power device is analyzed in respect to the DFIG and the PMSG system. Finally, during wind gusts, an optimized thermal behavior can be achieved by circulating the reactive power within the DFIG system itself.

In Chapter 4, the lifetime and the reliability of the wind power converter are investigated and assessed both in the DFIG system and in the PMSG system, in which the mission profile and the grid codes are taken into account. Moreover, an optimized reactive power flow in the DFIG system is proposed for a balanced lifetime between the back-to-back power electronics converters.

Chapter 5 deals with the energy loss of wind turbine system considering the modern grid codes. The additional energy loss caused by the reactive power injection is studied

for the DFIG and PMSG system, respectively. Then, an improved grid filter design is proposed to optimize the cost of reactive power in the DFIG system.

In Chapter 6, the internal and external challenges for the DFIG system are described and addressed. During the LVRT operation, if the reactive current injection of the modern grid codes is taken into account, an optimized coefficient of the demagnetizing current control is designed. It is able to keep the minimum thermal stress of the rotor-side converter, which meets with the long-term reliable operation of the wind turbine system.

Chapter 7 concludes the thesis, summarizes the main contributions of this research, and discusses some potential proposals for future work.

The obtained results of this thesis are disseminated via a number of papers published in international conference proceedings and journals. A list of the published papers is given below:

Journal papers

[J.1] **D. Zhou**, F. Blaabjerg, M. Lau, M. Tonnes, "Thermal behavior optimization in multi-MW wind power converter by reactive power circulation," *IEEE Trans. on Industry Applications*, vol. 50, no. 1, pp. 433-440, Jan. 2014. (Also *in Proc. of APEC 2013*, pp. 2863-2870, 2013)

[J.2] **D. Zhou**, F. Blaabjerg, M. Lau, M. Tonnes, "Thermal cycling overview of multi-megawatt two-level wind power converter at full grid code operation," *IEEJ Journal of Industry Applications*, vol. 2, no. 4, pp. 173-182, Jul. 2013.

[J.3] **D. Zhou**, F. Blaabjerg, M. Lau, M. Tonnes, "Optimized reactive power flow of DFIG power converters for better reliability performance considering grid codes," *IEEE Trans. on Industrial Electronics*, IEEE early access.

Conference papers

[C.1] F. Blaabjerg, K. Ma, **D. Zhou**, "Power electronics and reliability in renewable energy systems," *in Proc. of ISIE 2012*, pp. 19-30, 2012.

[C.2] **D. Zhou**, F. Blaabjerg, M. Lau, M. Tonnes, "Thermal analysis of multi-MW two-level wind power converter," *in Proc. of IECON 2012*, pp. 5858-5864, 2012.

[C.3] H. Wang, **D. Zhou**, F. Blaabjerg, "A reliability-oriented design method for power electronic converters," *in Proc. of APEC 2013*, pp. 2921-2928, 2013.

[C.4] **D. Zhou**, F. Blaabjerg, M. Lau, M. Tonnes, "Reactive power impact on lifetime prediction of two-level wind power converter," *in Proc. of PCIM 2013*, pp. 564-571, 2013.

[C.5] **D. Zhou**, F. Blaabjerg, M. Lau, M. Tonnes, "Thermal profile analysis of doubly-fed induction generator based wind power converter with air and liquid cooling methods," *in Proc. of EPE 2013*, pp. 1-10, 2013.

[C.6] **D. Zhou**, F. Blaabjerg, "Thermal analysis of two-level wind power converter under symmetrical grid fault," *in Proc. of IECON 2013*, pp. 1904-1909, 2013.

[C.7] **D. Zhou**, F. Blaabjerg, M. Lau, M. Tonnes, "Thermal behavior of doubly-fed Induction generator wind turbine system during balanced grid fault," *in Proc. of APEC 2014*, pp. 3076-3083, 2014.

[C.8] **D. Zhou**, F. Blaabjerg, T. Franke, M. Tonnes, M. Lau, "Reduced cost of reactive power in doubly-fed induction generator wind turbine system with optimized grid filter," *in Proc. of ECCE 2014*, pp. 1490-1499, 2014.

[C.9] **D. Zhou**, F. Blaabjerg, T. Franke, M. Tonnes, M. Lau, "Reliability and energy loss in full-scale wind power converter considering grid codes and wind classes," *in Proc. of ECCE 2014*, pp. 3067-3074, 2014.

[C.10] **D. Zhou**, F. Blaabjerg, "Dynamic thermal analysis of DFIG rotor-side converter during balanced grid fault," *in Proc. of ECCE 2014*, pp. 3097-3103, 2014.

References

[1] GWEC. Global Wind Report 2013. (website: www.gwec.net)
[2] WWEA. 2012 Annual Report. (website: www.wwindea.org)
[3] European Commission. The EU Climate and Energy Package. (website: ec.europa.eu/clima/policies/package)
[4] International Energy Agency. China Wind Energy Development Roadmap 2050. (website: www.iea.org)
[5] C. Kost, J. Mayer, J. Thomsen, Levelized cost of electricity renewable energy technologies. (website: www.ise.fraunhofer.de)
[6] Z. Chen, J. M. Guerrero, F. Blaabjerg, "A review of the state of the art of power electronics for wind turbines," *IEEE Trans. on Power Electronics*, vol. 24, no. 8, pp. 1859-1875, Aug. 2009.
[7] F. Blaabjerg, Z. Chen, S. B. Kjaer, "Power electronics as efficient interface in dispersed power generation systems," *IEEE Trans. on Power Electronics*, vol. 19, no. 5, pp. 1184-1194, Sep. 2004.

[8] M. Liserre, R. Cardenas, M. Molinas, J. Rodriguez, "Overview of multi-MW wind turbines and wind parks," *IEEE Trans. on Industrial Electronics*, vol. 58, no. 4, pp. 1081-1095, Apr. 2011.

[9] H. Polinder, J. A. Ferreira, B. B. Jensen, A. B. Abrahamsen, K. Atallah, R. A. McMahon, "Trends in wind turbine generator systems," *IEEE Journal of Emerging and Selected Topics in Power Electronics*, vol. 1, no. 3, pp. 174-185, Sep. 2013.

[10] North American wind power. Top 15 Wind turbine suppliers of 2013 revealed. (Website: http://www.nawindpower.com/e107_plugins/content/content.php?content.12710)

[11] F. Blaabjerg, M. Liserre, K. Ma, "Power electronics converters for wind turbine systems," *IEEE Trans. on Industry Applications*, vol. 48, no. 2, pp. 708-719, Mar. 2012.

[12] F. Blaabjerg, K. Ma, "Future on power electronics for wind turbine systems," *IEEE Journal of Emerging and Selected Topics in Power Electronics*, vol. 1, no. 3, pp. 139-152, Sep. 2013.

[13] S. Faulstich, P. Lyding, B. Hahn and P. J. Tavner "Reliability of offshore turbines-identifying the risk by onshore experience," *in Proc. of European Offshore Wind Energy Conference and Exposition*, pp. 1-10, 2009.

[14] B. Hahn, M. Durstewitz, K. Rohrig "Reliability of wind turbines - experience of 15 years with 1500 WTs," *Wind Energy: Proceedings of the Euromech Colloquium*, pp. 329-332, Springer-Verlag, Berlin.

[15] R. Johan, B. L. Margareta, "Survey of failures in wind power systems with focus on Swedish wind power plants during 1997-2005," *IEEE Trans. on Energy Conversion*, vol. 22, no. 1, pp. 167-173, Mar. 2007.

[16] P. J. Tavner, J. Xiang, F. Spinato, "Reliability analysis for wind turbines," *Wind Energy*, vol. 10, no. 1, pp. 1-18, 2007.

[17] H. Wang, M. Liserre, F. Blaabjerg, P. Rimmen, J. Jacobsen, T. Kvisgaard, J. Landkildehus, "Transitioning to physics-of-failure as a reliability driver in power electronics," *IEEE Journal of Emerging and Selected Topics in Power Electronics*, vol. 2, no. 1, pp. 97-114, Mar. 2014.

[18] ZVEL, Handbook for robustness validation of automotive electrical/electronic modules, Jun. 2008.

[19] Y. Song, B. Wang, "Survey on reliability of power electronic systems," *IEEE Trans. on Power Electronics*, vol. 28, no. 1, pp. 591-604, Jan. 2013.

[20] C. Busca, R. Teodorescu, F. Blaabjerg, S. Munk-Nielsen, L. Helle, T. Abeyasekera, P. Rodriguez, "An overview of the reliability prediction related aspects of high power IGBTs in wind power applications," *Microelectronics Reliability*, vol. 51, no. 9-11, pp. 1903-1907, 2011.

[21] D. Hirschmann, D. Tissen, S. Schroder, R.W. De Doncker, "Reliability prediction for inverters in hybrid electrical vehicles," *IEEE Trans. on Power Electronics*, vol. 22, no. 6, pp. 2511-2517, Nov. 2007.

[22] N. Kaminski, "Load-cycle capability of HiPaks," ABB Application Note 5SYA 2043-01, 2004.

[23] O. S. Senturk, L. Helle, S. Munk-Nielsen, P. Rodriguez, R. Teodorescu, "Power capability investigation based on electro-thermal models of press-pack IGBT three-level NPC and ANPC VSCs for multi-MW wind turbines," *IEEE Trans. on Power Electronics*, vol. 27, no. 7, pp. 3195-3206, Jul. 2012.

[24] H. Wang, K. Ma, F. Blaabjerg, "Design for reliability of power electronic systems," *in Proc. of IECON 2012*, pp.33-44, 2012.

[25] F. Blaabjerg, K. Ma, D. Zhou, "Power electronics and reliability in renewable energy systems," *in Proc. of ISIE 2012*, pp.20-30, 2012.

[26] Y. Avenas, L. Dupont, Z. Khatir, "Temperature measurement of power semiconductor devices by thermo-sensitive electrical parameters – a review", *IEEE Trans. on Power Electronics*, vol. 27, no. 6, pp. 3081-3092, Jun. 2012.

[27] W. Lixiang, J. McGuire, R. A. Lukaszewski, "Analysis of PWM frequency control to improve the lifetime of PWM inverter," *IEEE Trans. on Industry Applications*, vol. 47, no. 2, pp. 922-929, Mar. 2011.
[28] U. Scheuermann, R. Schmidt "A new lifetime model for advanced power modules with sintered chips and optimized Al wire bonds," *in Proc. of PCIM 2013*, pp. 810-817, 2013.
[29] R. Amro, J. Lutz, A. Lindemann, "Power cycling with high temperature swing of discrete components based on different technologies," *in Proc. of PESC 2004*, pp. 2593-2598, 2004.
[30] Wintrich, U. Nicolai, T. Reimann, "Semikron Application Manual," pp. 128, 2011.
[31] M. Altin, O. Goksu, R. Teodorescu, P. Rodriguez, B. B. Jensen, L. Helle, "Overview of recent grid codes for wind power integration," *in Proc. of OPTIM 2010*, pp. 1152-1160, 2010.
[32] M. Tsili, S. Papathanassiou, "A review of grid code technical requirements for wind farms," *IET Renewable Power Generation*, vol. 3, no. 3, pp. 308-332, Sep. 2009.
[33] Energinet. Wind turbines connected to grids with voltages below 100 kV, May 2004.
[34] E.ON-Netz. Requirements for offshore grid connections, Apr. 2008.
[35] G. Abad, J. Lopez, M. Rodriguez, et al. Doubly Fed Induction Machine: Modeling and Control for Wind Energy Generation Applications. Wiley-IEEE Press, 2011.
[36] A. Mullane, M. O'Malley, "The inertial response of induction-machine-based wind turbines," *IEEE Trans. on Power Systems*, vol. 20, no. 3, pp. 1496-1503, Aug. 2005.

Chapter 2

Power device loadings in mainstream wind power converter

This chapter describes the design and modeling of the mainstream wind turbine systems, which is mainly focused on the loss dissipation of the power converter.

2.1 Basic design for typical configurations

It is known that the partial-scale power converter is always realized by a Doubly-Fed Inductor Generator (DFIG), while the full-scale power converter normally matches a direct-drive Permanent Magnet Synchronous Generator (PMSG). For simplicity, these two configurations are called the DFIG system and the PMSG system, in which a 2 MW wind turbine is selected for the case studies. The relationship between the wind speed, the turbine speed and the output power is shown in Fig. 2.1 [1], [2]. If a wind speed changes from the cut-in speed 4 m/s until the cut-off speed 25m/s, the speed of turbine rotor varies from 11 rpm to 19 rpm for the DFIG system, while the minimum rotor speed becomes 6 rpm for the PMSG system. It can be seen that the wind speed at 8.4 m/s is the synchronous operation point for the DFIG system.

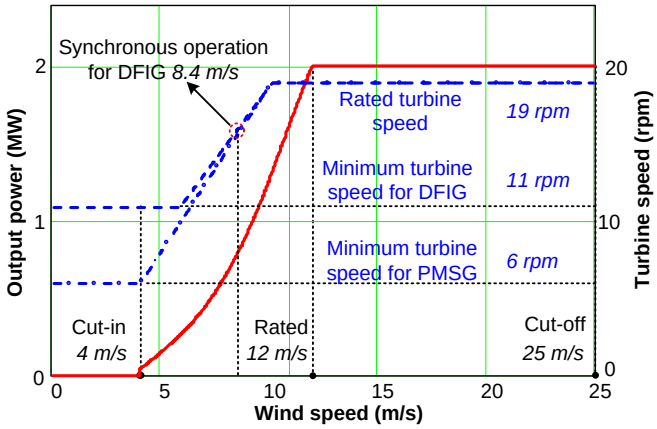

Fig. 2.1. Wind speed, turbine rotor speed and output power of the selected DFIG and PMSG systems.

Since the DFIG and the PMSG generator data is listed in Table 2-1 [3], [4], the loading of the back-to-back power converters at the rated power can be roughly calculated in Table 2-2. Due to their positions, the back-to-back power converters are named as the grid-side converter and the rotor-side converter/generator-side converter. It is noted that, in order to implement the low voltage power module with 1.7 kV, the dc-link voltage U_{dc} is kept at 1050 V. Moreover, the switching frequency f_s is usually very low for the multi-MW power converter, and is selected at 2 kHz.

Table 2-1 Basic data for 2 MW DFIG and PMSG [3], [4]

	DFIG	**PMSG**
Number of pole pairs	2	102
Gear ratio	94.7	/
Rated shaft speed [rpm]	1800	19
Rated fundamental frequency f_e [Hz]	10	32.3
Stator leakage inductance L_{ls} [mH]	0.038	0.276
Magnetizing inductance L_m [mH]	2.91	
Rotor leakage inductance L_{lr}, [mH]	0.064	/
Stator/rotor turns ratio k	0.369	/

Table 2-2 Data of two-level back-to-back power converters

	DFIG	**PMSG**
Converter rated power [kW]	400	2000
DC-link voltage U_{dc} [V_{dc}]	1050	
Switching frequency f_s [kHz]	2	
Grid-side converter		
Rated output voltage [V_{rms}]	690	690
Rated current [A_{rms}]	335	1674
Filter inductance L_q [mH]	0.50	0.15
Rotor-side converter/Generator-side converter		
Rated output voltage [V_{rms}]	374	554
Rated current [A_{rms}]	618	2085

2.1.1 DFIG configuration

Based on the characteristic of the DFIG, the stator active power and reactive power can be regulated by the rotor current [5]-[8]. As shown in Fig. 2.2, since majority of the active power flows into the grid through the stator of the generator, the rotor-side converter handles the rest of the slip power as well as the excitation power. The grid-side converter is designed to keep the dc-link constant in order to decouple the back-to-back power converters from each other. Furthermore, some amount of the reactive power can be provided in the case of the grid fault or in accordance with the demand from the Transmission System Operator (TSO).

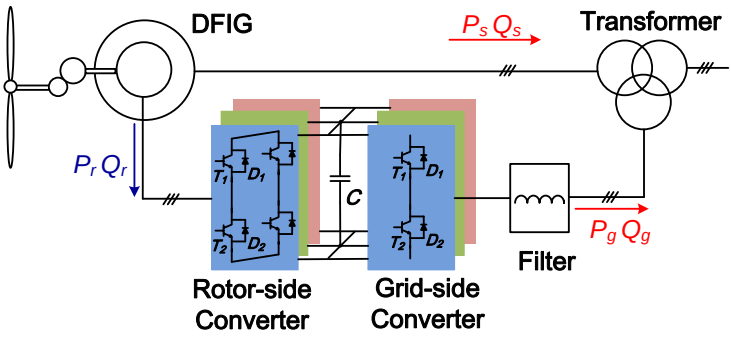

Fig. 2.2. Two-level back-to-back power converters of the DFIG system.

As listed in Table 2-2, it can be seen that the loading at the rated power between the power converters are quite unequal. Moreover, as the rotor-side converter is the main performing converter to ride through the fault situation [9], the design of the back-to-back power converters is chosen with high power capability. It leads to the two paralleled 1 kA/1.7 kV power modules employed in each arm the rotor-side converter, and only one power module used in each arm of the grid-side converter.

2.1.2 PMSG configuration

The typical PMSG system equipped with a full-scale power converter is shown in Fig. 2.3, which consists of a generator-side converter and a grid-side converter [10]-[13]. Compared with the DFIG system, both the converters are designed to handle the full power of the wind turbine, which implies more power modules to realize a higher

power. According to Table 2-2, four paralleled 1 kA/ 1.7 kV power modules are used to form a arm both in the generator-side converter and the grid-side converter.

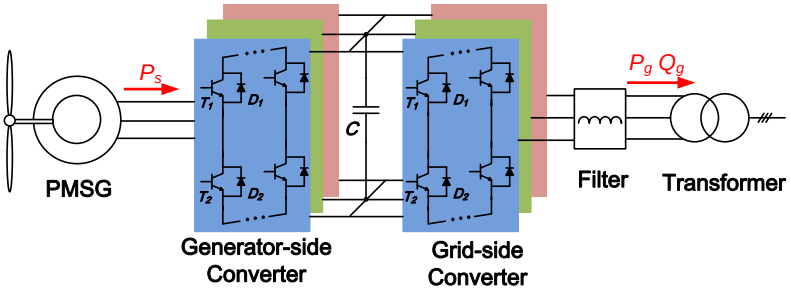

Fig. 2.3. Two-level back-to-back power converters of the PMSG system.

2.2 Loss breakdown of power device

2.2.1 Power loss model

The losses consumed in power semiconductor devices consist of the conduction loss (on-state loss) and the switching loss (dynamic loss) [14], [15].

The conduction loss in each power device P_{con} is an average loss within a fundamental frequency f_a [16],

$$P_{con} = f_a \cdot (\sum_{n=1}^{N} v_{CE}(|i_a(n)|) \cdot |i_a(n)| \cdot T_1(n) + \sum_{n=1}^{N} v_F(|i_a(n)|) \cdot |i_a(n)| \cdot (T_s - T_1(n))) \quad (2.1)$$

where the first term T_{con} is the conduction loss of the IGBT, and the second term D_{con} is the conduction loss of the freewheeling diode. i_a is the sinusoidal current through the power device, T_1 is the ON time of the upper bridge within a switching period T_s, v_{CE}, v_F are voltage drops of the IGBT and the diode, which are normally given by the manufacturer. N is the carrier ratio, which denotes the total switching times within a fundamental frequency, and the subscript n is the n^{th} switching pattern. It should be noted that the conduction loss in (2.1) is aimed for the entire bridge. For each power semiconductor (the IGBT or the diode), the loss will only be half.

As the v_{CE} and v_F curves are closely related to the junction temperature (25 ℃, 125 ℃ or 150 ℃), the characteristic of voltage drops at 150 ℃ are chosen as the worst case, and they can be expressed in terms of polynomial expression. Besides, the space vector modulation is widely used in three-phase three-wire systems due to its higher

utilization of the dc-link voltage. In order to guarantee the minimum harmonic, the symmetrical sequence arrangement of the non-zero vector and the zero-vector is normally used, so the conduction time of the upper bridge and lower bridge can be calculated by the phase angle of the voltage [17]. Furthermore, the phase angle between the converter output voltage and the current decides phase range of the current polarity, which is closely related to the conduction loss distribution between the IGBT and the diode.

On the other hand, the switching loss in each power device P_{sw} can be calculated as,

$$P_{sw} = \frac{U_{dc}}{U_{dc}^{*}} \cdot f_a \cdot (\sum_{n=1}^{N} (E_{on}(|i_a(n)|) + E_{off}(|i_a(n)|)) + \sum_{n=1}^{N} E_{rr}(|i_a(n)|)) \tag{2.2}$$

Similar as (2.1), the first term is the switching loss for the IGBT T_{sw}, and the second term D_{sw} is the switching loss for the freewheeling diode. E_{on}, E_{off} are turn-on and turn-off energy dissipated by the IGBT, while the E_{rr} is the reverse-recovery energy loss consumed by the diode, which are usually also tested by the manufacturer at a certain dc-link voltage U_{dc}^{*}. It is assumed that the switching energy is proportional to the actual dc-link voltage U_{dc}. With the help of curve fitting of the dynamical energy loss by using polynomial expression, the switching loss of the power semiconductor can be calculated by the accumulation of the switching patterns within one fundamental frequency. Similarly, it is noted that the switching loss in (2.2) is calculated for the entire bridge.

2.2.2 Grid-side converter

Based on equations of the conduction loss and the switching loss, the next step is to translate the active power and reactive power into the relevant voltage and current. Consequently, the grid-side converter and the rotor-side converter/generator-side converter will be uniformly addressed regardless of the DFIG system or the PMSG system.

A single inductor is used as a grid filter of the grid-side converter as shown in Fig. 2.4. If the current flow into the converter is defined as the reference direction, the current and voltage relationship between the grid and the converter become,

$$\overline{I_g} = I_{g\_\mathrm{Re}} + jI_{g\_\mathrm{Im}} \tag{2.3}$$

$$\overline{U_C} = U_{g\_\mathrm{Re}} + X_g \cdot I_{g\_\mathrm{Im}} + j(-X_g \cdot I_{g\_\mathrm{Re}}) \tag{2.4}$$

where X_g denotes filter reactance, U_g denotes the grid voltage, I_g and U_c denote the current and voltage of grid-side converter, respectively. Subscript *Im* and *Re* represents the real and imaginary part of the phasor. The phasor diagram of the grid-side converter output voltage and current is shown in Fig. 2.5. It is noted that the power flow of the grid-side converter in the DFIG system is bi-directional, while the grid-side converter of the PMSG system only provides the active power to the grid. A small phase difference between the grid and converter voltage can be found due to the voltage drop across the inductor filter, thus the phase angle of the converter output voltage and current can be deduced.

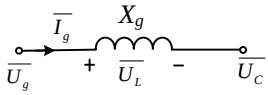

Fig. 2.4. Single phase L filter of the grid-side converter in phasor diagram.

Based on the grid-side converter model and the loss model, the process to calculate power loss of the grid-side converter can be summarized in Fig. 2.6, where D_g denotes the duty cycle in each switching pattern. Together with several typical wind speeds listed in Table 2-3, the loss profile of the each power device in the grid-side converter are then shown in Fig. 2.7 in terms of the DFIG system and the PMSG system.

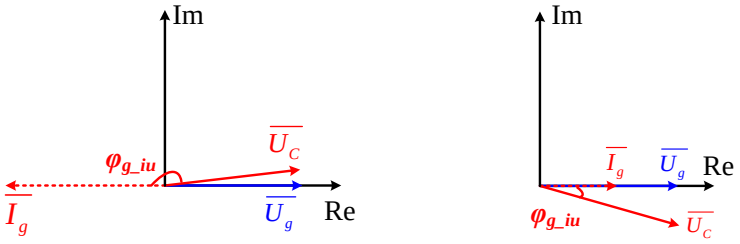

(a) (b)

Fig. 2.5. Phasor diagram of the grid-side converter output voltage and current. (a) Power flowing into the grid; (b) Power flowing out from the grid.

For the DFIG system, it is evident that the power loss becomes very low at the synchronous operation point due to the fact that no active power is flowing through the power converter. In respect to the conduction loss, because of the reversal of the power

direction, the IGBT dominates at super-synchronous mode, while the freewheeling diode accounts for the major part at sub-synchronous mode. In respect to the switching loss, the IGBT always dissipates higher switching loss than the diode due to higher energy loss in IGBT switching and compared to the diode.

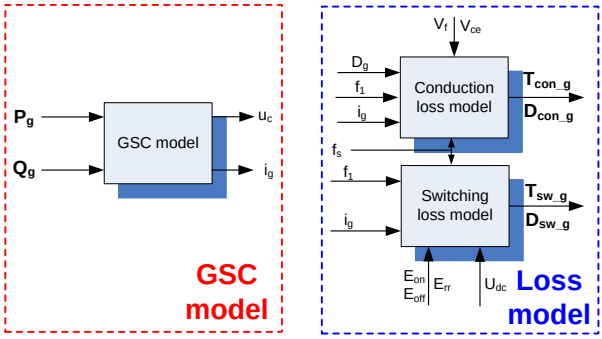

Fig. 2.6. Block diagram to calculate the power loss for the grid-side converter.

Table 2-3 Generator and converter data at different wind speeds (DFIG/PMSG)

Wind speed [m/s]	**Generated power [MW]**	**Turbine speed [rpm]**	**Slip**	**Fundamental frequency [Hz]**
5.9	0.26	11/10.1	0.3/0	15/17.2
6.8	0.39	12.7/12.0	0.2/0	10/20.4
7.6	0.55	14.2/13.7	0.1/0	5/23.3
8.4	0.74	15.8/15.4	0.02/0	1/26.2
9.2	0.98	17.2/17.1	-0.1/0	5/29.1
10.1	1.29	19/19	-0.2/0	10/32.3
12	2.00	19/19	-0.2/0	10/32.3
25	2.00	19/19	-0.2/0	10/32.3

For the PMSG system, it can be seen that the power loss increases continuously with higher wind speed until the rated value. The IGBT is always dominating the conduction loss as the power flows into the grid, and the IGBT still consumes the highest switching loss.

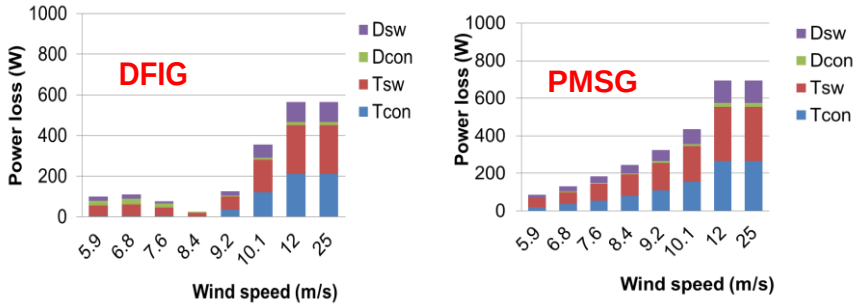

(a) (b)

Fig. 2.7. Loss profile of each power device in the grid-side converter. (a) DFIG system; (b) PMSG system.

2.2.3 Rotor-side converter/Generator-side converter

As the equivalent circuits of the DFIG generator and the PMSG generator are similar, the loss calculation of the rotor-side converter in the DFIG system is taken as an example, and similar approach can be extended to the generator-side converter in the PMSG system.

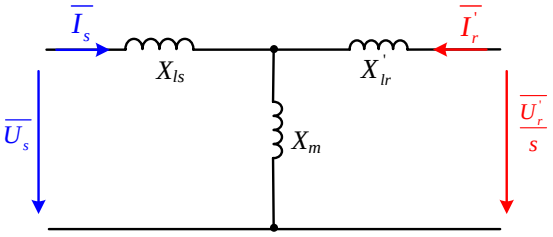

Fig. 2.8. Single phase DFIG equivalent circuit in phasor diagram.

Neglecting the stator resistance and the rotor resistance, the steady-state DFIG equivalent circuit is shown in Fig. 2.8 in terms of the phasor expression. According to the voltage equation and flux equation of the DFIG [18], the voltage and current relationship between the rotor-side $\overline{U_r'}$, $\overline{I_r'}$ and the stator-side $\overline{U_s}$, $\overline{I_s}$ are,

$$\overline{I_r'} = -\frac{X_s}{X_m} I_{s\_\mathrm{Re}} + j \cdot sign(s) \cdot (-\frac{U_{s\_\mathrm{Re}}}{X_m} - \frac{X_s}{X_m} I_{s\_\mathrm{Im}}) \tag{2.5}$$

$$\overline{U_r'} = s \cdot (\frac{X_r}{X_m} U_{s\_\mathrm{Re}} + \frac{\sigma X_r X_s}{X_m} I_{s\_\mathrm{Im}}) - j \cdot (sign(s)) \cdot (s \frac{\sigma X_r X_s}{X_m} I_{s\_\mathrm{Re}}) \tag{2.6}$$

where X_s, X_m and X_r denote stator reactance, the magnetizing reactance and the rotor reactance, respectively. σ is the leakage coefficient, defined as $(X_sX_r-X_m^2)/X_sX_r$. s is the slip value of the induction generator. Moreover, the sign function *sign(s)* means if s is positive, its value becomes 1. Alternatively, if s is negative, its value becomes -1.

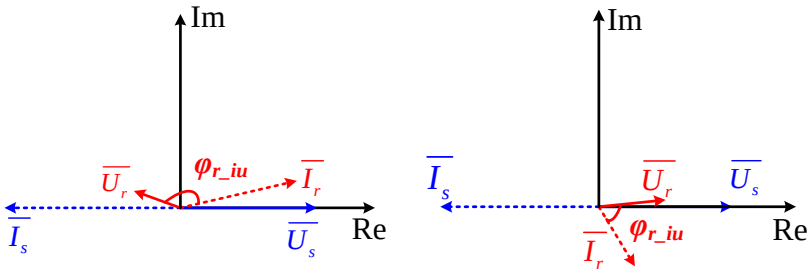

(a) (b)

Fig. 2.9. Phasor diagram of the voltage and current of the DFIG stator and rotor. (a) Super-synchronous mode; (b) Sub-synchronous mode.

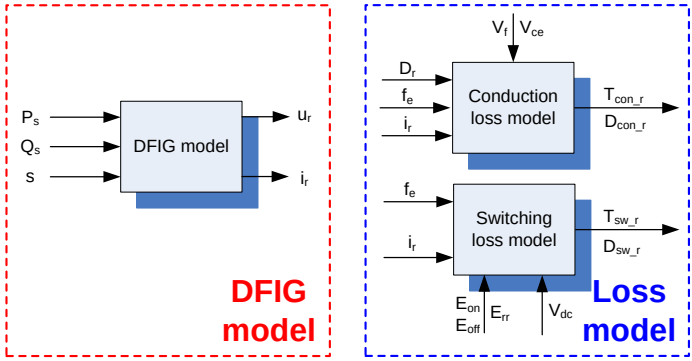

Fig. 2.10. Block diagram to calculate the power loss for the rotor-side converter of the DFIG system.

According to (2.5), (2.6), the phasor diagram of the stator and rotor in the DFIG is shown in Fig. 2.9. At the super-synchronous operation mode, the rotor voltage is almost in opposite direction to the stator voltage, as the slip value is negative. Moreover, the rotor current is almost lagging the rotor voltage 180 º, which indicates that the DFIG is providing the active power through the rotor-side, and the rotor-side converter is supplying the excitation energy to the induction generator. At the sub-synchronous mode, the rotor current is lagging the rotor voltage less than 90 º, implying

that the rotor-side converter provides both the active power and the reactive power to the induction generator.

The flow chart to calculate the power loss of the rotor-side converter can be summarized in Fig. 2.10, which includes the DFIG model and the loss model. Consequently, the loss profile of the rotor-side converter in the DFIG system and the generator-side converter in the PMSG system are shown in Fig. 2.11. It is noted that the loss of both power converters increases continuously with higher wind speed until the rated value. Compared with the two systems, the PMSG system consumes higher power loss than the DFIG system at the rated wind speed due to its higher current loading. It is also worth to mention that, in the DFIG system, a small frequency hysteresis of 1 Hz is introduced around synchronous operation point in order to avoid an unequal load among the three phases caused by the dc current.

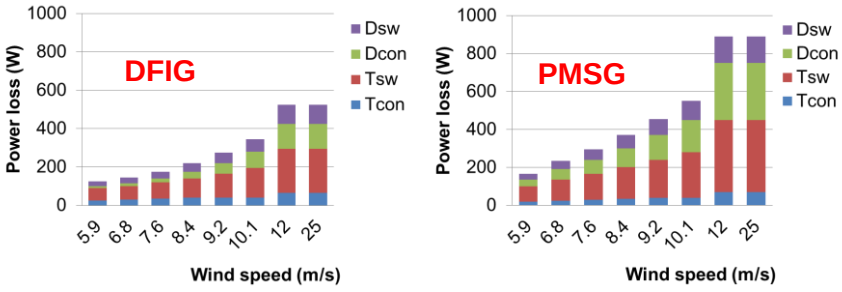

(a) (b)

Fig. 2.11. Loss profile of each power device in the rotor-side converter or the generator-side converter. (a) DFIG system; (b) PMSG system.

2.3 Efficiency comparison

The efficiency is traditional design criteria of the power electronics converter [19]-[20], especially for the MW wind turbine due to the limited nacelle space.

Although the loss produced in the wind turbine system consists of the generator loss, the power converter loss and the grid filter loss, this section considers the efficiency about these two mainstream wind power converters.

Based on the loss profiles of each power device in the DFIG system and the PMSG system, the total loss of the power electronics converter can be calculated and they are shown in Fig. 2.12(a) and Fig. 2.12(b), respectively. It can be seen that regardless of

the wind turbine systems, the rotor-side converter and the generator-side converter have the highest loss. Afterwards, the efficiency of two systems is summarized in Fig. 2.13. Although the power electronics converter of the PMSG system has higher loss than the DFIG, it can be seen that the PMSG system has generally higher efficiency due to the fact that only the slip power flows through the back-to-back power converter in the DFIG system.

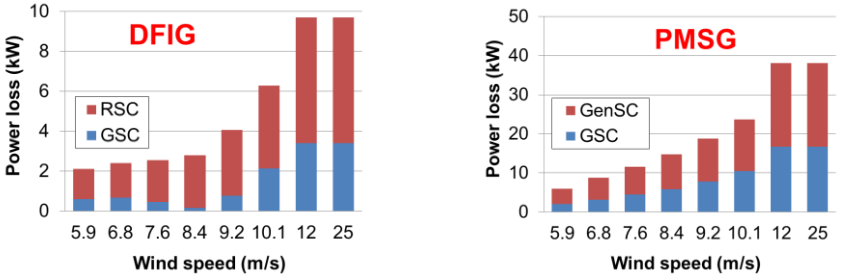

(a) (b)

Fig. 2.12. Loss of power electronics converters in the wind turbine systems. (a) DFIG system; (b) PMSG system.

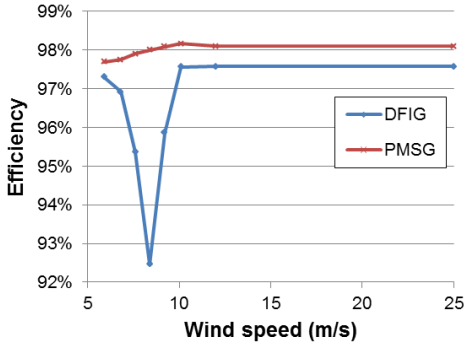

Fig. 2.13. Power converter efficiency curve of the DFIG system and the PMSG system.

2.4 Summary

This chapter describes the power loss dissipation of the power semiconductor devices, which is the basis of reliability assessment and energy loss evaluation for the next chapters. In order to achieve a similar loading of power device at rated power, the selection of the power module in 2 MW DFIG system and PMSG system is discussed.

Moreover, an analytical calculation of the power loss is proposed in order to quickly evaluate the effects of the power module selection, modulation scheme and power factor on the loss dissipation. Finally, the efficiency regarding the power converters of the two systems are compared at different loading conditions.

Relevant attached papers

[A.1] D. Zhou, F. Blaabjerg, M. Lau, M. Tonnes, "Thermal analysis of multi-MW two-level wind power converter," *in Proc. of IECON 2012*, pp. 5858-5864, 2012.

References

[1] Vestas. V80 – 2 MW wind turbine. (website: http://www.vestas.com).
[2] Enercon. E82 – 2 MW wind turbine. (website: http://www.enercon.de).
[3] C. Liu, F. Blaabjerg, W. Chen, D. Xu, "Stator current harmonic control with resonant controller for doubly fed induction generator," *IEEE Trans. on Power Electronics*, vol. 27, no. 7, pp. 3207-3220, Jul. 2012.
[4] H. Li, Z. Chen, H. Polinder, "Optimization of multibrid permanent-magnet wind generator systems," *IEEE Trans. on Energy Conversion*, vol. 24, no. 1, pp. 82-92, Mar. 2009.
[5] R. Pena, J. C. Clare, G. M. Asher, "Doubly fed induction generator using back-to-back PWM converters and its application to variable-speed wind-energy generation,", *in Proc. of Electric Power Application*, pp. 231-241, May 1996.
[6] S. Muller, M. Deicke, R. W. De Doncker, "Doubly fed induction generator systems for wind turbines," *IEEE Industry Applications Magazine*, vol. 8, no. 3, pp. 26-33, May 2002.
[7] Y. Lei, A. Mullane, G. Lightbody, R. Yacamini, "Modeling of the wind turbine with a doubly fed induction generator for grid integration studies," *IEEE Trans. on Energy Conversion*, vol. 21, no. 1, pp. 257-264, Mar. 2006.
[8] F. M. Hughes, O. Anaya-Lara, N. Jenkins, G. Strbac, "Control of DFIG-based wind generation for power network support," *IEEE Trans. on Power Systems*, vol. 20, no. 4, pp. 1958-1966, Nov. 2005.
[9] D. Xiang, L. Ran, P. J. Tavner, S. Yang, "Control of a doubly fed induction generator in a wind turbine during grid fault ride-through," *IEEE Trans. on Energy Conversion*, vol. 21, no. 3, pp. 652-662, Sep. 2006.
[10] M. Chinchilla, S. Arnaltes, J. C. Burgos, "Control of permanent-magnet generators applied to variable-speed wind-energy systems connected to the grid," *IEEE Trans. on Energy Conversion*, vol. 21, no. 1, pp. 130-135, Mar. 2006.
[11] M. E. Haque, M. Negnevitsky, K. M. Muttaqi, "A novel control strategy for a variable-speed wind turbine with a permanent-magnet synchronous generator," *IEEE Trans. on Industry Applications*, vol. 46, no. 1, pp. 331-339, Jan. 2010.
[12] S. M. Muyeen, R. Takahashi, T. Murata, J. Tamura, "A variable speed wind turbine control strategy to meet wind farm grid code requirements," *IEEE Trans. on Power Systems*, vol. 25, no. 1, pp. 331-340, Feb. 2010.
[13] M. Yin, G. Li, M. Zhou, C. Zhao, "Modeling of the wind turbine with a permanent magnet synchronous generator for integration," *in Proc. of IEEE Power Engineering Society General Meeting 2007*, pp.1-6, 2007.
[14] ABB. Applying IGBTs. (website: http://new.abb.com/products/semiconductors).

[15] T. B. Soeiro, J. W. Kolar, "Analysis of high-efficiency three-phase two- and three-level unidirectional hybrid rectifiers," *IEEE Trans. on Industrial Electronics*, vol. 60, no. 9, pp. 3589-3601, Sep. 2013.

[16] D. Zhou, F. Blaabjerg, M. Lau, M. Tonnes, "Thermal analysis of multi-MW two-level wind power converter," *in Proc. of IECON 2012*, pp. 5862-5868, 2012.

[17] K. Zhou, D. Wang, "Relationship between space-vector modulation and three-phase carrier-based PWM: a comprehensive analysis," *IEEE Trans. on Industrial Electronics*, vol. 49, no. 1, pp. 186-196, Feb. 2002.

[18] G. Abad, J. Lopez, M. Rodriguez, et al. Doubly Fed Induction Machine: Modeling and Control for Wind Energy Generation Applications. Wiley-IEEE Press, 2011.

[19] R. Takahashi, H. Ichita, J. Tamura, M. Kimura, M. Ichinose, M. Futami, K. Ide, "Efficiency calculation of wind turbine generation system with doubly-fed induction generator," *in Proc. of International Conference on Electrical Machines (ICEM) 2010*, pp. 1-4, 2010.

[20] A. G. Abo-Khalil, H. Park, D. Lee, "Loss minimization control for doubly-fed induction generators in variable speed wind turbines," *in Proc. of IECON 2007*, pp. 1109-1114, 2007.

Chapter 3

Thermal stress of wind power converter

On the basis of the loss breakdown analyzed in Chapter 2, this chapter further describes the thermal behavior of the wind power converter according to the electrical-thermal model of the power semiconductors, in which the influence of the grid codes on reactive power is taken into account. Then, the thermal performance of the power converter during a wind gust in the DFIG system is optimized by a proper control of the reactive power.

3.1 Thermal model of power device

The power density of the power electronics converter is steadily being increased, which is also pushing the improvement of an enhanced power range and a reduced impact on volume as well as the cost [1], [2]. In respect to the IGBT power module, many new techniques and novel materials are devoted to guarantee lower loss dissipation or higher operational junction temperature [3]-[5].

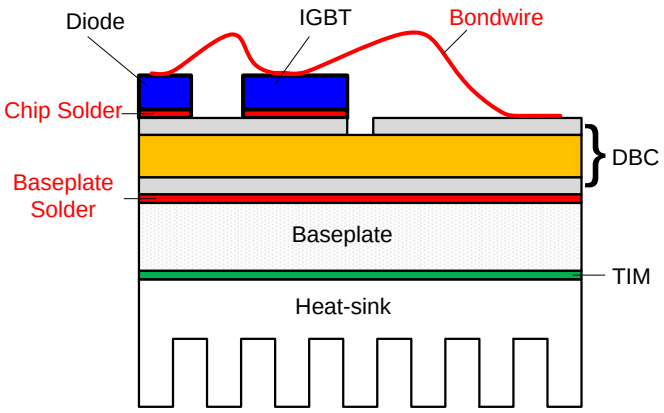

Fig. 3.1. Basic structure of a power semiconductor module.

The layout of a typical power semiconductor module is depicted in Fig. 3.1. A number of the power semiconductor chips – IGBTs and diodes are soldered onto the ceramic based substrates like Direct Bond Copper (DBC), which behaves as an electrical insulation. Then, the DBC can either be soldered onto a baseplate, or the

bottom copper layer is directly mounted to the heat-sink with a Thermal Interface Material (TIM) in between. The electrical connections between the chips and the conductor tracks on the DBC are normally realized by the thick bonding-wire, which is normally made of pure aluminum [4].

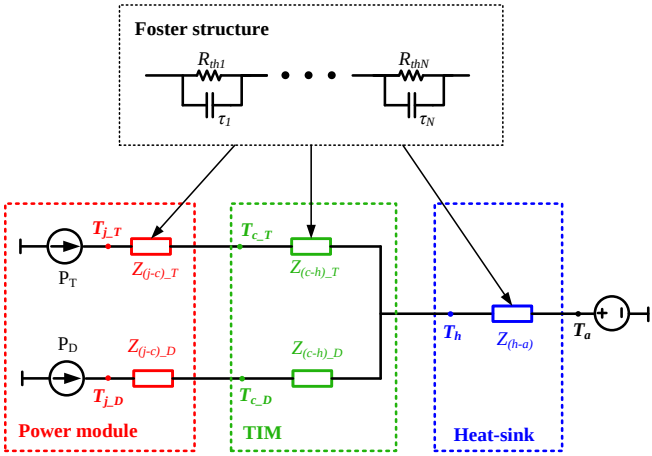

Fig. 3.2. Thermal model of the power devices in a module with a diode (D) and an IGBT (T).

As the thermal variables represented by electrical analogies are widely used [4]-[7], the power dissipation in the IGBT and the diode are expressed as a current source, the voltage source stands for the constant temperature level, and RC elements usually model the thermal impedance. Two kinds of RC networks are commonly adopted: the physical-meaning based Cauer structure and the test based Foster structure, and the latter is actually more preferred by the industry [8], [9]. The thermal model of power devices, including the IGBT and the freewheeling diode are shown in Fig. 3.2, in which the thermal impedance consists of the power module itself, the TIM and the heat-sink. For simplicity, the thermal coupling between the IGBT chip and diode chip is not considered.

The thermal impedances for the power module and the TIM are normally provided by the manufacturer datasheets. Fig. 3.3(a) shows the dynamic thermal impedance of the IGBT and the diode in the selected 1 kA/1.7 kV power module. It is noted that the steady-state thermal resistance of the diode is higher than the IGBT, due to the smaller chip area of the diode in the standard power module. Moreover, it can be seen that the

thermal time constant changes from hundreds of microseconds to hundreds of milliseconds.

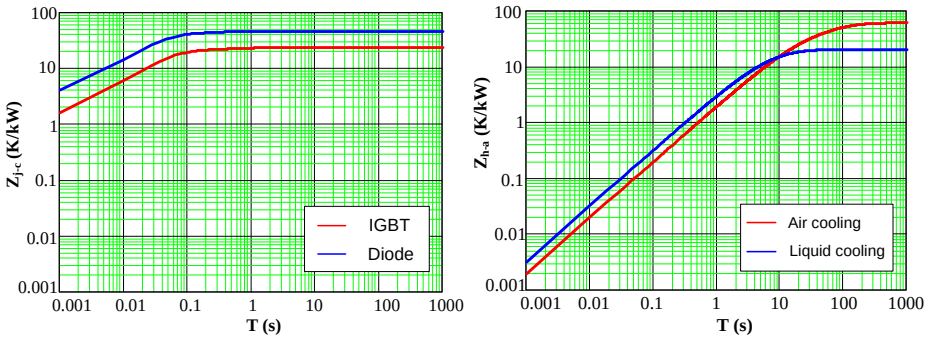

(a) (b)

Fig. 3.3. Dynamic thermal impedance. (a) IGBT and diode from junction to case; (b) Air and liquid cooling from heat-sink to ambient [13], [14]. Note: air flow=610 m^3/h, T_a=25 ℃, 500m above sea level; liquid flow=15 L/min, T_{fluid}=40 ℃, water/glycol ratio=50%/50%.

However, the thermal impedance for the cooling method is uncertain, as the power modules can be used in different applications according to the customer requirements. In a full-scale power converter, the typical amount of heat that has to be transported away from the power modules may be from 50 kW to 100 kW for a 2 MW wind turbine [10]. Because the cooling solutions take up considerable space available in wind turbine nacelle, the forced air cooling and the liquid cooling cover 95% of all power module application [11]. Correspondingly, the dynamic thermal impedance of the air and liquid cooling from the heat-sink to ambient can be deduced from Semikron datasheets as shown in Fig. 3.3(b) [12]-[14]. It is evident that the steady-state thermal resistance is three times higher in the air cooling system compared to the liquid cooling, and it can also be seen that the maximum time constant of the thermal impedance is much higher compared to the power module itself – hundreds of seconds for the air cooling and dozens of seconds for the liquid cooling.

Thermal profile of the power semiconductor for the wind power application usually contains long-term thermal cycling and short-term thermal cycling, which are imposed by the wind variation and the switched current within a fundamental frequency, respectively. At first glance, the lifetime and the reliability issues caused by the wind turbulence may be more crucial due to the higher junction temperature fluctuation of the power semiconductors. However, it is still essential to look at the influence of

short-term thermal cycling due to their larger magnitude of numbers, since the wind speed normally varies in several seconds, while the fundamental period of current changes only from dozens of milliseconds to hundreds of milliseconds.

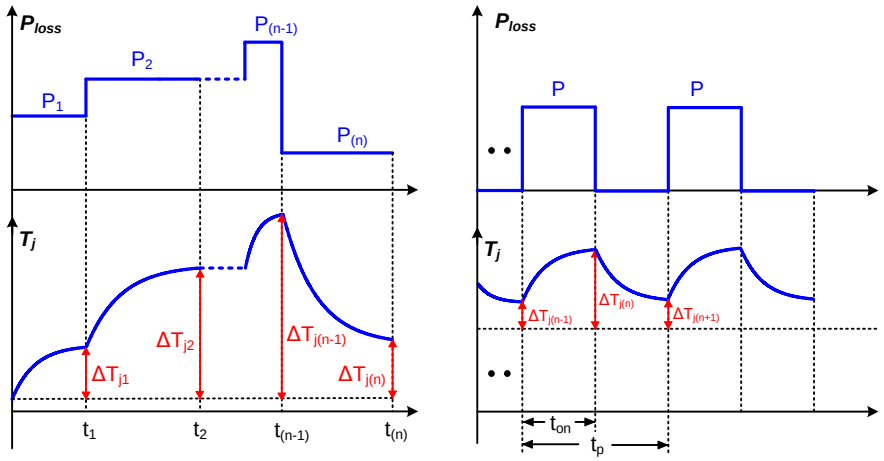

(a) (b)

Fig. 3.4. Power loss profile and junction temperature profile against time. (a) Step-pulse of power dissipation; (b) Periodical-pulse of power dissipation.

In respect to the long-term thermal cycling, the corresponding step-pulse of power loss is shown in Fig. 3.4(a). According to the Foster structure thermal model shown in Fig. 3.2, the junction temperature fluctuation $dT_{j(n)}$ during nth power loss pulse can be calculated as [4],

$$dT_{j(n)} = dT_{j(n-1)} \sum_{i=1}^{k} e^{-\frac{t_{(n)}-t_{(n-1)}}{\tau_i}} + P_{(n)} \sum_{i=1}^{k} R_i \left(1 - e^{-\frac{t_{(n)}-t_{(n-1)}}{\tau_i}}\right) \tag{3.1}$$

where the first item denotes the zero-input response of the previous junction temperature fluctuation $dT_{j(n-1)}$ at the instant $t_{(n-1)}$, and the second term denotes the zero-state response of the power loss $P_{(n)}$ until the instant $t_{(n)}$. R_i and τ_i indicate the ith thermal resistance and time constant in kth order Foster structure. According to (3.1), the junction temperature swing can easily be calculated from the power loss profile.

In respect to the short-term thermal cycling, Fig. 3.4(b) shows the thermal profile at periodical-pulse of power dissipation. According to (3.1), the junction temperature fluctuation at the moment $t_{(n)}$ and $t_{(n+1)}$ can be calculated based on previous states $t_{(n-1)}$

and $t_{(n)}$, respectively. Since $dT_{j(n+1)}$ has the same value as $dT_{j(n-1)}$ at the steady-state operation, the junction temperature fluctuation dT_j can be expressed as,

$$dT_j = P\sum_{i=1}^{k} R_i \frac{(1-e^{-\frac{t_{on}}{\tau_i}})^2}{1-e^{-\frac{t_p}{\tau_i}}} \tag{3.2}$$

where P is the peak value of periodical power pulse, t_{on} denotes the on-state time, t_p denotes the fundamental period of the converter output current, where t_p normally has twice value of t_{on}.

According to (3.2), Fig. 3.5 shows the relationship between the temperature swing and the time constant of the thermal impedance with typical operational frequencies listed in Table 2-3. Even in the minimum fundamental frequency of 1 Hz, the temperature fluctuation caused by the cooling method (thermal time constant from dozens of seconds to hundreds of seconds) can be almost neglected compared to thermal impedance of the power module (maximum of hundreds of milliseconds). Consequently, it can be concluded that, for the short-term thermal cycling, the junction temperature swing is only close to the thermal resistance and thermal capacitance of the power module rather than the cooling method.

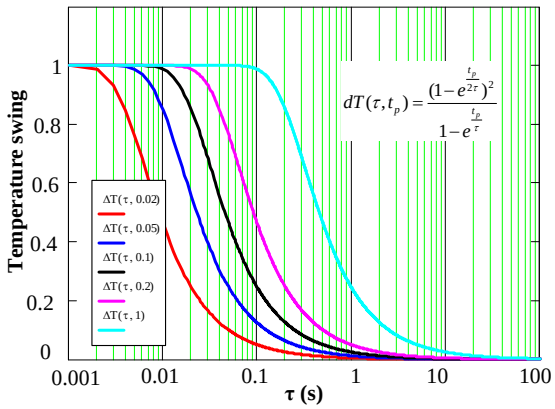

Fig. 3.5. Temperature swing dependence on time constant of thermal impedance with various fundamental frequencies.

Then, the mean junction temperature T_{jm} can be calculated as,

$$T_{jm} = \sum_{i=1}^{k} R_i \cdot \frac{P}{2} + T_a \tag{3.3}$$

where T_a denotes the ambient temperature, and it is set at 50 ℃ as an indication of the worst case.

Based on (3.2) and (3.3), the thermal behavior of the power device at steady-state can be analytically calculated, which avoids time-consuming simulation due to the huge difference between the switching period and the thermal time constant of the power device.

3.2 Thermal profile of wind power converter

According to the previously described thermal model, together with the loss breakdown calculated in Chapter 2, the thermal profile of the wind power converter can be studied at different grid code requirements of the reactive power.

3.2.1 Without reactive power injection

Assuming that the wind turbine system operates at the unity power factor, the simulation results of the junction temperature in each power semiconductor of the rotor-side converter in the DFIG system and the generator-side converter in the PMSG system are shown in Fig. 3.6(a) and Fig. 3.6(b), in which the converters run at rated power and in steady-state operation. It can be seen that the mean temperature of the diode is higher than in the IGBT in both the DFIG and the PMSG systems, and the thermal performance of the PMSG system shows a more unequal distribution.

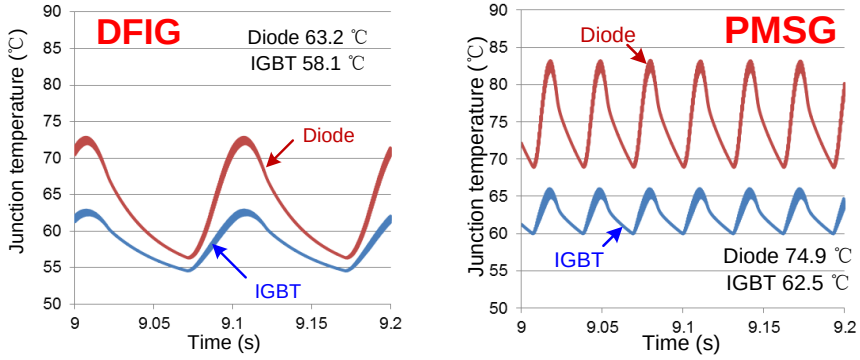

(a) (b)

Fig. 3.6. Simulated junction temperature in the rotor-side converter/generator-side converter at wind speed of 12 m/s. (a) DFIG system; (b) PMSG system.

For the junction temperature of the grid-side converter, the thermal results of the DFIG and the PMSG systems are shown in Fig. 3.7(a) and Fig. 3.7(b), respectively. It can be seen that the hottest power semiconductor device turns out to be the IGBT. Moreover, the junction temperature variation between the IGBT and the diode shows more equal distribution.

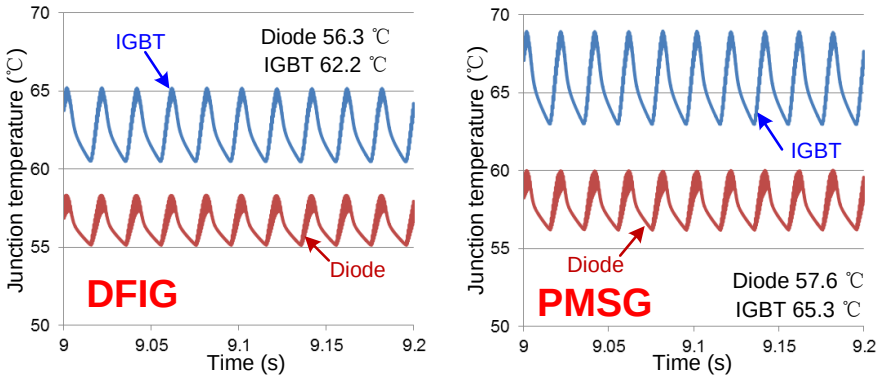

(a) (b)

Fig. 3.7. Simulated junction temperature in the grid-side converter at wind speed 12 m/s. (a) DFIG system; (b) PMSG system.

A further comparison of the thermal behavior for both the systems with different wind speed is shown in Fig. 3.8. For the rotor-side converter/generator-side converter, it can be seen that, in the PMSG system, the mean junction temperature and the temperature fluctuation of the power semiconductors above rated wind speed are the highest during the whole wind range, and the hottest device is the diode in the whole wind range. In the DFIG system, the hottest device changes from the IGBT in the sub-synchronous mode to the diode in the super-synchronous mode. Moreover, the temperature fluctuation of the power semiconductor becomes crucial around the synchronous operating point because of the low fundamental frequency. At the rated wind speed, although the mean junction temperature of the DFIG system is lower as shown in upper part of Fig. 3.8(a), the temperature fluctuation in the DFIG system is even larger due to smaller frequency of the thermal cycling as shown in lower part of Fig. 3.8 (a).

For the grid-side converter, both the mean junction temperature and the temperature fluctuation increase continuously with higher wind speed in the PMSG system, while

both the mean junction temperature and temperature fluctuation become very small around the synchronous operation in the DFIG system.

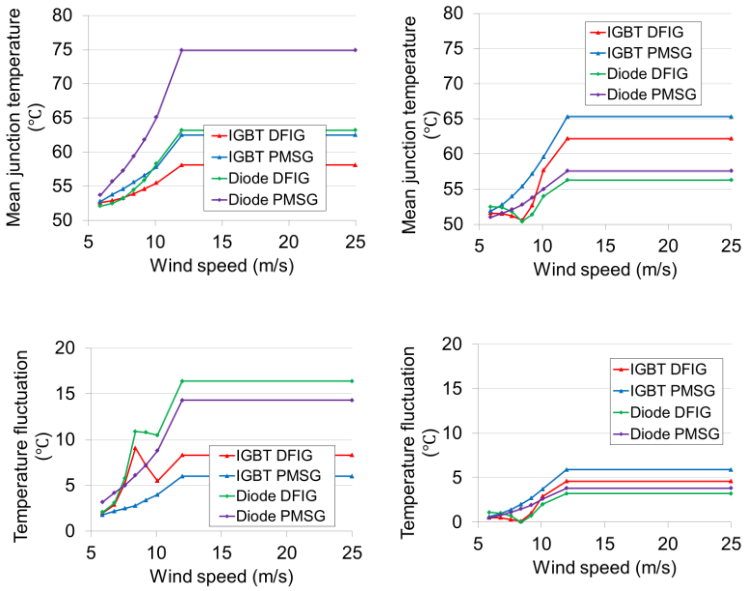

(a) (b)

Fig. 3.8. Mean junction temperature and temperature fluctuation in the chip versus wind speed for the DFIG and the PMSG system. (a) Rotor-side converter/generator-side converter; (b) Grid-side converter.

3.2.2 With reactive power injection

As the most stressed power semiconductor decides the reliability and lifetime in a power module, it is necessary to extract the thermal excursion of the most serious loading chips in both the DFIG and the PMSG system, and in this case the German grid codes are used. Fig. 1.8(b) shows the specific reactive power which needs to be compensated by the rotor-side converter in the DFIG system and by the grid-side converter in the PMSG system.

For the rotor-side converter of the DFIG system as shown in Fig. 3.9(a), the most stressed power semiconductor changes from the IGBT in sub-synchronous mode to the freewheeling diode in super-synchronous mode. It is noted that the over-excited reactive power requirement will impose thermal stress to the power semiconductor devices especially around the synchronous operating point.

For the grid-side converter of the PMSG system as shown in Fig. 3.9(b), the IGBT is the most stressed power semiconductor during the whole operating wind speed. The reactive power injection will induce higher mean junction temperature and junction temperature fluctuation. Moreover, the situation will become even worse at lower wind speed due to the lower output active power but the same amount of the reactive power.

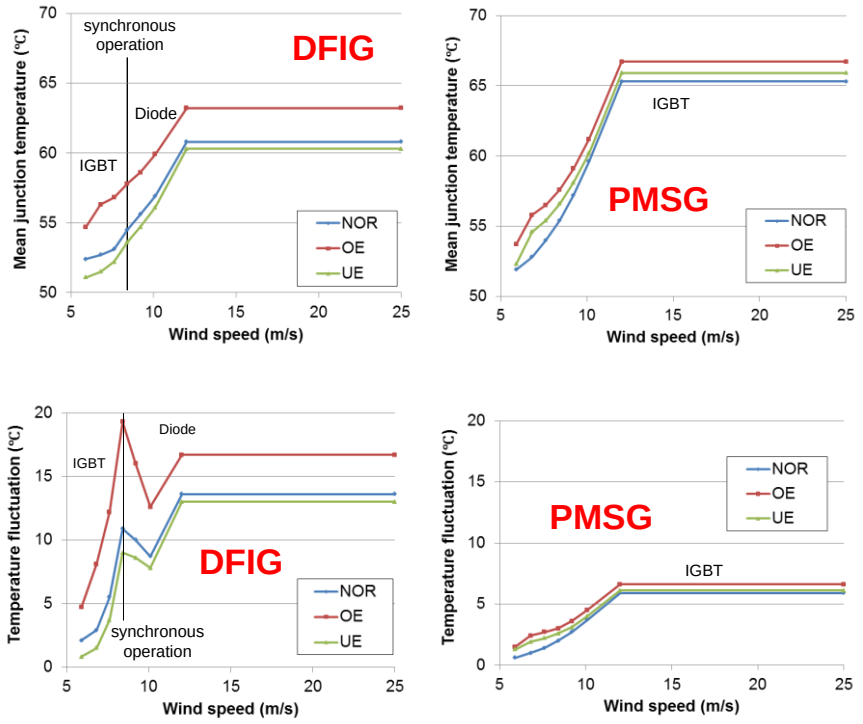

(a) (b)

Fig. 3.9. Thermal profile of the most stressed power semiconductor considering grid codes of reactive power. (a) Rotor-side converter of DFIG system; (b) Grid-side converter of PMSG system. Note: NOR, OE and UE indicate normal, over-excited and under-excited reactive power, respectively.

3.3 Thermal behavior optimization in DFIG system

In respect to the DFIG system, it is well known that the reactive power is usually provided by the rotor-side converter due to the stator and rotor winding ratio of the induction generator [15], [16]. Nevertheless, the grid-side converter is also able to partially supply the reactive power. As a consequence, the reactive power can be

circulated within the internal DFIG system without any unexpected power factor distortion to the grid. This section starts with the calculation the allowable reactive power circulation between the back-to-back power converters. Afterwards, an optimized control method of the reactive power circulation within the DFIG system is proposed to reduce the thermal stress of the power converter during wind gusts.

3.3.1 Allowable range of reactive power

Assuming a single inductor is used as the grid filter as shown in Fig. 2.4, the phasor diagram for the grid-side converter is shown in Fig. 3.10, in which the over-excited reactive power is applied. Due to the opposite polarity of the active power through the grid-side converter between the sub-synchronous mode and the super-synchronous mode, the direction of the active power is shown in Fig. 3.10(a) and Fig. 3.10(b), respectively. Accordingly, if the under-excited reactive power is introduced, the phasor diagram can be obtained by rotating the q-axis current 180 degree.

Similar as (2.4), the analytical formula for the converter output voltage U_c is expressed as,

$$U_C = \sqrt{(U_{gm} + i_{gq} X_g)^2 + (i_{gd} X_g)^2} \le \frac{U_{dc}}{\sqrt{3}} \tag{3.4}$$

where U_{gm}, U_{dc} denotes the rated peak phase voltage and dc-link voltage, X_g denotes filter reactance at 50 Hz, i_{gd} and i_{gq} denote the grid-side converter peak current in the d-axis and q-axis, respectively.

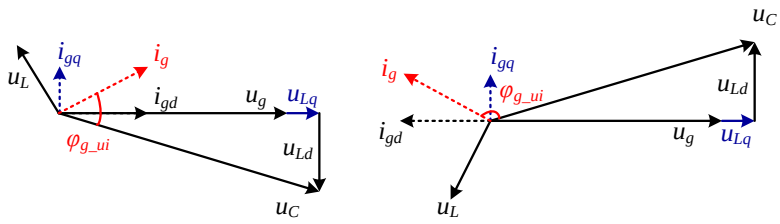

(a) (b)

Fig. 3.10. Phasor diagram of the grid-side converter (e.g. over-excited reactive power injection). (a) Operation under sub-synchronous mode; (b) Operation under super-synchronous mode.

It is evident that whatever the operation mode is, the amplitude of the converter output voltage is increased, if over-excited reactive power is introduced. Therefore, due

to the linear modulation, the relationship between the dc-link voltage and the converter output voltage can be calculated as (3.4).

Another restriction lies in the capacity of the power device,

$$\sqrt{{i_{gd}}^2 + {i_{gq}}^2} \le I_m \tag{3.5}$$

where I_m denotes the peak current of the power module.

Furthermore, the capacity of the induction generator Q_{DFIG} must be taken into account [17],

$$\frac{3}{2} U_{gm} i_{gq} \le Q_{DFIG} \tag{3.6}$$

Based on the above mentioned three limitations from (3.4)-(3.6), the boundary of the reactive power can be obtained. Moreover, the displacement angle is another important indicator for the power loss evaluation, whose feature is described in Fig. 3.10 as well.

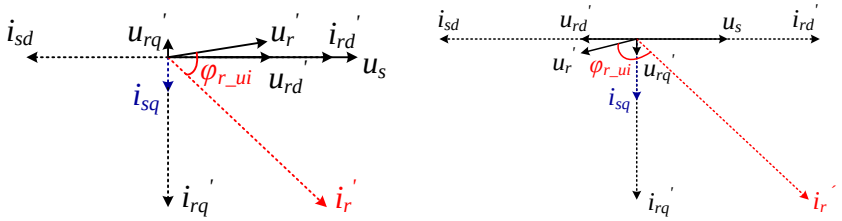

(a) (b)

Fig. 3.11. Phasor diagram of the rotor-side converter (e.g. over-excited reactive power injection). (a) Operation under sub-synchronous mode; (b) Operation under super-synchronous mode.

With the equivalent steady-state DFIG model as shown in Fig. 2.8, if the over-excited reactive power is provided, the phasor diagram for the rotor-side converter in the conditions of the sub-synchronous and the super-synchronous mode are depicted in Fig. 3.11(a) and Fig. 3.11(b), respectively. Based on the relationship between the DFIG stator and rotor as deduced in (2.5), (2.6), similar restrictions as the grid-side converter can be applied to the rotor-side converter, such as the linear modulation (3.7), the power device limitation (3.8) and the induction generator capacity (3.9),

$$\frac{\sqrt{{u_{rd}'}^2 + {u_{rq}'}^2}}{k} \le \frac{U_{dc}}{\sqrt{3}} \tag{3.7}$$

$$k\sqrt{{i_{rd}'}^2 + {i_{rq}'}^2} \le I_m \tag{3.8}$$

$$-\frac{3}{2}U_{sm}i_{sq} \le Q_{DFIG} \tag{3.9}$$

It is noted that the rotor current and voltage are transferred from the stator-side to the rotor-side with the help of stator/rotor winding turns ratio *k*, and U_{sm} denotes the peak value of the stator voltage. According to the equations of (3.4)-(3.6) and (3.7)-(3.9), it is concluded that the range of the reactive power in the rotor-side converter is limited by the induction generator capacity, while the DFIG capacity and the dc-link voltage affects the amount of the reactive power in the grid-side converter.

The current amplitude and the power factor angle of the power converter are regarded as two indicators for the power device loading, so the current characteristic based on the calculated reactive power range is then investigated.

Table 3-1 Range of the reactive power for the back-to-back power converter

	Sub-synchronous mode		**Super-synchronous mode**	
	GSC	**RSC**	**GSC**	**RSC**
Typical wind speed [m/s]	5.9		10.1	
Rated power [pu]	0.13		0.65	
Active power current [pu]	0.06	0.19	0.11	0.54
Range of reactive power [pu]	(-0.23, 0.06)	(-0.29, 0.23)	(-0.23, 0.06)	(-0.29, 0.23)

Note: GSC stands for the grid-side converter, and RSC stands for the rotor-side converter.

If two typical wind speeds of 5.9 m/s and 10.1 m/s are selected for the sub-synchronous and the super-synchronous operation [18], [19], the possible range of the reactive power in the grid-side converter and the rotor-side converter can be summarized and listed in Table 3-1. In order not to affect the power factor to the grid, a circulation current is the minimum range of the back-to-back power converter, which is restricted by the grid-side converter. As the horizontal axis is defined as the reactive power range of the grid-side converter, the injection of the additional power not only affects the current amplitude, but also changes the power factor angle as shown in Fig. 3.12.

For the characteristic of the current amplitude, regardless of the sub-synchronous or the super-synchronous operation mode, it is evident that the minimum current appears

almost under no reactive power injection for the grid-side converter, while for the rotor-side converter, the current decreases with higher over-excited reactive power. Unfortunately, the over-excited reactive power is much smaller than the under-excited reactive power, which prevents the rotor-side converter current to reach the minimum power loss.

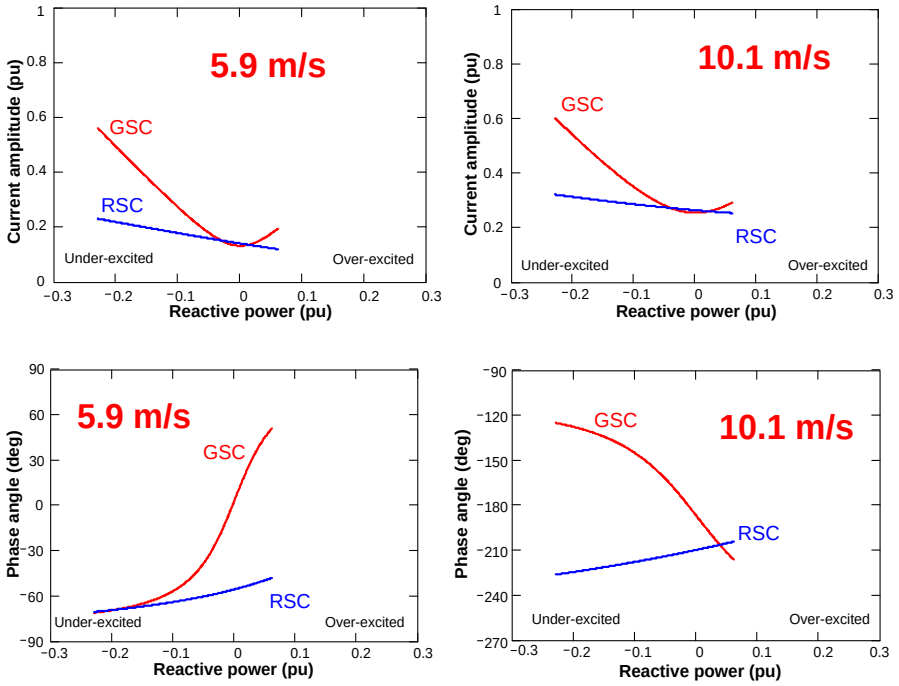

(a) (b)

Fig. 3.12. Influence of reactive power circulation on the back-to-back power converter in a DFIG system. (a) Sub-synchronous mode at wind speed 5.9 m/s; (b) Super-synchronous mode at wind speed 10.1 m/s.

For the characteristic of the power factor angle of the grid-side converter, it is noted that in response to the additional reactive power injection, unity power factor becomes either leading or lagging. For the rotor-side converter, it is noted that the power factor angle presents a tendency to be in phase under sub-synchronous mode or inverse under super-synchronous mode with the increasing over-excited reactive power. However, the phase shift looks insignificant.

3.3.2 Thermal performance during a wind gust

As seen above, the injection of the reactive power may change the converter current, thus influence the thermal behavior of the power device. Therefore, it is possible to control the junction temperature fluctuation under wind gusts by a proper thermal-oriented reactive power control in a DFIG system, as shown in Fig. 3.13.

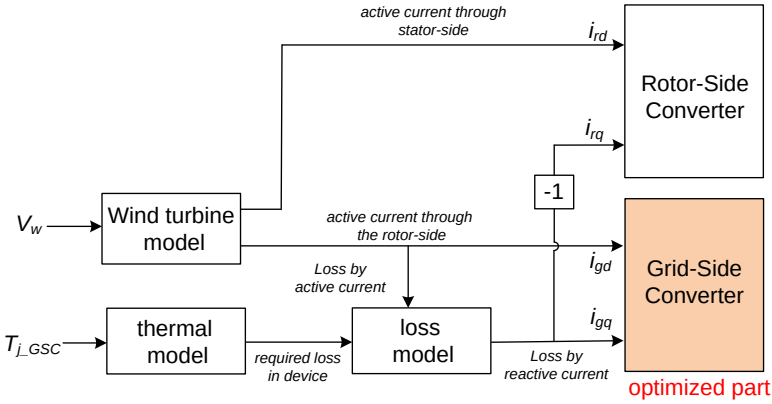

Fig. 3.13. Thermal-oriented control diagram of the back-to-back power converters during a wind gust.

The typical one-year return period wind gust is defined in IEC, Mexican-hat-like curve [19]. As shown in Fig. 14, the wind speed deceases from an average of 10 m/s to a trough of 8 m/s, increases to a crest of 16 m/s, and returns to 10 m/s within eight seconds, where 8.4 m/s is the synchronous operation wind speed.

The thermal cycling of the back-to-back power converters with and without thermal-oriented reactive power control is shown in Fig. 3.14(a) and Fig. 3.14(b), respectively. As shown in Fig. 3.14(a), the active power reference becomes zero at the synchronous operation point. Moreover, it can be seen that the minimum junction temperature appears at the synchronous operation point and the maximum junction temperature appears above the rated wind speed. The thermal stress becomes the least serious at the synchronous wind speed due to no active power flows in the grid-side converter, while it becomes the most serious in the rotor-side converter because of the rotor current at very low frequency.

As shown in Fig. 3.14(b), it is noted that the maximum junction temperature fluctuation in the grid-side converter is decreased from 11 ℃ to 7 ℃ due to the

introduction of additional reactive power under small active power, which can actively heat up the device, while the maximum junction temperature fluctuation in the rotor-side converter remains the same 18 ℃ because of the rather higher active power reference in the entire wind speed. However, when the additional reactive power is introduced, the thermal behavior of the diode in the grid-side converter becomes more variable but still has less fluctuation compared to the IGBT. In the rotor-side converter, the thermal behavior of the IGBT and the diode are slightly changed.

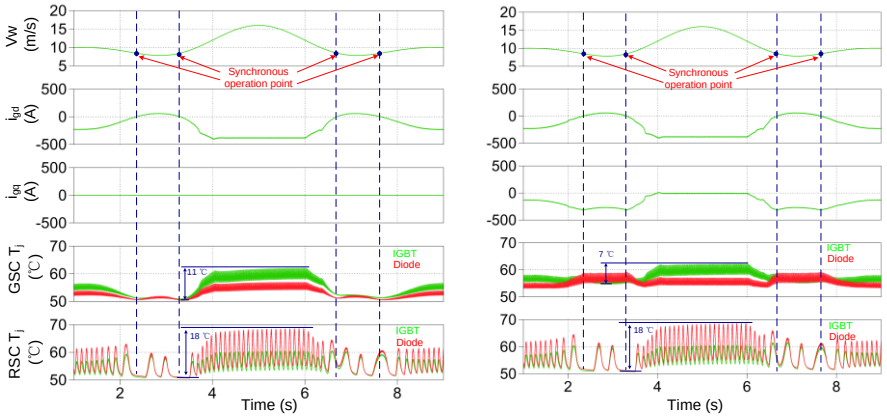

(a) (b)

Fig. 3.14. Thermal cycling of the back-to-back power converters during wind gusts in a DFIG system. (a) Without thermal-oriented reactive power control; (b) With thermal-oriented reactive power control.

3.4 Summary

As the thermal behavior of the power semiconductor device is regarded as the important indicator of the reliability assessment, this chapter focuses on the thermal stress evaluation of wind power converter. According to the physical layout of the power module, the thermal model is established in terms of the power module itself and the cooling methods. Afterwards, the variations of the junction temperature in the DFIG configuration and the PMSG configuration are calculated, in which the grid codes are taken into account. It is concluded that the reactive power injection will inevitably affect the thermal performance of the power device. Moreover, due to the fact that both the grid-side converter and the rotor-side converter have the capability to provide the reactive power support in the DFIG system, an optimized thermal control

method of the grid-side converter can be achieved during a wind gust, while the thermal performance of the rotor-side converter is almost unaffected.

Relevant attached papers

[A.2] D. Zhou, F. Blaabjerg, M. Lau, M. Tonnes, "Thermal behavior optimization in multi-MW wind power converter by reactive power circulation," *IEEE Trans. on Industry Applications*, vol. 50, no. 1, pp. 433-440, Jan. 2014. (Also *in Proc. of APEC 2013*, pp. 2863-2870, 2013)

[A.3] D. Zhou, F. Blaabjerg, M. Lau, M. Tonnes, "Thermal cycling overview of multi-megawatt two-level wind power converter at full grid code operation," *IEEJ Journal of Industry Applications*, vol. 2, no. 4, pp. 173-182, Jul. 2013.

[A.4] D. Zhou, F. Blaabjerg, M. Lau, M. Tonnes, "Thermal profile analysis of doubly-fed induction generator based wind power converter with air and liquid cooling methods," *in Proc. of EPE 13*, pp.1-10, 2013.

References

[1] J. Kolar, J. Biela, S. Waffler, T. Friedli, U. Badstuebner, “Performance trends and limitations of power electronic systems,” *in Proc.of Integr. Power Electron. Syst. Rec.*, pp. 17–36, 2010.

[2] Y. Song, B. Wang, “Survey on reliability of power electronic systems,” *IEEE Trans. on Power Electronics*, vol. 28, no. 1, pp. 591-604, Jan. 2013.

[3] G. Majumdar, T. Minato, "Recent and future IGBT Evolution," *in Proc. of PCC 2007*, pp. 355-359, 2007.

[4] A. Wintrich, U. Nicolai, T. Reimann, “Semikron Application Manual,” 2011.

[5] ABB. Applying IGBTs. (website: http://new.abb.com/products/semiconductors).

[6] K. Ma, F. Blaabjerg, "Multilevel converters for 10 MW wind turbines," *in Proc. of EPE 2011*, pp. 1-10, 2011.

[7] H. Wang, K. Ma, F. Blaabjerg, “Design for reliability of power electronic systems,” *in Proc. of IECON 2012*, pp. 33-44, 2012.

[8] R. Schnell, M. Bayer, S. Geissmann, “Thermal design and temperature ratings of IGBT modules,” ABB Application Note, 5SYA 2093-00, 2011.

[9] T. Schutze, “Thermal equivalent circuit models,” Infineon Application Note, AN2008-03, 2008.

[10] Q. Gao, C. Liu, B. Xie, X. Cai, "Evaluation of the mainstream wind turbine concepts considering their reliabilities," *IET on Renewable Power Generation*, vol. 6, no. 5, pp. 348-357, Sep. 2012.

[11] K. Olesen, F. Osterwald, M. Tonnes, R. Drabek, R. Eisele, “Designing for reliability, liquid cooled power stack for the wind industry,” *in Proc. of IEMDC* 2011, pp. 896-901, 2011.

[12] D. Zhou, F. Blaabjerg, M. Lau, M. Tonnes, "Thermal profile analysis of doubly-fed induction generator based wind power converter with air and liquid cooling methods," *in Proc. of EPE 13*, pp.1-10, 2013.

[13] Semikron datasheet: SKiiP 1814 GB17E4-3DUL.
[14] Semikron datasheet: SKiiP 1814 GB17E4-3DUW.
[15] S. Engelhardt, I. Erlich, C. Feltes, J. Kretschmann, F. Shewarega, "Reactive power capability of wind turbines based on doubly fed induction generators," *IEEE Trans. on Energy Conversion,* vol. 26, no. 1, pp. 364-372, Mar. 2011.
[16] M. Kayikci, J. V. Milanovic, "Reactive power control strategies for DFIG-based plants," *IEEE Trans. on Energy Conversion*, vol. 22, no. 2, pp. 389-396, Jun. 2007.
[17] C. Liu, F. Blaabjerg, W. Chen, D. Xu, "Stator current harmonic control with resonant controller for doubly fed induction generator," *IEEE Trans. on Power Electronics*, vol. 27, no. 7, pp. 3207-3220, Jul. 2012.
[18] K. Xie, Z. Jiang, W. Li, "Effect of wind speed on wind turbine power converter reliability," *IEEE Trans. on Energy Conversion*, vol. 27, no. 1, pp. 96-104, Mar. 2012.
[19] Wind turbines, part 1: Design requirements, IEC 61400-1, 3rd edition, International Electrotechnical Commission, 2005.

Chapter 4
Reliability assessment of wind power converter

According to the thermal stress of the power switching device, together with the common used Coffin-Manson lifetime model, this chapter further estimates the lifespan of the investigated wind power converter, in which various wind profiles and various requirements from the grid codes of the reactive power injection are taken into account as well.

4.1 Methods for reliability analysis

Reliable and robust operation of the power electronics converter is closely related to its mission profile - the representation of all relevant conditions that a system can be exposed to in all of its intended application throughout its entire life cycle [1]. Then, the failure may happen during the violation of the strength and stress analysis, in which the stressor factors may be due to the environmental loads (like thermal, mechanical, humidity, etc.), or the functional loads (such as usage profiles, electrical operation). Moreover, it is concluded that the thermal cycling accounts for more than a half failure probability among the stressors distribution [2]-[3].

An approach for the lifetime estimation is adopted on the basis of several typical wind speeds in [4]. However, since the concept of the Mean-Time To Failures (MTTF) is already outdated and obsolete, the reliability assessment is currently moving into a more physical based approach, involving not only the mathematics and the statistics from the damaged device, but also the root cause behind the failures. As stated in [5], it points out that the thermal cycling of the power converter basically consists of the fundamental frequency based small cycles and the load variation based larger cycles. A more complicated method based on the mission profile analysis is proposed in [6], where the long-term, medium-term and short-term characteristic of the annual wind profile are individually studied due to the various inertia times of the different parts in the wind turbine system. On the basis of the universal approach of the power semiconductor device reliability assessment as stated in [6], [7], the lifespan of the

power electronics converter is focused on in terms of thermal cycling caused by the alternative current with one fundamental period.

Power cycling test is defined that the power components are actively heated up by losses in the semiconductor and cooled down again with the aid of a cooling system, which is of higher importance from the power device manufacturer point of view. This test could detect the thermo-mechanical stress between the layers with different thermal expansion coefficients. The connection between the chip and Direct Bonded Copper (DBC), the linking of the bond wire and the chip area seem to be the most frequent failure mechanisms [7]-[9]. In order to accelerate the test, the introduced current for the thermal loading is almost equal to the rated current, and the time cycling is normally between some seconds to dozens of seconds. The number of the power cycles can be obtained at higher junction temperature fluctuation, and then the values at lower temperature variation can be extrapolated by the Coffin-Manson equation [10].

$$N = A \cdot dT_j^{\alpha} \cdot \exp\left(\frac{E_a}{k_b \cdot T_{jm}}\right) \tag{4.1}$$

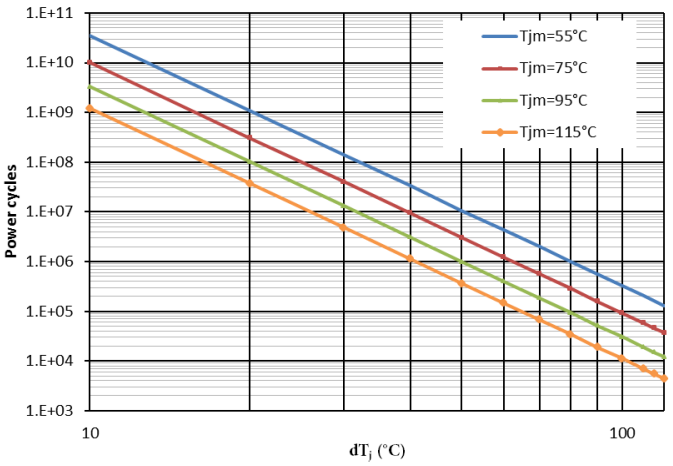

Fig. 4.1. Example of fitting power cycles curve versus the mean junction temperature and the junction temperature fluctuation according to Coffin-Manson model.

According to [10], [11], t_{on} - which is the half value of the fundamental period, is also closely relevant to the power cycle capability, and this factor should be taken into account as well,

$$\frac{N(t_{on})}{N(0.7s)} = \left(\frac{t_{on}}{0.7s}\right)^{-0.463} \tag{4.2}$$

Based on the simplified assumption of uniform failure mechanism over the entire temperature range, the B10 power cycle (90% of sample components fail if power cycles reach this value) is shown in Fig. 4.1 with various mean junction temperatures and various junction temperature fluctuations.

Based on the previously mentioned loss evaluation in Chapter 2, the universal procedure of lifetime estimation is shown in Fig. 4.2. The mean junction temperature and the junction temperature variation of the most stressed power semiconductor device can be obtained with the aid of the Foster structure thermal model as illustrated in Chapter 3. Then, together with the on-state time of the loading current within one fundamental frequency, the power cycles can be calculated according to Coffin-Manson lifetime equation given in (4.1).

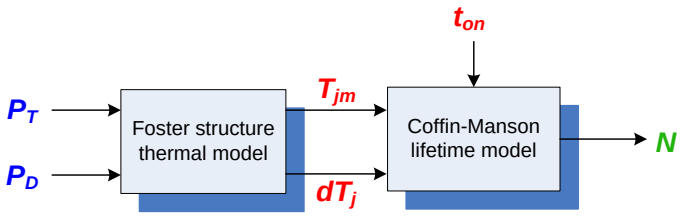

Fig. 4.2. Framework to estimate the power cycles of the power semiconductors.

Afterwards, the concept of the Consumed Lifetime per year (CL) is introduced by,

$$CL_i = \rho_i \cdot \frac{365 \cdot 24 \cdot 3600 \cdot f_a}{N_i} \tag{4.3}$$

where subscript i denotes a certain wind speed from cut-in to cut-out wind speed, ρ denotes the wind speed probability of yearly wind speed, f_1 is the fundamental frequency of converter output current, and N denotes the power cycles of Coffin-Manson equation. As a result, CL_i denotes the power cycles consumed per year at the wind speed i.

Assuming the linear damage accumulation, the Miner's rule [4], [6] is applied in order to calculate the Total Consumed Lifetime (TCL),

$$TCL = \sum_{i=4}^{25} CL_i \tag{4.4}$$

Besides, the power electronics reliability involves multidisciplinary knowledge. It covers the analytical physics to understand the failure mechanisms of the power electronic products, the design for reliability and robustness validation process to build in reliability and sufficient robustness during the development process of the power electronics device, and intelligent control and condition monitoring to ensure reliable field operation under specific mission profile. Therefore, the lifetime estimation for the power semiconductor device is not an easy task, and the following assumptions are made in this chapter,

a. Although the bond-wire lift-off and the soldering cracks between the different layers occur frequently in the fatigued power modules [7], [8], a unified failure mechanism is assumed;

b. The Miner's rule is used [1] for lifetime calculation, which means that the linear damage accumulation in fatigue and the no parameter deviation driving the system operation are supposed;

c. As most of the manufacturers cannot provide the numbers of power cycle with small temperature swings and high cycling frequency, the extended data is obtained through the conventional Coffin-Manson lifetime model [10];

d. The confidence level is not of concern in this chapter, and only the B10 lifetime model is used [7].

4.2 Lifetime estimation for wind power converter

It is evident that the most stressed power device decides the lifetime of a power module. On the basis of the thermal stress evaluation in Chapter 3, it is concluded that regardless of the topologies in the wind turbine system, the IGBT is the most loaded in the grid-side converter, while the diode has the worst thermal performance in the rotor-side converter/generator-side converter. As a consequence, these two kinds of power devices will be in focus in order to estimate the lifetime of the back-to-back power converters.

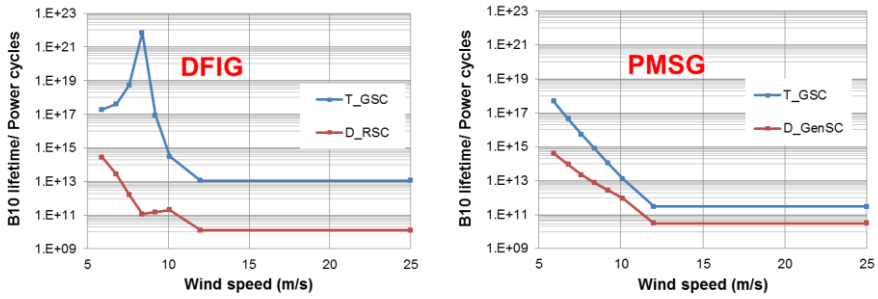

(a) (b)

Fig. 4.3. Steady-state power cycles of the most stressed power semiconductor at various wind speeds. (a) DFIG system; (b) PMSG system.

As shown in Fig. 4.3, the steady-state power cycles are calculated according to (4.1) and (4.2). The curve for the back-to-back power converters in the DFIG system is shown in Fig. 4.3(a). For the grid-side converter, it can be seen that the power cycles become very high at the synchronous operation, because both the mean junction temperature and the junction temperature fluctuation have the lowest value as shown in Fig. 3.8(b). However, for the rotor-side converter, the power cycles at the synchronous operation yield very low value by the factor of two, not only due to its higher junction temperature fluctuation as shown in Fig. 3.8(a), but also because of the very low operational frequency, which further reduces the power cycles as illustrated in (4.2). For the PMSG system, if the wind speed is below rated value, the power cycles continuously becomes lower with higher wind speed in both the grid-side converter and the generator-side converter.

In order to evaluate the consumed lifetime per year and the total consumed lifetime, the wind profile needs to be taken into account as well. Wind class is one of the important factors which need to be considered during the complex process of planning a wind power plant. It is mainly defined by the average annual wind speed, the speed of the extreme gust that could occur over 50 years, and how much turbulence exists at the wind site [13]. In respect to the steady-state power cycles, only the average annual wind speed is taken into consideration. According to the IEC standard [12], Class I - high, Class II - medium and Class III - low wind are defined with annual average speeds of 10 m/s, 8.5 m/s and 7.5 m/s, respectively.

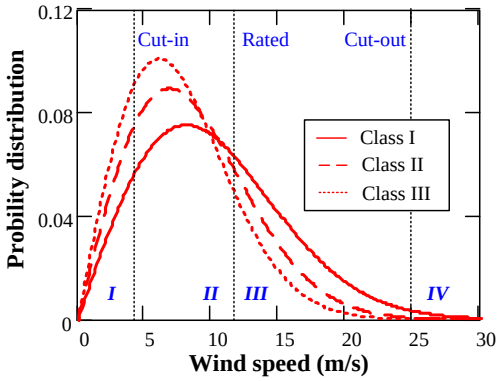

Fig. 4.4. Annual wind distribution with different wind classes defined by IEC standard.

There are two most commonly used density distribution of the wind speed – Weibull and Rayleigh function, and the Weibull distribution is adopted in this study [14],

$$f(v) = \frac{k}{A}\left(\frac{v}{A}\right)^{k-1} \exp\left(-\left(\frac{v}{A}\right)^{k}\right) \tag{4.5}$$

in which the shape parameter k is 2, and three scale parameters A (11.4, 9.6 and 8.5) are used to represent various IEC wind class I, II and III.

Annual wind distribution of various wind classes is shown in Fig. 4.4, and wind class I is considered as a case study. The consumed lifetime per year is then obtained according to (4.3) and is graphically shown in Fig. 4.5. The DFIG system and the PMSG system are individually studied in Fig. 4.5(a) and Fig. 4.5(b), respectively. It is noted that the wind speed from the cut-in to the cut-out value (region II and region III in Fig. 4.4) contributes to the lifetime consumption. In respect to the DFIG system, the back-to-back power converters perform different behaviors. The consumed lifetime of the grid-side converter changes more dramatically compared to the rotor-side converter around the synchronous operation due to the various characteristic of the B10 power cycles as shown in Fig. 4.3(a). In respect to the PMSG system, the turning point of both the generator-side converter and the grid-side converter occurs at the rated wind speed. Above the rated wind speed, the consumed lifetime continuously reduces with the higher wind speed, because of the same value of the B10 power cycle but the lower wind speed distribution.

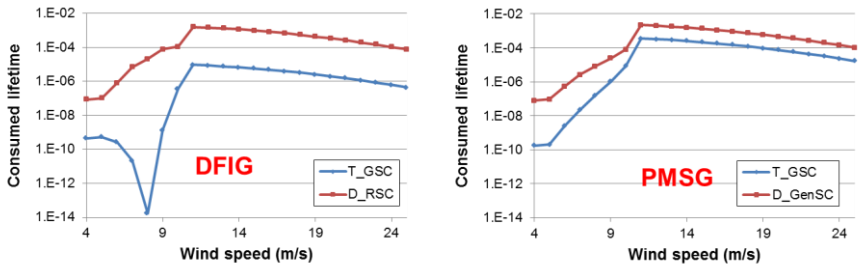

(a) (b)

Fig. 4.5. Consumed lifetime per year of the back-to-back power converter based on class I wind profile. (a) DFIG system; (b) PMSG system.

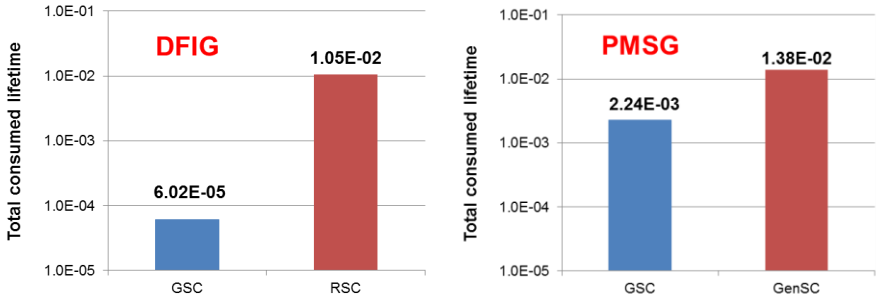

(a) (b)

Fig. 4.6. Comparison of the total consumed lifetime between grid-side converter and rotor-side converter/generator-side converter. (a) DFIG system; (b) PMSG system.

By summing up the individual consumed lifetime, the total consumed lifetime for the both the topologies are shown in Fig. 4.6. It is evident that the lifespan between the two used back-to-back power converters is more balanced in the PMSG system.

4.3 Mission profile effect on lifetime

This section considers the mission profile influence on the lifetime estimation (e.g. grid codes, wind profile, etc.). As the rotor-side converter of the DFIG system is generally responsible to support grid codes, while it is the grid-side converter of the PMSG system that is obliged to fulfill the grid codes, those two power converters will be investigated.

4.3.1 Grid codes

It is known that the reactive power is preferred for the LVRT operation in order to rebuild the normal grid voltage. Nevertheless, many pioneering countries of wind energy production (like Germany, Denmark, UK, etc.) have issued grid codes that also during normal operation should be able to deliver the reactive power. As shown in Fig. 1.8(b), one of the strictest grid requirements is established by German TSO, in which up to 40% Over-Excited (OE) and 30% Under-Excited (UE) reactive power should be delivered if the produced active power is above 20%.

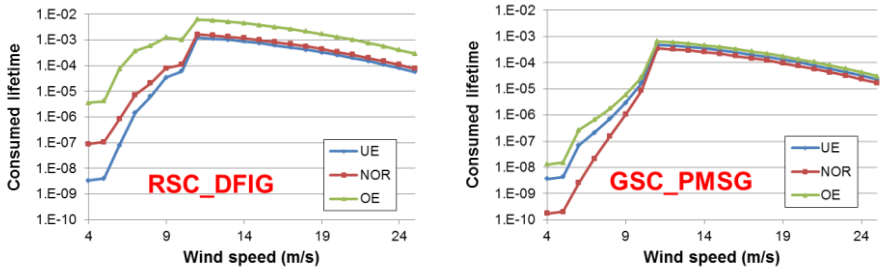

(a) (b)

Fig. 4.7. Consumed lifetime with various reactive power injections. (a) Rotor-side converter of the DFIG system; (b) Grid-side converter of the PMSG system.

Fig. 4.7 depicts the consumed lifetime of the power semiconductor at three different amounts of reactive power (UE, NOR and OE). For the DFIG system, the OE operation significantly reduces the reliability of the power semiconductors compared to the NOR operation, while the UE operation reversely enhances the reliability slightly. For the PMSG system, both the OE and the UE operation results in higher consumed lifetime at all wind speeds.

The effect of the grid code influence on the cost of the reliability is shown in Fig. 4.8. For the DFIG system, if the over-excited reactive power is provided all year around, it can be seen that the OE operation will shorten the lifetime substantially, almost 1/4 compared to the NOR operation. In respect to the PMSG system, the worst case of the OE operation almost reduces the lifetime to 1/2 compared to the NOR operation.

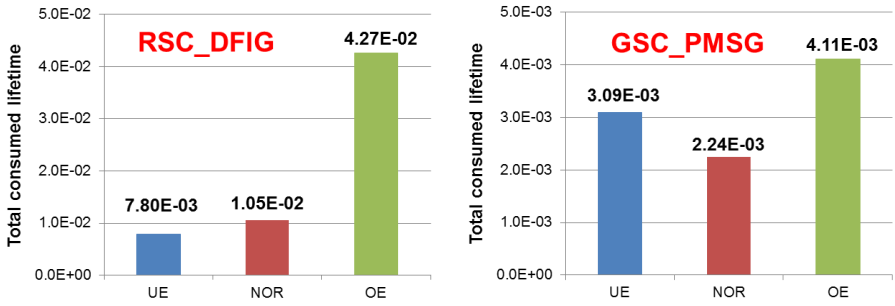

(a) (b)

Fig. 4.8. Grid codes influence on the consumed lifetime. (a) Rotor-side converter of the DFIG system; (b) Grid-side converter of the PMSG system.

4.3.2 Wind profile influence

Three wind classes defined by IEC standard in Fig. 4.4 are used to compare the effect of the different wind profiles, and the consumed lifetime is shown in Fig. 4.9. For both the DFIG system and the PMSG system, a slight difference of the consumed lifetime occurs at region II wind speed. Besides, since the class I has highest probability for region III wind speed, its consumed lifetime is highest from the rated speed until the cut-out speed, then followed by class II and class III wind profile. As summarized in Fig. 4.10, it is seen that higher wind class will give lower lifetime of the power converter in both configurations.

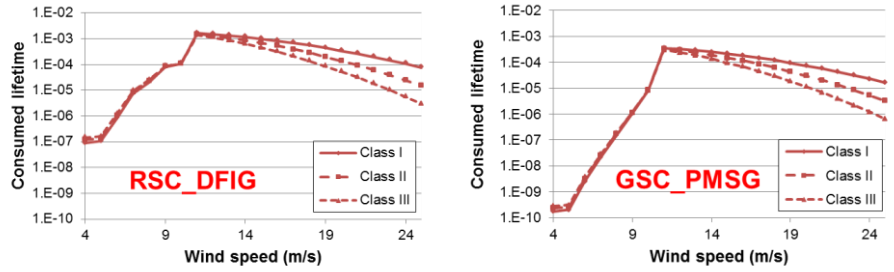

(a) (b)

Fig. 4.9. Consumed lifetime at various wind classes. (a) Rotor-side converter of the DFIG system; (b) Grid-side converter of the PMSG system.

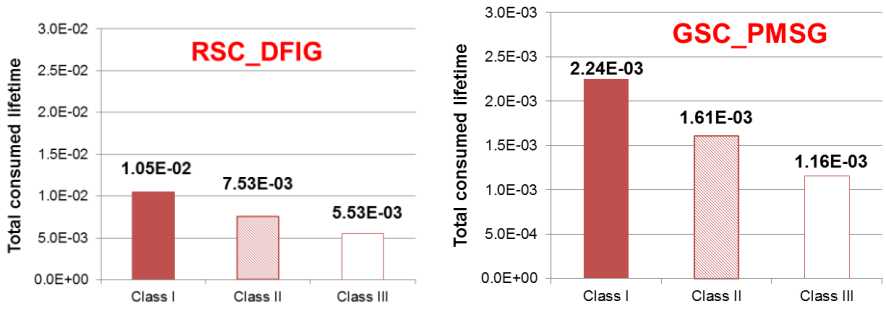

(a) (b)

Fig. 4.10. Total consumed lifetime at various wind classes. (a) Rotor-side converter of the DFIG system; (b) Grid-side converter of the PMSG system.

4.4 DFIG optimized reactive power flow

Due to the various characteristic of the power converter in the DFIG wind turbine system, the lifetime expectancy of the rotor-side converter could be significantly less than the grid-side converter. In order to fulfill the modern grid codes, the over-excited reactive power injection will further reduce the lifetime of the rotor-side converter. However, for the DFIG concept, it is known that both the grid-side converter and the rotor-side converter have the possibility to compensate for the reactive power.

As illustrated in (2.5) and (2.6), the rotor current and the rotor voltage of the DFIG is closely related to the generated active power by the wind energy, as well as the reactive power exchange between the DFIG and the grid. Similarly, it can be seen that the current of the grid-side converter and its interfacing voltage also depend on the active power and reactive power from (2.3) and (2.4). Consequently, the reactive current support introduces the current stress to the power device as well as the voltage stress in dc-link voltage for both the rotor-side converter and the grid-side converter [15]. As these two factors are tightly linked to the loss dissipation of the power semiconductor, the effects of the reactive power injection on the current and voltage stress of the power device are shown in Fig. 4.11, where the wind speed 12 m/s, 8.4 m/s and 5.9 m/s indicate the super-synchronous mode, synchronous mode and sub-synchronous mode of the DFIG operation.

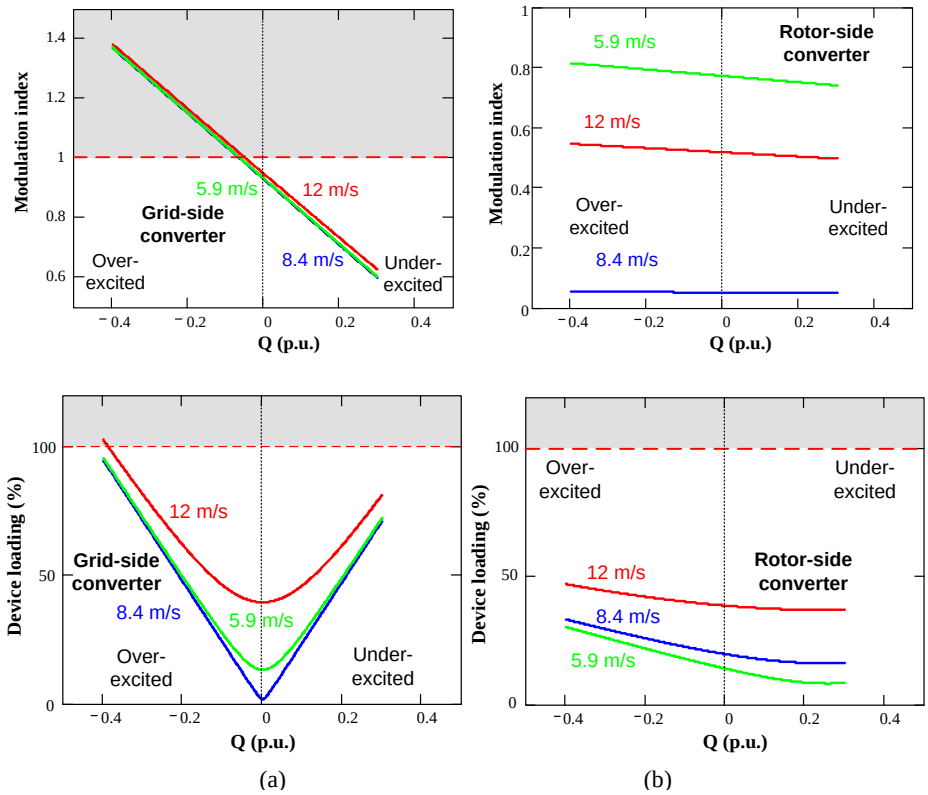

(a) (b)

Fig. 4.11. Effects of the reactive power injection on the current and voltage stress of the power device for the DFIG system. (a) Grid-side converter; (b) Rotor-side converter.

For the grid-side converter as shown in Fig. 4.11(a), when there is no reactive power exchange between the DFIG and the grid, the modulation index almost becomes full at three typical wind speeds. The synchronous mode has the relatively minimum value due to the fact that a very small slip power flows through the converter. The over-excited reactive power stresses the dc-link voltage significantly, while the under-excited reactive power reliefs, because the over-excited or the under-excited reactive power introduces the same or opposite direction of voltage drop across the filter inductance in respect to the grid voltage. Moreover, both the over-excited and the under-excited reactive power considerably increase the current loading of each device.

For the rotor-side converter, the rotor voltage is jointly decided by the stator and rotor winding ratio and slip value. As a result, the modulation index at different wind speeds is found in Fig. 4.11(b), in which the highest slip value causes the highest

modulation index. For the device loading of the rotor-side converter, the situation is better than the grid-side converter in the case of making reactive power injection. It is interesting to note that the under-excited reactive power injection reliefs the current stress of the power device, because the excitation energy actually comes from the grid.

As the over-modulation affects the dynamic performance in a power electronics converter [16], the different control strategies should all be realized within the linear modulation range. As shown in Fig. 4.11, only the over-excited reactive power injection increases the current stress of the power device, and it will reduce the lifetime of the rotor-side converter. As shown in Fig. 4.6(a), over-excited reactive power further unbalance the lifetime of the back-to-back power converters, so only this kind of the reactive power is taken into account. Different share of the reactive power between the rotor-side converter and the grid-side converter can be achieved by Table 4-1, where the dc-link voltage varies to ensure that the linear modulation range can be obtained for the grid-side converter.

Table 4-1 Different strategies for the DFIG joint reactive power compensation

	RSC (pu)	**GSC (pu)**	**U_{dc} (V)**
Case I	0	-0.4	1500
Case II	-0.1	-0.3	1350
Case III	-0.2	-0.2	1200
Case IV	-0.3	-0.1	1100
Case V	-0.4	0	1050

Note: It is assumed that 0.4 pu over-excited reactive power is needed.

The lifetime consumed per year of the individual wind speed is shown in Fig. 4.12 for the five different control strategies to accommodate the joint reactive power compensation. For the rotor-side converter, a smaller amount of reactive power injected from the rotor-side converter will give a smaller consumed lifetime. For the grid-side converter, the lifetime consumed per year of the individual wind speed changes significantly with different compensation strategies.

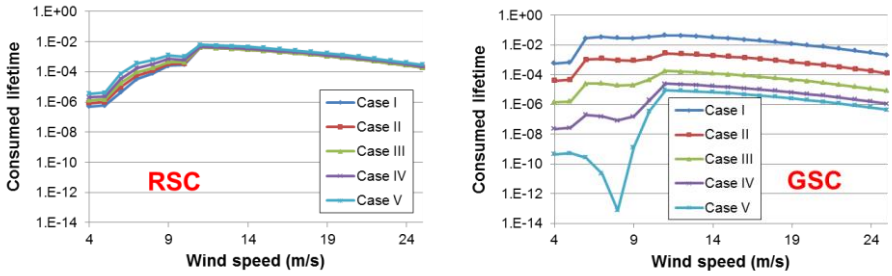

(a) (b)

Fig. 4.12. Consumed lifetime of the most stressed power semiconductor for joint reactive power compensations in the DFIG system. (a) Rotor-side converter; (b) Grid-side converter.

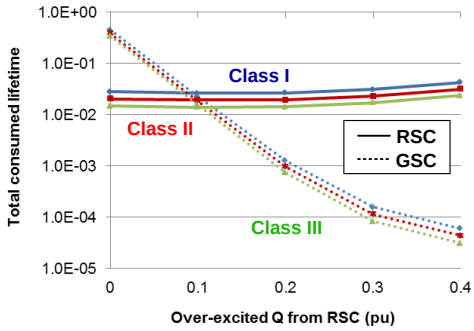

Fig. 4.13. Comparison of total consumed lifetime among different compensation strategies of the DFIG system, where the various wind classes are also investigated.

The total consumed lifetime of the five combined reactive power support strategies from the grid-side converter and the rotor-side converter is shown in Fig. 4.13. In the case of the wind Class I, at different compensation schemes, it is noted that the total consumed lifetime stays almost constant in a log-scale for the rotor-side converter, while for the grid-side converter, the total consumed lifetime varies significantly. Moreover, it can be seen that the most balanced lifetime share between the rotor-side converter and the grid-side converter appears in Case II, in which 0.1 pu over-excited reactive power is done by the rotor-side converter and 0.3 pu is compensated by the grid-side converter. It is evident that the total consumed lifetime of the rotor-side converter can be optimized from 4.27E-2 (Case V) to 2.65E-2 (Case II), which implies that the lifespan can almost be enhanced by 1.6 times. If the different wind classes are taken into account, the tendencies are almost consistent with the case of wind Class I.

4.5 Summary

This chapter addresses the approach of reliability assessment of power converters, and estimates and compares lifespan of the wind power converter. By using the well-known Coffin-Manson lifetime model and the annual wind profile, the concepts of the consumed lifetime per year and total consumed lifetime are introduced. Then, various wind profiles and grid codes influence on the lifetime estimation are also studied. It is found that the total consumed lifetime is considerably affected if the reactive power specified by the grid codes is required all year around. It can also be seen that the lifetime of the wind power converter is closely related to the wind profile. For the DFIG configuration, if the over-excited reactive power is required all year around, a reasonable share between the rotor-side converter and the grid-side converter can enhance the lifespan of the most stressed power converter, and thereby obtain a balanced lifetime of the back-to-back power converters.

Relevant attached papers

[A.5] D. Zhou, F. Blaabjerg, M. Lau, M. Tonnes, "Reactive power impact on lifetime prediction of two-level wind power converter," *in Proc. of PCIM 2013*, pp. 564-571, 2013.

[A.6] D. Zhou, F. Blaabjerg, M. Lau, M. Tonnes, "Optimized reactive power flow of DFIG power converters for better reliability performance considering grid codes," *IEEE Trans. on Industrial Electronics*, IEEE early access.

References

[1] "ZVEI - Handbook for robustness validation of automotive electrical/electronic modules," Jun. 2013.

[2] Y. Song, B. Wang, "Survey on reliability of power electronic systems," *IEEE Trans. on Power Electronics*, vol. 28, no. 1, pp. 591-604, Jan. 2013.

[3] D. Hirschmann, D. Tissen, S. Schroder, R. W. De Doncker, "Reliability prediction for inverters in hybrid electrical vehicles," *IEEE Trans. on Power Electronics*, vol. 22, no. 6, pp. 2511-2517, Nov. 2007.

[4] L. Wei, R. J. Kerkman, R. A. Lukaszewski, H. Lu, Z. Yuan, "Analysis of IGBT power cycling capabilities used in doubly fed induction generator wind power system," *IEEE Trans. on Industry Applications*, vol. 47, no. 4, pp. 1794-1801, July. 2011.

[5] D. Weiss, H. Eckel, "Fundamental frequency and mission profile wearout of IGBT in DFIG converters for windpower", *in Proc. of EPE 2013*, pp. 1-6, 2013.

[6] K. Ma, M. Liserre, F. Blaabjerg, T. Kerekes, "Thermal loading and lifetime estimation for power device considering mission profiles in wind power converter," *IEEE Trans. on Power Electronics*, IEEE early access.
[7] ABB Application Note, Load-cycling capability of HiPaks, 2004.
[8] A. Wintrich, U. Nicolai, T. Reimann, "Semikron Application Manual," 2011.
[9] D. Zhou, F. Blaabjerg, M. Lau, M. Tonnes, "Thermal cycling overview of multi-megawatt two-level wind power converter at full grid code operation," *IEEJ Journal of Industry Applications*, vol. 2, no. 4, pp. 173-182, Jul. 2013.
[10] U. Scheuermann, R. Schmidt, "A new lifetime model for advanced power modules with sintered chips and optimized Al wire bonds", *in Proc. of PCIM 2013*, pp. 810-813, 2013.
[11] D. Zhou, F. Blaabjerg, M. Lau, M. Tonnes, "Thermal profile analysis of doubly-fed induction generator based wind power converter with air and liquid cooling methods," *in Proc. of EPE 2013*, pp. 1-10, 2013.
[12] Wind turbines – part I: design requirements", IEC 61400-1, 3rd edition.
[13] Vestas website (Available: http://www.vestas.com/en/wind-power-plants/wind-project-planning/siting/wind-classes.aspx?action=3#/vestas-univers).
[14] The Swiss wind power data website. (Available: http://wind-data.ch/tools/weibull.php).
[15] D. Zhou, F. Blaabjerg, M. Lau, M. Tonnes, "Thermal behavior optimization in multi-MW wind power converter by reactive power circulation," *IEEE Trans. on Industry Applications*, vol. 50, no. 1, pp.433-440, Jan. 2014.
[16] S. Busquets-Monge, R. Maheshwari, S. Munk-Nielsen, "Over-modulation of n-level three-leg DC–AC diode-clamped converters with comprehensive capacitor voltage balance," *IEEE Trans. on Industrial Electronics*, vol. 60, no. 5, pp.1872-1883, May 2013.

Chapter 5

Energy loss evaluation of wind turbine systems

With the increasing wind power proportion of the total energy production, the lower cost per kWh is preferred. This chapter is going to analyze and investigate the impacts of mission profile on the cost of energy both in the PMSG system and in the DFIG system.

5.1 Important concepts of energy loss

According to the power curve of the wind turbine as shown in Fig. 2.1, the Annual Energy Production (AEP – unit: MWh) from wind energy can be obtained with the aid of the produced power P_{Pro} at certain wind speed i, and the annual duration of this wind speed T [1].

$$AEP = \sum_{i=4}^{25} P_{Pro}(i) \cdot T(i) \tag{5.1}$$

In respect to the AEP, it is noted that the typical addressed wind speeds are from the cut-in wind speed (4 m/s) until the cut-out wind speed (25 m/s).

During the process of the wind energy harvesting, some of the energy is consumed by the wind turbine system. Generally, it is called the Energy Loss Per Year (ELPY – unit: MWh) and it can be calculated as,

$$ELPY = \sum_{i=4}^{12} (P_{Gen}(i) + P_{Conv}(i)) \cdot T(i) \tag{5.2}$$

where the P_{Gen} denotes the generator loss and the P_{Conv} denotes the power converter loss. It is worth to mention that the ELPY is only of interest from the cut-in wind speed (4 m/s) to the rated wind speed (12 m/s) seen from an energy production point of view, because if the wind speed is higher than the rated value, it is assumed that the power loss dissipated in the wind turbine system can be compensated from the mechanical power from the wind turbine blades.

The Annual Loss Of Energy (ALOE – unit: %) is achieved by dividing the ELPY from the AEP,

$$ALOE = \frac{ELPY}{AEP} \cdot 100\% \tag{5.3}$$

As a result, Fig. 5.1 graphically shows the framework to predict the cost of energy loss in terms of the AEP, ELPY and ALOE. It can be seen that different wind profiles and different reactive power requirements of the grid codes can be analyzed by such tool.

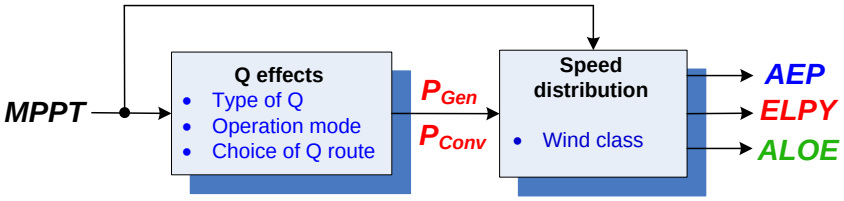

Fig. 5.1. Framework to predict the cost of energy loss in the wind turbine system.

5.2 Mission profile effects on PMSG system

As the TSO recently tightens the LVRT capability of renewable energy systems, a PMSG based wind turbine system with full-scale power converter seems to be more widely employed due to its advantage of full power controllability [2]-[6]. The back-to-back power converters consist of the generator-side converter and the grid-side converter as shown in Fig. 5.2. As only the grid-side converter is responsible to react to the grid code requirements, this part is mainly focuses on a 2 MW PMSG system.

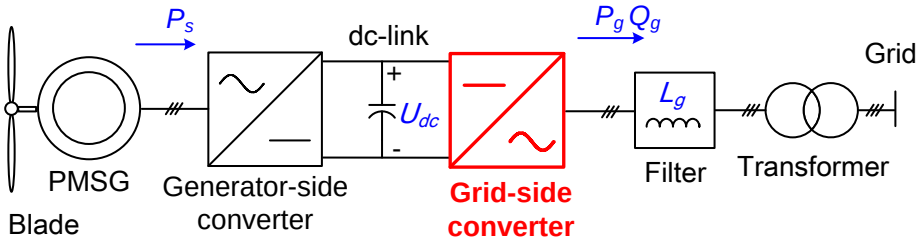

Fig. 5.2. Configuration of the full-scale power converter based permanent magnet synchronous generator wind turbine system.

As mention in Chapter 1, one of the strictest grid requirements is established by German TSO as shown in Fig. 5.3. Different control objectives can be taken by having various amount of reactive power injection like an Extreme Reactive Power (EQ)

injection or the Constant Power Factor (CPF) operation. In the case of CPF operation, the power factor of the OE reactive power injection is slightly smaller than the UE reactive power injection. Moreover, the whole range of the reactive power is enveloped by the EQ operation.

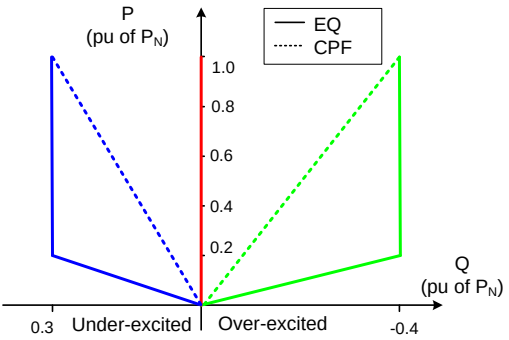

Fig. 5.3. Supportive reactive power range of modern wind power system stated in German grid codes [7]. Note: EQ denotes operation mode of the extreme reactive power injection and CPF denotes operation mode of the constant power factor.

According to a 2 MW wind turbine power curve [1], the envelope of the grid converter current amplitude and the displacement angle is calculated and shown in Fig. 5.4(a) and Fig. 5.4(b) from the cut-in 4 m/s until the cut-out 25 m/s, in which the maximum range of the reactive power as well as no reactive power exchange (NOR) are taken into account. It is noted that both the current amplitude and the displacement angle become constant, if the wind speed reaches the rated 12 m/s. Moreover, the introduction of either the OE or the UE reactive power imposes additional current stress. Another turning point occurs in the case of the reactive power compensation during the increase of the wind speed because the produced active power gets 0.2 pu at such wind speed. In respect to the displacement angle, the dominant reactive current at lower wind speed forces the converter current almost to be leading or lagging 90 degree compared to the converter voltage. However, at the higher wind speed, the converter current and voltage are nearly in opposite direction as the component of active current takes up the majority of the total current.

Because the change of reactive power alters the current loading of the power device, it is worth to translate this information further into the power dissipation of the power

device. Using the conventional symmetrical space vector modulation [8]-[10], the power dissipation of the IGBT and the freewheeling diode can then analytically be calculated as shown in Fig. 5.5(a) and Fig. 5.5(b), respectively. It can be seen that the loading of the IGBT is heavier than the diode due to the direction of the active power flow. Furthermore, the loss in the case of the EQ and the CPF reactive power injections are also highlighted.

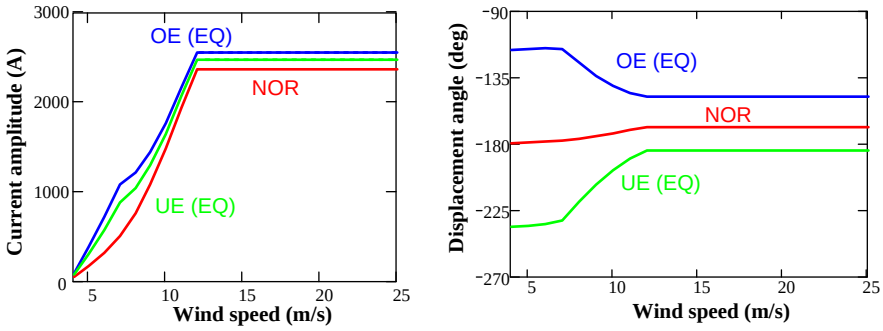

(a) (b)

Fig. 5.4. Reactive power effects on power device loading of the grid-side converter in the PMSG system. (a) Current amplitude versus wind speed; (b) Displacement angle versus wind speed.

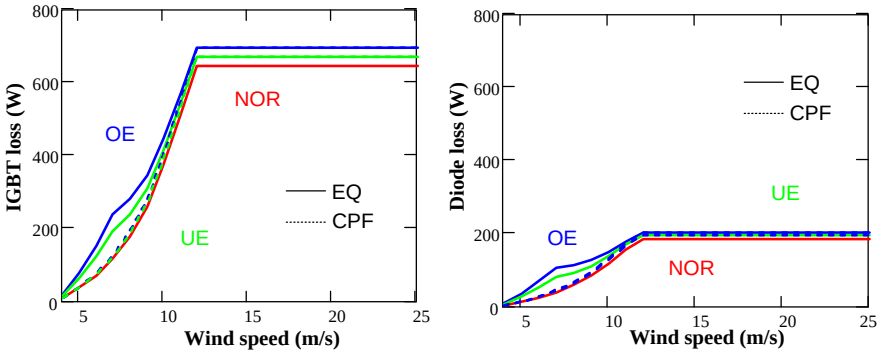

(a) (b)

Fig. 5.5. Loss profile of power semiconductor in the PMSG grid-side converter. (a) IGBT loss; (b) Diode loss.

5.2.1 Various wind classes

As shown in Fig. 4.4, taking the Class I wind profile for an example, the energy loss of the grid-side converter is shown in Fig. 5.6(a) at various types of reactive power injection. It is noted that only the difference between the cut-in and rated wind speed is taken into account. Due to the fact that the OE reactive power gives the most energy loss, and it is then considered at various wind profiles. As shown in Fig. 5.6(b), it can be seen that the shape of the energy loss at each wind speed is consistent with the wind distribution using this strategy of the reactive power injection.

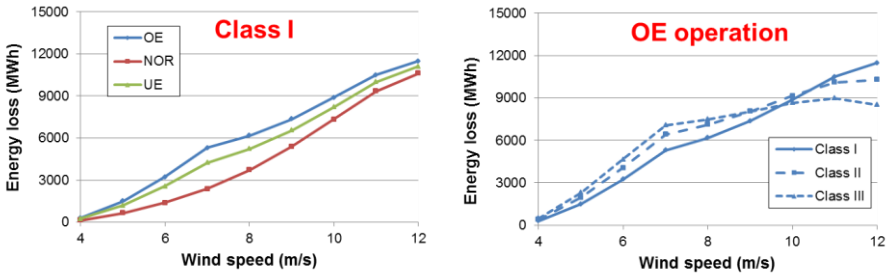

(a) (b)

Fig. 5.6. Energy loss evaluation from cut-in to rated wind speed. (a) Various types of reactive power at the Class I wind profile; (b) Various wind classes in the case of over-excited reactive power.

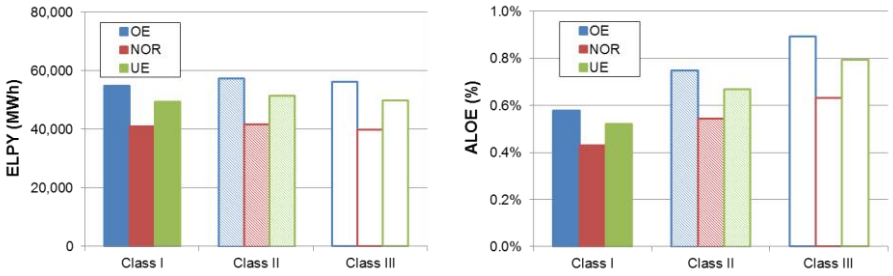

(a) (b)

Fig. 5.7. Cost of energy with different wind classes. (a) Energy Loss Per Year (ELPY); (b) Annual Loss Of Energy (ALOE).

By adding the energy loss of the individual wind speed together, the ELPY is shown Fig. 5.7(a), in which both the UE and the OE reactive power injection increase the ELPY for all kinds of wind classes. Moreover, it is interesting to see that all wind classes have almost a similar EPLY regardless of the reactive power type. Due to the

calculated AEP for each wind class, the ALOE is shown in Fig. 5.7(b). It is evident that the higher the wind class causes the lower the ALOE, because a higher wind class actually yields larger amount of the AEP. Besides, the highest ALOE 0.89 % appears at Class III, if the OE reactive power is injected all year around.

5.2.2 Various operation modes of reactive power injection

In respect to the operation modes at wind Class I, the EQ and the CPF reactive power injection control method are compared. As shown in Fig. 5.8, regardless of the OE or the UE reactive power, the CPF operation mode is the most cost-effective compared to the EQ operation mode, as the consumed energy is less in the CPF mode.

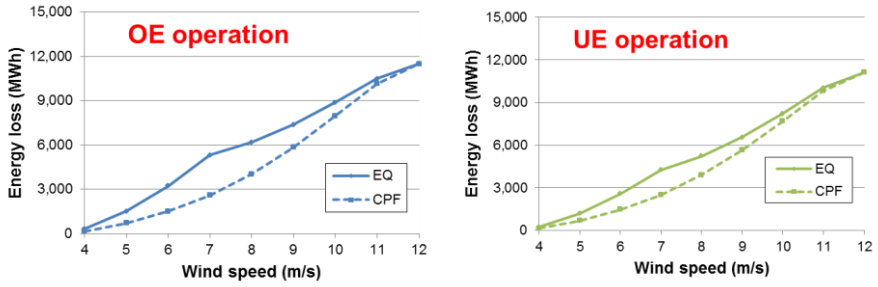

(a) (b)

Fig. 5.8. Influence of the different operational modes on energy loss for the PMSG wind turbine. (a) Over-excited reactive power injection; (b) Under-excited reactive power injection.

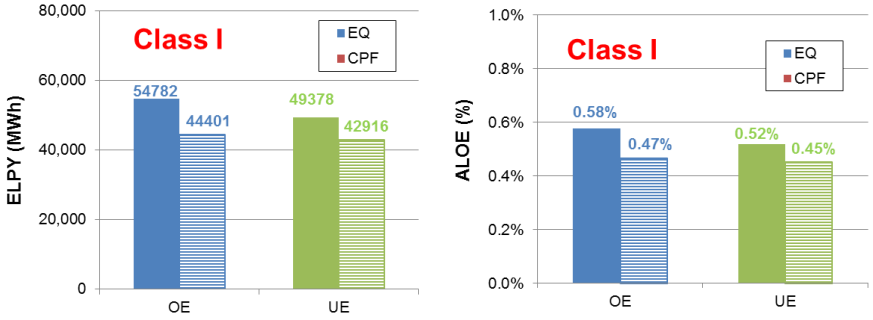

(a) (b)

Fig. 5.9. Energy loss per year with different operation modes under wind Class I. (a) Energy Loss Per Year (ELPY); (b) Annual Loss Of Energy (ALOE).

Consequently, as shown in Fig. 5.9(a), the CPF control scheme saves considerable energy both in the OE reactive power and the UE reactive power injection. According

to Fig. 5.9(b), the ALOE is reduced from 0.58% to 0.47%, if the operation mode switches from EQ to CPF operation, implying 19.0% energy saving for the CPF compared to the EQ, if the OE reactive power is required all year around. It is also valid for the UE reactive power injection, 13.5% energy saving can be obtained, if the control scheme changes from the EQ operation to the CPF operation.

5.3 Reduced cost of reactive power in DFIG system

If a reactive power is demanded by the TSO, it is of interest to compare the loss of the whole DFIG system, as the reactive power supported by the grid-side converter only affects the loss of the grid-side converter, while the reactive provided by the rotor-side converter not only influences the loss of the rotor-side converter, but also the loss of the DFIG generator itself.

5.3.1 Loss model of DFIG itself

As shown in Fig. 5.10, the common-adopted methodology to compensate the reactive power is from the stator of the induction generator, due to the fact that it introduces a small increase of the rotor-side current because of the winding ratio between the stator and the rotor of the DFIG [11]. However, this approach not only affects the loss of the rotor-side converter, but also imposes the loss of the DFIG itself.

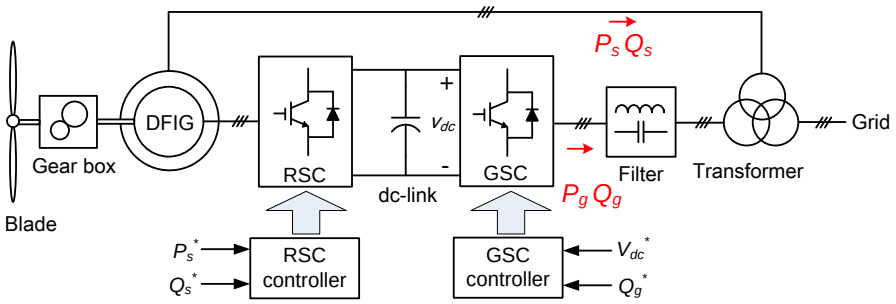

Fig. 5.10. Typical DFIG configuration in a wind turbine system (GSC: Grid-Side Converter, RSC: Rotor-Side Converter).

Loss dissipation inside the induction generator generally consists of the copper loss and iron loss as shown in Fig. 5.11 [12]. If the stator voltage oriented control is applied, the stator-side active power P_s and reactive power Q_s are independently in line with the

stator d-axis current i_{sd} and q-axis current i_{sq}. Due to the flux equation in the DFIG, the relationship between the rotor and stator current under d-axis and q-axis are,

$$\begin{cases} i_{rd}^{'} = -\dfrac{L_{ls}+L_m}{L_m} i_{sd} \\ i_{rq}^{'} = -\dfrac{U_{sm}}{\omega_1 \cdot L_m} - \dfrac{L_{ls}+L_m}{L_m} i_{sq} \end{cases} \tag{5.4}$$

where L_{ls} and L_m denote the stator leakage inductance and the magnetizing inductance, U_{sm} denotes the rated grid phase-voltage, and ω_1 is the fundamental electrical angular frequency.

The copper loss P_{cu} is resistive losses occurring in the winding coils and can be calculated using the equivalent d-q axis circuit stator resistance R_s and rotor resistance R_r as shown in Fig. 5.11,

$$P_{cu} = \frac{3}{2} \cdot [(i_{sd}^2 + i_{sq}^2) \cdot R_s + (i_{rd}^2 + i_{rq}^2) \cdot R_r] \tag{5.5}$$

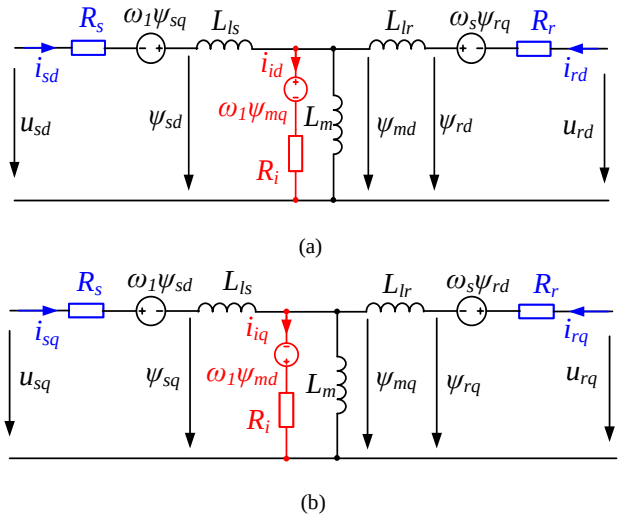

Fig. 5.11. DFIG equivalent circuit considering copper loss and iron loss. (a) d-axis circuit; (b) q-axis circuit.

where i_s and i_r denote the stator current and the rotor current, and the subscript d and q denote the value at d-axis and q-axis circuit, respectively. It can be seen that the copper loss of the induction generator is dependent on the stator active power and reactive power.

Generally, the iron loss is produced by the flux change, and it consists of eddy current loss and hysteresis loss, both of which are tightly connected with the operation frequency and flux density [12]. A calculation method is based on empirical formula in advance, and the calculation is normally done according to the Finite Element Method (FEM). Alternatively, iron losses can be estimated from an electrical point of view [13], [14]. In other words, it can be expressed by the equivalent iron resistance R_i in parallel with the magnetizing inductance as shown in Fig. 5.11.

The voltage equations for the additional iron resistor are,

$$\begin{cases} R_i \cdot i_{id} = \dfrac{d\psi_{md}}{dt} - \omega_1 \cdot \psi_{mq} \\ R_i \cdot i_{iq} = \dfrac{d\psi_{mq}}{dt} + \omega_1 \cdot \psi_{md} \end{cases} \tag{5.6}$$

where i_i is the equivalent iron loss current, and ψ_m is the magnetizing flux. Moreover, with the aid of the relationship between the stator flux and magnetizing flux, it is possible to derive,

$$\begin{cases} \psi_{md} = \psi_{sd} - L_{ls} \cdot i_{sd} \\ \psi_{mq} = \psi_{sq} - L_{ls} \cdot i_{sq} \end{cases} \tag{5.7}$$

where ψ_s denotes the stator flux.

Due to the stator voltage orientation, ψ_{md} is nearly zero, and ψ_{mq} is a constant value because of the stiff grid with the constant voltage and constant frequency. Substituting (5.7) into (5.6), the iron current can be calculated,

$$\begin{cases} i_{id} = \dfrac{\omega_1 L_{ls}}{R_i} \cdot i_{sq} + \dfrac{U_{sm}}{R_i} \\ i_{iq} = -\dfrac{\omega_1 L_{ls}}{R_i} \cdot i_{sd} \end{cases} \tag{5.8}$$

According to (5.8), it is noted that the d-axis iron loss current depends on the reactive power, while the q-axis iron loss current is related with the active power P_s. As a consequence, the iron loss P_{fe} can be calculated as,

$$P_{fe} = \frac{3}{2} \cdot [(i_{id}^2 + i_{iq}^2) \cdot R_i] \tag{5.9}$$

In respect to the losses of the power converter of the DFIG system, it is well described in [15]. If the reactive power is provided by the rotor-side converter, the loss model of the generator (copper loss and iron loss) and the rotor-side converter (conduction loss and switching loss both in the IGBT and the freewheeling diode) can be calculated. With the aid from the grid-side converter, another approach may be realized to compensate the reactive power, which stresses the grid-side converter and affects the loss of the grid-side converter and its filter. Similarly, as the conduction loss and switching loss of the IGBT and the diode are analytically solved, thus the grid-side converter loss can be calculated. Compared with the grid-side converter losses, the grid filter loss is small enough [16], and it is simply calculated by its parasitic Equivalent Series Resistance (ESR).

5.3.2 Optimized design of grid filter

For the DFIG system, if the reactive power of the grid codes is provided by the grid-side converter [7], [17], [18], in the case of the constant dc-link voltage, the modulation index is closely related to the filter inductance, and it will increase very fast to over-modulation, especially when over-excited reactive power is needed [19]. There are two ways to deal with this issue – increase the dc-link voltage which gives higher switching losses and power rating of the converter, or design an optimized grid filter, where the inductance is reduced.

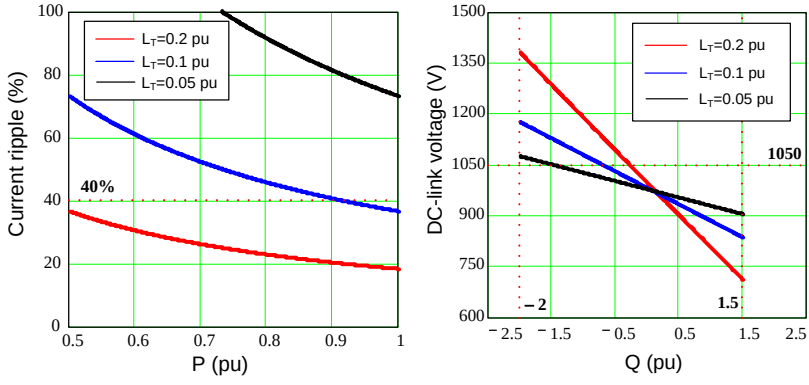

(a) (b)

Fig. 5.12. Influence of grid filter inductance on the grid-side converter performance. (a) Current ripple rate; (b) Reactive power range.

As recommended in IEEE 519-1992, harmonics higher than 35th should be explicitly limited [20]. If a simple L filter is assumed to be used, the current ripple amplitude is jointly decided by the dc-link voltage, the switching frequency and inductance value [21]. For a typical 2 MW DFIG based wind turbine system, the relationship between the current ripple and the loading is shown in Fig. 5.12(a). It is noted that the higher inductance gives the lower switching current ripple at the same switching frequency as expected.

As mentioned, the value of the filter inductance also affects the modulation index. Fig. 5.12(b) indicates the relationship between the dc-link voltage and the reactive power (a full modulation index is assumed). In order to fulfill the reactive power demand stated in E.ON Netz [7], the DFIG system should cover up to 0.4 pu OE and 0.3 pu UE reactive power in respect to the generator power rating. As the pu value is normally defined by the power rating of the induction generator, the used pu value in Fig. 5.12(b) becomes 2.0 pu OE and 1.5 pu UE reactive power in respect to the grid-side converter, which is five times higher than the pu value seen from the induction generator due to the rated slip power through the grid-side converter. It can be seen that the minimum dc-link voltage increases considerably with higher inductance if OE reactive power control is needed. On the other hand, the higher inductance results in a lower switching ripple. Thus, it is a trade-off procedure of the inductance selection. However, for the DFIG system, the final current ripple of the grid side is calculated as the sum of the stator current and the grid-side converter current. Generally, the stator current is much higher than the grid-side converter current, which implies that 40% current ripple at the grid-side converter is acceptable and it is used as the design criteria. As a result, the inductance of the grid filter is selected at 0.1 pu based on Fig. 5.12(a).

The equivalent single-phase grid-side converter with LCL filter is shown in Fig. 5.13, which typically has no additional sensors compared to the conventional L filter configuration. Although the different positions of the voltage and current sensors may have their own advantages [21], the current sensors on the converter side is chosen, because it can be designed to protect the power semiconductor and it is commonly used in industrial application.

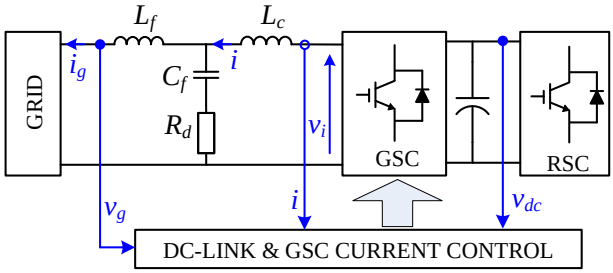

Fig. 5.13. Equivalent single-phase grid-side converter with the LCL filter.

As shown in Fig. 5.13, L_c is the converter side inductance, L_f is the grid side inductance, and C_f is the capacitor bank, which is connected to a damping resistance R_d. The converter current and the grid current are represented by i, i_g. Moreover, the voltage of the converter output and the point of common coupling are represented by v_i, v_g, respectively.

Table 5-1 L and LCL filter parameters

L filter	Filter inductor L_g	500 μH
LCL filter	Converter-side inductor L_c	125 μH
	Grid-side inductor L_f	125 μH
	Filter capacitor C_f	220 μF
	Damping R_d	0.5 mΩ

A step-by-step design procedure for LCL filter is described in [22]. This design is focused on that the total inductance of the LCL filter is able to reduce to half compared to the L filter but with similar current ripple at the grid side. Afterwards, a proper inductance sharing into L_c (0.025 pu) and L_g (0.025 pu) is realized in order to achieve the desired current ripple reduction. The capacitance value (0.1 pu) is then determined by the absorbed reactive power at the rated conditions, in which the resonant frequency becomes 1.35 kHz (67.5% of f_s). The passive damping is inevitably designed to overcome the resonant problem, where its power dissipation is also taken into account [22]-[24]. The used filter parameters are summarized in Table 5-1. Alternatively, active damping in LCL filter is also widely used [25], [26].

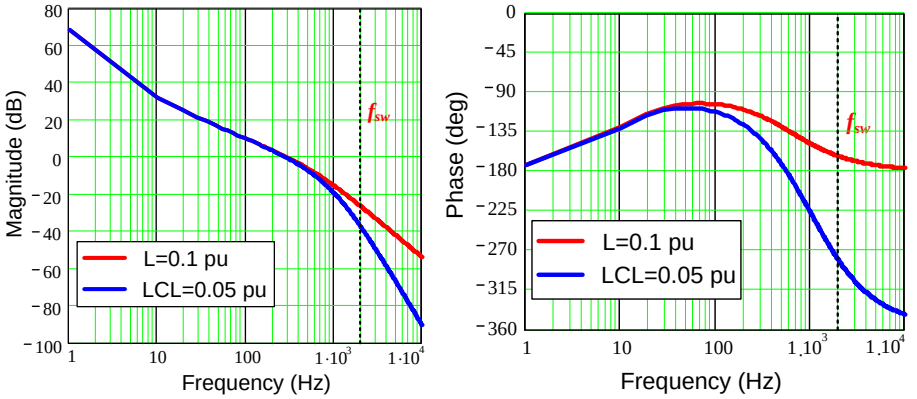

(a) (b)

Fig. 5.14. Bode plot comparison between pure L filter (0.1 pu) and designed LCL filter (0.05 pu). (a) Magnitude diagram; (b) Phase diagram.

If the transfer functions of the PI current controller, the modulation technique as well as some delays introduced by digital control are considered, the open-loop Bode plots of the L and the LCL filter from the grid-side converter current reference to the line current are then shown in Fig. 5.14. It is clear that the magnitude and phase characteristic between the L and LCL filter are exactly the same at lower frequency, if the PI parameter used in the current controller is properly designed. It is also noted that smaller magnitude of the LCL filter appears at the switching frequency compared to the L filter. Moreover, the damping of the LCL filter has a better performance compared to the L filter above the switching frequency.

5.3.3 Cost of energy in DFIG system

The loss distribution of the whole DFIG system is firstly evaluated at the normal operation (NOR), i.e. no reactive power is exchanged between the DFIG system and the grid. Then, the loss distribution is calculated in the case of the OE reactive power is fully from the rotor-side converter (OE_RSC) or the GSC. As the type of the grid filter only influences the loading of the grid-side converter, it can be further divided into the L filter (OE_L_GSC) and the LCL filter (OE_LCL_GSC). The above cases are summarized in Table 5-2. It is worth to mention that the dc-link voltage can be different at various compensation schemes. It can be seen that the OE_L_GSC has

higher dc voltage compared to the OE_LCL_GSC, due to the higher total inductance of the filter.

Table 5-2 Cases for normal operation and over-excited reactive power injection

	Q_s (pu)	Q_g (pu)	U_{dc} (V)
NOR	0	0	1050
OE_RSC	0.4	0	1050
OE_L_GSC	0	0.4	1250
OE_LCL_GSC	0	0.4	1100

The loss breakdown at the rated power for the four cases in terms of the DFIG, the rotor-side converter, the grid-side converter and its filter is then shown in Fig. 5.15. In respect to the generator loss, it can be seen that the generator losses (especially copper losses) increase only in the OE_L_RSC operation compared to the NOR operation in Fig. 5.15(a), because the reactive power injection by the rotor-side converter changes the generator's stator and rotor current amplitude. In respect to the rotor-side converter losses, it also increases considerably in the OE_L_RSC. Moreover, the power loss (especially the switching loss) increases slightly in OE_L_GSC and OE_LCL_GSC operation modes compared to NOR operation, since the dc-link voltage becomes higher. For the grid-side converter losses, OE_L_RSC stays the same with the NOR operation. However, if the reactive power is supported by the grid-side converter, both the conduction losses and the switching losses increase significantly because of the dominating reactive current, and it also becomes three times higher than in the case that the reactive power is injected by the rotor-side converter. The tendency of the grid filter loss is similar to the grid-side converter because of the same current through them. It is noted that if the OE reactive power is compensated from the grid-side converter, the LCL filter consumes lower power loss due to the smaller ESR compared to the pure L filter. Besides, compared with the loss of the DFIG and the power converters, the loss dissipated in the DFIG is dominant.

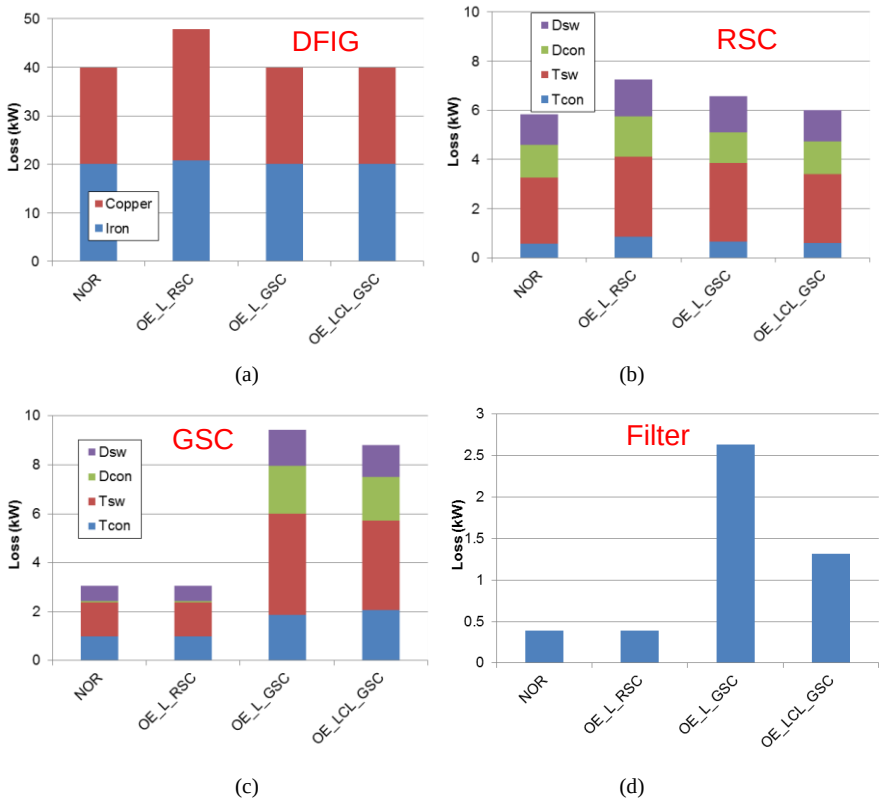

Fig. 5.15. Loss breakdown at rated wind speed with various reactive power compensation schemes. (a) DFIG itself; (b) Rotor-side converter; (c) Grid-side converter; (d) Grid filter.

The annual wind is distributed according to the IEC standard - Class I [27], where a mean wind speed 10 m/s is shown in Fig. 4.4. As each loss (kW) at various wind speeds can be calculated by a wind speed step of 1 m/s, as well as the yearly wind speed distribution (hours), the annual loss of energy can be calculated. It is worth to mention that the annual loss of energy is only of concern from the cut-in wind speed to the wind speed of rated power.

The annual energy loss of the DFIG system at various operation modes is shown in Fig. 5.16(a). It is evident that the energy consumed by the induction generator is much higher than in the back-to-back power converters. Moreover, it can be seen that, although the OE reactive power compensation from the grid-side converter significantly imposes the loading of the grid-side converter itself and its filter, the

OE_LCL_GSC still has the lowest cost of energy, while the OE_RSC consumes the highest energy loss, as the OE reactive power compensated from the rotor-side converter further increases the loss of the DFIG.

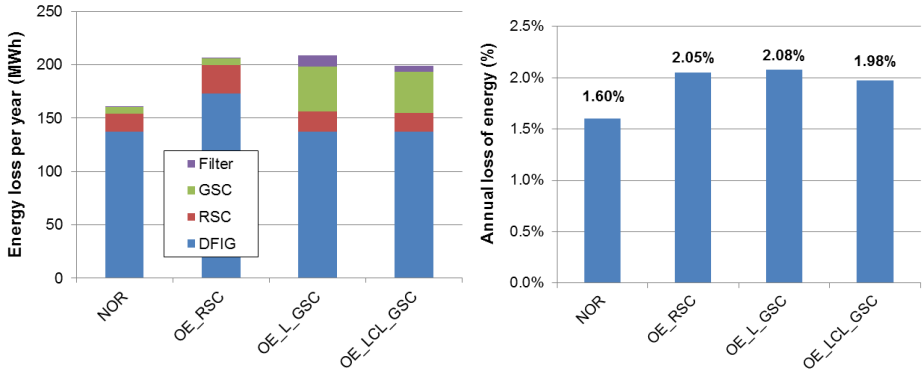

(a) (b)

Fig. 5.16. Annual loss of energy in normal operation and if the over-excited reactive power is required all year around. (a) Energy loss per year (MWh); (b) Annual loss of energy (%).

It is also an interesting perspective to express the annual energy loss in terms of the percentage over the yearly produced energy, which is accumulated from the cut-in until the cut-off wind speed. As shown in Fig. 5.16(b), under the assumption that the OE reactive power is required all year around, the worst case is the OE_RSC that takes up 2.05% annual energy, while the best situation is achieved by the OE_LCL_GSC 1.98%, which implies 3.73% energy savings per year.

5.3.4 Experimental verification of loss dissipation

In order to validate the loss dissipation of the DFIG system at different reactive power compensation methods, a down-scaled 7.5 kW test rig is built up and it is shown in Fig. 5.17. The DFIG is externally driven by a prime motor, and two 5.5 kW Danfoss motor drives are used for the grid-side converter and the rotor-side converter, both of which are controlled with dSPACE 1006 controllers. Besides, the LCL filter is employed as the grid filter, whose capacitor branch can be bypassed to realize the L type filter. The important parameters of the test setup are summarized in Table 5-3. It is noted that, as the rated rotor speed is 1800 rpm, the pu value of the grid filter is calculated based on the slip power of the DFIG.

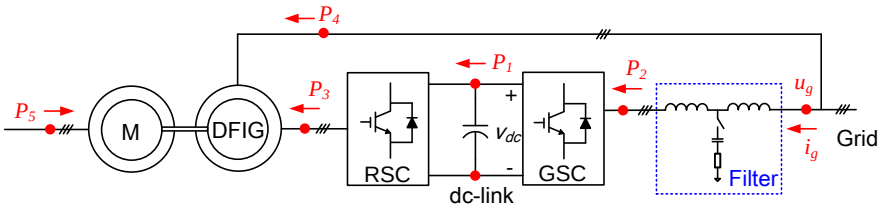

Fig. 5.17. Setup of 7.5 kW DFIG test rig.

Table 5-3 Test rig with 7.5 kW generator and 5.5 kW back-to-back power converters

Generator	Rated power	7.5 kW
	Rated line voltage	380 V
	Stator leakage inductance	0.056 pu
	Rotor leakage inductance	0.084 pu
	Magnetizing inductance	1.294 pu
	Stator resistance	0.022 pu
	Rotor resistance	0.033 pu
	Equivalent iron loss resistance	35.734 pu
	Ratio of stator and rotor winding	0.336
Power converters	Rated power	5.5 kW
	Grid-side converter rated current	10 A
	Rotor-side converter rated current	10 A
	Switching frequency	5 kHz
Grid filters	L type	
	Interface inductance L_l	0.059 pu
	LCL type	
	Converter-side inductor L_c	0.036 pu
	Grid-side inductor L_f	0.023 pu
	Filter capacitor C_f	0.200 pu
	Damping R_d	0.134 pu

Under the condition that the full power of the DFIG 7.5 kW is realized at 1800 rpm, 0.4 pu reactive power according to the grid codes is compensated from the grid-side converter, the current injecting to the grid from the back-to-back power converter is compared with the LCL and L filter as shown in Fig. 5.18. It is noted that the fundamental currents of the L and the LCL filter both are 4.2 A, and the currents are

leading the grid voltage 90 degree, as the majority of which belongs to the reactive component. Furthermore, the maximum value of the harmonic spectrum around the switching frequency is 105 mA with the L filter, which is much higher than the LCL filter giving 25 mA.

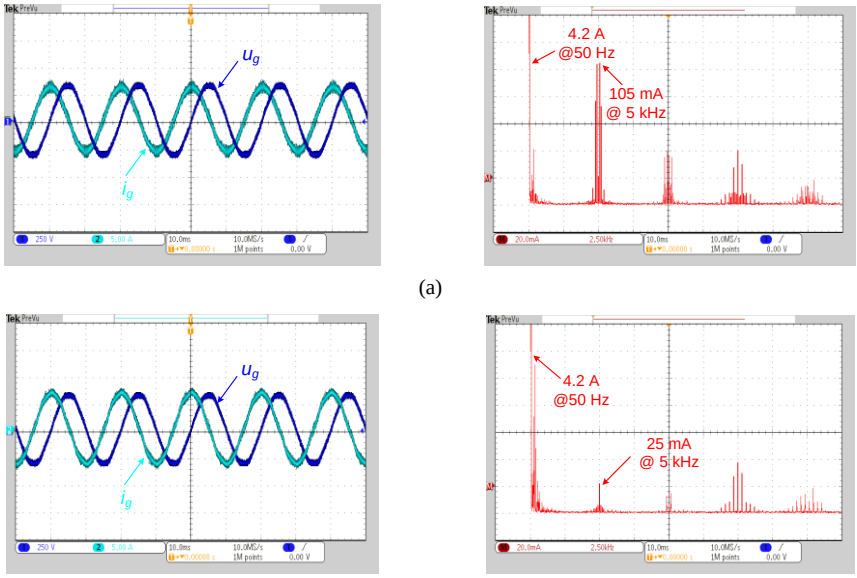

Fig. 5.18. Measured waveform and the harmonic of the grid current in the DFIG system. (a) L filter; (b) LCL filter.

The loss dissipation of the various parts in the down-scaled DFIG system is monitored by Yokogawa Power Analyzer WT3000. The loss of the DFIG itself, the rotor-side converter, the grid-side converter and the grid filter are tested separately and the results are shown in Fig. 5.19. It is worth to mention that the dc-link used in the above four cases is 600 V, 600 V, 750 V and 650 V, respectively. In respect to the loss of the DFIG itself and the rotor-side converter, they consume the highest loss in the case that the reactive power is compensated from the rotor-side converter. However, regarding the grid-side converter, the reactive power supported by the grid-side converter with an L filter leads to the highest power loss. Since the loss consumed in the DFIG actually contains the both the DFIG loss and the prime motor loss, the loss dissipation is much higher compared to the power electronic converters. A better result would have been obtained if the shaft power was measured. The loss distribution of various parts is quite

similar as analyzed in Fig. 5.15. The experimental result of total loss dissipation in the DFIG system at 1800 rpm is then shown in Fig. 5.20.

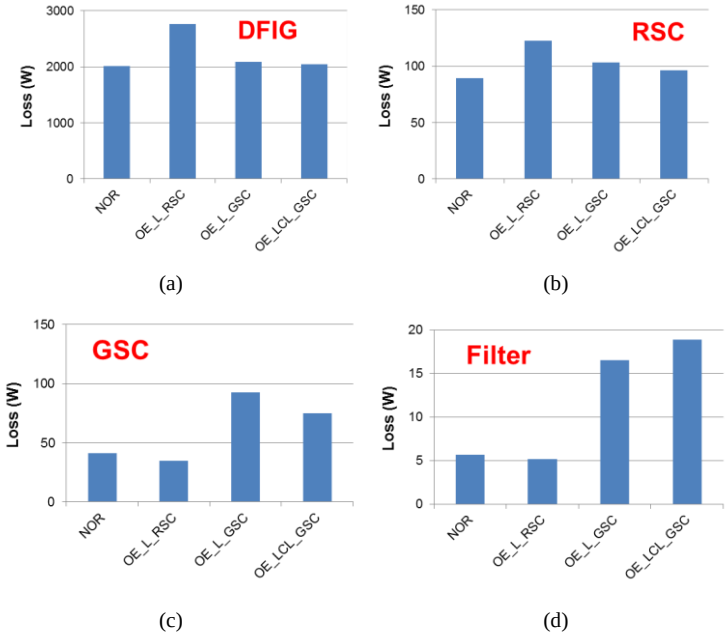

Fig. 5.19. Experimental result of loss dissipation in the DFIG system at 1800 rpm in case of the normal operation and the various reactive power compensation schemes. (a) DFIG itself; (b) Rotor-side converter; (c) Grid-side converter; (d) Grid filter.

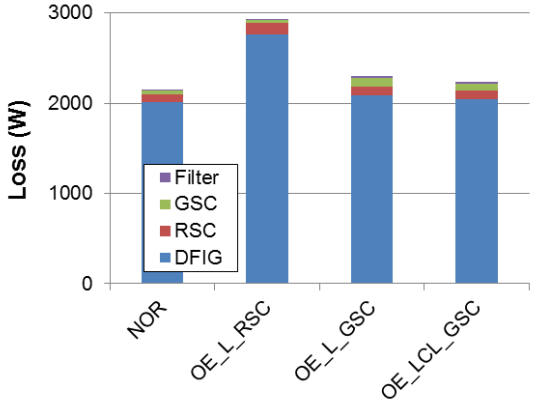

Fig. 5.20. Experimental result of total loss dissipation in the DFIG system at 1800 rpm in the case of the normal operation and the various reactive power compensation schemes.

5.4 Summary

This chapter addresses the energy loss evaluation of wind turbine system for the DFIG and PMSG system. In respect to the PMSG system, different wind classes and different operation modes of the reactive power injection are taken into account. It is found that both the over-excited and the under-excited reactive power increase the energy loss per year significantly, if the operation modes are provided all year around. Moreover, it is also concluded that in order to realize energy savings of the wind turbine system, a constant power factor control strategy is more preferred compared to an extreme reactive power injection. For the DFIG system, the over-excited reactive power compensated either by the DFIG itself or the grid-side converter is compared. It can be seen that over-excited reactive power injected from the grid-side converter has lower energy loss per year compared to the over-excited reactive power covered by the rotor-side converter. Furthermore, it is also found that the annual energy loss could become lower by using an optimized filter and thereby more energy can be produced by the wind turbine system. Moreover, the losses distribution of the DFIG system between the L and LCL filter are compared in a down-scaled 7.5 kW DFIG test rig with different control strategies of the reactive power.

Relevant attached papers

[A.7] D. Zhou, F. Blaabjerg, T. Franke, M. Tonnes, M. Lau, "Reduced cost of reactive power in doubly-fed induction generator wind turbine system with optimized grid filter," *in Proc. of ECCE 2014*, pp. 1490-1499, 2014.

[A.8] D. Zhou, F. Blaabjerg, T. Franke, M. Tonnes, M. Lau, "Reliability and energy loss in full-scale wind power converter considering grid codes and wind classes," *in Proc. of ECCE 2014*, pp. 3067-3074, 2014.

References

[1] Vestas website (Available: http://www.vestas.com/en/wind-power-plants/wind-project-planning/siting/wind-classes.aspx?action=3#/vestas-univers).

[2] F. Blaabjerg, K. Ma, "Future on power electronics for wind turbine systems," *IEEE Journal of Emerging and Selected Topics in Power Electronics*, vol. 1, no. 3, pp. 139-152, Sep. 2013.

[3] H. Polinder, J. A. Ferreira, B. B. Jensen, A. B. Abrahamsen, K. Atallah, R. A. McMahon, "Trends in wind turbine generator systems," *IEEE Journal of Emerging and Selected Topics in Power Electronics*, vol. 1, no. 3, pp. 174-185, Sep. 2013.

[4] H. Wang, M. Liserre, F. Blaabjerg, P. Rimmen, J. Jacobsen, T. Kvisgaard, J. Landkildehus, "Transitioning to physics-of-failure as a reliability driver in power electronics," *IEEE Journal of Emerging and Selected Topics in Power Electronics*, vol. 2, no. 1, pp. 97-114, Mar. 2014.

[5] M. Liserre, R. Cardenas, M. Molinas, J. Rodriguez, "Overview of multi-MW wind turbines and wind parks," *IEEE Trans. Industrial Electronics*, vol. 58, no. 4, pp. 1081-1095, Apr. 2011.

[6] J. Dai, D. Xu, B. Wu, "A novel control scheme for current-source-converter-based PMSG wind energy conversion systems," *IEEE Trans. on Power Electronics*, vol. 24, no. 4, pp. 963-972, Apr. 2009.

[7] E.ON-Netz. Requirements for offshore grid connections, Apr. 2008.

[8] J. W. Kolar, H. Ertl, F. C. Zach, "Influence of the modulation method on the conduction and switching losses of a PWM converter system," *IEEE Trans. on Industry Applications*, vol. 27, no. 6, pp. 1063-1075, Nov. 1991.

[9] Y. Ren, M. Xu, J. Zhou, F. C. Lee, "Analytical loss model of power MOSFET," *IEEE Trans. on Power Electronics*, vol. 21, no. 2, pp. 310-319, Mar. 2006.

[10] B. Backlund, R. Schnell, U. Schlapbach, R. Fischer, E. Tsyplakov, "Applying IGBTs", ABB Application Note, Apr. 2009.

[11] S. Engelhardt, I. Erlich, C. Feltes, J. Kretschmann, F. Shewarega, "Reactive power capability of wind turbines based on doubly fed induction generators," *IEEE Trans. Energy Conversion*, vol. 26, no. 1, pp. 364-372, Mar. 2011.

[12] R. Takahashi, H. Ichita, J. Tamura, M. Kimura, M. Ichinose, M. Futami, K. Ide, "Efficiency calculation of wind turbine generation system with doubly-fed induction generator," *in Proc. of International Conference on Electrical Machines (ICEM) 2010*, pp. 1-4, 2010.

[13] S. Wee, M. Shin, D. Hyun, "Stator-flux-oriented control of induction motor considering iron loss," *IEEE Trans. on Industrial Electronics*, vol. 48, no. 3, pp. 602-608, Jun. 2001.

[14] A. G. Abo-Khalil, H. Park, D. Lee, "Loss minimization control for doubly-fed induction generators in variable speed wind turbines," *in Proc. of IECON 2007*, pp. 1109-1114, 2007.

[15] D. Zhou, F. Blaabjerg, M. Lau, M. Tonnes, "Thermal cycling overview of multi-megawatt two-level wind power converter at full grid code operation," *IEEJ Journal of Industry Applications*, vol. 2, no. 4, pp. 173-182, Jul. 2013.

[16] C. Sintamarean, F. Blaabjerg, H. Wang, "Comprehensive evaluation on efficiency and thermal loading of associated Si and SiC based PV inverter applications," *in Proc. of IECON 2013*, pp. 555-560, 2013.

[17] M. Tsili, S. Papathanassiou, "A review of grid code technical requirements for wind farms," *IET on Renewable Power Generation*, vol. 3, no. 3, pp. 308-332, Sep. 2009.

[18] A. Camacho, M. Castilla, J. Miret, R. Guzman, A. Borrell, "Reactive power control for distributed generation power plants to comply with voltage limits during grid faults," *IEEE Trans. on Power Electronics*, IEEE early access.

[19] D. Zhou, F. Blaabjerg, M. Lau, M. Tonnes, "Thermal behavior optimization in multi-MW wind power converter by reactive power circulation," *IEEE Trans. on Industry Applications*, vol. 50, no. 1, pp. 433-440, Jan. 2014.

[20] A. Nagel, R. W. De Doncker, "Systematic design of EMI-filters for power converters," *in Proc. of IAS 2000*, pp. 2523-2525, 2000.

[21] R. Teodorescu, M. Liserre, P. Rodriguez, Grid Converters for Photovoltaic and Wind Power Systems. Hoboken, NJ, USA: Wiley, 2011.

[22] M. Liserre, F. Blaabjerg, S. Hansen, "Design and control of an LCL-filter-based three-phase active rectifier," *IEEE Trans. on Industry Applications*, vol. 41, no. 5, pp. 1281-1291, Sep. 2005.

[23] R. Pena-Alzola, M. Liserre, F. Blaabjerg, R. Sebastian, J. Dannehl, F. W. Fuchs, "Analysis of the passive damping losses in LCL-filter-based grid converters," *IEEE Trans. on Power Electronics*, vol. 28, no. 6, pp. 2642-2646, Jun. 2013.

[24] W. Wu, Y. He, T. Tang, F. Blaabjerg, "A new design method for the passive damped LCL and LLCL Filter-based single-phase grid-tied inverter," *IEEE Trans. on Industrial Electronics*, vol. 60, no. 10, pp. 4339-4350, Oct. 2013.

[25] M. Liserre, R. Teodorescu, F. Blaabjerg, "Stability of photovoltaic and wind turbine grid-connected inverters for a large set of grid impedance values," *IEEE Trans. on Power Electronics*, vol. 21, no. 1, pp. 263-272, Jan. 2006.

[26] M. Liserre, A. D. Aquila, F. Blaabjerg, "Genetic algorithm-based design of the active damping for an LCL-filter three-phase active rectifier," *IEEE Trans. on Power Electronics*, vol. 19, no. 1, pp. 76-86, Jan. 2004.

[27] Wind turbines – part I: design requirements", IEC 61400-1, 3rd edition.

Chapter 6
Reliability-oriented control strategies during grid fault

Due to the excellent fault ride-through ability of the full-scale power converter based wind energy generation system, where the back-to-back power converters completely decouple the generator from the grid connection, this chapter only focuses on control solutions of the partial-scale power converter equipped with the Doubly-Fed Induction Generator (DFIG) during the grid fault [1], [2]. The internal and external challenges for DFIG to ride through a grid fault are firstly analyzed and addressed. Afterwards, a novel control scheme is proposed and developed seen from a reliable operation perspective of the power electronics converter.

6.1 Existing issues for DFIG during grid fault

The DFIG configuration provides the advantages of variable speed operation and four-quadrant active and reactive power capabilities using the power converter only a small fraction of the generator rated power (20%-30%) [3]-[5]. However, on detecting a grid fault, the generator unit is usually disconnected to protect the vulnerable rotor converter by using crowbar [6]. This approach makes the DFIG to act as traditional squirrel-cage motor, absorbing the reactive power from the grid, which is against the modern grid codes [7], [8]. Another hardware solution for fault ride-through operation is to apply a dc chopper to prevent the dc-link over-voltage, which is an important solution to dissipate the produced power [9]. On the other hand, many studies have been conducted to overcome the grid fault seen from a software solution with the advantages of reduced cost and easy implementation [10]-[12]. However, the thermal behavior of the power switching device is seldom discussed during the fault occurrence, and it is closely related to the reliability of the long-term operation of wind turbine system.

A typical DFIG system is depicted in Fig. 6.1, in which a dc chopper is employed to realize the Low Voltage Ride-Through (LVRT). As the stator of the induction

generator is directly linked to the grid, the stator flux cannot be changed instantaneously when the grid fault occurs. Correspondingly, the component of the stator flux can be divided into the positive and natural stator flux in the case of the balanced voltage dip, while an extra negative component is introduced during the imbalanced grid fault [13], [14]. For simplicity, only the balanced grid voltage dip is analyzed in this study.

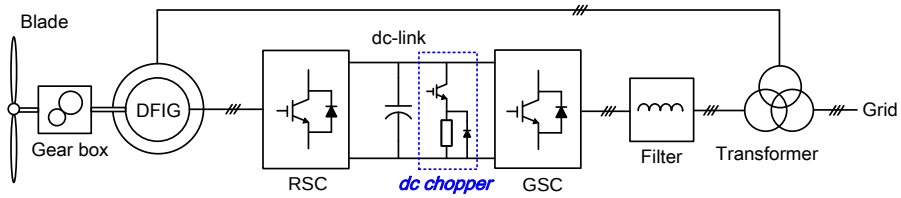

Fig. 6.1. Doubly-Fed Induction Generator (DFIG) wind turbine system for Low Voltage Ride-Through (LVRT) with a dc chopper. (GSC: Grid-side converter; RSC: Rotor-side converter).

Besides, as described in Chapter 1, the external grid codes specify that the DFIG is not only required to survive for certain period of the grid voltage dip, but also is expected to provide the reactive current to support the grid voltage recovery [7].

6.2 LVRT challenge from DFIG itself

The normal positive stator flux is rotating with the synchronous speed in respect to the stator winding, and the Electro-Motive Force (EMF) is proportional to the slip speed. In contrast, the natural flux stands still in respect to the stator winding during a balanced voltage dip, and he EMF is related to the rotor speed [14]. It can be seen that the induced rotor voltage during the grid fault becomes much higher, which may cause an over-voltage of the rotor converter, and may even induce over-current problems due to the loss of the current control.

6.2.1 DFIG model during balanced grid fault

If a balanced grid fault occurs on the terminal of the wind turbine system, as the stator flux cannot be changed abruptly, a stator natural flux ψ_{sn} will be introduced, and it is a dc component, decaying with the time constant τ_s [11],

$$\psi_{sn} = p \cdot \frac{U_s}{j\omega_0} \cdot e^{-\frac{t}{\tau_s}} \tag{6.1}$$

where p denotes the voltage dip level, U_s denotes the original stator voltage, ω_0 denotes synchronous speed. Moreover, the typical time constant of the stator flux for multi-MW induction generator is normally several seconds [11], which is decided by the ratio of the stator inductor and the stator resistance. As a consequence, it could be difficult for the rotor converter to overcome the fault duration without any assistance from the controller or some hardware protections.

Meanwhile, the remaining grid voltage introduces a stator forced flux ψ_{sf}, which is rotating with the grid frequency.

$$\psi_{sf} = (1-p) \cdot \frac{U_s}{j\omega_0} \cdot e^{j\omega_0 t} \tag{6.2}$$

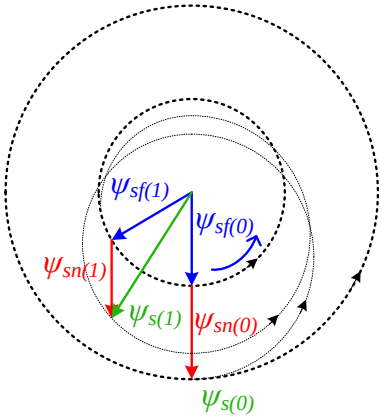

Fig. 6.2. Transient stator flux evolution in the case of a balanced voltage dip.

The transient stator flux evolution is then shown in Fig. 6.2. At the moment of the grid fault occurrence, the original flux $\psi_{s(0)}$ divides into the natural flux $\psi_{sn(0)}$ and the forced flux $\psi_{sf(0)}$. During the period of the grid fault, the amplitude of the rotating forced flux remains the same from $\psi_{sf(0)}$ to $\psi_{sf(1)}$, while the freezing natural flux exponentially decreases from $\psi_{sn(0)}$ to $\psi_{sn(1)}$. The final evolution of the stator flux may become a smaller circle compared to the original stator flux evolution.

According to the superposition principle, the dynamic model of the DFIG is thus expressed in terms of two independent circuits: the forced machine model and the

natural machine model. For the forced machine model as shown in Fig. 6.3(a), it stands for the steady-state operation of the DFIG, where the stator connects to the remaining grid voltage, and no transient stator flux is considered. On the other hand, as shown in Fig. 6.3(b), the natural machine model is used for a transient period, whose stator is short-circuited, and an initial natural flux exists in the stator. In order to investigate the dynamic response of the DFIG under the grid fault, only the natural machine model is focused in the following.

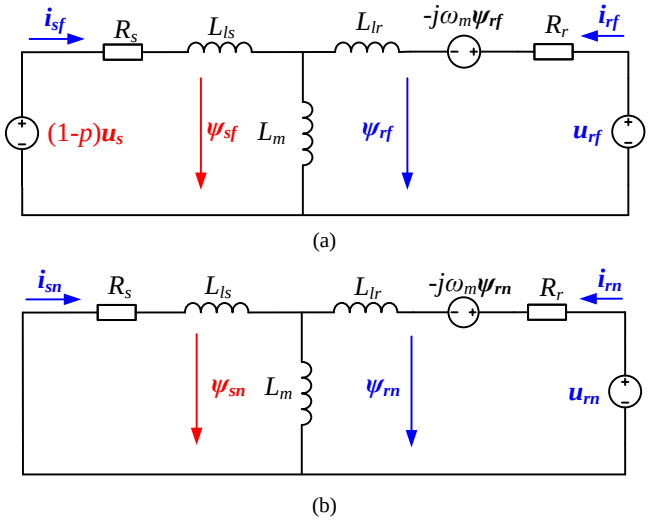

Fig. 6.3. Dynamic model of the DFIG during a balanced grid fault. (a) Forced machine model; (b) Natural machine model.

6.2.2 Demagnetizing current control

As proposed in [11]-[14], the demagnetizing current control can be regarded as an effective way to overcome the transient period of the decaying natural flux. As shown in Fig. 6.4, the basic idea of the demagnetizing current control is to control the rotor current in the opposite direction in respect with the natural stator flux.

$$i_{rn} = -k \cdot \psi_{sn} \tag{6.3}$$

In d-q axis, the natural flux can be extracted from the total stator flux by using band-pass filter. By the definition of a negative demagnetizing coefficient k, the modulated rotor voltage can be obtained through a traditional PI controller.

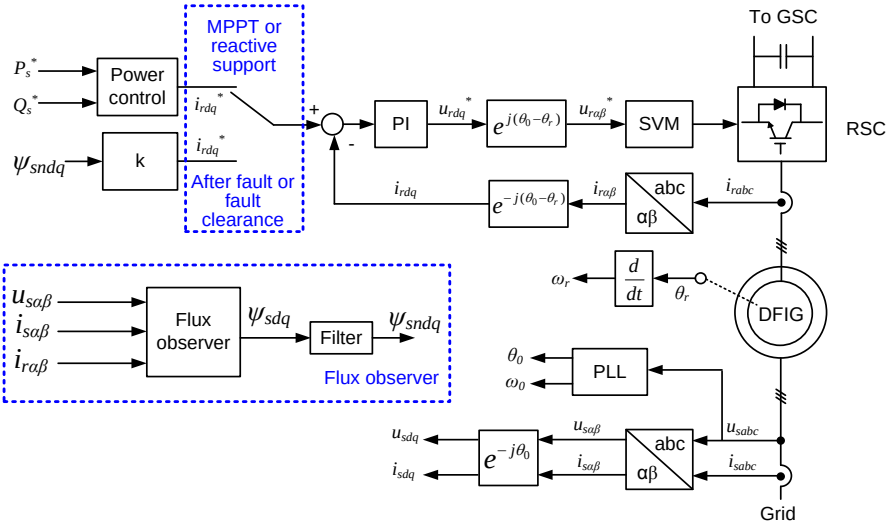

Fig. 6.4. Control schemes of vector control and demagnetizing current control.

As claimed in [11], [13], if the demagnetizing current control is applied, the rotor voltage u_r can be expressed in terms of the rotor current i_r as,

$$u_r = \omega_r(\sigma L_r i_r - \frac{p \cdot U_s}{\omega_0}) + j(R_r + R_s)i_r \tag{6.4}$$

where R_r and R_s denote the rotor and stator resistance, σL_r denotes the rotor transient inductance, and ω_r denotes the rotor speed. It is noted that the rotor voltage is not only related to the amount of the demagnetizing current, but also to the dip level as well as the rotor speed. The relationship between the rotor voltage and the rotor current can graphically be shown in Fig. 6.5.

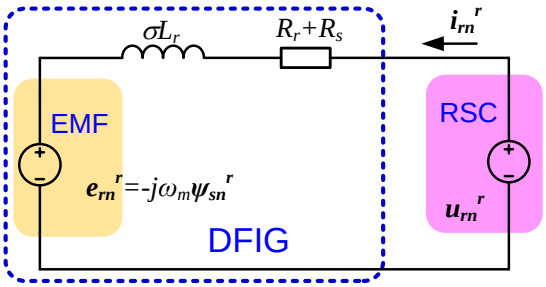

Fig. 6.5. Single-phase equivalent machine model in viewpoint of the rotor.

6.2.3 DFIG ride through capability

A case study is performed in a 2 MW DFIG wind turbine system, and the parameters of the generator and the rotor-side converter have already been described in Chapter 2. In respect to the Safety Operation Area (SOA) of the rotor-side converter, it is largely dependent on the capacity of the power semiconductor. It is noted that the rotor-side converter can support up to 2.0 pu rotor current with the given power device. Furthermore, assuming that a full modulation index is achieved, 1050 V dc-link voltage is transferred to 2.0 rotor voltage. For a 1.7 kV power module, the dc-link voltage should be limited at 1300 V, thus 2.5 pu rotor voltage is regarded as the limitation of the voltage stress.

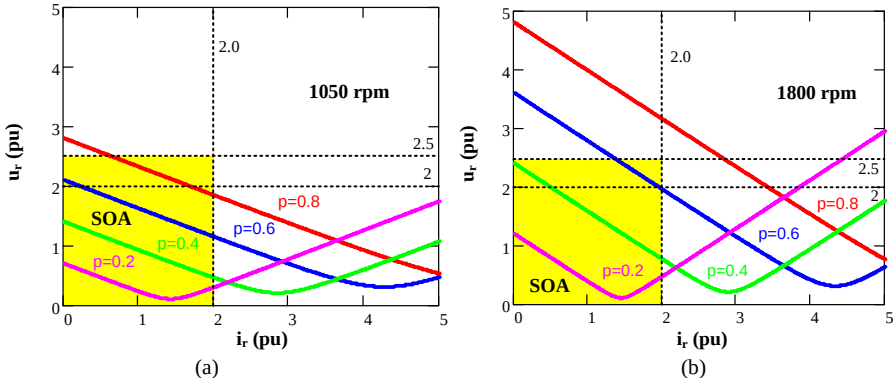

Fig. 6.6. Demagnetizing current effects on rotor terminal voltage with various voltage dip levels. (a) Rotor speed at 1050 rpm; (b) Rotor speed at 1800 rpm.

Two rotor speeds at 1050 rpm and 1800 rpm are selected to represent the sub-synchronous mode and super-synchronous mode of the DFIG, and their SOAs are shown in Fig. 6.6. If the DFIG operates at the same rotor speed, it is evident that the severe voltage dip induces higher EMF on the rotor side, which implies that in the case of severe voltage fault, a higher amount of the demagnetizing current is required to counteract the EMF in order to make the induced rotor voltage not to exceed the dc-link voltage limitation. If the same level of voltage dip happens at the various rotor speeds, it can be seen that higher rotor speed causes higher EMF, which gives more challenges to realize the fault ride-through operation.

If the demagnetizing current is applied from the 0.5 pu to 2.0 pu, the characteristic of the rotor voltage and voltage dip level are shown in Fig. 6.7, where the minimum speed (1050 rpm) and the maximum speed (1800 rpm) are again taken into account. It is clear that, at the rotor speed of 1050 rpm, the DFIG can fully ride through the balanced grid fault, if 2.0 pu demagnetizing current is provided. However, at a rotor speed of 1800 rpm, although 2.0 pu demagnetizing current is used, the DFIG can only survive within the voltage dip level of 0.7. Consequently, the following study will focus on the dip area below 0.7. Moreover, it is noted that the higher demagnetizing current results in the easier fault ride-through for the rotor-side converter.

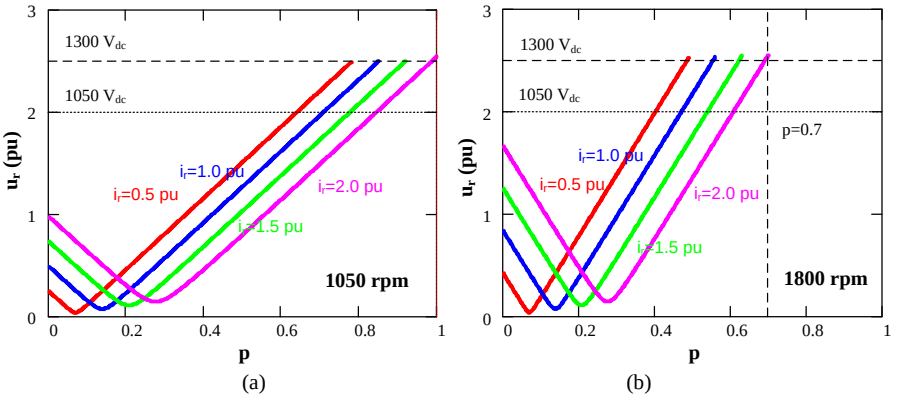

Fig. 6.7. Capability of the DFIG to ride through various dip levels for different rotor currents and dc voltage levels. (a) 1050 rpm; (b) 1800 rpm.

6.3 LVRT challenge from grid codes

After the description of the LVRT challenge seen from the DFIG itself, this section will continue to address the potential problems required by the grid codes.

6.3.1 Effects of reactive current injection

During the grid fault, different countries demand various response time of the reactive current injection. According to a Spanish grid codes, it is specified that 150 ms response time is preferred [7], [8].

For the DFIG configuration, the additional reactive current is normally injected from the stator side of the induction generator, and it will certainly causes the extra current seen from the rotor side given by,

$$i_{r\_Q} = \frac{(1-p)\cdot U_s}{\omega_0 L_m} - \frac{L_s}{L_m}\cdot i_{s\_Q} \tag{6.5}$$

where i_{s_Q} and i_{r_Q} denotes the stator current and rotor current in terms of the reactive power, and L_m denotes the magnetizing inductance.

According to Fig. 1.9(b), Fig. 6.8 shows the effect of the dip level on the stator and rotor current. It can be seen that, if the dip level is higher than 0.5, the stator current keeps constant. However, the rotor current reaches the highest value in the case of dip level at 0.5. As the DFIG can only ride through the dip level up to 0.7, 1.05 pu reactive current is needed seen from the rotor side.

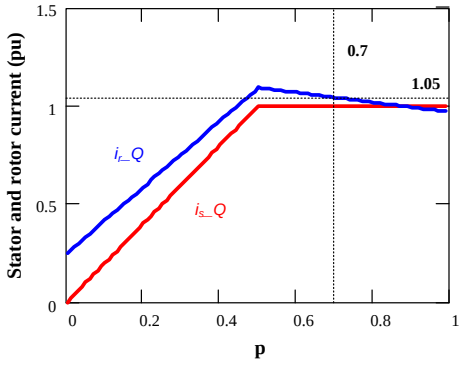

Fig. 6.8. Requirement of reactive current injection in terms of stator current and rotor current.

6.3.2 Effects of natural flux decaying

As mentioned in [10], [11], another advantage of using the demagnetizing current control accelerates the decaying of the natural flux,

$$\tau = \frac{L_s}{R_s}\cdot\frac{1}{1+\frac{L_m\omega_0}{pU_s}\cdot i_{rn}} \tag{6.6}$$

The influence of the voltage dip level on the flux decaying is shown in Fig. 6.9(a). It is noted that the same amount of the demagnetizing current leads to different time constants of the flux decaying at various voltage dips. Furthermore, it can be seen that, in the case of the same voltage dip, the higher demagnetizing current results in a shorter period of the stator natural flux. As shown in Fig. 6.9(b), the damping time constant is only related to the dip level and demagnetizing current. Specifically, if a 2.0 pu demagnetizing current is selected, the decaying time constant can be reduced from

normal flux of 1750 ms to 140 ms, which significantly accelerates the flux transient period.

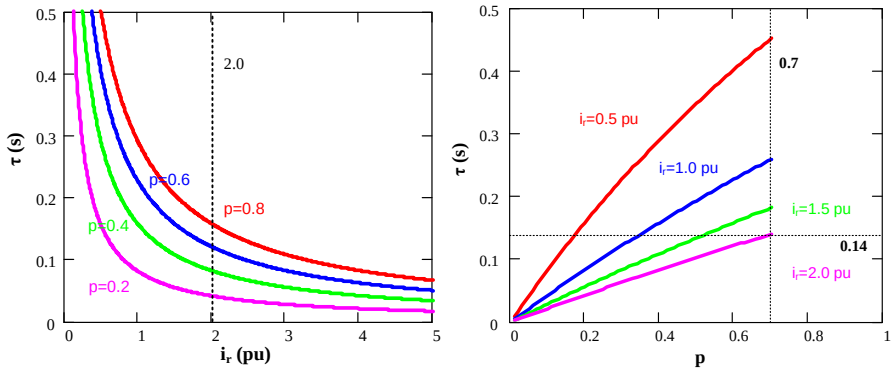

Fig. 6.9. Decaying time of stator flux in the case of a balanced grid fault. (a) Voltage dip level influence on flux decaying; (b) Demagnetizing current influence on flux decaying.

6.4 Optimum control scheme

As the design of the optimum demagnetizing coefficient is still uncertain, this section will propose an optimized design procedure viewed from both the SOA of the rotor converter and the grid codes requirement. Besides, the minimum junction temperature swing is another important concern during a balanced grid fault.

6.4.1 Design criteria of demagnetizing coefficient

If the control strategy of the demagnetizing current is preferred, the residual demagnetizing current exponentially decays during the fault period, and it is expressed as,

$$i_{r\_RES} = i_r \cdot e^{-\frac{t_Q}{\tau}} \tag{6.7}$$

where t_Q denotes the instant when the reactive current is needed (i.e. 150 ms according to the Spanish grid code).

Consequently, the residual demagnetizing current is shown in Fig. 6.10 in relation with the voltage dip. It should be emphasized that in order to keep the minimum junction temperature swing of the rotor-side converter during the grid fault, the maximum amplitude of the rotor current should occur at the moment of the fault

incident, rather than the instant when the reactive current is required. In other words, at the instant of t_Q, the total rotor current may not exceed the designed demagnetizing current.

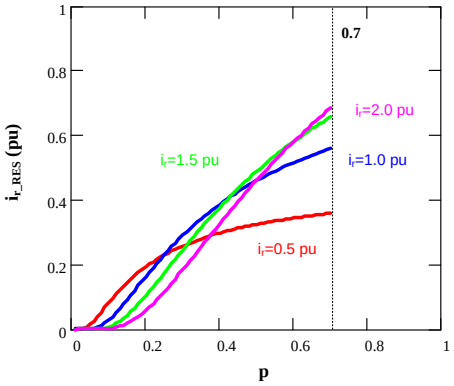

Fig. 6.10. Residual demagnetizing current at the moment of the reactive current injection.

The control strategy of the rotor-side converter during the grid fault is that, once the fault is detected, the demagnetizing current is provided immediately. At the moment of reactive current injection, an additional component of the reactive current is expected besides the exponential decaying of the demagnetizing current. Seen from the similar loading of the power converter, the optimum demagnetizing coefficient is obtained if the amplitude of the total rotor current at the moment of the reactive current injection equals the amplitude of the maximum demagnetizing current (the moment of the grid fault occurrence).

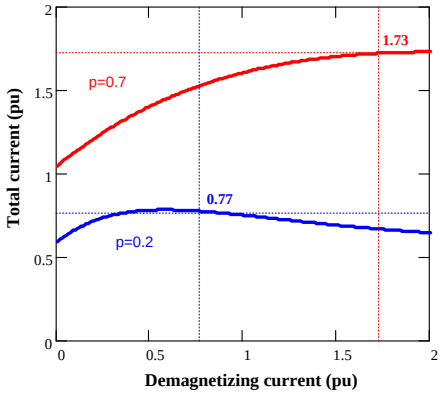

Fig. 6.11. Effects of various demagnetizing currents on total rotor current at the moment of the reactive current injection.

The relationship between the total rotor current (the reactive component plus demagnetizing component of the rotor current) and the designed demagnetizing current at the moment the reactive power response time is shown in Fig. 6.11, in which the dip levels of 0.7 and 0.2 are used. It can be seen that different demagnetizing coefficients are expected in the cases of the various voltage dip levels.

6.4.2 Simulation validation

In order to prevent the power module from a too high dc-link voltage, a dc brake is used in the simulation, whose threshold values for turn-on and turn-off the switch are set at 1300 V and 1100 V for a hysteresis control [9]. Assuming a 0.7 balanced grid voltage dip occurs at the moment of 0.5 s, and the duration is 300 ms, the simulated comparisons between the traditional vector control and optimized demagnetizing current control are shown in Fig. 6.12, in which the DFIG operates with rotor speed at 1800 rpm.

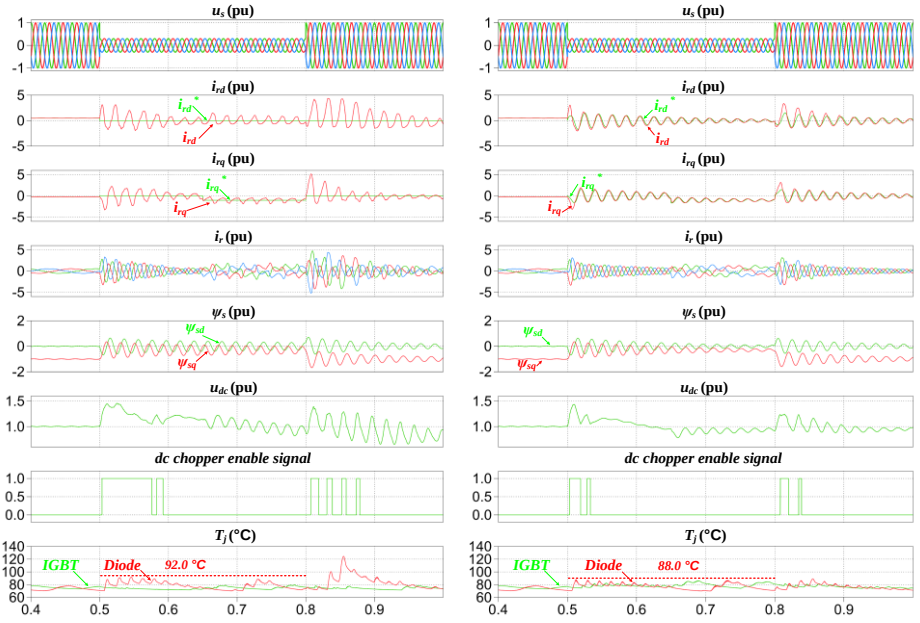

Fig. 6.12. Simulated results in the case of the DFIG to ride through 0.7 dip balanced grid fault with various control schemes. (a) Traditional vector control; (b) Optimized demagnetizing control.

For the traditional vector control as shown in Fig. 6.12(a), once the grid fault is detected, both the active current and reactive current are cut to zero. However, due to the existence of natural flux, the rotor current cannot track the reference, and the enable time duration of the dc chopper almost lasts 90 ms. Moreover, in accordance with the grid codes, a 1.0 pu reactive current is injected at the instant of 0.65 s, and the maximum junction temperature of the diode appears during the period of the zero reactive current injection, which almost reaches 92.0 ℃. As shown in Fig. 6.12(b), when the grid fault occurs, a 1.73 pu demagnetizing current is selected according to the previous analysis. During the fault period, the rotor current is almost kept within the desired value, and the enable time of the dc chopper is reduced to 35 ms. Besides, compared with the period of demagnetizing control and reactive current injection, it is noted that the diode is almost equally stressed and its maximum junction temperature is reduced to 88 ℃. Furthermore, since the recovery of the grid voltage also introduces the natural flux and the effects of the natural flux can be superposed in the traditional vector control, it can be found that the maximum junction temperature of the diode with optimized control is much lower.

6.5 Summary

This chapter addresses the existing issues for the doubly-fed induction generator system to ride through a balanced grid fault. If the reactive current injection of the modern grid codes is taken into account, a new design procedure of the demagnetizing coefficient for the conventional demagnetizing current control is proposed in order to realize a minimum junction temperature swing during the period of the low voltage ride-through. It is concluded that the optimized demagnetizing control has a lower thermal stress compared to conventional vector control during a balanced grid fault.

Relevant attached papers

[A.9] D. Zhou, F. Blaabjerg, "Thermal behavior of doubly-fed Induction generator wind turbine system during balanced grid fault," *in Proc. of APEC 2014*, pp. 3076-3083, 2014.

[A.10] D. Zhou, F. Blaabjerg, "Dynamic thermal analysis of DFIG rotor-side converter during balanced grid fault," *in Proc. of ECCE 2014*, pp. 3097-3103, 2014.

References

[1] H. Polinder, J. A. Ferreira, B. B. Jensen, A. B. Abrahamsen, K. Atallah, R. A. McMahon, "Trends in wind turbine generator systems," *IEEE Journal of Emerging and Selected Topics in Power Electronics*, vol. 1, no. 3, pp. 174-185, Sep. 2013.

[2] D. Zhou, F. Blaabjerg, "Thermal analysis of two-level wind power converter under symmetrical grid fault," *in Proc. of IECON 2013*, pp. 1904-1909, 2013.

[3] R. Cardenas, R. Pena, S. Alepuz, G. Asher, "Overview of control systems for the operation of DFIGs in wind energy applications," *IEEE Trans. on Industrial Electronics*, vol. 60, no. 7, pp. 2776-2798, Jul. 2013.

[4] S. Xiao, G. Yang, H. Zhou, H. Geng, "An LVRT control strategy based on flux linkage tracking for DFIG-based WECS," *IEEE Trans. on Industrial Electronics*, vol. 60, no. 7, pp. 2820-2832, July 2013.

[5] M. Liserre, R. Cardenas, M. Molinas, J. Rodriguez, "Overview of multi-MW wind turbines and wind parks," *IEEE Trans. on Industrial Electronics*, vol. 58, no. 4, pp. 1081-1095, Apr. 2011.

[6] G. Pannell, D. J. Atkinson, B. Zahawi, "Minimum-threshold crowbar for a fault-ride-through grid-code-compliant DFIG wind turbine," *IEEE Trans. on Energy Conversion*, vol. 25, no. 3, pp. 750-759, Sep. 2010.

[7] E.ON-Netz. Requirements for offshore grid connections, Apr. 2008.

[8] M. Tsili, S. Papathanassiou, "A review of grid code technical requirements for wind farms," *IET Renewable Power Generation*, vol. 3, no. 3, pp. 308-332, Sep. 2009.

[9] G. Pannell, B. Zahawi, D. J. Atkinson, P. Missailidis, "Evaluation of the performance of a DC-link brake chopper as a DFIG low-voltage fault-ride-through device," *IEEE Trans. on Energy Conversion*, vol. 28, no. 3, pp. 535-542, Sep. 2013.

[10] D. Xiang, L. Ran, P. J. Tavner, S. Yang, "Control of a doubly fed induction generator in a wind turbine during grid fault ride-through,", *IEEE Trans. on Energy Conversion*, vol. 21, no. 3, pp. 652-662, Sep. 2006.

[11] J. Lopez, E. Gubia, E. Olea, J. Ruiz, L. Marroyo, "Ride through of wind turbines with doubly fed induction generator under symmetrical voltage dips," *IEEE Trans. on Industrial Electronics*, vol. 56, no. 10, pp. 4246-4254, Oct. 2009.

[12] W. Chen, D. Xu, M. Chen, F. Blaabjerg, "Comparison of current control strategies for DFIG under symmetrical grid voltage dips," *in Proc. of IECON 2013*, pp. 1540-1545, Nov. 2013.

[13] J. Lopez, E. Gubia, E. Olea, J. Ruiz, L. Marroyo, "Ride through of wind turbines with doubly fed induction generator under symmetrical voltage dips," *IEEE Trans. on Industrial Electronics*, vol. 56, no. 10, pp. 4246-4254, Oct. 2009.

[14] G. Abad, J. Lopez, M. Rodriguez, L. Marroyo, G. Iwanski, *Doubly fed induction machine-modeling and control for wind energy generation*. Piscataway, NJ: IEEE Press, 2011.

Chapter 7
Conclusions

According to the obtained results, this chapter summarizes the work and concludes the main contributions presented in the thesis. Finally, several new research perspectives are included in the section for future work.

7.1 Summary

In order to overcome the emerging challenges in wind turbine systems described in Chapter 1, the scope of this thesis covers mainly three parts in terms of the partial-scale power converter based DFIG system and the full-scale power converter based PMSG system: mission profile based reliability assessment, energy loss evaluation as well as reliability-oriented control strategy.

Chapter 2 is the basis of reliability assessment and energy loss evaluation, in which the power loss dissipation in the power semiconductor devices is mainly highlighted. In order to achieve the similar loading of power devices at rated power, the selection of the power modules in a 2 MW DFIG system and PMSG system is discussed. Moreover, an analytical calculation of power loss is proposed in order quickly to evaluate the effects of the power module selection, modulation scheme and power factor on the loss dissipation. Finally, the efficiency of the power converter of the two systems is compared at different loading conditions.

Since the thermal behavior of the power semiconductor device is an important indicator for the reliability assessment, Chapter 3 focuses on the thermal stress evaluation of the wind power converter. According to the physical layout of the power module, a thermal model is established in terms of the power module itself and the cooling approaches. Afterwards, the variations of the junction temperature in the popular DFIG configuration and PMSG configuration are calculated and simulated, in which the grid codes are taken into account. It is concluded that the reactive power injection will inevitably affect the thermal performance of the power device. Due to the fact that both the grid-side converter and the rotor-side converter have the capability to provide reactive power support in the DFIG system, during wind gusts, the optimized

thermal behavior of the grid-side converter can be achieved by using reactive power circulation within the DFIG system internally, while the thermal performance of the rotor-side converter is almost unaffected.

On the basis of the loss profile and the thermal profile obtained from Chapter 2 and Chapter 3, Chapter 4 further analyzes the reliability of the wind power converter. According to the well-known Coffin-Manson lifetime model and the annual wind profile, the concepts of the consumed lifetime per year and total consumed lifetime are introduced. Then, various wind profile and grid codes influence on the lifetime estimation is also studied. It is found that the total consumed lifetime is considerably affected if the reactive power is required all year around according to the grid codes. It can also be seen that the lifetime of the wind power converter is closely related to the wind profile. For the DFIG configuration, if the over-excited reactive power is required all year around, a reasonable share between the rotor-side converter and the grid-side converter can enhance the lifespan of the most stressed power converter, and thereby obtain a balanced lifetime of the back-to-back power converters.

Chapter 5 addresses the energy loss evaluation of the wind turbine system for the DFIG and PMSG system. In respect to the PMSG system, different wind classes and different operation modes of the reactive power injection are taken into account. It is found that both the over-excited and the under-excited reactive power mode of operation increase the energy loss per year significantly if they are provided all year around. Moreover, it is also concluded that in order to realize an energy saving of the wind turbine system, a constant power factor control strategy is more preferred compared to using an extreme reactive power injection (full reactive power all time). For the DFIG system, the over-excited reactive power compensated either by the DFIG itself or the grid-side converter is compared. It can be seen that the over-excited reactive power injected from the grid-side converter has lower energy loss per year compared to the over-excited reactive power covered by the rotor-side converter. Furthermore, it is also found that the annual energy loss could become lower with an optimized filter and thereby gain more energy production for the wind turbine. Moreover, the losses distribution of the DFIG system between the L and LCL filter are

compared in a down-scaled 7.5 kW DFIG test rig with different control strategies of the reactive power.

Chapter 6 addresses the existing issues for the doubly-fed induction generator system to ride through a balanced grid fault. If the reactive current injection of the modern grid codes is taken into account, a new design procedure of the demagnetizing coefficient for the conventional demagnetizing current control is proposed in order to realize a minimum junction temperature swing during the period of the low voltage ride-through. It is concluded that the optimized demagnetizing control has a lower thermal stress compared to conventional vector control during a balanced grid fault.

7.2 Contributions

In this thesis, following contributions can be highlighted:

- ✓ **Mission profile based reliability assessment tool**

A generalized multi-disciplinary approach to evaluate the power device reliability in a wind turbine system is proposed, whose flow chart mainly consists of a loss model, thermal model and a lifetime model. Analytical equations behind the loss model, in which the power device selection, modulation scheme, and power factor are taken into account, are deduced and verified using PLECS modeling and simulation. In order to avoid the time-consuming simulation due to a mismatched time step between loss model (dozens of microseconds) and thermal model (several seconds), simplified analytical equations to calculate the thermal performance of the power device are also proposed. Based on an annual wind profile, the reliability of the power device can be assessed in terms of the consumed lifetime per year and total consumed lifetime.

- ✓ **Evaluation of energy loss for wind turbine system**

The annual energy loss of the wind turbine system (kWh) is closely related to the cost of the wind power generation. It can be consumed both by the generator and the power electronics converters below the rated wind speed (if the wind speed is above the rated wind speed, the energy loss can be compensated from the mechanical part). On the basis of the loss model of the power devices as well as the annual wind profile, the total energy loss can be estimated as well as the total production.

✓ **Reactive power effects on reliability and cost of energy**

Modern grid codes push the wind power plant to behave as the traditional power source, which has the capability to provide reactive power even when the grid voltage is normal. As a consequence, the effects of the reactive power injection on the reliability and the cost of energy are investigated and evaluated both for the DFIG system and the PMSG system. For the DFIG system, since the rotor-side converter and the grid-side converter are able to provide the reactive power support, a balanced lifetime consumption between the back-to-back power converters can be achieved by a reasonable reactive power share between them. Moreover, with an optimized grid filter design, the reactive power fully provided from the grid-side converter may even reduce the cost of energy.

✓ **Reliability-oriented control strategy**

The thermal cycling of the DFIG system is investigated during the low voltage ride-through operation. Due to the poor ride-through capability of the DFIG system, a new design procedure of the demagnetizing coefficient for the conventional demagnetizing current control is proposed in order to realize a minimum junction temperature swing during the period of the low voltage ride-through.

7.3 Future work

Although many aspects have been documented in this thesis, there are still a lot of possibilities for technology improvement and further studies. Some issues of high interest for future investigations are listed:

- **More advanced methods to evaluate reliability**
  - Lifetime estimation can be extended to different failure mechanisms of the power semiconductor (e.g. bond-wire liftoff, soldering cracks).
  - As this study mainly focuses on lifetime calculation according to the short-term mission profile (several milliseconds to several seconds), the long-term mission profile regarding variations wind speed and ambient temperature (several minutes) can be further investigated, as well as medium-term mission profile regarding mechanical reaction of wind turbine (several seconds).

- The relationship between the reliability and cost of power device can be evaluated with various chip numbers or different chip areas, which can lead to an optimized design of the power semiconductor device.
- Other kind of stressors can be taken into account (humidity, vibration, cosmic irradiation, etc.).

- **Experimental validations of the thermal cycling**
  - Measurement of the junction and case temperature can be used in order to valid the used thermal model in power module.
  - Experimental results can be performed in respect to the steady-state thermal cycling.
  - Thermal performance of power module during the LVRT operation can be tested.

- **Reliability assessment of the converter-level and system-level**
  - Lifetime estimation can be extended to the passive components (e.g. capacitors).
  - Optimized design can be used for balanced lifetime seen from the converter-level other than the component-level.
  - Approaches of the reliability assessment can be found from the component-level to the system-level.

Part II Publications

[A.1] D. Zhou, F. Blaabjerg, M. Lau, M. Tonnes, "Thermal Analysis of Multi-MW Two-Level Wind Power Converter," *in Proc. of IECON 2012*, pp. 5858-5864, 2012.

Thermal Analysis of Multi-MW Two-level Wind Power Converter

Dao Zhou, Frede Blaabjerg

Department of Energy Technology
Aalborg University
Pontoppidanstraede 101, Aalborg, DK-9220, Denmark
zda@et.aau.dk, fbl@et.aau.dk

Mogens Lau, Michael Tonnes

Danfoss Silicon Power GmbH

Husumer Strasse 251, Flensburg, D-24941, Germany
mogens.lau@danfoss.com, michael.tonnes@danfoss.com

***Abstract*- In this paper, the multi-MW wind turbine of partial-scale and full-scale two-level power converter with DFIG and direct-drive PMSG are designed and compared in terms of their thermal performance. Simulations of different configurations regarding loss distribution and junction temperature in the power device in the whole range of wind speed are presented and analyzed. It is concluded that in both partial-scale and full-scale power converter the most thermal stressed power device in the generator-side converter will have higher mean junction temperature and larger junction temperature fluctuation compared to grid-side converter at the rated wind speed. Moreover, the thermal performance of the generator-side converter in the partial-scale power converter becomes crucial around the synchronous operating point and should be considered carefully.**

I. INTRODUCTION

Over the last two decades, the wind power industry has expanded greatly, and has become the fastest developing renewable energy technology in this period. In response to the steady growth of wind power demand, lower cost per kWh, increased power density and higher reliability of wind turbines are essential parameters [1]-[3]. Power electronic converters, as efficient interface between power grid and wind generator, play a key role in wind power generation system. Although the power level of single wind turbine is even pushed up to 7 MW, the size power ratings of 1.5-3 MW are still the dominating on the commercial market. Furthermore, wind turbine converters are being designed for a lifetime of 20-25 years, which is more prolonged compared to typical industrial applications. Therefore the thermal behavior of the power devices is an important factor affecting lifetime of the converter.

Some researchers have already focused on the evaluation of the thermal profile. The thermal stress with partial-scale converter is investigated and it points out an unbalanced thermal performance among different legs at around the particular synchronous operating point [4]. In [5], several promising multilevel configurations with full-scale power converter are compared regarding the thermal behavior of the power devices. As stated in [6], the cycle numbers to failure is quite relevant to the junction temperature fluctuation as well as the mean junction temperature of power semiconductor.

The scope of this paper is to compare and analyze the thermal profile of multi-MW wind turbine with low-voltage partial-scale and full-scale power converter. First, the typical configurations for variable speed wind turbine system will be briefly introduced. Then, the basic design and the control strategy will be described. Finally loss distribution and thermal analysis will be presented and compared in respect to the power device performance for the two different configurations.

II. TYPICAL CONFIGURATIONS

Due to the extensive and well-established knowledge, as well as the simpler structure and fewer components, the two-level back-to-back voltage source converter is the most attractive solution in commercial market of wind turbines [3]. The utilization of the power electronics in wind turbine system can be further divided into two categories, namely: a wind turbine system with partial-scale power converter and a wind turbine system with full-scale power converter, which both are illustrated in Fig. 1.

A. Wind turbine system with partial-scale power converter

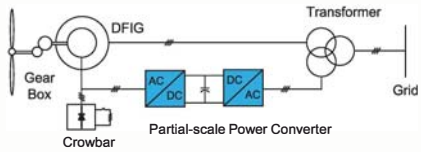

(a) Wind turbine system with partial-scale power converter

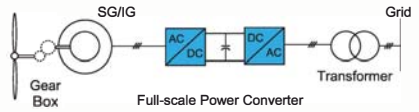

(b) Wind turbine system with full-scale power converter

Fig. 1. Typical configurations for wind turbine system.

A popular wind turbine configuration, normally based on Doubly-Fed Induction Generator (DFIG), is to employ a

978-1-4673-2421-2/12/$31.00 ©2012 IEEE

power converter rated to approximate by 30% of the nominal generator power and it is shown in Fig. 1a.

The power converter is connected to the rotor through the slip-rings and makes the rotor current as well as rotor speed under control, while the stator links to the grid without any decoupling. If the generator operates in super-synchronous mode, the electrical power is delivered through both the rotor and stator. If the generator is running sub-synchronously, the electrical power is only delivered into the grid from the stator.

The fraction of slip power through the converter makes this concept attractive from an economical point of view. However, the main drawbacks lie in the use of slip rings, and also an additional crowbar is needed to protect the generator-side converter under grid faults [7].

B. Wind turbine system with full-scale power converter

As shown in Fig. 1b, another full-scale power converter configuration equipped with Synchronous Generator (SG) or Induction Generator (IG) is considered as a promising technology for multi-MW wind turbine system.

The generator stator winding is connected to the grid through the full-scale power converter, which performs the reactive power compensation and a smooth grid connection for the entire speed. Some variable speed wind turbine system may become gearless by introducing the multi-pole generator.

The elimination of the slip rings, simpler gearbox and full power controllability during the grid faults are the main advantages. However, in order to satisfy the power rating, the widely used approach nowadays is to implement several converter modules or power devices in parallel, which of course are challenging the complexity and reliability of the whole wind turbine system.

III. BASIC DESIGN OF POWER CONVERTER

As the partial-scale power converter is normally realized by DFIG, while the full-scale power converter matches a direct-drive Permanent Magnet Synchronous Generator (PMSG), for simplicity, these two configurations are called the DFIG system and the PMSG system respectively. In order to evaluate and compare the thermal performance for the above two systems, the mathematical model and simulation platform will firstly be established.

A. Wind turbine model

A 2 MW wind turbine system is used for the case studies. The energy transferred from the kinetic wind power to mechanical power can be expressed as [8]

$$P_G = \frac{1}{2}\rho\pi R^2 C_p(\lambda,\beta)v_w^3 \tag{1}$$

where ρ denotes the air density (kg/m^3), R denotes the radius of turbine blade (m), and v_w denotes the wind speed (m/s). Depending on the blade pitch angle β and tip speed ratio λ, the power coefficient C_p represents the transfer efficiency, whose maximum value can be obtained under optimal tip speed ratio. As claimed in [9], the parameters of the wind turbine are summarized in Table I. Meanwhile, the relationship between the wind speed and turbine rotor speed, produced output power is depicted in Fig. 2.

TABLE I
PARAMETERS FOR 2 MW WIND TURBINE (DFIG/PMSG)

Wind turbine parameters	
Rated power P_G [MW]	2
Blade radius R [m]	41.3
Cut-in wind speed v_{wcut_in} [m/s]	4
Rated wind speed v_{w_rate} [m/s]	12
Cut-off wind speed v_{wcut_off} [m/s]	25
Optimal tip speed ratio λ_{opt}	8.1
Maximum power coefficient C_{pmax}	0.383
Rated turbine speed n_{rot_rate} [rpm]	19
Minimum turbine speed n_{rot_min} [m/s]	11/6

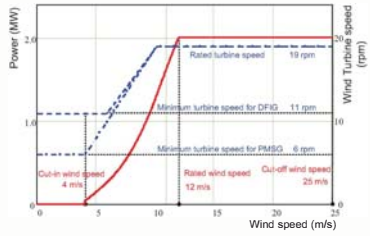

Fig. 2. Relationship between wind speed, turbine rotor speed and output power for the two different systems.

B. Control scheme for DFIG system

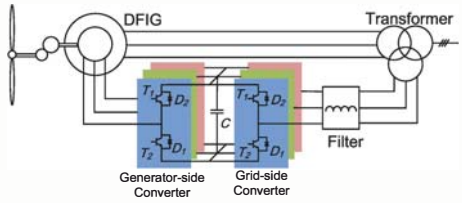

Fig. 3. Two-level back-to-back converter of the DFIG system.

Fig. 3 shows a DFIG system that consists of a generator, a partial-scale power converter, a filter and a transformer. Since the stator is directly connected to low-voltage grid, the DC-link voltage is set as low as possible from the power device lifetime point of view. Moreover, the filter inductance is designed to limit the current ripple within 0.25 pu [10].

Due to the DC capacitor decoupling, the power converter can be divided into the generator-side converter and the grid-side converter. Each of the control schemes can be designed separately.

For the generator-side converter, although the generator may operate in super-synchronous or sub-synchronous mode,

one of the control objectives focuses on transferring the produced active power to the grid. The other purpose is to provide the excited current for the DFIG. As shown in Fig. 4 ("Generator-side control"), the active and reactive power in the stator can be described by rotor d-axis and q-axis current respectively when applied to the stator voltage oriented control [11]. Furthermore, since the coupling current in d-axis and q-axis is induced by Park-transformation, feed-forward compensation method is used to offset their influence. Therefore, the reference of d-axis current is determined by the produced active power, while the reference of q-axis is related to desired reactive power in the stator of the DFIG.

The grid-side converter will keep the DC-link voltage fixed and meet the reactive power demand according to the grid codes. As shown in Fig. 4 ("Grid-side control"), the active and reactive power can simply be controlled by d-axis and q-axis current using the grid voltage oriented control. This control strategy contains two cascaded loops. The inner loop takes care of the grid current; the outer loops control the DC-link voltage and reactive power for the grid-side converter. The DC-link voltage is closely dependent on the active power, thus the adjustment can be regarded as the reference of the d-axis current. Normally, a unity power factor is required, in other words, the reference of q-axis is set to zero unless the grid operator needs reactive power compensation. Furthermore, Space-vector Pulse Width Modulation (SVPWM) is used to generate the switching signals for the power semiconductors in both converters.

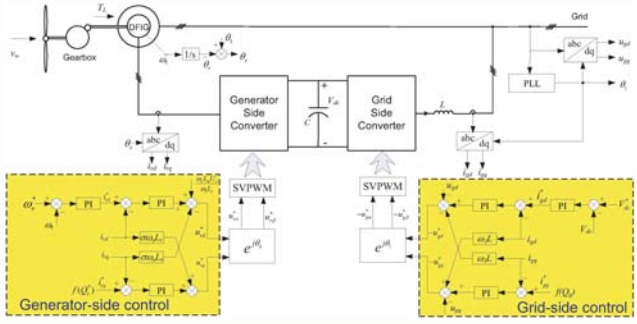

Fig. 4. Control scheme for the DFIG system with Generator-side and Grid-side control.

C. Control scheme for PMSG system

The typical PMSG system equipped with a full-scale power converter is shown in Fig. 5, which consists of a generator-side converter and a grid-side converter. Compared to the DFIG system, the current through both converters will be much higher under same power rating of the wind turbines, which means the selection of power devices in the two configurations will be quite different in order to realize similar power device loading. Nevertheless, the design method of the DC-link voltage and the filter inductance in the PMSG system can be referred to the DFIG system.

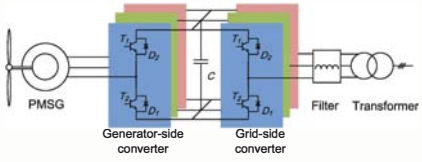

Fig. 5. Two-level back-to-back converter in a PMSG system.

Considering the control scheme of the generator-side converter, the current through the stator of the generator should be controlled to adjust the rotating speed for maximum power. As shown in Fig. 6 ("Generator-side control"), this can easily be achieved by controlling the electromagnetic torque through a closed loop control structure with the aid of the stator Field Oriented Control (FOC), where the electromagnetic torque is controlled indirectly through the stator current in the synchronous reference frame. The torque is only controlled by q-axis current component. The cascaded loop structure of the generator-side converter is realized by three PI-controllers: one speed controller and two current controllers. The outer PI-controller controls the mechanical speed of the generator and produces the q-axis current reference for inner current controller. On the contrary, the reference of the d-axis current is set to zero for minimum power loss [8]. Compensation terms are added to improve the dynamic response.

For the grid–side converter, the outer DC-link voltage and inner current closed loop have the ability to perform a fast active power performance and to control the injected or absorbed reactive power, which are almost the same as the grid-side converter in a DFIG system.

IV. Power Loss Modelling

In order to compare the different two-level back-to-back wind power converter configurations, analysis of the loss distribution will be presented in this section.

A. Power device selection

As mentioned, the produced energy through the power converter semiconductors is quite different in the DFIG and

the PMSG system. Consequently, it is important to select the suitable power devices for both systems in order to obtain a fair comparison for the thermal loading.

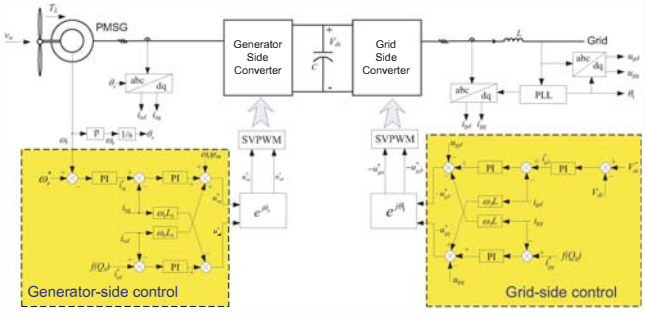

Fig. 6. Control scheme for the PMSG system with Generator-side and Grid-side control.

It is assumed that the two systems are using the wind turbine system as illustrated in Table I. Typical parameters for the generators are summarized in Table II. The PMSG system is a direct-drive for multi-pole structure, while for the DFIG system, a gearbox is still required as a multi-pole low-speed DFIG is not technically feasible.

TABLE II

2 MW GENERATOR DATA FOR DFIG AND PMSG [11], [12]

	DFIG	PMSG
Rated wind speed v_{w_rate} [m/s]	12	
Rated turbine speed n_{rot_rate} [rpm]	19	
Number of pole pairs p	2	102
Gear ratio	94.7	/
Rated shaft speed n_s [rpm]	1800	19
Rated fundamental frequency f_e [Hz]	10	32.3
Stator leakage inductance $L_{l\sigma}$ [mH]	0.038	0.276
Magnetizing inductance L_m [mH]	2.91	
Rotor leakage inductance $L_{l\sigma'}$ [mH]	0.064	/
Stator/rotor turns ratio n	0.369	/

The most important data for the two-level back-to-back converter are listed in Table III. The switching frequency in both configurations and both converters are set to 2 kHz. The rated active power in the DFIG system is much smaller than the PMSG system, as only slip power flows through both converters. Based on the active power, together with the rated converter voltage output, the current in the converter needs to be calculated.

It is noted that in the DFIG system the rated current in the grid-side converter and the generator-side converter is much more unequal, while the situation is better in the PMSG system. Furthermore, a parallel structure of multiple power components is a more used solution for multi-MW wind turbines today. Consequently, a common 1700V/1000A power device is selected. A single module in the grid-side converter and two paralleled modules in the generator-side converter are the solutions for the DFIG system, and four paralleled modules in both converters for the PMSG system are selected.

TABLE III

TWO-LEVEL BACK-TO-BACK POWER CONVERTER DATA

	DFIG	PMSG
Rated active power P_C [kW]	400	2000
DC-link voltage U_{dc} [V_{dc}]	1050	
Switching frequency f_s [kHz]	2	
Grid-side Converter		
Rated output voltage [V_{rms}]	704	704
Rated current [A_{rms}]	328	1641
Filter inductance [mH]	0.50	0.15
Generator-side Converter		
Rated output voltage [V_{rms}]	374	554
Rated current [A_{rms}]	618	2085

B. Power loss calculation

The power losses in the back-to-back converter consist of the generator-side converter loss and the grid-side converter loss. They are mainly divided into the switching losses and the conduction losses. Since no unbalance is taken into account in this paper, it is possible to consider the behavior of half of one leg in both side converters due to the symmetrical characteristic and the fixed DC-link voltage.

No matter what the current direction is, the switching losses in each switching period always contain one turn-on loss E_{on}, one turn-off loss E_{off} in the IGBT, and one diode recovery loss E_{rr}. E_{on}, E_{off} and E_{rr} are almost proportional to the DC-link voltage, thus the formula for switching loss in each power device P_{sw} can be expressed as:

$$P_{sw} = f_e \frac{U_{dc}}{U_{dc}^*} \sum_{n=1}^{N} \left[E_{on}(|i_a(n)|) + E_{off}(|i_a(n)|) + E_{rr}(|i_a(n)|) \right] \quad (2)$$

where f_e denotes the fundamental frequency of the phase current, U_{dc}^* denotes the tested DC-link voltage, N denotes the

total cycle numbers in each fundamental frequency, E_{on}, E_{off} and E_{rr} denote the switching loss energy in each switching period when the switching current equals to the phase current $|i_a(n)|$. E_{on}, E_{off}, E_{rr} and U_{dc}^{*} can be directly acquired from the power device datasheets.

The conduction losses mainly lie in the IGBT and the freewheeling diode. The conduction power loss in each power device P_{con} can be calculated as:

$$P_{con} = f_e \sum_{n=1}^{N} \left[v_{CE}(|i_a(n)|) \cdot |i_a(n)| \cdot T_1(n) + v_F(|i_a(n)|) \cdot |i_a(n)| \cdot (T_s - T_1(n)) \right] \quad (3)$$

where v_{CE} denotes the collector-emitter saturation voltage drop of the IGBT, v_F denotes the forward on-state voltage drop of the freewheeling diode, $T_1(n)$ denotes the conduction time of the IGBT during n^{th} switching period, which in line with the modulation strategies and the phase angle between phase current and phase voltage. T_s denotes the switching period.

C. Power loss distribution in the systems

Simulation of the power loss can be realized based on PLECS block in Simulink [13]. The simulation settings correspond to the design parameters shown in Table II and Table III. In addition, the simulation circuit runs at rated wind speed under normal grid condition and the power factor is set to unity. Fig. 7 and Fig. 8 indicate the loss distribution of each power semiconductor under the DFIG and the PMSG systems in terms of the generator-side converter and the grid-side converter, respectively. The name of the power semiconductor can be found in Fig. 3 and Fig. 5.

TABLE IV

PARAMETERS FOR CONVERTERS AT DIFFERENT WIND SPEED (DFIG/PMSG)

Wind speed [m/s]	Generator power [MW]	Wind turbine speed [rpm]	Slip	Fundamental frequency [Hz]
5.9	0.26	11/10.1	0.3/0	15/17.2
6.8	0.39	12.7/12.0	0.2/0	10/20.4
7.6	0.55	14.2/13.7	0.1/0	5/23.3
8.4	0.74	15.8/15.4	0/0	0/26.2
9.2	0.98	17.2/17.1	-0.1/0	5/29.1
10.1	1.29	19/19	-0.2/0	10/32.3
12	2	19/19	-0.2/0	10/32.3
25	2	19/19	-0.2/0	10/32.3

Comparing the back-to-back power converter in both systems, the power losses dissipated in the generator-side converter are more equal. It is because the turn-on and turn-off loss of IGBT are higher than the recovery loss of freewheeling diode for the same current, from (2) the switching loss in the diode is always smaller. The conduction loss is mainly related to the power direction. At rated active power, the generator-side converter is operating as a rectifier, and therefore more conduction losses are seen in the freewheeling diode. On the contrary, the grid-side converter is operating as an inverter, where most conduction losses are dissipated in the IGBT, which result in an unequal loading.

For the DFIG and the PMSG systems, the power loss dissipated in the PMSG system is larger. The reason is that as summarized in Table III, the current through each power semiconductor is higher.

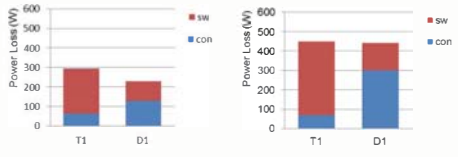

(a) DFIG system (b) PMSG system

Fig. 7. Loss distribution in generator-side converter for each device (wind speed: 12 m/s).

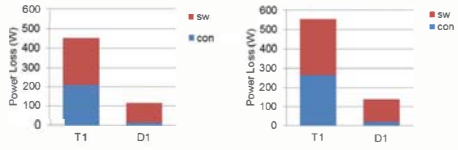

(a) DFIG system (b) PMSG system

Fig. 8. Loss distribution in grid-side converter for each device (wind speed: 12 m/s).

Note: **sw** and **con** are switching losses and conduction losses, respectively

In order to investigate the loss behavior in different operation modes, several wind speeds are chosen with slip values from -0.3 to 0.2 in the DFIG system and shown in Table IV. It is noted that the wind speed at 8.4 m/s is regarded as the synchronous operating point as it is seen in Fig. 2 and in Table II.

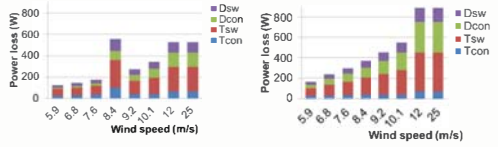

(a) DFIG system (b) PMSG system

Fig. 9. Power loss of each device vs. wind speed (generator-side converter).

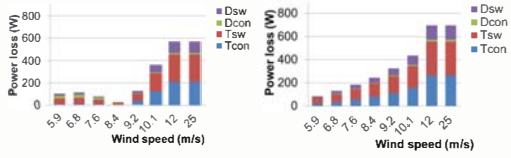

(a) DFIG system (b) PMSG system

Fig. 10. Power loss of each device vs. wind speed (grid-side converter).

The power loss in the generator-side converter at different wind speed is shown in Fig. 9. At synchronous operating point of the DFIG system, the rotor current becomes the DC component, the power loss in three legs will be significantly unbalanced. The most stressed IGBT and diode are illustrated in Fig. 9a, whose power loss is even higher than those at rated wind speed. In the super-synchronous mode, the power loss increases with larger wind speed, and the growth rate is relatively slower since the larger slip, which will decrease the converter current. It is noted that the conduction loss in the diode is dominating. However, in the sub-synchronous mode,

the conduction loss in the IGBT is dominating. For the PMSG system, the power loss increases with the wind speed consecutively.

The power loss in the grid-side converter at different wind speed is shown in Fig. 10. For the DFIG system, the lowest power loss appears in the synchronous operating point due to the fact that no active power flow and only the switch ripple current affects, while the highest one appears at rated wind power. Furthermore, the IGBT suffers more loss in super-synchronous mode and the diode suffers more loss in sub-synchronous mode. For the PMSG system, the power loss increases with the wind speed consecutively.

V. THERMAL ANALYSIS OF THE SYSTEMS

As the thermal performance of the power devices are closely related to the reliability and the cost of the whole power converter system, a comparison of the thermal cycling of the DFIG and the PMSG systems are done.

A. Thermal model

In order to describe the thermal behavior of the power semiconductors, an appropriate thermal model needs to be developed. The thermal models of single IGBT and the freewheeling diode are shown in Fig. 11, and share the same design idea as discussed in [5], the thermal resistance R_{th} will determine the steady-state mean junction temperature, and along with the thermal capacitance (function of time constant τ) will determine the junction temperature fluctuation.

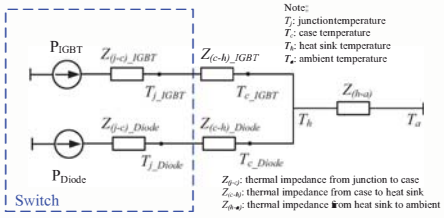

Fig. 11. Thermal models of the power semiconductors.

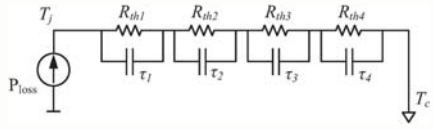

Fig. 12. RC Foster network of thermal impedance from junction to case of the power semiconductor devices.

The thermal impedance from the junction to case $Z_{(j-c)}$ is modeled as four-layer Foster RC network as depicted in Fig. 12, whose parameters are collected from the datasheet of the power device. The case-to-heatsink thermal impedance is modelled as a simple thermal resistor, neglecting the much higher thermal capacitance due to the less significant dynamic behavior of junction temperature and faster thermal simulation. Meanwhile the heatsink-to-ambient resistance is considered small compared to the thermal resistance in the MW power converter. Furthermore, the ambient temperature is set to 50 ℃.

B. Analysis of thermal cycling

The simulation results of the junction temperature in each power semiconductor of the generator-side converter under the DFIG and the PMSG systems are shown in Fig. 13 in which the converters run at rated power and in steady-state operation. It can be seen that the mean temperature of the diode is higher than the IGBT's in both the DFIG and the PMSG systems, and the thermal performance of the PMSG system shows more unequal distribution, where the difference of junction temperature between the IGBT and the diode is 12.4 ℃ compared to 5.1 ℃ in the DFIG system. For the junction temperature of the grid-side converter, the thermal results of the DFIG and the PMSG systems are shown in Fig. 14a and Fig. 14b respectively. It can be seen that the hottest power semiconductor device turns out to be the IGBT. Moreover, the junction temperature variation between the IGBT and the diode show more equal distribution.

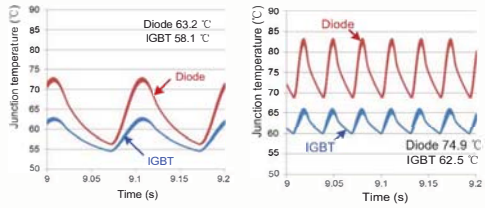

(a) DFIG system (b) PMSG system

Fig. 13. Junction temperature in the generator-side converter (Wind speed: 12 m/s).

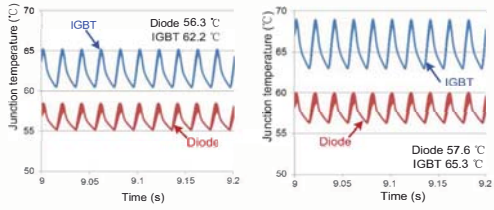

(a) DFIG system (b) PMSG system

Fig. 14. Junction temperature in the grid-side converter (Wind speed: 12 m/s).

A further comparison of thermal behavior for both systems with different wind speed is shown in Fig. 15. For the generator-side converter, it can be seen that, in the PMSG system the mean junction temperature and the temperature fluctuation of the power semiconductors above rated wind speed are the highest among the whole operation range of the wind. The hottest device is the diode in the whole range of the wind speed. In the DFIG system, the hottest device changes from the IGBT in the sub-synchronous mode to the diode in the super-synchronous mode. Moreover, the mean junction temperature and the temperature fluctuation of the power semiconductors become crucial around the synchronous operating point. Although the mean junction temperature is all

higher in the PMSG system except for the region around synchronous operation as shown in upper Fig. 15a, at rated wind speed the temperature fluctuation in the DFIG system is even larger due to less frequency power loss cycling as shown in lower Fig. 15a. For the grid-side converter in the PMSG system, the mean junction temperature and the junction temperature fluctuation of power semiconductors above rated wind speed becomes the highest in the whole operation range of the wind. In the DFIG system, the hottest device changes from the diode in the sub-synchronous mode to the IGBT in the super-synchronous mode. Moreover, the mean junction temperature as well as the junction temperature fluctuation becomes the least crucial around the synchronous operating point. As the power loss of the PMSG system is higher than the DFIG system, the mean junction temperature is higher in the PMSG system as shown in upper Fig. 15b. Moreover, the junction temperature fluctuation in the DFIG system is smaller due to same frequency power loss cycling as shown in lower Fig. 15b under rated wind speed.

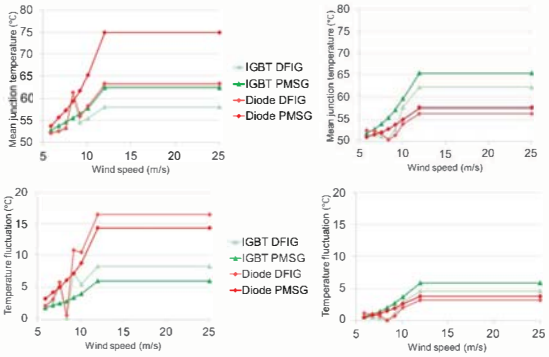

(a) Generator-side converter (b) Grid-side converter

Fig. 15. Mean junction temperature and temperature fluctuation in the chip vs. wind speed for both systems.

VI. CONCLUSION

In this paper, platforms for the popular 2 MW two-level wind turbine configurations (i.e. partial-scale and full-scale power converter) are established in the PLECS/Simulink to simulate the power losses and the thermal load cycling. A comparison of the loss distribution as well as thermal loading in the DFIG and the PMSG systems are investigated.

For the partial-scale power converter configuration, the thermal behavior between the generator-side converter and the grid-side converter are quite different. The operation area above the rated wind speed range of the grid-side converter is significant from the thermal stress point of view, while the generator-side converter not only concerns the above mentioned case, but also the wind speed range around the synchronous operation.

For the full-scale power converter configuration, whatever generator-side converter or grid-side converter, the crucial thermal stress lies in the operation area above the rated wind speed range.

Moreover, comparing the most stressed semiconductor device, the generator-side converter is the most critical part for thermal stress of the two-level back-to-back converter for high power applications. Furthermore, the reactive power support to the grid as well as the wind speed variation will affect the thermal profile of the power semiconductors.

References

[1] Z. Chen, J.M. Guerrero, F. Blaabjerg, "A review of the state of the art of power electronics for wind turbines," *IEEE Trans. on Power Electronics*, vol.24, no.8, pp.1859-1875, Aug. 2009.

[2] F. Blaabjerg, Z. Chen, S.B. Kjaer, "Power electronics as efficient interface in dispersed power generation systems," *IEEE Trans. on Power Electronics,* vol.19, no.5, pp. 1184- 1194, Sep. 2004.

[3] M. Liserre, R. Cárdenas, M. Molinas, J. Rodriguez, "Overview of multi-MW wind turbines and wind parks," *IEEE Trans. on Industrial Electronics*, vol.58, no.4, pp.1081-1095, Apr. 2011.

[4] M. Bruns, B. Rabelo, W. Hofmann, "Investigation of doubly-fed induction generator drives behaviour at synchronous operating point in wind turbines," *in Proc. of EPE'09*, pp.1-10, Sep. 2009.

[5] K. Ma, F. Blaabjerg, "Multilevel converters for 10 MW wind turbines," in *Proc. of EPE'11*, pp.1-10, 2011.

[6] A. Wintrich, U. Nicolai, T. Reimamm, "Semikron Application Manual," pp.128, 2011.

[7] F. Blaabjerg, M. Liserre, K. Ma, "Power electronics converters for wind turbine systems," *IEEE Trans. on Industry Applications*, vol.48, no.2, pp.708-719, Mar. 2012.

[8] M. Chinchilla, S. Arnaltes, J.C. Burgos, "Control of permanent-magnet generators applied to variable-speed wind-energy systems connected to the grid," *IEEE Trans. on Energy Conversion,* vol.21, no.1, pp. 130-135, Mar. 2006.

[9] "Vestas." [Online]. Available: http://www.vestas.com/.

[10] A.A. Rockhill, M. Liserre, R. Teodorescu, P. Rodriguez, "Grid-filter design for a multi-megawatt medium-voltage voltage-source inverter," *IEEE Trans. on Industrial Electronics,* vol.58, no.4, pp.1205-1217, Apr. 2011.

[11] C. Liu, F. Blaabjerg, W. Chen, D. Xu, "Stator current harmonic control with resonant controller for doubly fed induction generator," *IEEE Trans. on Power Electronics*, vol.27, no.7, pp.3207-3220, Jul. 2012.

[12] H. Li, Z. Chen, H. Polinder, "Optimization of multibrid permanent-magnet wind generator systems," *IEEE Trans. on Energy Conversion*, vol.24, no.1, pp.82-92, Mar. 2009.

[13] User manual of PLECS blockset version 3.2.7 March 2011. (Available: http://www.plexim.com/files/plecsmanual.pdf

[A.2] D. Zhou, F. Blaabjerg, M. Lau, M. Tonnes, "Thermal behavior optimization in multi-MW wind power converter by reactive power circulation," *IEEE Trans. on Industry Applications*, vol. 50, no. 1, pp. 433-440, Jan. 2014. (Also *in Proc. of APEC 2013*, pp. 2863-2870, 2013)

Thermal Behavior Optimization in Multi-MW Wind Power Converter by Reactive Power Circulation

Dao Zhou, *Student Member, IEEE*, Frede Blaabjerg, *Fellow, IEEE*, Mogens Lau, and Michael Tonnes

***Abstract*—The influence of actively controlled reactive power on the thermal behavior of a multimegawatt wind power converter with a doubly fed induction generator is investigated. First, the allowable range of internal reactive power circulation is mapped depending on the dc-link voltage and the induction generator and power device capacity. Then, the effects of reactive power circulation on current characteristic and thermal distribution of the two-level back-to-back power converter are analyzed and compared. Finally, the thermal-oriented reactive power control method is introduced to the system for the conditions of constant wind speed and during wind gust. It is concluded that the thermal performance will be improved by injecting proper reactive power circulation within the wind turbine system, thereby being able to reduce the thermal cycling and enhance the reliability of the power converter.**

***Index Terms*—Doubly fed induction generator (DFIG), reactive power, thermal cycling.**

I. Introduction

OVER the last two decades, wind power has greatly expanded and is forecasted to continue increasing with an average annual growth over 15%. As the power level of single wind turbine is even pushed up to 8 MW (e.g., V164-offshore, Vestas), medium voltage may become a promising technology in such applications. However, this solution is known to be costly and difficult to repair [1]–[3]. It is still reasonable to consider low-voltage technology in wind power systems with an input and output isolation transformer. Furthermore, wind power converters are being designed for a much prolonged lifetime of 20–25 years. Industrial experience indicates that dynamic loading and uncertain and harsh environments are leading to fatigue and a risk of a higher failure rate for power semiconductors. Therefore, more and more efforts are devoted to the thermal behavior and reliability of the power devices in power converters.

Today, it is widely accepted that the reliability of the power semiconductor is closely related to thermal performance, particularly the junction temperature fluctuation and the average junction temperature [4]–[13]. Some research has focused on the thermal analysis of wind power converters. In [14], it is noted that the thermal stress of the machine-side converter becomes serious during synchronous operation of the doubly fed induction generator (DFIG). The different control schemes of the DFIG system can also affect the power device lifetime [15]. For full-scale power converters, as stated in [16], the thermal performance of the grid-side converter (GSC) may be improved by circulating proper reactive power among the wind farms.

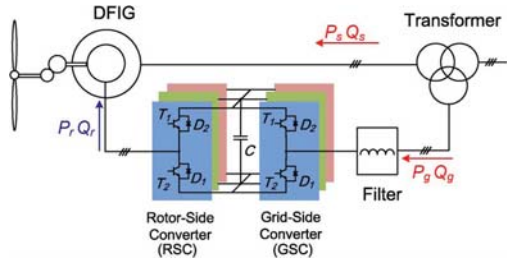

Fig. 1. Typical configuration of a DFIG wind turbine system.

The scope of this paper, aiming at the DFIG wind turbine system, is first to calculate the allowable reactive power circulation between the back-to-back power converter in different operation modes. Then, the thermal behavior of the back-to-back power converter is investigated under different types of reactive power injection. Finally, a method to improve the lifetime of the power module by proper thermal-oriented control in the conditions of constant wind speed and wind gusts is proposed.

II. Basic Concept for a DFIG System

Due to extensive and well-established knowledge, as well as simpler structure and fewer components, the two-level back-to-back voltage source converter is the most attractive solution in the commercial market of wind turbine systems. A popular wind turbine configuration, normally based on a DFIG, is to employ a partial-scale power converter, as shown in Fig. 1. The function of the rotor-side converter (RSC) is not only to transfer the slip active power from/to the grid but also to provide excitation current for the induction generator, whereas the GSC is designed to keep the dc-link voltage fixed and also supply some of the reactive power required by the grid codes.

The parameters of the induction generator and the back-to-back converter used in this paper are summarized in Tables I and II, respectively. The turns ratio between the generator's

Manuscript received December 4, 2012; revised February 3, 2013; accepted March 8, 2013. Date of publication June 10, 2013; date of current version January 16, 2014. Paper 2012-IPCC-705.R1, presented at the 2013 IEEE Applied Power Electronics Conference and Exposition, Long Beach, CA, USA, March 17–21, and approved for publication in the IEEE Transactions on Industry Applications by the Industrial Power Converter Committee of the IEEE Industry Applications Society.

D. Zhou and F. Blaabjerg are with the Department of Energy Technology, Aalborg University, 9220 Aalborg East, Denmark (e-mail: zda@et.aau.dk; fbl@et.aau.dk).

M. Lau and M. Tonnes are with Danfoss Silicon Power GmbH, 24941 Flensburg, Germany (e-mail: mogens.lau@danfoss.com; michael.tonnes@danfoss.com).

Color versions of one or more of the figures in this paper are available online at http://ieeexplore.ieee.org.

Digital Object Identifier 10.1109/TIA.2013.2267511

TABLE I
PARAMETERS FOR A 2-MW DFIG

Rated power P_m	2 MW
Reactive power range Q_s	-570 kVar ~ +450 kVar
Rated peak stator phase voltage U_{sm}	563 V
Stator/rotor turns ratio k	0.369
Stator inductance L_s	2.95 mH
Rotor inductance L_r	2.97 mH
Magnetizing inductance L_m	2.91 mH

TABLE II
PARAMETERS FOR THE BACK-TO-BACK POWER CONVERTER

Rated power P_g	330 kW
Rated peak grid phase voltage U_{gm}	563 V
DC-link voltage U_{dc}	1050 V
Filter inductance L_g	0.5 mH
RSC and GSC switching frequency f_s	2 kHz
Power device in each GSC cell	1.7 kV/1 kA
Power device in each RSC cell	1.7 kV/1 kA // 1.7 kV/1 kA

stator and the GSC is assumed 1 : 1, which implies that the rated stator voltage and the rated grid voltage are the same. Moreover, a common low-voltage power module is selected (1.7 kV/1 kA). Because of the significantly unequal current through the GSC and the RSC, for the sake of similar power device loading, a single power device and two paralleled power devices are the solutions in each GSC and RSC cell, respectively.

III. EFFECTS OF REACTIVE POWER ON CURRENT CHARACTERISTIC

With the reference direction of the power flow indicated in Fig. 1, both the GSC and the RSC have the ability to control the reactive power. In other words, the system can perform an operation to circulate the reactive power internally without any unexpected power factor distortion to the grid. Although the reactive power flow in the power system will induce voltage drop, additional power dissipation, and higher capacity of transmission equipment (e.g., cable, transformer, etc.), the proper excited power for the induction generator sharing between the stator and rotor sides can be used to vary the loss distribution of the back-to-back power converter and even to enhance the power converter efficiency [17].

A. Range of Reactive Power in the GSC

Fig. 2 depicts a simplified single-phase diagram of the GSC, where L_g represents the filter inductance, U_g represents the grid phase voltage, and U_C represents the output voltage of the GSC. Depending on the definition of power flow, whose direction is consistent with the illustration in Fig. 1, the phasor diagram for the GSC is shown in Fig. 3, in which the capacitive reactive power is applied. Due to the opposite polarity of active power through the GSC between subsynchronous mode and supersynchronous mode, the active power current reference will

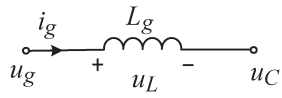

Fig. 2. Simplified single-phase diagram of the GSC.

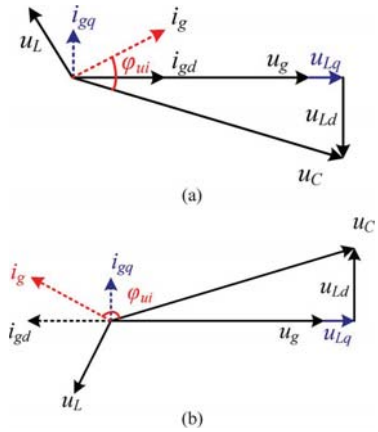

Fig. 3. Phasor diagram for the GSC (e.g., capacitive reactive power injection). (a) Operating under subsynchronous mode. (b) Operating under supersynchronous mode.

be as shown in Fig. 3(a) and (b), respectively. Accordingly, if the inductive reactive power is introduced, the phasor diagram can be obtained by rotating the q-axis current 180°.

The analytical formula for the converter output voltage U_c is expressed as

$$U_C = \sqrt{(U_{\rm gm} + i_{\rm gq}X_g)^2 + (i_{\rm gd}X_g)^2} \le \frac{U_{\rm dc}}{\sqrt{3}} \qquad (1)$$

where $U_{\rm gm}$ and $U_{\rm dc}$ denote the rated peak grid phase voltage and the dc-link voltage, respectively; X_g denotes the filter reactance at 50 Hz, which is also consistent with Table II; and $i_{\rm gd}$ and $i_{\rm gq}$ denote the GSC's peak current in the d- and q-axes, respectively.

It is evident that, whatever the operation mode is, the amplitude of the converter output voltage will be increased if the capacitive reactive power is introduced. Therefore, due to linear modulation, the relationship between the dc-link voltage and the output voltage of the GSC is also illustrated in (1).

The other restriction lies in the capacity of the power device/converter, i.e.,

$$\sqrt{i_{\rm gd}^2 + i_{\rm gq}^2} \le I_m \qquad (2)$$

where I_m denotes the peak current of the power module stated in the data sheet.

Furthermore, the induction generator's capacity Q_s must also be taken into account according to Table I, i.e.,

$$\frac{3}{2}U_{\rm gm}i_{\rm gq} \le Q_s. \qquad (3)$$

Based on the aforementioned three limitations, the boundary of reactive power can be obtained. Moreover, the power angle

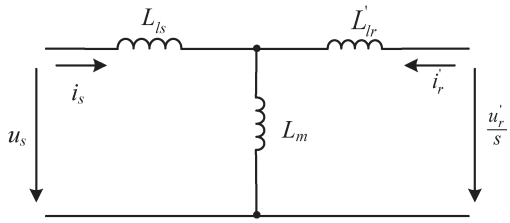

Fig. 4. Equivalent DFIG circuit diagram in steady-state operation.

is another important indicator for the power loss evaluation, whose feature is described in Fig. 3 as well.

B. Range of Reactive Power in the RSC

Ignoring the stator and rotor resistance, the equivalent DFIG circuit in steady-state operation is shown in Fig. 4, where the parameters of the rotor side are referred to the stator side by the stator/rotor winding turns ratio k. The equations of the rotor current $i'_{\rm rd}$ and $i'_{\rm rq}$ and rotor voltage $u'_{\rm rd}$ and $u'_{\rm rq}$ under a d–q frame in terms of stator current are

$$\begin{cases} i'_{\rm rd} = -\frac{X_s}{X_m} i_{\rm sd} \\ i'_{\rm rq} = -\frac{U_{\rm sm}}{X_m} - \frac{X_s}{X_m} i_{\rm sq} \end{cases} \tag{4}$$

$$\begin{cases} u'_{\rm rd} = s\left(\frac{X_r}{X_m} U_{\rm sm} + \frac{\sigma X_r X_s}{X_m} i_{\rm sq}\right) \\ u'_{\rm rq} = -s\frac{\sigma X_r X_s}{X_m} i_{\rm sd} \end{cases} \tag{5}$$

where s denotes the rotor slip value; σ denotes the leakage factor of the induction generator; $U_{\rm sm}$ denotes the rated peak stator phase voltage of the induction generator; X_s, X_r, and X_m denote stator, rotor, and magnetizing reactance at 50 Hz, which is consistent with Table I; and $i_{\rm sd}$ and $i_{\rm sq}$ denote the RSC's peak current in the d- and q-axes, respectively.

If the capacitive reactive power is provided, the phasor diagram for the RSC in the condition of subsynchronous and supersynchronous mode is depicted in Fig. 5(a) and (b), respectively. Similar restrictions with the GSC, i.e., the linear modulation, the power device limitation and induction generator capacity

$$\frac{\sqrt{{u'_{\rm rd}}^2 + {u'_{\rm rq}}^2}}{k} \le \frac{U_{\rm dc}}{\sqrt{3}} \tag{6}$$

$$k\sqrt{{i'_{\rm rd}}^2 + {i'_{\rm rq}}^2} \le I_m \tag{7}$$

$$-\frac{3}{2} U_{\rm sm} i_{\rm sq} \le Q_s. \tag{8}$$

It can be seen that the range of reactive power in the RSC is limited by the induction generator capacity, whereas in the GSC, the induction generator capacity affects and the dc-link voltage limits the amount of capacitive reactive power.

C. Current Characteristic of the Back-to-Back Power Converter

The current amplitude and the power factor angle of the back-to-back power converter are regarded as two indicators for the power device loading; hence, it is interesting to investigate the current characteristic based on the reactive power range.

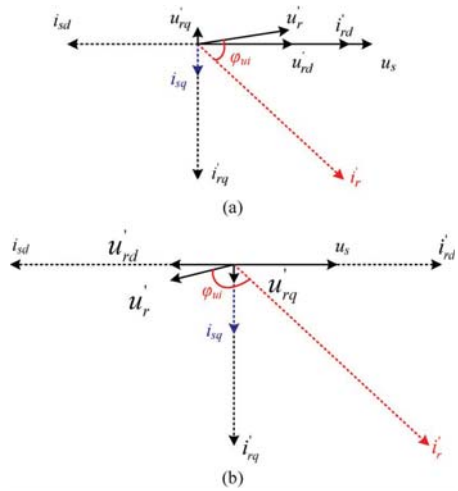

Fig. 5. Phasor diagram for the RSC (e.g., capacitive reactive power injection). (a) Operating under subsynchronous mode. (b) Operating under supersynchronous mode.

If two typical wind speeds of 5.9 and 10.1 m/s are selected for subsynchronous and supersynchronous operation (these two wind speeds are regarded as the two highest probability wind speeds in wind farms [18]), the range of reactive power in the GSC and RSC can be summarized, as listed in Table III. In order not to affect the power factor to the grid, the circulation current is the minimum range of the back-to-back power converter, which is $(-0.23,\ 0.06)$ from the GSC point of view. As the horizon axis is defined as the reactive power range of the GSC, the injection of additional power not only affects the current amplitude but also changes the power factor angle φ_{ui}, as shown in Fig. 6.

For the characteristic of current amplitude, regardless of subsynchronous or supersynchronous operation mode, it is evident that the minimum current appears almost under no reactive power injection for the GSC, whereas for the RSC, the current decreases with larger capacitive reactive power. Unfortunately, the capacitive reactive power is much smaller than the inductive reactive power, which prevents the RSC's current to reach the minimum power losses.

For the characteristic of power factor angle, for the GSC, it is noted that, in response to the additional reactive power injection, unity power factor becomes either leading or lagging power factor. For the RSC, it is noted that the power factor angle presents a tendency to be in phase under subsynchronous mode or inverse under supersynchronous mode with the increasing capacitive reactive power. However, the phase shift looks insignificant.

IV. Effects of Reactive Power on Thermal Behavior in Power Devices

Different distribution of the excitation energy between the induction generator's rotor and stator will definitely change the

TABLE III
RANGE OF THE REACTIVE POWER FOR THE BACK-TO-BACK POWER CONVERTER

	Sub-synchronous Mode		Super-synchronous Mode	
	Grid-Side Converter	Rotor-Side Converter	Grid-Side Converter	Rotor-Side Converter
Typical wind speed [m/s]	5.9		10.1	
Rated power [p.u.]	0.13		0.65	
Active power current [p.u.]	0.06	0.19	0.11	0.54
Range of reactive power [p.u.]	(-0.23,0.06)	(-0.29,0.23)	(-0.23,0.06)	(-0.29,0.23)

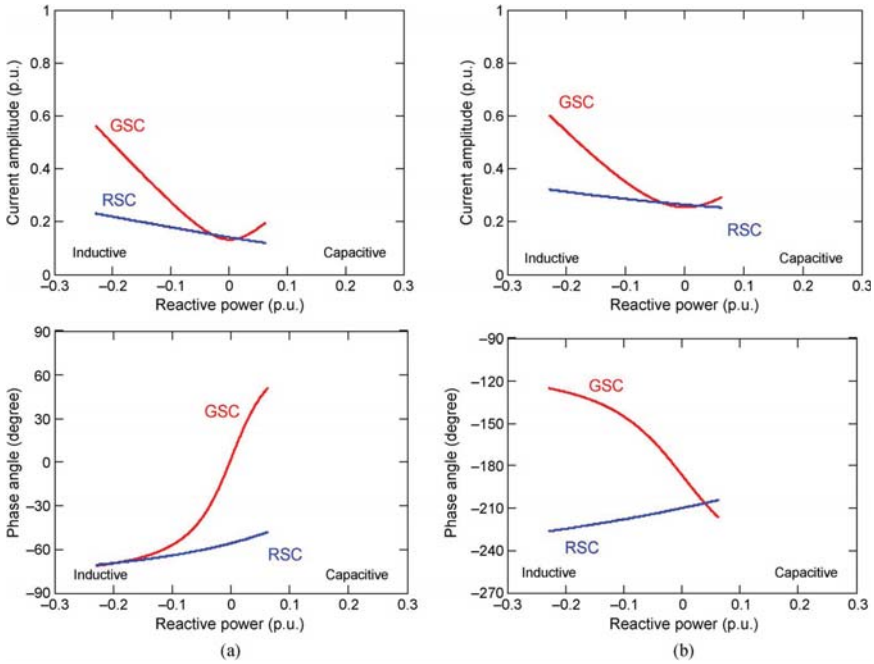

Fig. 6. Current characteristic of the back-to-back power converter at two different wind speeds. (a) Subsynchronous mode (wind speed: 5.9 m/s). (b) Supersynchronous mode (wind speed: 10.1 m/s).

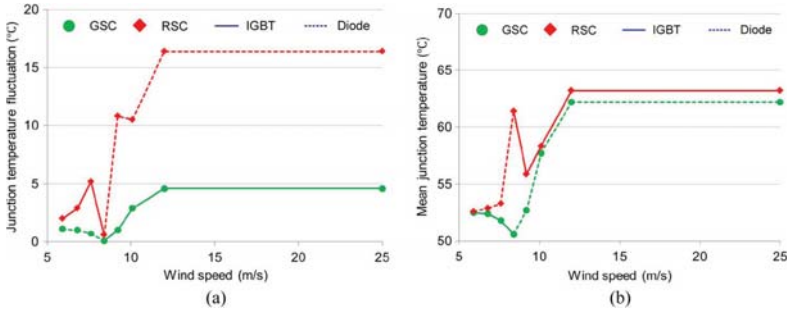

Fig. 7. Thermal profile of the back-to-back power converter versus wind speed. (a) Junction temperature fluctuation. (b) Mean junction temperature.

current characteristic of the back-to-back power converter. The influence on the thermal performance of the power semiconductor will be investigated here.

A. Thermal Profile for Normal Operation

Power losses in power semiconductor can be divided into two categories, namely, conduction losses and switching losses.

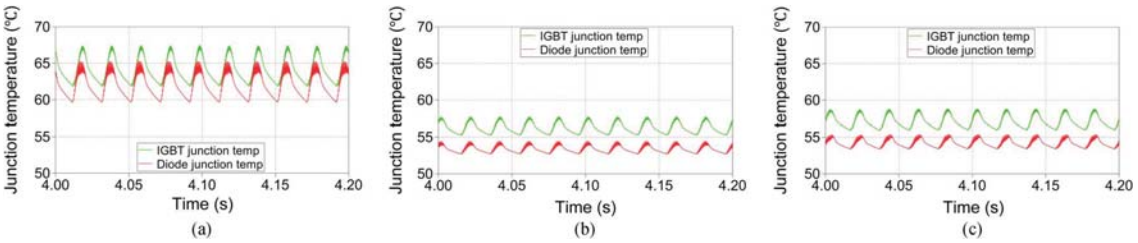

Fig. 8. Thermal distribution of the GSC at supersynchronous mode (wind speed: 10.1 m/s). (a) Inductive Q. (b) No Q. (c) Capacitive Q.

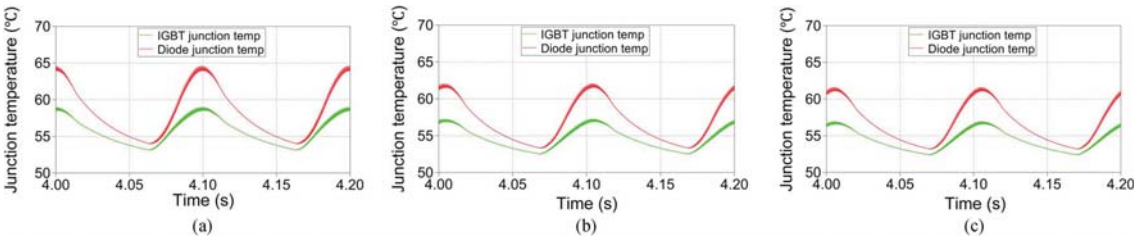

Fig. 9. Thermal distribution of RSC at supersynchronous mode (wind speed: 10.1 m/s). (a) Inductive Q. (b) No Q. (c) Capacitive Q.

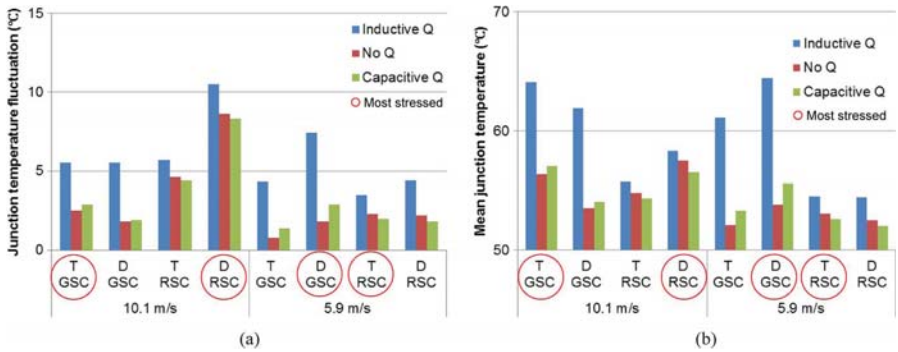

Fig. 10. Thermal profile of the back-to-back power converter operating under subsynchronous and supersynchronous mode. (a) Junction temperature fluctuation. (b) Mean junction temperature.

Based on the loss energy curves provided by the manufacturer, the accumulated power dissipation in every switching cycle can be obtained within one fundamental frequency. Simulations have been realized by the piecewise linear electrical circuit simulation block in Simulink [20].

With the aid of a 1-D thermal model mentioned in [19], under normal operation, the relationship between the wind speed and the junction temperature of each power semiconductor of the back-to-back power converter is shown in Fig. 7 in terms of junction temperature fluctuation and mean junction temperature. In particular, the wind speed at 8.4 m/s is regarded as the synchronous operation for the DFIG wind turbine system.

It can be seen that, when the wind speed increases over the synchronous operation mode of the DFIG, the direction of the power flow in the back-to-back power converter starts to reverse. In the RSC, because the higher power loss changes from the insulated-gate bipolar transistor (IGBT) in subsynchronous mode to the freewheeling diode in supersynchronous mode, the most thermal stressed power device switches from the IGBT to the freewheeling diode, whereas similarly in the GSC, the most thermal stressed power device changes from the freewheeling diode to the IGBT.

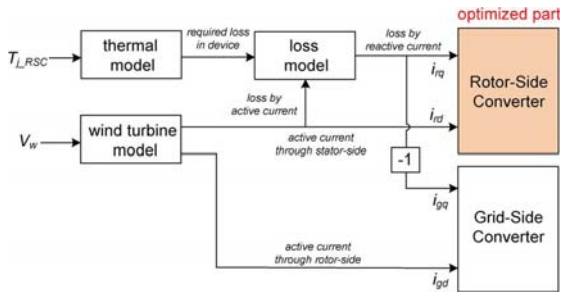

Fig. 11. Thermal-oriented control diagram of the back-to-back power converter under constant wind speed.

Furthermore, the RSC shows a higher value both in the junction temperature fluctuation and the mean junction temperature

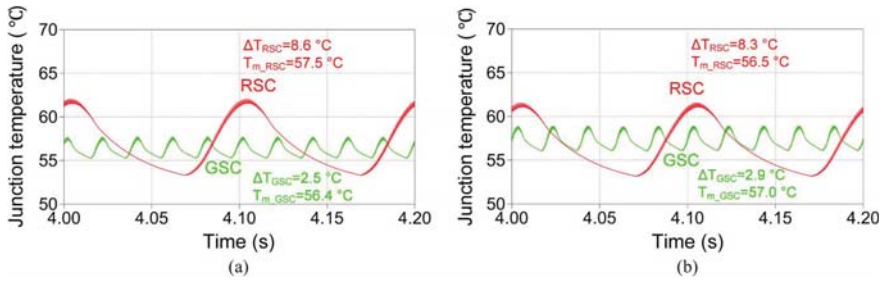

Fig. 12. Thermal cycling of the most stressed power device in both converters under constant wind speed (e.g., supersynchronous mode: wind speed is equal to 10.1 m/s). (a) Without thermal-oriented reactive power control. (b) With thermal-oriented reactive power control.

throughout the entire wind speed, which indicates that the lifetime between the back-to-back power converter will be significantly unbalanced.

B. Thermal Profile Under Reactive Power Injection

According to the reactive power range circulation within the DFIG system summarized in Table III, the thermal distribution of the GSC and the RSC can be analyzed in the conditions of inductive Q, no Q, and capacitive Q. A case study under supersynchronous operation is taken as an example, where the wind speed is selected at 10.1 m/s. The thermal behavior of the GSC is shown in Fig. 8, where the red curve indicates the freewheeling diode, and the green curve indicates the IGBT. The thermal behavior of the RSC is depicted in Fig. 9 as well.

Regarding the thermal performance in the GSC, as illustrated in Fig. 8, the minimum temperature fluctuation, as well as the mean junction temperature, appears at no Q, which is consistent with the current characteristics in Fig. 6(b), while due to a much higher additional reactive power range, the two indicators become more serious in the case of inductive Q compared with capacitive Q.

However, for the RSC, the minimum junction temperature fluctuation, as well as the mean junction temperature, appears at capacitive Q, as shown in Fig. 9. The junction temperature fluctuation and mean junction temperature remain at three conditions almost the same. This is due to the fact that compared with the maximum allowable reactive power, i.e., inductive reactive power, the active power reference is dominating, as shown in (4). Furthermore, the RSC's two paralleled power modules and the transformation of rotor current in line with the stator/rotor turns ratio result in more stable power device loading, which will lead to nearly a constant junction temperature.

Similarly, if a case of the subsynchronous mode at the wind speed of 5.9 m/s is taken into account, the thermal profile of the back-to-back power converter can be illustrated in Fig. 10 in terms of the junction temperature fluctuation and the mean junction temperature, where the power semiconductor with the red circle is the most stressed.

From the GSC point of view, it can be seen that the least thermal stress appears at no reactive power injection. Moreover, it is noted that the injection of reactive power, particularly inductive reactive power, could change the junction temperature fluctuation significantly. From the RSC point of view, the additional capacitive reactive power could help to reduce the thermal stress slightly.

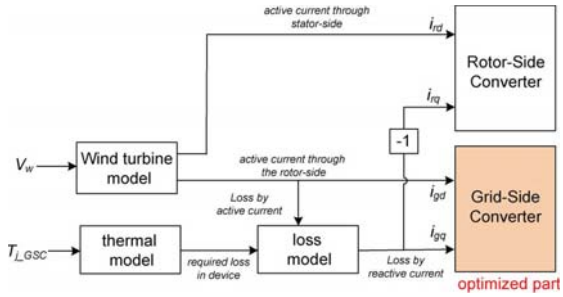

Fig. 13. Thermal-oriented control diagram of the back-to-back power converter during wind gust.

V. Thermal Performance Improvement by Reactive Power Control

A. Thermal Behavior Improvement Under Constant Wind Speed

As illustrated in Fig. 7, the RSC is regarded as the most stressed in the back-to-back power converter. Reactive power circulation within the DFIG system may change the thermal distribution both in the GSC and in the RSC; thus, it provides the possibility of achieving smaller temperature fluctuation in the most stressed power converter with proper reactive power under constant wind speed. The control diagram is shown in Fig. 11.

Fig. 12 illustrates the simulation result of operation at the wind speed of 10.1 m/s under supersynchronous mode. The junction temperature fluctuation and mean junction temperature of the most stressed power converter could both be decreased, which of course will enhance the power device's lifetime. However, from the GSC point of view, the two reliability indicators both become slightly worse. Therefore, it is a tradeoff, as well as a possibility, in order to realize similar performance for the back-to-back power converter with respect to the reliability.

B. Thermal Behavior Improvement Under Wind Gust

As aforementioned, the injection of the reactive power may influence the thermal behavior of the power device. Therefore,

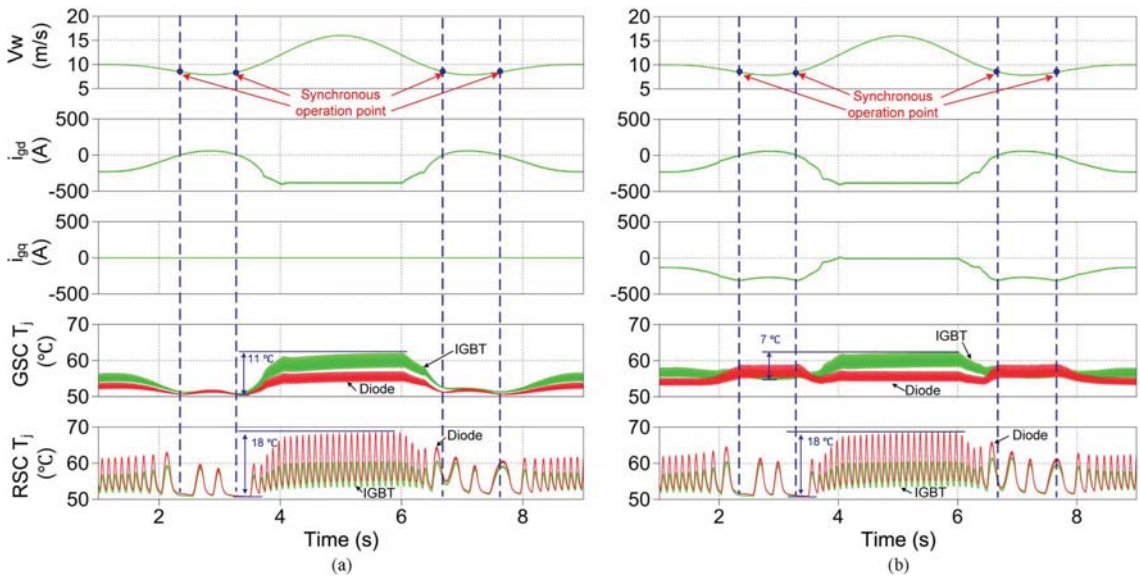

Fig. 14. Thermal cycling of the back-to-back power converter during wind gusts. (a) Without thermal-oriented reactive power control. (b) With thermal-oriented reactive power control.

it is possible to stabilize the temperature fluctuation under wind gust by proper thermal-oriented reactive power control, as shown in Fig. 13.

The typical one-year return period wind gust is defined in the International Electrotechnical Commission, i.e., Mexican-hat-like curve [21]. As shown in Fig. 14, the wind speed decreases from an average of 10 m/s to a trough of 8 m/s, increases to a crest of 16 m/s, and returns to 10 m/s within 8 s, where 8.4 m/s is the synchronous operation wind speed.

The thermal cycling of both converters with and without thermal-oriented reactive power control is shown in Fig. 14(a) and (b), respectively. It is worth noting that the most stressed power device of the RSC is selected during the synchronous operation point.

In Fig. 14(a), the active power reference becomes zero at the synchronous operation point. Moreover, it can be seen that the minimum junction temperature appears at the synchronous operation point and that the maximum junction temperature appears above the rated wind speed. The thermal stress becomes the least serious at synchronous wind speed due to no active power flow in the GSC, whereas it becomes the most serious at the extreme low-frequency current in the RSC.

In Fig. 14(b), it is noted that, by injecting proper thermal-oriented reactive power, the maximum junction temperature fluctuation in the GSC is decreased from 11 °C to 7 °C, due to the introduction of additional thermal-oriented reactive power under small active power in order to actively heat up the device, which will enhance the lifetime of the power converters, whereas the maximum junction temperature fluctuation in the RSC remains the same 18 °C due to the rather higher active power reference in the entire wind speed.

However, when introducing additional reactive power to the wind turbine system in the GSC, the thermal behavior of the diode will become more variable but still has less fluctuation compared with that of the IGBT. In the RSC, the thermal behavior of the IGBT and the diode are slightly changed.

VI. Conclusion

This paper has studied the range of reactive power circulation internally between the GSC and the RSC in a DFIG system. It is the GSC that determines the reactive power allowance, which is limited by the dc-link voltage and induction generator capacity. Meanwhile, the range of the capacitive reactive power is much higher than the inductive reactive power.

The additional reactive power will influence the back-to-back power converter's current characteristic and thereby the thermal loading of the power devices. Therefore, it provides the possibility of relieving the thermal cycling either in the GSC or the RSC.

If the wind stays at constant speed, the most stressed power semiconductor of the GSC and the RSC will be more balanced by the thermal-oriented reactive power injection, which will enhance the temperature loading of the power module.

During a wind gust, the junction temperature fluctuation of the most stressed power semiconductor will be remarkably reduced in the GSC by the thermal-oriented control, which will improve the reliability of the wind power converter. Moreover, the impact on the RSC is not significant.

References

[1] Z. Chen, J. M. Guerrero, and F. Blaabjerg, "A review of the state of the art of power electronics for wind turbines," *IEEE Trans. Power Electron.*, vol. 24, no. 8, pp. 1859–1875, Aug. 2009.

[2] F. Blaabjerg, Z. Chen, and S. B. Kjaer, "Power electronics as efficient interface in dispersed power generation systems," *IEEE Trans. Power Electron.*, vol. 19, no. 5, pp. 1184–1194, Sep. 2004.

[3] M. Liserre, R. Cardenas, M. Molinas, and J. Rodriguez, "Overview of multi-MW wind turbines and wind parks," *IEEE Trans. Ind. Electron.*, vol. 58, no. 4, pp. 1081–1095, Apr. 2011.
[4] Y. Song and B. Wang, "Survey on reliability of power electronic systems," *IEEE Trans. Power Electron.*, vol. 28, no. 1, pp. 591–604, Jan. 2013.
[5] A. Bryant, N. Parker-Allotey, D. Hamilton, I. Swan, P. Mawby, T. Ueta, T. Nishijima, and K. Hamada, "A fast loss and temperature simulation method for power converters, Part I: Eletrothermal modeling and validation," *IEEE Trans. Power Electron.*, vol. 27, no. 1, pp. 248–257, Jan. 2012.
[6] C. Busca, R. Teodorescu, F. Blaabjerg, S. Munk-Nielsen, L. Helle, T. Abeyasekera, and P. Rodriguez, "An overview of the reliability prediction related aspects of high power IGBTs in wind power applications," *Microelectron. Reliab.*, vol. 51, no. 9–11, pp. 1903–1907, Sep./Nov. 2011.
[7] B. Lu and S. Sharma, "A literature review of IGBT fault diagnostic and protection methods for power inverters," *IEEE Trans. Ind. Appl.*, vol. 45, no. 5, pp. 1770–1777, Sep./Oct. 2009.
[8] D. Hirschmann, D. Tissen, S. Schroder, and R. W. De Doncker, "Reliability prediction for inverters in hybrid eletrical vehicles," *IEEE Trans. Power Electron.*, vol. 22, no. 6, pp. 2511–2517, Nov. 2007.
[9] N. Kaminski, "Load-cycle capability of HiPaks," ABB Appl. Note 5SYA 2043-01, Sep 2004.
[10] O. S. Senturk, L. Helle, S. Munk-Nielsen, P. Rodriguez, and R. Teodorescu, "Power capability investigation based on electrothermal models of press-pack IGBT three-level NPC and ANPC VSCs for multi-MW wind turbines," *IEEE Trans. Power Electron.*, vol. 27, no. 7, pp. 3195–3206, Jul. 2012.
[11] H. Wang, K. Ma, and F. Blaabjerg, "Design for reliability of power electronic systems," in *Proc. IEEE IECON*, 2012, pp. 33–44.
[12] Y. Avenas, L. Dupont, and Z. Khatir, "Temperature measurement of power semiconductor devices by thermo-sensitive electrical parameters—A review," *IEEE Trans. Power Electron.*, vol. 27, no. 6, pp. 3081–3092, Jun. 2012.
[13] W. Lixiang, J. McGuire, and R. A. Lukaszewski, "Analysis of PWM frequency control to improve the lifetime of PWM inverter," *IEEE Trans. Ind. Appl.*, vol. 47, no. 2, pp. 922–929, Mar./Apr. 2011.
[14] J. Jung and W. Hofmann, "Investigation of thermal stress in rotor of doubly-fed induction generator at synchronous operating point," in *Proc. IEMDC*, 2011, pp. 896–901.
[15] M. Musallam and C. M. Johnson, "Impact of different control schemes on the lifetime consumption of power electronic modules for variable speed wind turbines," in *Proc. EPE*, 2011, pp. 1–9.
[16] K. Ma, M. Liserre, and F. Blaabjerg, "Reactive power influence on the thermal cycling of multi-MW wind power inverter," *IEEE Trans. Ind. Appl.*, vol. 49, no. 2, pp. 922–930, Mar./Apr. 2013.
[17] B. C. Rabelo, W. Hofmann, J. L. da Silva, R. G. da Oliveria, and S. R. Silva, "Reactive power control design in doubly fed induction generators for wind turbines," *IEEE Trans. Ind. Electron.*, vol. 56, no. 10, pp. 4154–4162, Oct. 2009.
[18] K. Xie, Z. Jiang, and W. Li, "Effect of wind speed on wind turbine power converter reliability," *IEEE Trans. Energy Convers.*, vol. 27, no. 1, pp. 96–104, Mar. 2012.
[19] D. Zhou, F. Blaabjerg, M. Lau, and M. Tonnes, "Thermal analysis of multi-MW two-level wind power converter," *IEEE Trans. Ind. Electron.*, to be published.
[20] *User Manual of PLECS Blockset Version 3.2.7*, Plexim GmbH, Zurich, Switzerland, Mar. 2011.
[21] *Wind Turbines, Part 1: Design Requirements*, IEC 61400-1, 2005, 3rd ed.

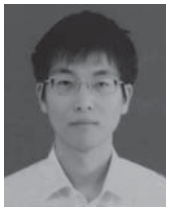

Dao Zhou (S'12) received the B.Sc. degree in electrical engineering from Beijing Jiaotong University, Beijing, China, in 2007 and the M.Sc. degree in power electronics from Zhejiang University, Hangzhou, China, in 2010. He is currently working toward the Ph.D. degree in the Department of Energy Technology, Aalborg University, Aalborg East, Denmark.

His research interests include two-level power electronics converters and their application in wind power generation systems.

Frede Blaabjerg (S'86–M'88–SM'97–F'03) received the Ph.D. degree from Aalborg University, Aalborg East, Denmark, in 1995.

From 1987 to 1988, he was with ABB-Scandia, Randers, Denmark. He is currently with the Department of Energy Technology, Aalborg University, where he became an Assistant Professor in 1992; an Associate Professor in 1996; a Full Professor in power electronics and drives in 1998; and was the Dean of the Faculty of Engineering, Science, and Medicine in 2006–2010. He was a Part-Time Research Leader in wind turbines with the Research Center Risoe. In 2009, he was a Visiting Professor with Zhejiang University, China. His research areas are in power electronics and applications, such as wind turbines, photovoltaic systems, and adjustable-speed drives.

Dr. Blaabjerg was a recipient of the 1995 Angelos Award for his contributions to modulation technique and the Annual Teacher Prize from Aalborg University. In 1998, he was a recipient of the Outstanding Young Power Electronics Engineer Award from the IEEE Power Electronics Society. He was a recipient of ten IEEE prize paper awards and another prize paper award at the International Conference on Power Electronics and Intelligent Control for Energy Conversation (PELINCEC 2005) in Poland. He was a recipient of the IEEE PELS Distinguished Service Award in 2009 and the 14th International Power Electronics and Motion Control Conference (EPE-PEMC 2010) Council Award. Since 2006, he has been the Editor-in-Chief of the IEEE TRANSACTIONS ON POWER ELECTRONICS. He was a Distinguished Lecturer of the IEEE Power Electronics Society from 2005 to 2007 and the IEEE Industry Applications Society from 2010 to 2011.

Mogens Lau received the M.Sc. degree in electrical engineering from Aalborg University, Aalborg East, Denmark, in 1999.

He was a Development Engineer, a Project Manager, and a Line Manager within power electronics at leading companies such as Danfoss, Grundfoss, and Vestas. He is currently the R&D Manager of Danfoss power stacks at Danfoss Silicon Power GmbH, Flensburg, Germany.

Michael Tonnes received the Ph.D. degree in electrical engineering from Aalborg University, Aalborg East, Denmark.

He is currently the Senior Director of Danfoss power stacks at Danfoss Silicon Power GmbH, Flensburg, Germany.

[A.3] D. Zhou, F. Blaabjerg, M. Lau, M. Tonnes, "Thermal cycling overview of multi-megawatt two-level wind power converter at full grid code operation," *IEEJ Journal of Industry Applications*, vol. 2, no. 4, pp. 173-182, Jul. 2013.

Paper

Thermal Cycling Overview of Multi-Megawatt Two-Level Wind Power Converter at Full Grid Code Operation

Dao Zhou*a) Non-member Frede Blaabjerg* Non-member
Mogens Lau** Non-member Michael Tonnes** Non-member

In this paper, two promising multi-megawatt wind turbines equipped with a doubly-fed induction generator-based partial-scale and a permanent magnet synchronous generator-based full-scale two-level power converter are designed and compared. Simulations of the two configurations with respect to loss distribution and junction temperature variation for the power device over the entire wind speed range are presented and analyzed both for normal operation and operation with various specific grid codes. It is concluded that in both partial-scale and full-scale power converters, the most thermal stressed power device in the generator-side converter will have a higher mean junction temperature and also junction temperature variation compared to the grid-side converter at the rated wind speed, and the thermal performance of the generator-side converter in the partial-scale power converter becomes crucial around the synchronous operating point and needs to be considered carefully. Moreover, reactive power injection directed by the grid codes will affect the thermal profile of the power semiconductors, especially at lower wind speeds.

Keywords: two-level wind power converter, power losses, thermal cycling, grid codes.

1. Introduction

Over last two decades, the wind power industry has expanded greatly. Meanwhile, the European countries commit themselves to realize 20% of the total electricity production through wind energy by 2020 [1]. In response to the steady growth of the wind power demand, several significant trends emerge: The power level of a single wind turbine is increasing from dozens of kW up to 10 MW in order to obtain lower cost per kWh as well as increasing the power density of the system. The location of wind farm is moving from onshore to offshore to reduce environment impact due to land limitation and richer wind energy resources. Moreover, due to the higher cost after failure, the lifetime of wind power generation system is in turn prolonged to 20-25 years, which requires for a more reliable and durable wind power system [2],[3].

Unfortunately, the investigation of wind turbines in north Germany in time period of 1993-2006 indicates that the increasing power rating of the wind turbine will have a higher risk of failure [4]. Considering the failure rate and down time distribution within a wind turbine system, as shown in Fig. 1, although the gearbox and generator have the longest down time, it is the power converters that in this survey dominate the failures [5]-[7].

Power semiconductors are nowadays playing a key role in power electronic system, and more and more efforts are devoted to the reliability characteristic. As different stressors distribution shown in Fig. 2, temperature cycling is regarded as having the most significant impact [8]. It is widely accepted that the thermal profile of the power semiconductor is an important indicator of lifetime [9]-[19] and it has an influence on the lifetime. The power cycle numbers to failure [20] is relevant to the junction temperature fluctuation ΔT_j as well as the mean junction temperature T_{jm} of power semiconductors, which is analyzed in Fig. 3.

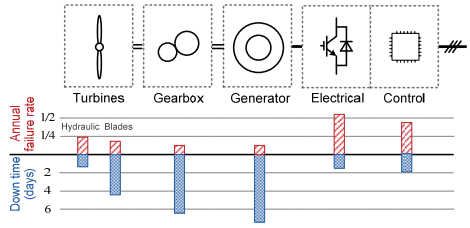

Fig. 1. Distribution of failure rate and down time for different parts in a wind turbine system [5].

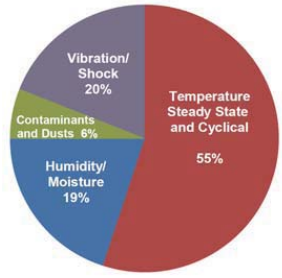

Fig. 2. Stressors distribution in a power electronics system [8].

The scope of this paper is to analyze and simulate the thermal cycling of multi-MW partial-scale and full-scale power converter through an electro-thermal approach, and compare the power semiconductor junction temperature mean value and variation in order to do an initial reliability assessment. First, the typical

a) Correspondence to: Dao Zhou. E-mail: zda@et.aau.dk
* Department of Energy Technology, Aalborg University, Pontoppindanstraede 101, Aalborg, DK-9220, Denmark
** Danfoss Silicon Power GmbH, Husumer Strasse 251, Flensburg, D-24941, Germany

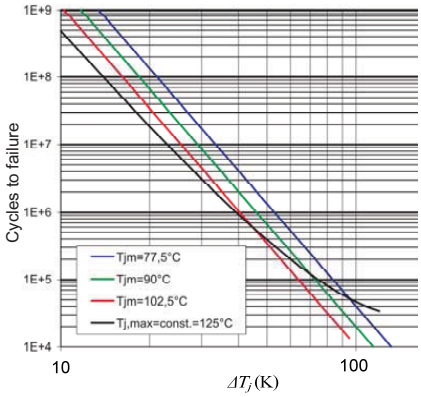

Fig. 3. Typical example of cycles to failure v.s. ΔT_j and T_{jm} in IGBT module [20].

configurations for variable speed wind turbine system will be introduced. Then, the basic design of the wind power converter as well as the relevant grid codes will be described. Finally, loss distribution and thermal analysis will be presented and compared in respect to the power device performance for the two different configurations.

2. Typical wind turbine configurations

Due to the extensive and well-established knowledge, as well as the simpler circuit structure and fewer components, the two-level back-to-back voltage source converter is the most attractive solution in the commercial market of wind turbines [3]. The utilization of the power electronics in wind turbine system can be further divided into two categories, namely: a wind turbine system with partial-scale power converter and a wind turbine system with full-scale power converter, which both are illustrated in Fig. 4.

2.1 Wind turbine system with partial-scale power converter A popular wind turbine configuration, normally based on the Doubly-Fed Induction Generator (DFIG), is to employ a power converter rated approximately 30% of the nominal generator power in order to handle around 30% of the slip power. The topology is shown in Fig. 4 (a).

The power converter is connected to the rotor through slip-rings and makes the rotor current as well as rotor speed under control, while the stator is linked to the grid without any decoupling. If the generator operates in super-synchronous mode, the electrical power is delivered through both the rotor and stator. If the generator is running sub-synchronously, the electrical power is only delivered into the grid from the stator.

The fraction of slip power through the converter makes this concept attractive from an economical point of view. However, the main drawbacks lie in the use of slip rings, and also an additional crowbar is needed to protect the generator-side converter under grid faults [21].

2.2 Wind turbine system with full-scale power converter As shown in Fig. 4 (b), another full-scale power converter configuration equipped with Synchronous Generator (SG) or Induction Generator (IG) is considered as a promising technology for multi-MW wind turbine system.

The generator stator winding is connected to the grid through a

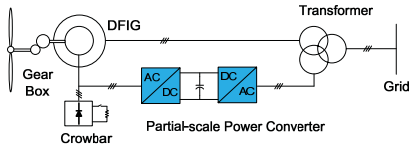

(a) Wind turbine system with partial-scale power converter

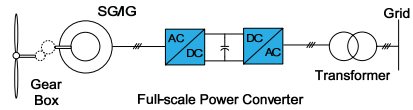

(b) Wind turbine system with full-scale power converter

Fig. 4. Typical configurations for wind turbine system.
DFIG: Doubly-Fed Induction Generator,
SG: Synchronous Generator, IG: Induction Generator.

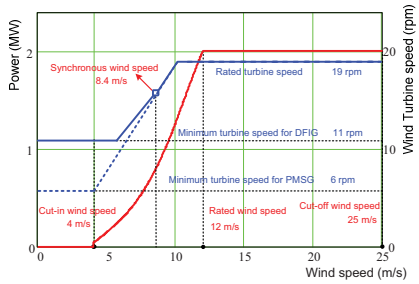

Fig. 5. Relationship between wind speed, turbine rotor speed and output power for the two different 2 MW systems.

full-scale power converter, which performs the reactive power compensation and also a smooth grid connection for the entire operating speed. Some variable speed wind turbine system may become gearless by introducing the multi-pole generator.

The elimination of the slip rings, simpler gearbox and full power controllability during the grid faults are the main advantages. However, in order to satisfy the power rating, the widely used approach nowadays is to implement several converter modules or power devices in parallel, which of course are challenging the complexity and reliability of the whole wind turbine system.

3. Operation of the wind turbine system

As shown in Fig. 4, the partial-scale power converter is normally connected to a DFIG, while the full-scale power converter equips a Permanent Magnet Synchronous Generator (PMSG). For simplicity, these two configurations are named the DFIG system and the PMSG system, respectively. In order to evaluate and compare the thermal performance for the above two systems, a mathematical model and a simulation platform will first be established.

3.1 Wind turbine model A 2 MW wind turbine system is used for the case studies. The energy transferred from the kinetic wind power to mechanical power can be expressed as [22]

$$P_G = \frac{1}{2}\rho\pi R^2 C_p(\lambda,\beta)v_w^3 \quad (1)$$

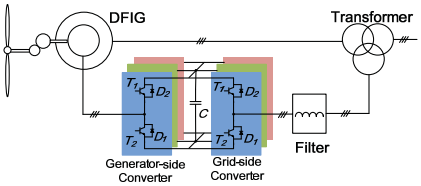

Fig. 6. Two-level back-to-back converter of a DFIG system.

Table 1. Parameters for 2 MW wind turbine (DFIG/PMSG)

Wind turbine parameters	
Rated power P_G [MW]	2
Blade radius R [m]	41.3
Cut-in wind speed v_{wcut_in} [m/s]	4
Rated wind speed v_{w_rate} [m/s]	12
Cut-off wind speed v_{wcut_off} [m/s]	25
Optimal tip speed ratio λ_{opt}	8.1
Maximum power coefficient C_{pmax}	0.383
Rated turbine speed n_{rot_rate} [rpm]	19
Minimum turbine speed n_{rot_min} [rpm]	11/6

where ρ denotes the air density (kg/m^3), R denotes the radius of turbine blade (m), and v_w denotes the wind speed (m/s). Depending on the blade pitch angle β and tip speed ratio λ, the power coefficient C_p represents the aerodynamical transfer efficiency, whose maximum value can be obtained under optimal tip speed ratio.

The parameters of the wind turbine are summarized in Table 1 [23]. Also, the relationship between the wind speed, turbine rotor speed and produced output power is shown in Fig. 5.

3.2 Power device selection in two different systems

Fig. 6 shows a DFIG system that consists of a generator, a partial-scale power converter, a filter and a transformer. Since the stator is directly connected to low-voltage grid, the DC-link voltage is set as low as possible seen from the power device lifetime point of view. Moreover, the filter inductance is designed to limit the current ripple within 0.25 p.u. [24].

Due to the DC capacitor decoupling, the power converter can be divided into the generator-side converter and the grid-side converter. Each of the control schemes can be designed separately.

For the generator-side converter, one of the control objectives focuses on transferring produced active power to the grid. The other purpose is to provide the excitation current for the DFIG. The grid-side converter will keep the DC-link voltage fixed and meet the reactive power demand according to the grid codes. Furthermore, Space-Vector Pulse Width Modulation (SVPWM) is used to generate the switching signals for the power semiconductors in both converters.

The typical PMSG system equipped with a full-scale power converter is shown in Fig. 7, which consists of a generator-side converter and a grid-side converter. Compared to the DFIG system, the current through both converters will be much higher under the same power rating of the wind turbines, which means the selection of power devices in the two configurations will be quite different

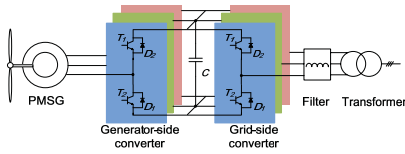

Fig. 7. Two-level back-to-back converter of a PMSG system.

Table 2. 2 MW generator data for DFIG and PMSG [26], [27]

	DFIG	PMSG
Rated wind speed v_{w_rate} [m/s]	12	
Rated turbine speed n_{rot_rate} [rpm]	19	
Number of pole pairs p	2	102
Gear ratio	94.7	/
Rated shaft speed n_s [rpm]	1800	19
Fundamental frequency at rated power f_e [Hz]	10	32.3
Stator leakage inductance L_{ls} [mH]	0.038	0.276
Magnetizing inductance L_m [mH]	2.91	
Rotor leakage inductance $L_{lr'}$ [mH]	0.064	/
Stator/rotor turns ratio n	0.369	/

in order to realize similar power device loading. Nevertheless, the design method of the DC-link voltage and the filter inductance in the PMSG system can be referred to as the DFIG system.

Considering the control scheme of the generator-side converter, the current through the stator of the generator should be controlled to adjust the rotating speed for maximum power. On the contrary, the reference of the d-axis current is set to zero for minimum power loss [25].

For the grid–side converter, the outer DC-link voltage and inner current closed loop have the ability to perform a fast active power control performance and to control the injected or absorbed reactive power, which are almost the same as the grid-side converter in the DFIG system. As mentioned before, the produced power through the power converter semiconductors is quite different in the DFIG and the PMSG system. Consequently, it is important to select suitable power devices for both systems in order to obtain a fair comparison for the thermal loading.

It is assumed that the two systems are using the wind turbine system as illustrated in Table 1. The typical parameters for the generators are summarized in Table 2. The PMSG system is a direct-drive for multi-pole structure, while for the DFIG system, a gearbox is still required as a multi-pole low-speed DFIG is not technically feasible.

The most important data for the two-level back-to-back converter are listed in Table 3. The switching frequency in both configurations and both converters are set to 2 kHz. The rated active power in the DFIG system is much smaller than the PMSG system, as only slip power flows through both converters. Based on the active power, together with the rated converter voltage output, the current in the converter needs to be calculated.

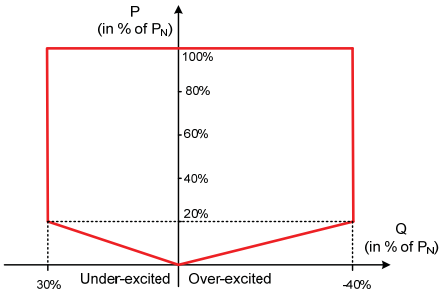

Fig. 8. Offshore wind turbine requirement of active and reactive power defined by E.on-Netz [30].

Table 3. Two-level back-to-back power converter data

	DFIG	PMSG
Rated active power P_C [kW]	400	2000
DC-link voltage U_{dc} [V_{dc}]	1050	
Switching frequency f_s [kHz]	2	
Grid-side Converter		
Rated voltage [V_{rms}]	704	704
Rated current [A_{rms}]	328	1641
Filter inductance [mH]	0.50	0.15
Power modules in each arm	1 kA/1.7 kV, single	1 kA/1.7 kV, 4 in parallel
Generator-side Converter		
Rated voltage [V_{rms}]	374	554
Rated current [A_{rms}]	618	2085
Power modules in each arm	1 kA/1.7 kV, 2 in parallel	1 kA/1.7 kV, 4 in parallel

It is noted that in the DFIG system the rated current in the more unequal, while the situation is more equal in the PMSG system.

Furthermore, a parallel structure of multiple power components is a more used solution for multi-MW wind turbines today. Consequently, a common 1.7kV/1kA power device is selected. A single module in the grid-side converter and two paralleled modules in the generator-side converter are the solutions for the DFIG system, and four paralleled modules in both converters for the PMSG system are selected.

3.3 Grid codes Power system operators are challenged by the increasing wind power penetration level to maintain the stability and reliability of the power system. Consequently, grid codes are issued and updated by transmission system operators of the different countries [28].

Reactive power control in the power system is considered as an important aspect in normal operation. As a large number of wind farms are continuously being installed in remote area of the power transmission system, the weak connections demand the ability of reactive power supply in order to support the voltage regulation [29].

For instance, the German code has imposed additional specifications concerning the minimum active/reactive power requirement for offshore wind power application as shown in Fig. 8, within a range of +/-5% around nominal voltage.

4. Power loss distribution of the systems

4.1 Power loss model The power losses in the back-to-back converter consist of the generator-side converter loss and the grid-side converter loss. They are mainly divided into the switching losses and the conduction losses [31]. Since no unbalance is taken into account in this paper, it is possible to consider the behavior of half of one leg in both power converters due to the symmetrical characteristic and the fixed DC-link voltage.

No matter what the current direction is, the switching losses in each switching period always contain one turn-on loss E_{on}, one turn-off loss E_{off} in the IGBT, and one diode recovery loss E_{rr}. E_{on}, E_{off} and E_{rr} are almost proportional to the DC-link voltage, thus the formula for switching loss in each power device P_{sw} can be expressed as:

$$P_{sw} = f_e \frac{U_{dc}}{U_{dc}^*} \sum_{n=1}^{N} \left[E_{on}(|i_a(n)|) + E_{off}(|i_a(n)|) + E_{rr}(|i_a(n)|) \right] \quad (2)$$

where f_e denotes the fundamental frequency of output current, U_{dc}^* denotes the tested DC-link voltage, N denotes the total cycle numbers in each fundamental frequency, E_{on}, E_{off} and E_{rr} denote the switching loss energy in each switching period when the switching current equals to the phase current $|i_a(n)|$. E_{on}, E_{off}, E_{rr} and U_{dc}^* can typically be directly acquired from the power device datasheets.

The conduction losses mainly lie in the IGBT and the freewheeling diode. The conduction power loss in each power device P_{con} can be calculated as:

$$P_{con} = f_e \sum_{n=1}^{N} \left[v_{CE}(|i_a(n)|) \cdot |i_a(n)| \cdot T_1(n) + v_F(|i_a(n)|) \cdot |i_a(n)| \cdot (T_s - T_1(n)) \right] \quad (3)$$

where v_{CE} denotes the collector-emitter saturation voltage drop of the IGBT, v_F denotes the forward on-state voltage drop of the freewheeling diode, $T_1(n)$ denotes the conduction time of the IGBT during n^{th} switching period, which in line with the modulation strategies and the phase angle between phase current and phase voltage. T_s denotes the switching period.

4.2 Power loss distribution under normal operation Simulation of the power loss can be realized based on PLECS block in Simulink [32]. The simulation settings correspond to the design parameters shown in Table 2 and Table 3. In addition, the simulation circuit runs at rated wind speed under normal grid condition and the power factor is set to unity. Fig. 9 and Fig. 10 indicate the loss distribution of each power semiconductor under the DFIG and the PMSG systems in terms of the generator-side converter and the grid-side converter, respectively. The name of the power semiconductors can be found in Fig. 6 and Fig. 7.

Comparing the back-to-back power converter in both systems, the power losses dissipated in the generator-side converter are more equal. It is because the turn-on and turn-off loss of IGBT are higher than the recovery loss of freewheeling diode for the same current, from (2) the switching loss in the diode is always smaller. The conduction loss is mainly related to the power direction. At rated active power, the generator-side converter is operating as a rectifier, and therefore more conduction losses are seen in the

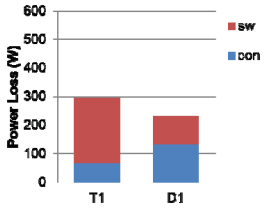

(a) DFIG system

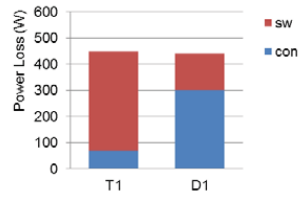

(b) PMSG system

Fig. 9. Loss distribution in generator-side converter for each power module (wind speed: 12 m/s).
Note: sw and con are switching losses and conduction losses, respectively

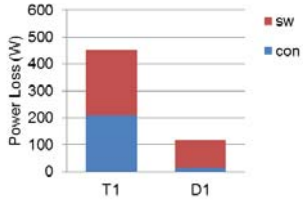

(a) DFIG system

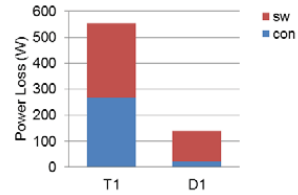

(b) PMSG system

Fig. 10. Loss distribution in grid-side converter for each power module (wind speed: 12 m/s).
Note: sw and con are switching losses and conduction losses, respectively

freewheeling diode. On the contrary, the grid-side converter is operating as an inverter, where most of the conduction losses are dissipated in the IGBT, which results in an unequal loading.

For the DFIG and the PMSG systems, the power loss dissipated in the PMSG system is larger. The reason is that as summarized in Table 3, the current through each power semiconductor is higher.

In order to investigate the loss behavior in different operation modes, several wind speeds are chosen with slip values from -0.3 to 0.2 in the DFIG system and the parameters are shown in Table 4. It is noted that the wind speed at 8.4 m/s is regarded as the synchronous operating point as it is seen in Fig. 5 and also in Table 2.

The power loss in the generator-side converter at different wind speed is shown in Fig. 11. In order to avoid the extremely unbalanced power device loading at synchronous operating point, a small turbine speed hysteresis is introduced for minimum rotor frequency 1 Hz in the DFIG system [33]. The loss distribution of the IGBT and diode are illustrated in Fig. 11 (a). In the super-synchronous mode, the power loss increases with larger wind speed, and the growth rate is relatively slower since the larger slip, which will decrease the converter current. Regarding the conduction loss, it is noted that the conduction loss in the diode is dominating. However, in the sub-synchronous mode, the conduction loss in the IGBT is dominating. For the PMSG system, as shown in Fig. 11 (b), the power loss increases with the wind speed consecutively.

The power loss in the grid-side converter at different wind speed is shown in Fig. 12. For the DFIG system, the lowest power loss appears in the synchronous operating point due to the fact that no active power flow exist and only the switching ripple current affects, while the highest one appears at rated wind power. Furthermore, the IGBT suffers more loss in super-synchronous mode and the diode suffers more loss in sub-synchronous mode.

Table 4. Parameters for converters at different wind speed (DFIG/PMSG)

Wind speed [m/s]	Generator power [MW]	Wind turbine speed [rpm]	Slip	Fundamental frequency of output current [Hz]
5.9	0.26	11/10.1	0.3/0	15/17.2
6.8	0.39	12.7/12.0	0.2/0	10/20.4
7.6	0.55	14.2/13.7	0.1/0	5/23.3
8.4	0.74	15.8/15.4	0.02/0	0/26.2
9.2	0.98	17.2/17.1	-0.1/0	5/29.1
10.1	1.29	19/19	-0.2/0	10/32.3
12	2	19/19	-0.2/0	10/32.3
25	2	19/19	-0.2/0	10/32.3

For the PMSG system, the power loss increases with the wind speed consecutively.

4.3 Power loss distribution considering grid codes If the German grid codes as shown in Fig. 8 are taken further into account, additional power loss will be introduced by reactive power injection. In the DFIG system, because of the winding ratio of the induction generator, higher current amplitude and larger power angle shift will be induced in the grid-side converter than in the generator-side converter, which means the reactive power compensated from the generator-side converter is a better choice [34]. For the PMSG system, the reactive power compensation can only be injected into the grid-side converter.

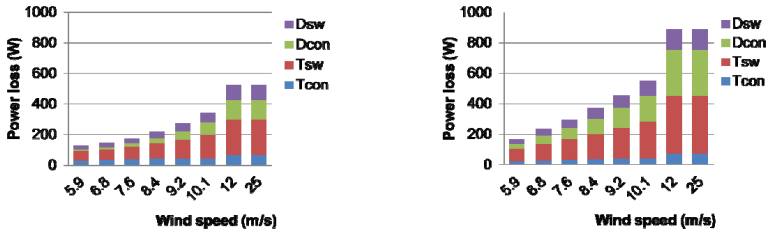

(a) DFIG system (b) PMSG system

Fig. 11. Power loss of each power module vs. wind speed (generator-side converter).

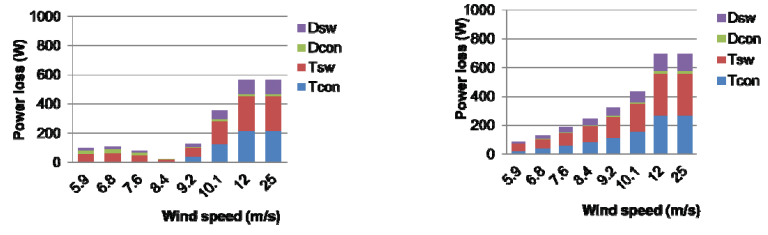

(a) DFIG system (b) PMSG system

Fig. 12. Power loss of each power module v.s. wind speed (grid-side converter).

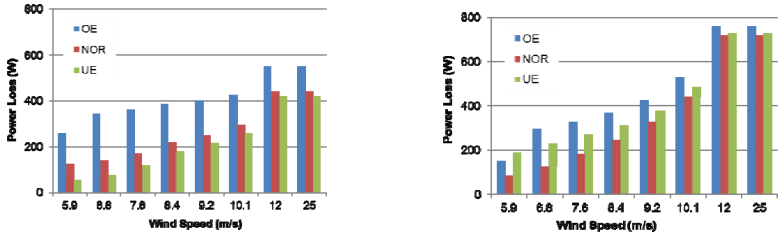

(a) Generator-side converter in the DFIG system (b) Grid-side converter in the PMSG system

Fig. 13. Power loss profile of different system considering grid codes.
Note: OE, NOR and UE indicate over-excited, normal and under-excited reactive power.

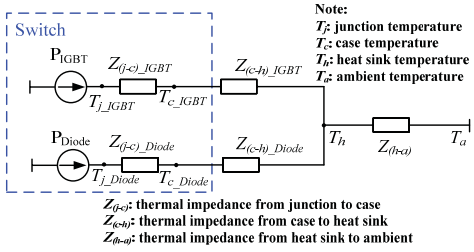

Fig. 14. Thermal model of the power module.

Therefore, the power loss profile is illustrated in Fig. 13 in terms of under-excited reactive power, normal operation and over-excited reactive power. For the DFIG system, it is noted that, due to the excitation energy for the induction generator is supplied by the grid code, the under-excited reactive power will relieve the power loss in the power device, while over-excited reactive power will make the DFIG system more stressed. For the PMSG system,

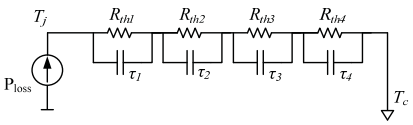

Fig. 15. RC Foster network of thermal impedance from junction to case of the power semiconductor devices.

no excitation energy is required for the PMSG. Consequently, both the over-excited and under-excited reactive power will increase the power loss.

5. Thermal analysis of the systems

5.1 Thermal model As the thermal performance of the power devices are closely related to the reliability and the cost of the whole power converter system, a comparison of the thermal cycling of the DFIG and the PMSG systems will be investigated.

In order to describe the thermal behavior of the power semiconductors, an appropriate thermal model needs to be

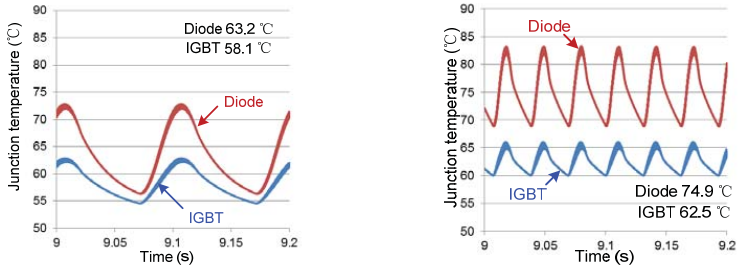

(a) DFIG system (b) PMSG system

Fig. 16. Junction temperature in the generator-side converter for the two wind turbine systems (Wind speed: 12 m/s).

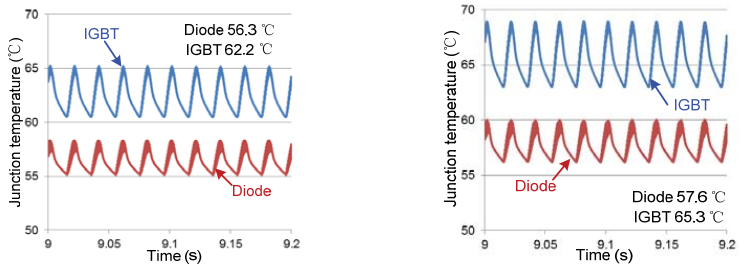

(a) DFIG system (b) PMSG system

Fig. 17. Junction temperature in the grid-side converter for the two wind turbine systems (Wind speed: 12 m/s).

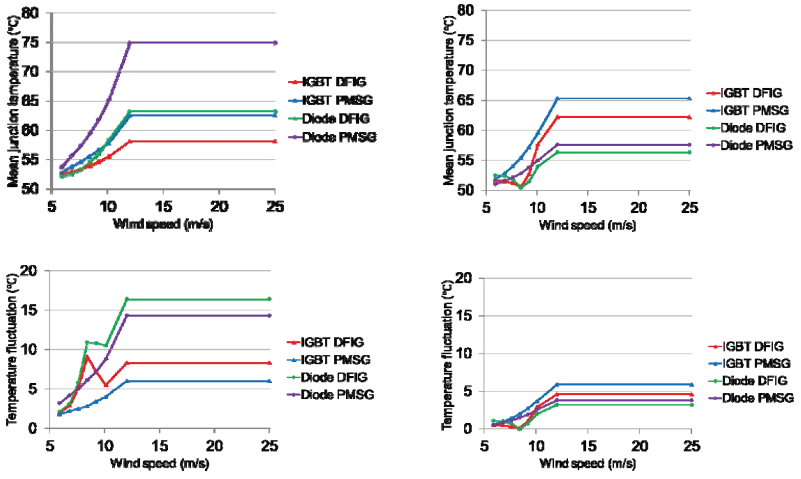

(a) Generator-side converter (b) Grid-side converter

Fig. 18. Mean junction temperature and temperature fluctuation in the chip vs. wind speed for both systems (unity power factor).

developed. The thermal models of single IGBT and the freewheeling diode are shown in Fig. 14, and share the same design idea as discussed in [35], [36], the thermal resistance R_{th} will determine the steady-state mean junction temperature, and along with the thermal capacitance (function of time constant τ) will determine the junction temperature fluctuation.

The thermal impedance from the junction to case $Z_{(j\text{-}c)}$ is modeled as a four-layer Foster RC network as depicted in Fig. 15, whose parameters are collected from the datasheet of the power device. The case-to-heatsink thermal impedance is modeled as a simple thermal resistor, neglecting the much higher thermal capacitance due to the less significant dynamic behavior of the junction temperature and also obtain a faster thermal simulation. Meanwhile the heatsink-to-ambient resistance is considered small

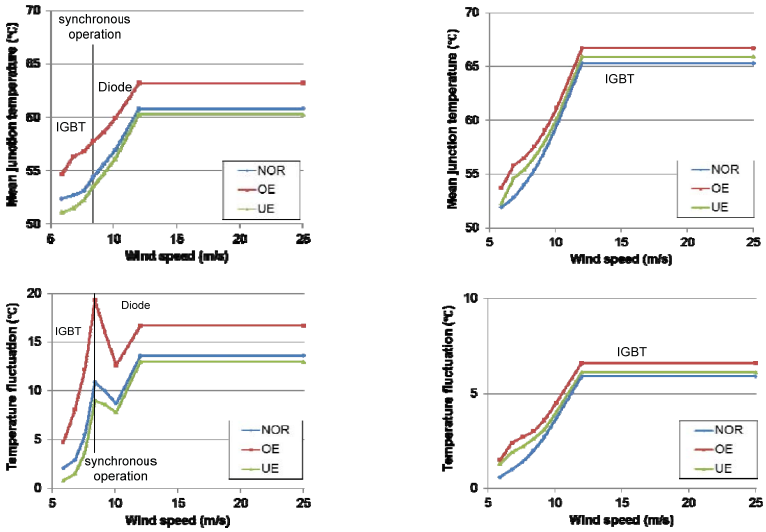

(a) Generator-side converter in the DFIG system

(b) Grid-side converter in the PMSG system

Fig. 19. Thermal profile of the most stressed power semiconductor in the two different system considering grid codes.
Note: NOR, OE and UE indicate normal, over-excited and under-excited reactive power, respectively.

compared to the thermal resistance in the MW power converter. Furthermore, the ambient temperature is set to 50 °C.

5.2 Thermal cycling under normal operation The simulation results of the junction temperature in each power semiconductor of the generator-side converter under the DFIG and the PMSG systems are shown in Fig. 16 in which the converters run at rated power and in steady-state operation. It can be seen that the mean temperature of the diode is higher than the IGBT's in both the DFIG and the PMSG systems, and the thermal performance of the PMSG system shows more unequal distribution, where the difference of junction temperature between the IGBT and freewheeling diode is 12.4 °C compared to 5.1 °C in DFIG system. For the junction temperature of the grid-side converter, the thermal results of the DFIG and the PMSG systems are shown in Fig. 17 (a) and Fig. 17 (b), respectively. It can be seen that the hottest power semiconductor device turns out to be the IGBT. Moreover, the junction temperature variation between the IGBT and the diode show more equal distribution.

A further comparison of thermal behavior for both systems with different wind speed is shown in Fig. 18. For the generator-side converter, it can be seen that, in the PMSG system the mean junction temperature and the temperature fluctuation of the power semiconductors above rated wind speed are the highest all during the whole operation range of the wind. The hottest device is the diode in the whole wind speed range. In the DFIG system, the hottest device changes from the IGBT in the sub-synchronous mode to the diode in the super-synchronous mode. Moreover, the temperature fluctuation of the power semiconductors becomes crucial around synchronous operating point. Although the mean junction temperature is all higher in the PMSG system except for the region around synchronous operation as shown in upper Fig. 18 (a), at rated wind speed the temperature fluctuation in the DFIG system is even larger due to less frequency power cycling as shown in lower Fig. 18 (a).

5.3 Thermal cycling considering grid codes As the most stressed power semiconductor decides the reliability and lifetime in a power module, it is necessary to extract the thermal excursion of the most serious loading chips in both the DFIG and PMSG system considering German grid codes shown in Fig. 8.

For the generator-side converter of the DFIG system as shown in Fig 19 (a), the most stressed power semiconductor changes from the IGBT in sub-synchronous mode to the freewheeling diode in super-synchronous mode. It is also noted that the over-excited reactive power requirement will impose thermal stress to the power semiconductor especially at synchronous operating point. For the grid-side converter of the PMSG system, the IGBT is the most stressed power semiconductor during the whole operating wind speed. The reactive power injection will induce higher mean junction temperature and junction temperature fluctuation. Moreover, the situation will become worse at lower wind speed due to the lower output active power but the same amount of the reactive power is demanded.

6. Conclusion

In this paper, platforms for the popular 2 MW two-level wind turbine configurations (i.e. partial-scale and full-scale power converter) are established in the PLECS/Simulink to simulate the power losses and the thermal load cycling. A comparison of the loss distribution as well as thermal loading in the DFIG and the PMSG systems are investigated when considering the grid codes.

For the partial-scale power converter configuration, the thermal behavior between the generator-side converter and the grid-side converter are quite different. The operation area above the rated wind speed range of the grid-side converter is significant from the thermal stress point of view, while the generator-side converter not only concerns the above mentioned case, but also the wind speed

range around the synchronous speed operation.

For the full-scale power converter configuration, whatever generator-side converter or grid-side converter, the crucial thermal stress lies in the operation area above the rated wind speed range.

Moreover, comparing the most stressed semiconductor device, the generator-side converter is the most critical part for thermal stress of the two-level back-to-back converter.

Furthermore, the reactive power support to the grid will affect the power loss profile and thermal profile of the power semiconductors, especially at lower wind speed.

References

(1) Z. Chen, J.M. Guerrero and F. Blaabjerg, "A review of the state of the art of power electronics for wind turbines," *IEEE Trans. Power Electronics*, vol.24, no.8, pp.1859-1875 (2009)

(2) F. Blaabjerg, Z. Chen and S.B. Kjaer, "Power electronics as efficient interface in dispersed power generation systems," IEEE Trans. Power Electronics, vol.19, no.5, pp. 1184- 1194 (2004)

(3) M. Liserre, R. Cárdenas, M. Molinas and J. Rodriguez, "Overview of multi-MW wind turbines and wind parks," IEEE Trans. Industrial Electronics, vol.58, no.4, pp.1081-1095 (2011)

(4) S. Faulstich, P. Lyding, B. Hahn and P. J. Tavner "Reliability of offshore turbines- identifying the risk by onshore experience," in Proc. of European Offshore Wind Energy Conference and Exposition (2009)

(5) B. Hahn, M. Durstewitz and K. Rohrig "Reliability of wind turbines - Experience of 15 years with 1500 WTs," Wind Energy: Proceedings of the Euromech Colloquium, pp. 329-332, Springer-Verlag, Berlin.

(6) R. Johan and B. L. Margareta, "Survey of failures in wind power systems with focus on Swedish wind power plants during 1997-2005," IEEE Trans. Energy Conversion, vol. 22, no. 1, pp. 167-173 (2007)

(7) P. J. Tavner, J. Xiang and F. Spinato, "Reliability analysis for wind turbines," Wind Energy, vol. 10, no.1, pp. 1-18 (2007)

(8) ZVEL, Handbook for robustness validation of automotive electrical/electronic modules, Jun. (2008)

(9) Y. Song and B. Wang, "Survey on reliability of power electronic systems," IEEE trans. Power Electronics, vol.28, no.1, pp 591-604 (2013)

(10) A. Bryant, N. Parker-Allotey, D. Hamilton, I. Swan, P.Mawby, T. Ueta, T. Nishijima and K. Hamada, "A fast loss and temperature simulation method for power converters, part I: eletrothermal modeling and validation", IEEE trans. Power Electronics, vol. 27, no.1, pp 248-257 (2012)

(11) C. Busca, R. Teodorescu, F. Blaabjerg, S. Munk-Nielsen, L. Helle, T. Abeyasekera and P. Rodriguez, "An overview of the reliability prediction related aspects of high power IGBTs in wind power applications," Microelectronics Reliability, vol. 51, no. 9-11, pp. 1903-1907 (2011)

(12) B. Lu and S. Sharma, "A literature review of IGBT fault diagnostic and protection methods for power inverters," IEEE trans. Industry Applications, vol. 45, no.5, pp 1770-1777 (2009)

(13) D. Hirschmann, D. Tissen, S. Schroder and R.W. De Doncker, "Reliability prediction for inverters in hybrid eletrical vehicles," IEEE trans. Power Electronics, vol. 22, no. 6, pp 2511-2517 (2007)

(14) N. Kaminski, "Load-cycle capability of HiPaks," ABB Application Note 5SYA 2043-01 (2004)

(15) O.S. Senturk, L. Helle, S. Munk-Nielsen, P. Rodriguez and R. Teodorescu, "Power capability investigation based on electrothermal models of press-pack IGBT three-level NPC and ANPC VSCs for multi-MW wind turbines," IEEE Trans. on Power Electronics, vol. 27, no. 7, pp. 3195-3206, (2012)

(16) H. Wang, K. Ma and F. Blaabjerg, "Design for reliability of power electronic systems," in Proc. of IECON 2012, pp.33-44 (2012)

(17) F. Blaabjerg, K. Ma and D. Zhou, "Power Electronics and Reliability in Renewable Energy Systems," in Proc. of ISIE 2012, pp.20-30 (2012)

(18) Y. Avenas, L. Dupont and Z. Khatir, "Temperature measurement of power semiconductor devices by thermo-sensitive electrical parameters – a review", IEEE trans. Power Electronics, vol. 27, no.6, pp 3081-3092 (2012)

(19) W. Lixiang, J. McGuire and R.A. Lukaszewski, "Analysis of PWM frequency control to improve the lifetime of PWM inverter," IEEE Trans. Industry Applications, vol. 47, no. 2, pp. 922-929 (2011)

(20) A. Wintrich, U. Nicolai and T. Reimann, "Semikron Application Manual," pp. 128 (2011)

(21) F. Blaabjerg, M. Liserre and K. Ma, "Power electronics converters for wind turbine systems," IEEE Trans. Industry Applications, vol.48, no.2, pp.708-719 (2012)

(22) M. Chinchilla, S. Arnaltes, J.C. Burgos, "Control of permanent-magnet generators applied to variable-speed wind-energy systems connected to the grid," IEEE Trans. Energy Conversion, vol.21, no.1, pp. 130-135 (2006)

(23) "Vestas". [Online]. Available: http://www.vestas.com/.

(24) A.A. Rockhill, M. Liserre, R. Teodorescu and P. Rodriguez, "Grid-filter design for a multi-megawatt medium-voltage voltage-source inverter," IEEE Trans. on Industrial Electronics, vol.58, no.4, pp.1205-1217 (2011)

(25) M. Chinchilla, S. Arnaltes and J.C. Burgos, "Control of permanent-magnet generators applied to variable-speed wind-energy systems connected to the grid," IEEE Trans. Energy Conversion, vol.21, no.1, pp. 130-135 (2006)

(26) C. Liu, F. Blaabjerg, W. Chen and D. Xu, "Stator current harmonic control with resonant controller for doubly fed induction generator," IEEE Trans. Power Electronics, vol.27, no.7, pp.3207-3220 (2012)

(27) H. Li, Z. Chen and H. Polinder, "Optimization of multibrid permanent-magnet wind generator systems," IEEE Trans. Energy Conversion, vol.24, no.1, pp.82-92 (2009)

(28) M. Altin, O. Goksu, R. Teodorescu, P. Rodriguez, B. Bak-Jensen and L. Helle, "Overview of recent grid codes for wind power integration," in Proc. of OPTIM'2010, pp.1152-1160 (2010)

(29) M. Tsili and S. Papathanassiou, "A review of grid code technical requirements for wind farms," IET Renewable Power Generation, vol.3, no.3, pp.308-332 (2009)

(30) E.ON-Netz. Requirements for offshore grid connections, (2008)

(31) B. Backlund, R. Schnell, U. Schlapbach, R. Fischer and E. Tsyplakov, "Applying IGBTs," (2011)

(32) User manual of PLECS blockset version 3.2.7 March 2011. (Available: http://www.plexim.com/files/plecsmanual.pdf)

(33) J. Jung, W. Hofmann, "Investigation of thermal stress in rotor of doubly-fed induction generator at synchronous operating point," in Proc. of IEMDC 2011, pp. 896-901 (2011)

(34) S. Engelhardt, I. Erlich, C. Feltes, J. Kretschmann and F. Shewarega, "Ractive power capability in wind turbines based on doubly fed induction generators," IEEE Trans. Energy Conversion, vol.26, no.1, pp.364-372 (2011)

(35) K. Ma and F. Blaabjerg, "Multilevel converters for 10 MW wind turbines," in Proc. of EPE 2011, pp.1-10 (2011)

(36) D. Zhou, F. Blaabjerg, M. Lau and M. Tonnes, "Thermal analysis of multi-MW two-level wind power converter," in Proc. of IECON 2012, pp.5862-5868 (2012)

Dao Zhou (Non-member) received the B.Sc. in electrical engineering from Beijing Jiaotong University, Beijing, China, in 2007, and the M. Sc. in power electronics from Zhejiang University, Hangzhou, China, in 2010. From 2012, he is pursuing the Ph.D degree in the Department of Energy Technology, Aalborg University, Aalborg, Denmark.

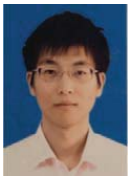

His research interests include two-level power electronics converters and their application in wind power generation systems.

Frede Blaabjerg (Non-member) received the M.Sc.EE. and Ph.D degrees from Aalborg University, Aalborg East, Denmark in 1987 and 1995, respectively.

He was employed at ABB-Scandia, Randers, from 1987-1988. During 1988-1992 he was PhD. student at Aalborg University, Denmark, became Assistant Professor in 1992, Associate Professor in 1996 and full professor in power electronics and drives in 1998. He has been part-time research leader at Research Center Risoe in wind turbines. In 2006-2010 he was dean of the faculty of Engineering, Science and Medicine and became visiting professor at Zhejiang University, China in 2009. His research areas are in power electronics and its applications like wind turbines, PV systems and adjustable speed drives. Since 2006 he has been Editor in Chief of the IEEE Transactions on Power Electronics. He was Distingueshed lecturer for the IEEE Power Electronics Society 2005-2007 and for IEEE Industry Applications Society from 2010-2011.

Dr. Blaabjerg received the 1995 Angelos Award for his contribution in modulation technique and the Annual Teacher prize at Aalborg University.

In 1998 he received the Outstanding Young Power Electronics Engineer Award from the IEEE Power Electronics Society. He has received ten IEEE Prize paper awards and another prize paper award at PELINCEC Poland 2005. He received the IEEE PELS Distingueshed Service Award in 2009 and the EPE-PEMC 2010 Council award.

Mogens Lau (Non-member) received the M.Sc. in Electrical engineering from Aalborg University, Aalborg, Denmark, in 1999. He worked as development engineer, project manager and line manager within power electronics at leading companies like Danfoss, Grundfoss and Vestas. Currently he is the R&D manager of Danfoss power stacks at Danfoss Silicon Power GmbH.

Michael Tonnes (Non-member) received the Ph.D in electrical engineering from Aalborg University, Aalborg, Denmark. Currently he is the senior director of Danfoss power stacks at Danfoss Silicon Power GmbH.

[A.4] D. Zhou, F. Blaabjerg, M. Lau, M. Tonnes, "Thermal profile analysis of doubly-fed induction generator based wind power converter with air and liquid cooling methods," *in Proc. of EPE 13*, pp.1-10, 2013.

Thermal Profile Analysis of Doubly-Fed Induction Generator Based Wind Power Converter with Air and Liquid Cooling Methods

Dao Zhou[1], Frede Blaabjerg[1], Mogens Lau[2], Michael Tonnes[2]
[1] Aalborg University
Pontoppidanstraede 101, DK-9220
Aalborg, Denmark
[2] Danfoss Silicon Power GmbH
Husumer Strasse 251, D-24941
Flensburg, Germany
E-Mail: zda@et.aau.dk

Acknowledgements

The author would like to thank Klaus Olesen from Danfoss power electronics for his kind help on the liquid cooling technique.

Keywords

«Wind power converter», «Thermal profile», «Air cooling», «Liquid cooling».

Abstract

Today, wind power generation system keeps on moving from onshore to offshore and also upscaling in size. As the lifetime of the wind power converter is prolonged to 20-25 years, this paper will investigate and compare different cooling methods for power modules – the air cooling and the liquid cooling seen from a thermal profile assessment point of view. Firstly, an analytical approach from loss profile to thermal profile for the power semiconductor is proposed and verified in a 2 MW Doubly-Fed Induction Generator (DFIG) based wind turbine system. Then, the typical air cooling and liquid cooling in wind power converter are analyzed and compared in terms of the mean junction temperature and the junction temperature fluctuation. It is concluded that the liquid cooling approach has a similar junction temperature fluctuation but gives a lower mean junction temperature than the air cooling approach.

Introduction

By 2020, the European Union is ambitious to meet its climate and energy target, known as the "20-20-20" strategy [1]. The utilization of power electronic converter is nowadays playing a key role to fulfill these climate and energy targets in renewable energy conversion and industrial application (e.g. wind and solar power generation, motor drives, rail traction and hybrid-electric vehicles). Many of these converters have highly variable loads [2], [3], and more and more efforts are devoted into the reliability characteristic, in which the thermal cycling is regarded as the most significant impact among the different stressors (vibration, contaminants, humidity, etc.). It is widely accepted that the thermal profile of power semiconductor is an important indicator of the lifetime and it has an influence on the reliable operation. The power cycle number to failure is quite relevant to the junction temperature fluctuation as well as the mean junction temperature [4].

The power density is steadily being increased [5], [6] – although it has benefits in an improvement of functions, an enhanced power range and a reduced impact on volume and cost, it demand extra amount of the heat-sink for the power converter in order to extract the same dissipating energy from a smaller heat-sink size, which is potentially increasing the severity of the thermal cycling and reducing the device reliability [7]. In a full-scale power converter, the typical amount of heat that has to be transported away from the power modules may be from 50 kW to 100 kW for a 2 MW wind turbine

[8]. Because the cooling solutions take up considerable space available in a typical wind turbine nacelle, it is interesting to investigate and analyze the different cooling system, where the forced air cooling and the liquid cooling cover 95% of all power module application.

The scope of this paper is to analyze and compare the thermal profile of power modules for conditions of air cooling and liquid cooling. Firstly, an analytical approach from loss profile to thermal profile for power semiconductor is proposed and verified in a multi-MW Doubly-Fed Induction Generator (DFIG) based wind turbine system. Then, the typical approaches for air cooling and liquid cooling in wind power converter are evaluated and compared in terms of the mean junction temperature and the junction temperature swing.

Analytical approach to evaluate thermal profile

According to the basic layout of the power semiconductor module, the one-dimension thermal model is given in forms of typical power module configurations. Then, an analytical approach to evaluate the thermal profile from the power loss profile is proposed.

Power module assemblies

The layout of a typical power semiconductor module is depicted in Fig. 1. A number of power semiconductor chips – IGBTs and diodes are soldered onto the ceramic based substrates like DBC (Direct Bond Copper), which acts as an electric isolator. The DBC substrate can be either soldered onto a baseplate, or the bottom copper layer is directly mounted to a heat-sink with Thermal Interface Material (TIM) in between. The electrical connections between chips and conductor tracks on the DBC are normally realized by thick wire-bonding of pure aluminum.

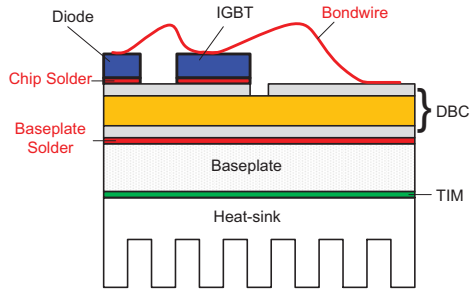

Fig. 1: Basic structure of a power semiconductor module.

Thermal model

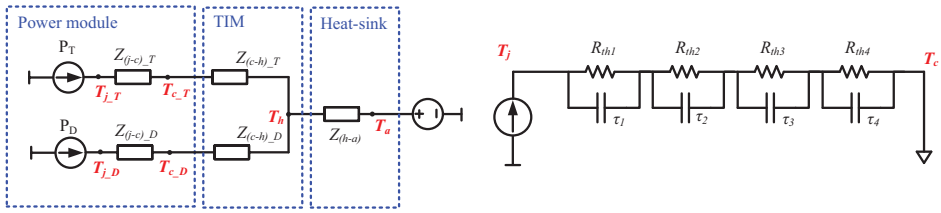

(a) (b)

Fig. 2: Thermal model of the power devices. (a) Thermal model of single IGBT and diode (from junction to ambient). (b) Equivalent Foster RC thermal network (from junction to case).

The thermal model of power devices, including the IGBT and the freewheeling diode are shown in Fig. 2(a) in forms of the power module, the thermal grease and the heat-sink. The electrical analogies representing thermal variable are used [9]-[12], in which the power dissipation in the IGBT and the

diode are expressed as the current source, the voltage source stand for the constant temperature levels, and RC elements are used to signify the thermal impedance.

The thermal impedance from junction to case is modeled as a four-layer Foster RC network as shown in Fig. 2(b), whose values are normally provided by the manufacturer's datasheet. Meanwhile, the ambient temperature is set to 50 ºC as an indication of the worst case.

Analytical method for thermal profile

A typical thermal profile of the power semiconductor in a wind power converter contains large thermal cycles and small thermal cycles, which are driven by wind turbulence and bidirectional current within a fundamental frequency, respectively. At first glance, the lifetime and reliability issue of the wind energy generation system induced by wind turbulence is more crucial due to the larger junction temperature fluctuation of the power semiconductor. However, it is still essential to look into the influence of small thermal cycles due to their greater order of magnitude, because the loading current normally changes in several seconds, while the fundamental period of current is actually from dozens of milliseconds to hundreds of milliseconds.

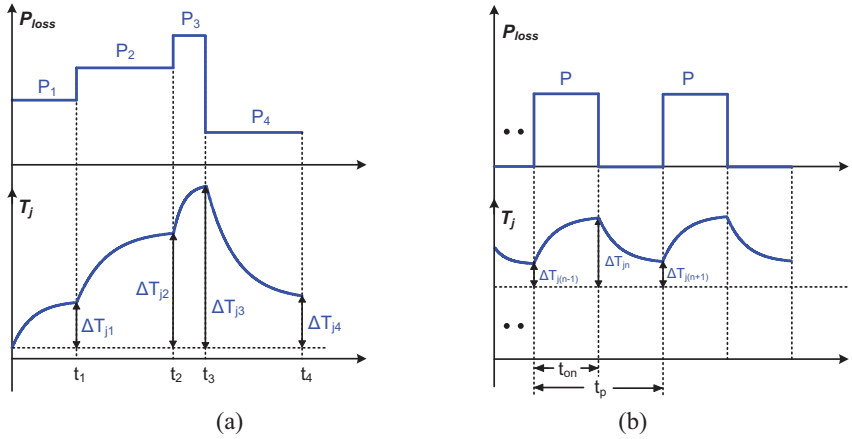

Fig. 3: Power loss profile and junction temperature profile against time. (a) Step pulse of power dissipation. (b) Periodical pulse of power dissipation.

Fig. 3(a) shows the step pulse of power loss, and according to the thermal model in Fig. 2(b), the junction temperature fluctuation ΔT_{jn} during n^{th} power loss pulse can be deduced to,

$$\Delta T_{jn} = \Delta T_{j(n-1)} \sum_{i=1}^{4} e^{-\frac{t_n - t_{n-1}}{\tau_i}} + P_n \sum_{i=1}^{4} R_{thi} (1 - e^{-\frac{t_n - t_{n-1}}{\tau_i}}) \quad (1)$$

where the first item denotes the zero-input response of the previous junction temperature fluctuation $\Delta T_{j(n-1)}$ at the moment t_{n-1}, and the second term denotes the zero-state response of the power loss P_n at the moment t_n. R_{thi} and τ_i indicate i^{th} Foster structure thermal resistance and time constant, which are both consisted with the value shown in Fig. 2(b). According to equation (1), the junction temperature swing can be easily inferred from power loss profile in time domain.

Fig. 3(b) shows the case of thermal profile in the condition of periodical pulse of power dissipation. The junction temperature fluctuation at moment t_{n-1}, t_n, and t_{n+1} can be calculated by equation (1), respectively. Since $\Delta T_{j(n+1)}$ has the same value as $\Delta T_{j(n-1)}$ at the steady-state operation, the junction temperature fluctuation and the mean junction temperature are expressed as equation (2) and (3), respectively.

$$\Delta T_j = P \sum_{i=1}^{4} R_{thi} \frac{(1 - e^{-\frac{t_{on}}{\tau_i}})^2}{1 - e^{-\frac{t_p}{\tau_i}}} \quad (2)$$

$$T_{jm} = \sum_{i=1}^{4} R_{thi} \cdot \frac{P}{2} + T_a \tag{3}$$

where P is the peak value of periodical power pulse, t_{on} denotes the on-state time, t_p denotes the fundamental period of converter output current, and T_a denotes the ambient temperature. It is noted that t_p is twice value of t_{on}. Based on equation (2) and (3), the thermal behavior of the power device at steady-state can be analytically deduced, which avoids time-consuming simulation due to the huge difference between the switching period and the thermal time constant of the power device.

Case study in a 2 MW DFIG wind turbine system

In this section, based on the power loss profile of the back-to-back power converter in a 2 MW DFIG wind turbine system, the analytical method for power device junction temperature will be evaluated and analyzed. In order to verify the analytical estimation for thermal behavior of the power semiconductor, a comparison with the simulation results is then implemented.

Basic concept and power loss profile of DFIG system

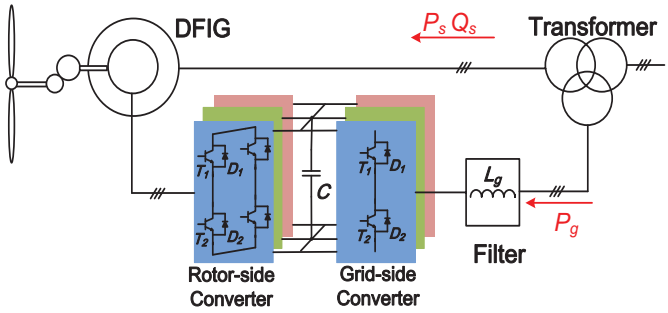

Fig. 4: Typical configuration of a DFIG wind turbine system.

Due to the extensive and well-established knowledge, as well as the simpler structure and fewer components, the two-level back-to-back voltage source converter is the most attractive solution in the commercial market of wind turbine system. A popular wind turbine configuration, normally based on a DFIG, is to employ a partial-scale power converter, as shown in Fig. 4. The function of the rotor-side converter is not only to transfer the slip active power from/to the grid, but also to provide excitation energy for the induction generator, while the grid-side converter is designed to keep the DC-link voltage fixed and supply part of the reactive power required by the grid codes. The parameters of the used induction generator and back-to-back power converter are summarized in Table I and Table II, respectively. It is noted that due to the significantly unequal current through the grid-side converter and rotor-side converter, single common low-voltage power device (1.7 kV/1 kA) and two paralleled power devices is the solution for each the grid-side converter and the rotor-side converter bridge arm for a 2 MW wind turbine system.

Table I: Parameters for a 2 MW DFIG

Rated power P_m	2 MW
Reactive power range Q_s	-570 kVar ~ +450 kVar
Rated peak stator voltage U_{sm}	563 V
Stator/rotor turns ratio k	0.369
Stator inductance L_s	2.95 mH
Rotor inductance L_r	2.97 mH
Magnetizing inductance L_m	2.91 mH

Table II: Parameters for back-to-back power converter

Rated power P_g	330 kW
Rated peak phase voltage U_{gm}	563 V
DC-link voltage U_{dc}	1050 V
Filter inductance L_g	0.5 mH
RSC and GSC switching frequency f_s	2 kHz
Power device in each grid-side converter cell	1.7 kV/1 kA
Power device in each rotor-side converter cell	1.7 kV/1 kA // 1.7 kV/1 kA

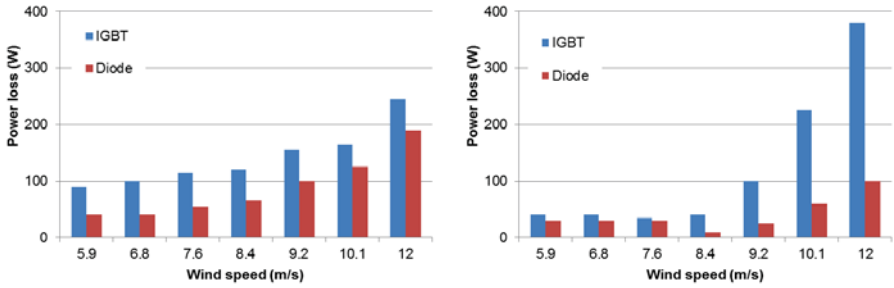

(a) (b)

Fig. 5: Power loss profile of each power device for the back-to-back power converter in the DFIG system. (a) Rotor-side converter. (b) Grid-side converter.

In order to investigate the loss behavior in different operation modes, several wind speeds are chosen in the DFIG system. It is worth to mention that the wind speed at 8.4 m/s is regarded as the synchronous operation point of the DFIG system. Based on the loss energy curves provided by the manufacturer, the accumulated power dissipation in every switching cycle can be obtained within one fundamental frequency. Simulations have been realized by the PLECS block in Simulink [13]. The loss distribution of the IGBT and diode in the rotor-side converter at different wind speeds is shown in Fig. 5(a). In order to avoid an extremely unbalanced power device loading at synchronous operation point, a small turbine speed hysteresis is introduced for the minimum rotor frequency 1 Hz [14]. The power loss in the grid-side converter at different wind speeds in shown in Fig. 5(b). The lowest power loss appears in synchronous operation due to the fact that no active power flow exist and only the switching ripple current affects, while the highest power loss emerges above rated wind speed.

Liquid cooling techniques for power module

Liquid cooling solutions for the power module are mainly divided into indirect cooling and direct cooling. Indirect cooling means that the power module is assembled on a closed cooler through a thin layer of thermal interface material (e.g. cold plate). On the other hand, direct cooling means that the coolant is in direct contact with the surface to be cooled, which is commonly done by pin fin designs or a paralleled liquid cooling of the whole base plate surface area. Direct liquid cooling eliminates the layer of thermal interface material that is traditionally needed between the backside of the power module and cold plate. As the thermal grease accounts for up to 50% of the thermal resistance from the junction to ambient [15], this elimination results in an improved thermal environment for the power module.

Thermal profile estimation by typical liquid cooling

Due to different materials as well as their unequal thermal expansion coefficient, the thermal impedance normally includes the junction to case, the case to heat-sink and the heat-sink to ambient. The thermal impedance from the junction to case is usually tested by the manufacturer, and their

values is given in terms of multi-layer Foster RC network, which is the curve fitting value and has no real physical meaning. Moreover, in order to evaluate the correct junction temperature, the thermal impedance from case to heat-sink and the heat-sink to ambient are essential to take into account, as even with the highest quality standards for application of thermal interface material, the thermal resistance of interface material is in the same magnitude as the module itself [16]. However, the series connection of Foster model will inevitably introduce significant errors, so the best method to estimate the junction temperature of the power semiconductor is to use the thermal impedance directly from the junction to ambient, and the thermal impedance of a direct liquid cooling per power device is illustrated in Fig. 6. It can be seen that the maximum time constant for the thermal network is several seconds. Furthermore, the diode has poorer dynamical thermal impedance than the transistor in the entire time domain and also it has a higher steady-state thermal resistance.

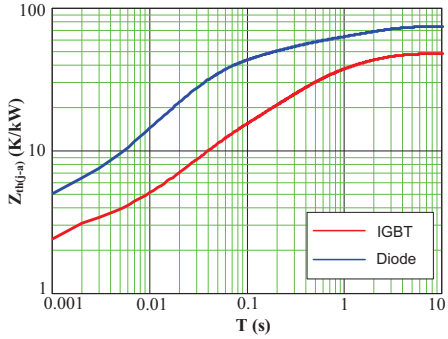

Fig. 6: Thermal impedance from junction to heat-sink of a typical liquid cooling.

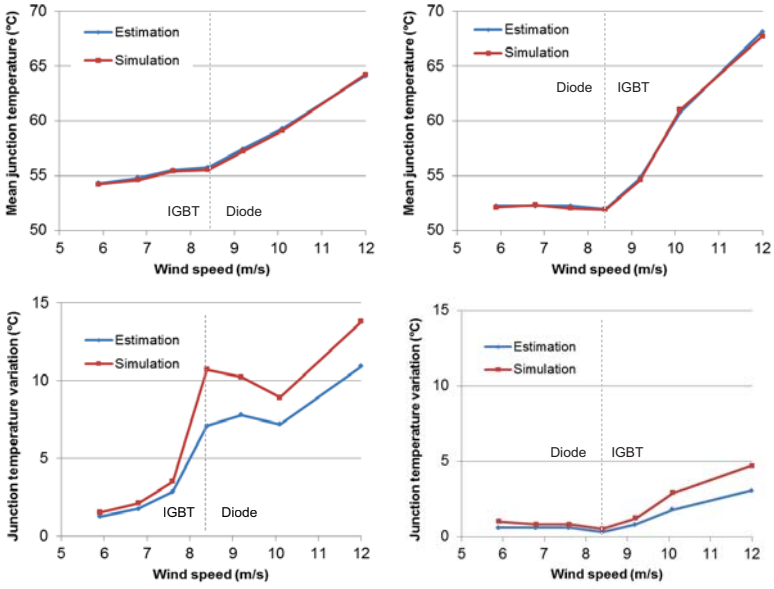

(a) (b)

Fig. 7: Analytical estimation vs. simulation results of the junction temperature profile in device-chips. (a) Rotor-side converter. (b) Grid-side converter. (Note: “IGBT” indicates the operating area where the IGBT is more loaded, and “Diode” indicates the operating area where the diode is more loaded).

In order to evaluate the thermal performance of the power device of the back-to-back power converter at different wind speeds, along with the power loss profile shown in Fig. (5), the junction temperature

fluctuation and the mean junction temperature can be calculated by equation (2) and (3), respectively, where for simplicity the instant sinusoidal power loss is regarded as step-changing power loss. As a consequence, a comparison of the junction temperature profile in the power semiconductors between analytical method and simulation is shown in Fig. 7, where the most stressed power devices of the rotor-side converter and the grid-side converter are extracted in Fig. 7(a) and Fig. 7(b), respectively. It is evident that the mean junction temperature is well predicted by the proposed method. However, the estimation results will have a lower junction temperature fluctuation due to the fact that the power dissipation is regarded as the step source instead of the sinusoidal. Moreover, for the rotor-side converter, the hottest device moves from the IGBT to the diode, if the DFIG operation change from sub-synchronous mode to super-synchronous mode, while for the grid-side converter, the IGBT has a higher mean junction temperature and the junction temperature fluctuation in case of the super-synchronous operation mode.

Thermal profile comparison between air cooling and liquid cooling

Nowadays air cooling and liquid cooling are the popular two cooling techniques for power modules. Thermal impedance for typical air and liquid cooling is first to be evaluated and analyzed, then improved thermal model for these two approaches are described, respectively. Thermal behavior between air cooling and liquid cooling is finally compared.

Analysis of typical air cooling and liquid cooling

Fig. 8(a) shows the typical heat-sink thermal impedance for these cooling approaches from Semikron [4]. It can be seen that the time constant from the heat-sink to ambient (dozens of seconds to hundreds of seconds) is much longer than that from the junction to case (dozens of milliseconds to several seconds). Regarding the mean junction temperature, it is noted that the steady-state thermal resistance of air cooling is three times larger than the liquid cooling.

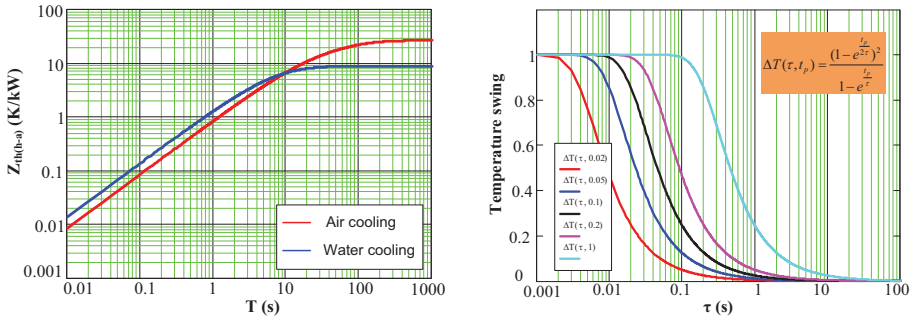

Fig. 8: Thermal impedance curve from Semikron [4]. (a) Dynamic thermal impedance of air and liquid cooling from heat-sink to ambient (Note: air flow=610 m^3/h, T_a=25 °C, 500m above sea level; liquid flow=15 L/min, T_{fluid}=40°C, water/glycol ratio=50%/50%). (b) Temperature swing dependence of thermal time constant and fundamental frequency.

In order to evaluate the influence of the cooling method on the junction temperature fluctuation, the relationship between the junction temperature swing and the time constant of the thermal impedance at all possible fundamental frequencies of the output current (from 20 milliseconds to 1 second) is shown in Fig. 8(b). It can be seen that the temperature swing can almost be ignored if the thermal time constant is above 10 seconds.

Practical thermal model

For the air cooling, the datasheet of the power module does not mention any thermal information from the heat-sink to ambient because of the different applications. Assuming that typical liquid cooling and

air cooling have the same thermal resistance from the case to heat-sink, along with that the thermal impedance from the junction to case is always provided by the manufacturer, the thermal impedance from heat-sink to ambient can be inferred. Moreover, as mentioned above, the thermal impedance from the heat-sink to ambient for typical air cooling is three times larger than the liquid cooling. The parameters of the whole thermal chain for liquid cooling and air cooling are summarized in Table III.

Table III: Parameters of the whole thermal chain for liquid cooling and air cooling

		$R_{th(j\_c)}$	$R_{th(c\_h)}$	$R_{th(h\_a)}$
IGBT [K/kW]	Liquid cooling	23	5	20
	Air cooling	23	5	60
Diode [K/kW]	Liquid cooling	45	11	20
	Air cooling	45	11	60

With the air cooling method, the calculated heat-sink temperature rise falsifies the junction temperature only to a very small degree, because the time constant of heat-sink (from dozens of seconds to several hundreds of seconds) is far above of the value for power module itself (several seconds). Therefore, since the junction temperature fluctuation mainly depends on the thermal impedance from the junction to case, the improved thermal model is shown in Fig. 9(a), where the steady-state temperature rise introduced by thermal grease and air cooling is depicted as the controlled temperature source.

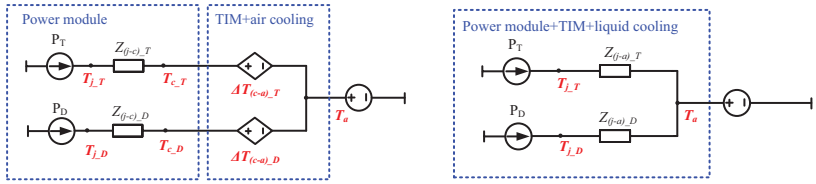

Fig. 9: Practical thermal model of the power devices. (a) Air cooling. (b) Liquid cooling.

On the other hand, the error induced by the liquid cooling is critical, since it have comparably low thermal capacities, i.e. corresponding low time constant. As a consequence, the whole thermal impedance from junction to ambient is shown in Fig. 9(b).

Thermal behavior comparison of air cooling and liquid cooling

With the aid of practical thermal model for air cooling and liquid cooling, the analytical prediction for the thermal performance of the power device can be implemented. Therefore, a comparison of the thermal cycling profile in terms of the mean junction temperature and the junction temperature fluctuation is shown in Fig. 10. For the rotor-side converter, the hottest device moves from the IGBT to the diode, if the DFIG changes from sub-synchronous operation mode to super-synchronous operation mode, while for the grid-side converter, the IGBT has a higher mean junction temperature and the junction temperature fluctuation in the case of the super-synchronous operation mode.

For the mean junction temperature, the liquid cooling has a better performance during the whole wind speed range due to its lower steady-state thermal impedance from the heat-sink to ambient. Moreover, it can be seen that, for the rotor-side converter, the mean junction temperature increases with the higher wind speed, while for the grid-side converter, the mean junction temperature will reach a minimum value at synchronous operation point. For the junction temperature fluctuation, the difference between both cooling methods becomes little.

Conclusion

In this paper, an analytical approach from loss profile to thermal profile for power semiconductor is proposed and verified in a 2 MW DFIG based wind turbine system. Moreover, the air cooling and the

liquid cooling used in wind power converter are analyzed and compared. It is demonstrated that the liquid cooling approach has a similar junction temperature fluctuation but gives a lower mean junction temperature than the air cooling.

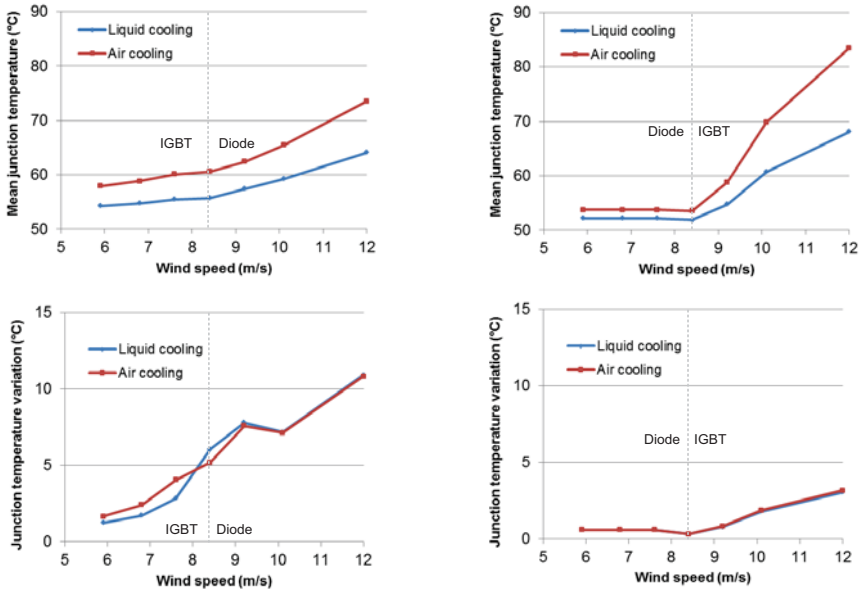

(a) (b)

Fig. 10: Thermal profile comparison between air cooling and liquid cooling. (a) Rotor-side converter. (b) Grid-side converter. (Note: "IGBT" indicates the operating area where the IGBT is more loaded, and "Diode" indicates the operating area where the diode is more loaded).

References

[1] The EU climate and energy package. (Available: http://ec.europa.eu/clima/policies/package/index_en.htm)

[2] ZVEL, Handbook for robustness validation of automotive electrical/electronic modules, Jun. 2008.

[3] F. Blaabjerg, Z. Chen, S. B. Kjaer, "Power electronics as efficient interface in dispersed power generation systems," *IEEE Trans. on Power Electronics*, vol. 19, no. 5, pp. 1184- 1194, Sep. 2004.

[4] A. Wintrich, U. Nicolai, W. Tursky, T. Reimann, "Application manual power semiconductors," Semikron international GmbH, Nuremburg, 2011.

[5] J. Kolar, J. Biela, S. Waffler, T. Friedli, U. Badstuebner, "Performance trends and limitations of power electronic systems," *in Proc.of Integr. Power Electron. Syst. Rec*., pp. 17–36, 2010.

[6] Y. Song, B. Wang, "Survey on reliability of power electronic systems," *IEEE Trans. on Power Electronics*, vol. 28, no. 1, pp. 591-604, Jan. 2013.

[7] A. Bryant, N. Parker-Allotey, D. Hamilton, I. Swan, P. Mawby, T. Ueta, T. Nishijima, K. Hamada, "A fast loss and temperature simulation method for power converters, part I: eletrothermal modeling and validation", *IEEE Trans. on Power Electronics*, vol. 27, no.1, pp. 248-257, Jan. 2012.

[8] Q. Gao, C. Liu, B. Xie, X. Cai, "Evaluation of the mainstream wind turbine concepts considering their reliabilities," *IET on Renewable Power Generation*, vol. 6, no. 5, pp. 348-357, Sep. 2012.

[9] K. Ma, F. Blaabjerg, "Multilevel converters for 10 MW wind turbines," *in Proc. of EPE 2011*, pp. 1-10, 2011.

[10] D. Zhou, F. Blaabjerg, M. Lau, M. Tonnes, "Thermal cycling overview of multi-MW two-level wind power converter at full grid codes operation," *IEEJ Journal of Industry Applications*, to be published.

[11] D. Zhou, F. Blaabjerg, M. Lau, M. Tonnes, "Thermal behavior optimization in multi-MW wind power converter by reactive power circulation," *IEEE Trans. on Industry Applications*, to be published.

[12] H. Wang, K. Ma, F. Blaabjerg, "Design for reliability of power electronic systems," *in Proc. of IECON 2012*, pp. 33-44, 2012.
[13] User manual of PLECS blockset version 3.2.7 March 2011. (Available: http://www.plexim.com/files/plecsmanual.pdf).
[14] J. Jung, W. Hofmann, "Investigation of thermal stress in rotor of doubly-fed induction generator at synchronous operating point," *in Proc. of EWEC 2010*, pp. 1-10, 2010.
[15] K. Olesen, F. Osterwald, M. Tonnes, R. Drabek, R. Eisele, "Designing for reliability, liquid cooled power stack for the wind industry," in Proc. of IEMDC 2011, pp. 896-901, 2011.
[16] R. Schnell, M. Bayer, S. Geissmann, "Thermal design and temperature ratings of IGBT modules," ABB Application Note, 5SYA 2093-00, 2011.

[A.5] D. Zhou, F. Blaabjerg, M. Lau, M. Tonnes, "Reactive power impact on lifetime prediction of two-level wind power converter," *in Proc. of PCIM 2013*, pp. 564-571, 2013.

Reactive Power Impact on Lifetime Prediction of Two-level Wind Power Converter

D. Zhou[1,2], F. Blaabjerg[1], M. Lau[2], M. Tonnes[2]

[1] Aalborg University, Pontoppidanstraede 101,DK-9220 Aalborg, Denmark

[2] Danfoss Silicon Power GmbH, Husumer Strasse 251, D-24941 Flensburg, Germany

Abstract

The influence of reactive power injection on the dominating two-level wind power converter is investigated and compared in terms of power loss and thermal behavior. Then the lifetime of both the partial-scale and full-scale power converter is estimated based on the widely used Coffin-Manson model. It is concluded that the injection of the reactive power could have serious impact on the power loss and thermal profile, especially at lower wind speed. Furthermore, the introduction of the reactive power could also shorten the lifetime of the wind power converter significantly.

1. Introduction

The penetration of wind power is expected to achieve 20% of the total electricity production by 2020 in Europe [1]. Because of the noise emission, land limits and richer wind energy, the wind turbines are moving from onshore to offshore. Meanwhile, the lifetime of the wind turbine system are inversely prolonged to 20-25 years under such uncertain and harsh environment, whose mission profile leads to a faster fatigue and higher failure rate. As the most vulnerable power electronic component, more and more efforts have been devoted to the reliable behavior of the power semiconductor recently due to the increased cost and time for repair after failures [2]-[4].

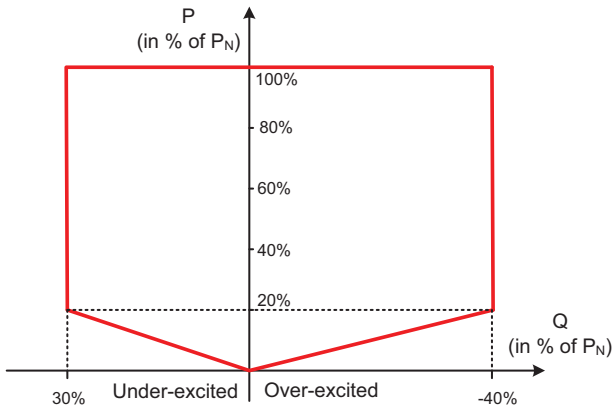

Fig. 1. Active/reactive power operation range of offshore wind farm defined by E.on-Netz [5]

A large number of wind farms are increasing being installed in terminal of the power transmission system. The weak connections demand the ability of reactive power supply in order

to support the voltage regulation (e.g. the active/reactive power requirement [5] for offshore wind power application issued by German transmission system operator).

The scope of this paper is first to analyze the effects of the reactive power based on commonly used partial-scale and full-scale wind power systems. Then the power loss and thermal behavior of the power device are mapped and compared in terms of whether reactive power is injected or not. Finally, the lifetime expectancy of the power semiconductor, which is closely related to the thermal profile, is estimated based on an annual wind profile.

2. Effect of reactive power on typical topologies

Due to extensive and well-established knowledge, as well as the simper structure and fewer components, the two-level back-to-back power converter is the most attractive solution in commercial market of wind turbines [6]. The utilization of power electronics in wind turbine system can be further divided into two categories, namely: Doubly Fed Induction Generator (DFIG) system based partial-scale power converter and Permanent Magnet Synchronous Generator (PMSG) system based full-scale power converter, which are both illustrated in Fig. 2.

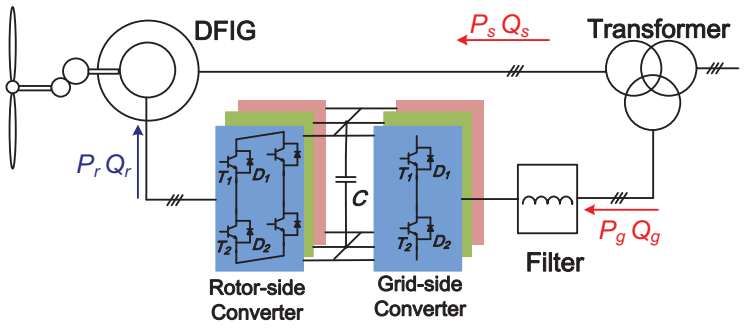

(a) DFIG-based partial-scale topology (with gearbox).

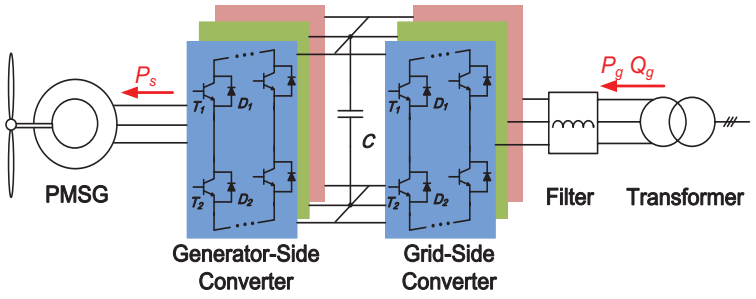

(b) PMSG-based full-scale topology (directly-drive).

Fig. 2. State-of-the-art configurations for two-level wind turbine system

For case study, Table 1 summarizes the relevant parameters of a 2 MW DFIG-based and PMSG-based wind turbine systems. As shown in Fig. 2(a), due to the dual links to the power grid in terms of the induction generator's stator and the partial-scale back-to-back power converter, there are two possibilities to compensate the reactive power by Q_g from the Grid-Side Converter (GSC) and Q_s from the Rotor-Side Converter (RSC). Consequently, it is interesting to investigate and compare the effects of these two compensation approaches on the performance of the power converter.

Table 1: Parameters for 2 MW DFIG & PMSG Wind Turbine Systems

	DFIG system	**PMSG system**
Power converter's rated Power P_g	330 kW	2000 kW
Rated grid phase voltage U_{gm}	564 V	564 V
DC-link voltage U_{dc}	1050 V	1100 V
Filter inductance L_g	0.5 mH	0.15 mH
Stator inductance L_s	2.94 mH	0.276 mH
Magnetizing inductance L_m	2.91 mH	
Rotor inductance L_r	2.97 mH	/
GSC and RSC switching freq. f_s	2 kHz	2 kHz
Power device in each GSC cell	1 kA/1.7 kV, single	1 kA/1.7 kV, four in paralleled
Power device in each RSC cell	1 kA/1.7 kV, two in paralleled	1 kA/1.7 kV, four in paralleled

If the reactive power is compensated from the RSC, owing to current limitation from power semiconductor, the rotor current will be,

$$k\sqrt{\frac{4}{9}\frac{X_s^2}{X_m^2U_{gm}^2}(P_s^2+Q_s^2)-\frac{4}{9}\frac{X_s}{X_m^2}Q_s+\frac{U_{gm}^2}{X_m^2}}\le 2I_m \tag{1}$$

where k denotes the generator's stator/rotor turns ratio, X_s, X_m, X_r denote stator reactance, magnetizing reactance and rotor reactance, all of which are consistent with the Table 1, I_m denotes the current capacity of a single power device.

Furthermore, the line-to-line rotor voltage amplitude cannot exceed DC-link voltage restricted by the linear modulation range,

$$\frac{|s|}{k}\sqrt{\frac{4}{9}(\frac{\sigma X_rX_s}{X_mU_{sm}})^2(P_s^2+Q_s^2)-\frac{4}{9}\frac{\sigma X_rX_s}{X_mU_{sm}}Q_s+(\frac{X_rU_{sm}}{X_m})^2}\le\frac{U_{dc}}{\sqrt{3}} \tag{2}$$

where s denotes slip value, σ denotes leakage factor of the induction generator, U_{dc} denotes the DC-link voltage.

Since the wind speed at 10 m/s is regarded as one of the highest probability among offshore wind speed distribution [7], the influence of the reactive power injection upon back-to-back power converter will be focused under this circumstance.

Substituting the parameter values indicated in Table 1, the range of reactive power from the RSC will satisfy the E.on-Netz requirement.

Similarly, if the reactive power is injected from the GSC, the converter's out current and voltage will be expressed like (3), (4), which is also restricted by power device current rating and linear modulation,

$$\sqrt{\frac{4}{9}\frac{P_g^2+Q_g^2}{U_{gm}^2}}\le I_m \tag{3}$$

$$\sqrt{(U_{gm}-\frac{2X_g}{3U_{gm}}Q_g)^2+(\frac{2X_g}{3U_{gm}}P_g)^2}\le\frac{U_{dc}}{\sqrt{3}} \tag{4}$$

Due to the DC-link limitation, the reactive power range is from 0.3 p.u. under-excited to 0.1 p.u. over-excited. As a result, the grid code on reactive requirement fails to meet, which also means the GSC require a higher DC-link voltage than the RSC in condition of the same amount of the over-excited reactive power.

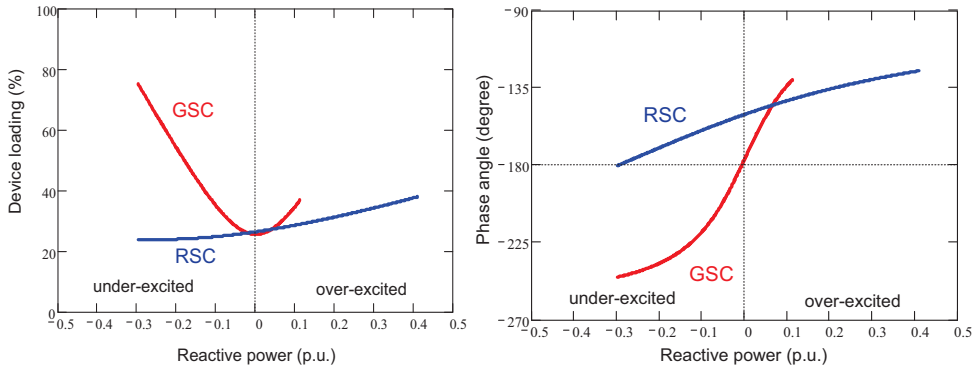

(a) Device loading vs. reactive power Q (b) Phase angle vs. reactive power Q

Fig. 3. Current characteristic of back-to-back power converter in a DFIG system (wind speed: 10 m/s)

The current characteristic of the back-to-back power converter in the DFIG system is illustrated in Fig. 3. For the characteristic of the device loading, it is clearly noted that the current will increase obviously in conditions of either under-excited or over-excited injection from the GSC, while the current will only change a little bit and even decrease in case of the under-excited reactive power injection, because the additional reactive power demand for grid code can contribute to the excitation of the induction generator. For the characteristic of power factor angle, for the GSC, it is noted that, in response to the additional reactive power injection, unity power factor easily becomes either leading or lagging power factor. For the RSC, it is noted that the phase shift looks insignificant.

For the PMSG system illustrated in Fig. 2(b), the reactive power compensation can only be fed through the GSC. It shares the same analysis criteria referred to the GSC in the DFIG system.

3. Loss distribution considering grid codes

The power loss model, consisting of the conduction losses and switching losses, can be referred to [8]. Based on the on-state voltage drop and switching energy against the load current and the DC-link voltage provided by the manufacturers, the conduction losses and switching losses are accumulated by every switching cycle within one fundamental frequency. The simulation of the power loss has been realized according to PLECS block in Simulink [9].

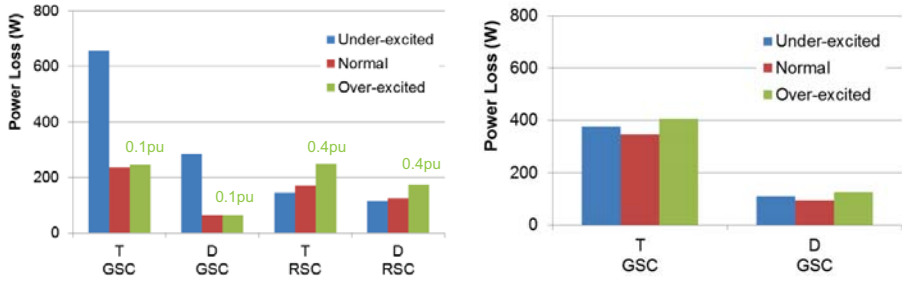

(a) (b)

Fig. 4. Loss distribution of each power device with extreme amount reactive power (a) Grid-side converter and rotor-side converter in a DFIG-based system. (b) Grid-side converter in a PMSG-based system. (wind speed: 10 m/s)

The analysis about the loss distribution of each power semiconductor with extreme amount of reactive power is shown in Fig. 4. For the DFIG system, the same amount of the reactive power injection from the RSC will have a slighter impact on the power loss than the GSC. Moreover, it will even reduce the power loss in case of the under-excited reactive current, which is consistent with above mentioned current characteristic analysis. Therefore, it is better to compensate the reactive power from the RSC. For the PMSG system, the injection of both under-excited and over-excited reactive power will increase the power loss insignificantly.

In order to evaluate the influence of the reactive power upon the power semiconductor among the whole operational wind range, Fig. 5 shows the generator's output power and turbine speed against wind speed of the wind power generation system. For the DFIG system, as stated in [8], the synchronous operation of the doubly-fed induction generator will induce the extremely unbalanced power device loading among the three-phase bridge in the RSC. As a result, a small turbine speed hysteresis is introduced for minimum rotor frequency 1 Hz.

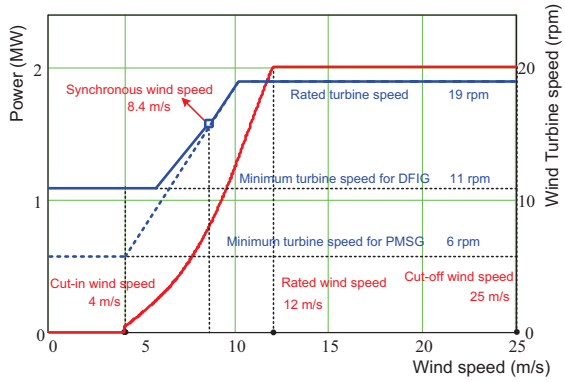

Fig. 5. Output power and turbine speed against wind speed

Accordingly, as shown in Fig. 6, the loss distribution of each power converter under the whole wind speed operation is mapped in conditions of over-excited, normal and under-excited reactive power requirements, where the reactive power is fed through RSC in the DFIG system and through GSC in the PMSG system. It can be seen that the power loss increase with the higher wind speed continuously in both systems. Moreover, it is evident that the reactive power influence to power loss is more serious in the DFIG than the PMSG system, and the reactive power introduces more additional power loss in condition of lower wind speed.

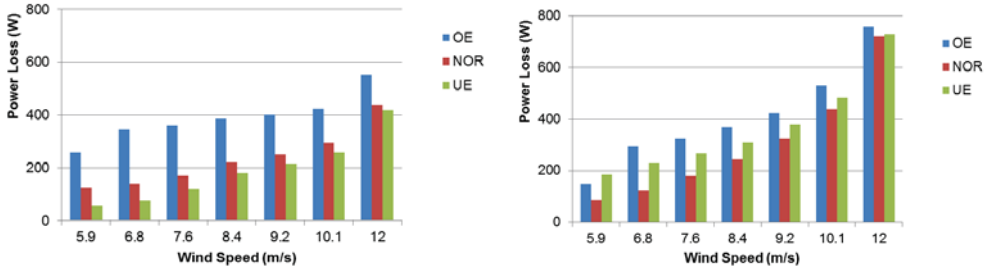

Fig. 6. Loss distribution of each power converter under the whole wind speed operation (a) Rotor-side converter in a DFIG-based system. (b) Grid-side converter in a PMSG-based system.

4. Thermal distribution considering grid codes

The one-dimensional thermal model of single IGBT and freewheeling diode share the same idea as discussed in [10]. With the aid of the previous power loss results, the junction temperature can be again simulated using PLECS-software. As the most stressed power semiconductor decides the reliability and lifetime in a power module, it is necessary to extract the thermal excursion of the most serious loading chips in both the DFIG and PMSG system considering the grid codes.

For the RSC of the DFIG system as shown in Fig. 7 (a), the most stressed power semiconductor changes from the IGBT in sub-synchronous mode to the freewheeling diode in super-synchronous mode. It is also noted that the over-excited reactive power requirement will impose thermal stress to the power semiconductor especially at synchronous operating point. For the GSC of the PMSG system as shown in Fig. 7(b), the IGBT is the most stressed power semiconductor during the whole operating wind speed. The reactive power injection will induce higher mean junction temperature and junction temperature fluctuation. Moreover, the situation will become worse at lower wind speed due to the lower output active power but the same amount of the reactive power is demanded.

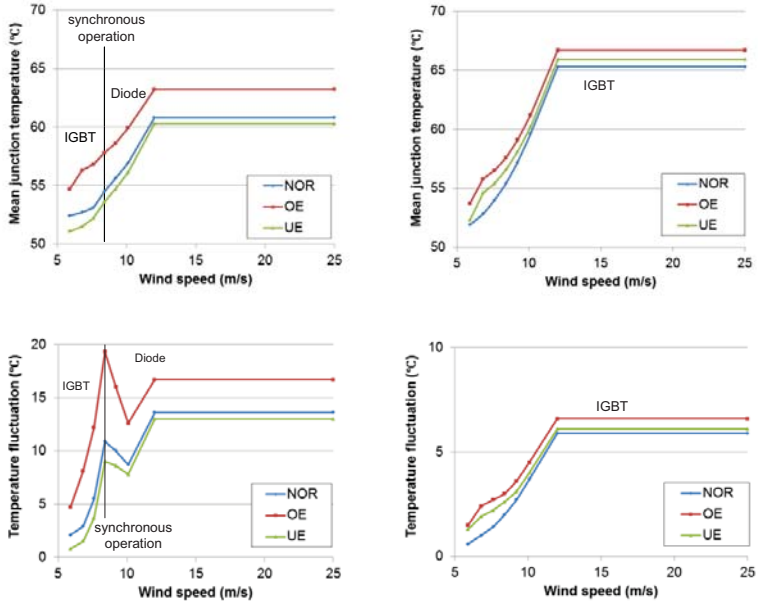

Fig. 7. Mean junction temperature and temperature fluctuation in the chip vs. wind speed for both systems. (a) Rotor-side converter in a DFIG-based system. (b) Grid-side converter in a PMSG-based system.

5. Lifetime estimation

The junction temperature excursion of the power semiconductor is the most dominant reason for failure mechanisms, e.g. wire bonds lift-off, solder joint of chips cracking and solder joint of conductor leads cracking [11], [12]. Hence, it is interesting to investigate the correlations between lifetime of a module and the thermal stress. One of the commonly accepted models is known as the Coffin-Manson formula,

$$N_f = A\left(\Delta T\right)^{\alpha} \cdot \exp\left(\frac{E_a}{k_b \cdot T_m}\right) \tag{5}$$

where the junction temperature swing ΔT and mean temperature T_m are taken into consideration, and A, α can be obtained by experimental measurements. Moreover, E_a and k_b denote activation energy and Boltzman constant, respectively.

Based on the power cycle test data of B10 lifetime (the number of cycles during which 10% of the total number of modules fail), the curves of power cycle with different temperature swings as well as mean temperatures are shown in Fig. 8, where the above mentioned model can fit the testing data well. Therefore, it can be extrapolated to the whole temperature variation range.

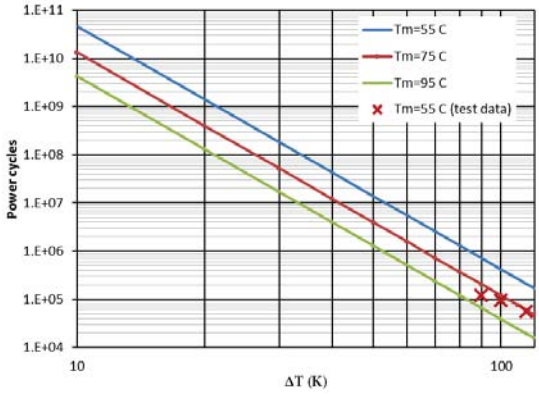

Fig. 8. B10 lifetime curve as a function of temperature swing and mean temperature

Many test results also indicate that time pulse duration t_{on} will have a considerable impact on the power cycles. It is assumed that a given number of power cycles N_{test} is tested at duration T_{on_test}. If the power modules are used for a different application with pulse duration T_{on_app}, the new power cycles N_{app} will equal to,

$$N_{app} = N_{test}\left(\frac{T_{on\_app}}{T_{on\_test}}\right)^{\beta} \tag{6}$$

where β can be obtained according to the test experience.

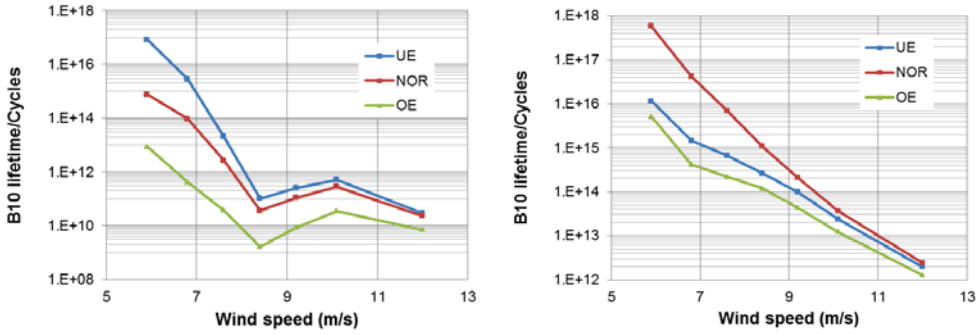

Fig. 9. Power cycle/B60 lifetime of the both systems. (a) Rotor-side converter in a DFIG-based system. (b) Grid-side converter in a PMSG-based system.

The effects of the reactive power injection to power cycle lifetime can be calculated at whole wind speed operation as shown in Fig. 9 in terms of the two dominating wind turbine systems. For the DFIG system, under-excited reactive power injection can contribute to the power converter's lifetime en-

hancement. Moreover, although the mean junction temperature increases with the wind speed, during synchronous operation the power cycles become extremely lower due to the higher junction temperature fluctuation. For the PMSG system, the wind system operation without reactive power injection has the highest power cycles, which is consistent with the thermal information indicated in Fig. 7(b).

With the typical wind profile as well as the Palmgren-Miner law [13], it can be inferred that, if the reactive power is introduced by grid codes, for the DFIG system, the lifetime of the RSC reduces from 498 to 102 years, while for the PMSG system, the lifetime of GSC varies from 11609 to 5785 years.

6. Conclusion

In this paper, the effect of reactive power on typical wind power converter (DFIG-based partial-scale and PMSG-based full-scale) is addressed and compared. Regarding the DFIG system, the injection of the reactive power from the rotor-side converter is proven a better choice due to more reactive power supply ability and less additional current stress.

According to the German grid codes, for the PMSG system, it will dissipate slightly more power loss in grid-side converter whatever the under-excited or over-excited reactive power is introduced. For the DFIG system, the influence on the power loss in rotor-side converter will be a little heavier in over-excited but even lower in under-excited than normal condition.

Based on the thermal information of the power device, along with the widely used lifetime Coffin-Manson model, it is noted that the introduction of the reactive power will also shorten the lifetime of the wind power converter significantly.

7. Literature

[1] European Commission Climate Action, "The EU climate and energy package," Mar. 2007.

[2] F. Blaabjerg, Z. Chen, S.B. Kjaer, "Power electronics as efficient interface in dispersed power generation systems," IEEE Trans. on Power Electronics, vol.19, no.5, pp. 1184-1194, Sep. 2004.

[3] F. Blaabjerg, K. Ma, D. Zhou, "Power electronics and reliability in renewable energy systems," in Proc. of ISIE'2012, pp.19-30, May. 2012.

[4] S. Yang, A. Bryant, P. Mawby, D. Xiang, L. Ran, P. Tavner, "An industrial-based survey of reliability in power electronic converters," IEEE Trans. on Industrial Applications, vol.47, no.3, pp. 1441-1451, May. 2011.

[5] E.ON-Netz. Requirements for offshore grid connections, Apr. 2008.

[6] M. Liserre, R. Cárdenas, M. Molinas, J. Rodriguez, "Overview of multi-MW wind turbines and wind parks," IEEE Trans. on Industrial Electronics, vol.58, no.4, pp.1081-1095, Apr. 2011.

[7] K. Xie, Z. Jiang, W. Li, "Effect of wind speed on wind turbine power converter reliability," IEEE Trans. on Energy Conversion, vol.27, no.1, pp.96-104, Mar. 2012.

[8] D. Zhou, F. Blaabjerg, M. Lau, M. Tonnes, "Thermal analysis of multi-MW two-level wind power converter," in Proc. of IECON'2012, pp. pp.5862-5868, Oct. 2012.

[9] User manual of PLECS blockset version 3.2.7 March 2011. (Available: http://www.plexim.com/files/plecsmanual.pdf.

[10] A. Wintrich, U. Nicolai, W. Tursky, T. Reimann, Application manual power semiconductors, Semikron International, 2011, ISBN: 9783938843666.

[11] L. Wei, R. J. Kerkman, R. A. Lukaszewski, H. Lu, Z. Yuan, "Analysis of IGBT Power Cycling Capabilities Used in Doubly Fed Induction Generator Wind Power System," IEEE Trans. on Industry Applications, vol. 47, no. 4, pp. 1794-1801, Aug. 2011.

[12] I.F. Kova evi, U. Drofenik, J.W. Kolar, "New physical model for lifetime estimation of power modules," in Proc. IPEC'2010, pp. 2106-2114, Jun. 2010.

[13] ABB Application Note, Load-cycling capability of HiPaks, 2004.

[A.6] D. Zhou, F. Blaabjerg, M. Lau, M. Tonnes, "Optimized reactive power flow of DFIG power converters for better reliability performance considering grid codes," *IEEE Trans. on Industrial Electronics*, IEEE early access.

This article has been accepted for publication in a future issue of this journal, but has not been fully edited. Content may change prior to final publication. Citation information: DOI 10.1109/TIE.2014.2359911, IEEE Transactions on Industrial Electronics

Optimized Reactive Power Flow of DFIG Power Converters for Better Reliability Performance Considering Grid Codes

Dao Zhou, *Student Member, IEEE*, Frede Blaabjerg, *Fellow, IEEE*, Mogens Lau and Michael Tonnes

***Abstract* – If there is no reactive power exchange between the Doubly-Fed Induction Generator (DFIG) and the grid, the various characteristics of the power converters in the DFIG wind turbine system cause the lifetime expectancy of the rotor-side converter significantly less than the grid-side converter. In order to fulfill the modern grid codes, over-excited reactive power injection will further reduce the lifetime of the rotor-side converter. In this paper, the additional stress of the power semiconductor due to the reactive power injection is firstly evaluated in terms of modulation index and the current loading. Then an optimized reactive power flow is proposed in the case an over-excited reactive power support is applied with the joint compensation from both the rotor-side converter and the grid-side converter. Finally, some experimental validations are performed at a down-scale DFIG prototype. It is concluded that, among the different combined reactive power support strategies, the best scheme will trade-off the lifetime between the grid-side converter and the rotor-side converter.**

***Index Terms* – Doubly-fed induction generator, reactive power, thermal behavior, consumed lifetime.**

I. INTRODUCTION

The worldwide wind capacity reached close to 320 GW by the end of the 2013 [1]. As the modern wind turbine is required to act like the conventional synchronous generator with independent reactive power and active power regulation in order to handle the power quality issues [2], the power electronics are nowadays playing a more and more important role even to the full-scale of the wind turbine generator (e.g. permanent-magnet synchronous generator). In order to reduce the cost of the wind power generation, the power rating of the wind turbine is now up-scaling to 8 MW. However, the feedback of the wind turbine market indicates that the best-seller is still those rated around 2-3 MW, in which the Doubly-Fed Induction Generator (DFIG) is normally employed together with the partial-scale power electronic converters [3]-[6].

Another progress in the wind turbine technology is the movement of wind farms from onshore to offshore to reduce the environment impact and also obtain even better wind conditions. Because of the expensive maintenance for the offshore wind farms, the lifetime of the whole system preserves normally 20-25 years, much longer than the traditional industrial standard [7]. Consequently, the reliability of the offshore wind turbine system becomes of interest from the manufacturer's perspective. As the-state-of-art agreement, the reliability engineering in power electronics is currently moving from a solely statistical approach to a more physics based approach, which involves not only the statistics but also the root cause behind the failures [8]-[13].

Considerable reliability tests have already been carried out by the leading power semiconductor manufacturers. In [14], [15], the power cycles of the power device are provided in traction systems from a thermal stress point of view, and the most important factors affecting the lifetime are summarized in [16] (e.g. mean junction temperature, junction temperature fluctuation, on-state time duration of a periodical current, etc.). A lot of papers also address the reliability issues in wind turbine systems [17]-[20], which implies that the thermal cycles of the power semiconductor generally include the small cycles (e.g. current commutation within one fundamental frequency) and the large cycles (e.g. the fluctuation of wind speed and environment temperature). This paper mainly focuses on the steady-state small thermal cycles. In the DFIG system, as the Rotor-Side Converter (RSC) and the Grid-Side Converter (GSC) are both able to provide the reactive power support, thereby the total minimum power can be achieved by using a proper reactive power share, which can enhance the system efficiency [21], [22]. Moreover, due to the various characteristics of the power converters in the DFIG system, it can also be seen that the lifetime expectancy between the RSC and the GSC could also be significantly unequal. This paper investigates a smart reactive power share between the Back-to-Back (BTB) power converters in order to balance their lifetime seen from the thermal stress of the power semiconductor.

The layout of this paper is organized as follows. In section II, the loss breakdown and the thermal behavior of the power device are estimated at some typical wind speeds, thus the consumed lifetime of the power converters can be obtained based on an annual wind profile. Section III describes the additional stress of the power device introduced by the reactive power support required by the modern grid codes. In

Manuscript received November 18, 2013; revised March 8, 2014, June 11, 2014 and July 30, 2014; accepted August 31, 2014.

This article has been accepted for publication in a future issue of this journal, but has not been fully edited. Content may change prior to final publication. Citation information: DOI 10.1109/TIE.2014.2359911, IEEE Transactions on Industrial Electronics

Section IV, as the reactive power can be supplied either from the GSC or the RSC, different combined reactive power compensation strategies are adopted in order to seek the best solution for the DFIG system in respect to the lifetime expectancy of the power converters. In Section V, the experimental results of the reactive power compensation strategies are tested in a down-scale DFIG system. Finally, some conclusions are drawn in Section VI for controlling this system.

II. Various Characteristics of BTB Power Converters in Respect to Reliability

The typical configuration of the DFIG based wind turbine system is shown in Fig. 1. As the BTB power converters have different performances (e.g. the control objectives, the interface voltages and the operational frequencies), different loss distributions in the power semiconductors can be expected, thus various thermal profiles inevitably induce an unbalanced lifetime between the GSC and the RSC. Based on a typical annual wind profile, this section will evaluate the estimated lifespan of the power electronic converters.

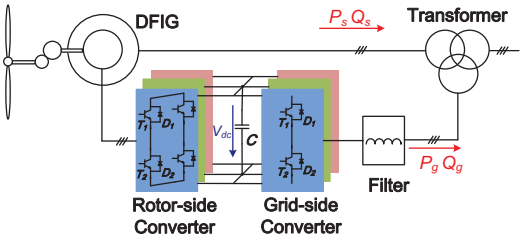

Fig. 1. Doubly-fed induction generator-based wind energy generation system.

A. Loss breakdown of power device

The power loss of the power device mainly includes the conduction loss and the switching loss [23]. The conduction loss in each power device P_{con} can be deduced as [24],

$$P_{con} = f \cdot \Big(\sum_{n=1}^{N} v_{CE}\big(|i_a(n)|\big) \cdot |i_a(n)| \cdot T_1(n) + \sum_{n=1}^{N} v_F\big(|i_a(n)|\big) \cdot |i_a(n)| \cdot (T_s - T_1(n))\Big) \quad (1)$$

where the first term is the conduction loss of the IGBT T_{con}, and the second term is the conduction loss of the freewheeling diode D_{con}. i_a is the sinusoidal current through the power device, T_1 is the ON time of the upper leg within a switching period T_s (in Fig. 1), v_{CE}, v_F are voltage drops of the IGBT and the diode during their on-state period, which are normally given by the manufacturer. N is the carrier ratio, whose value is the switching frequency over the fundamental frequency f, and the subscript n is the nth switching pattern.

The space vector modulation is widely used in a three-phase three-wire system due to its higher utilization of the DC-link voltage. In order to guarantee the minimum harmonic, the symmetrical sequence arrangement of the no-zero vector and zero-vector is normally used, and the conduction time of the upper and the lower switch of leg can thus be deduced based on the voltage angle [25]. Within one fundamental frequency of the converter output current, each IGBT in a leg always conducts only half period. The direction of the current is relevant to the conduction loss distribution between the IGBT and the diode. As a result, the phase angle between the converter voltage and the current is also important.

For the RSC, the phase angle is related to the power factor of the stator-side of the DFIG as well as the DFIG instinctive parameters. Neglecting the stator resistance and the rotor resistance, the steady-state DFIG equivalent circuit is shown in Fig. 2 in terms of the phasor expression.

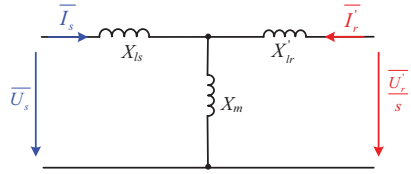

Fig. 2. One phase DFIG equivalent circuit in phasor diagram.

Taking phase A as an example, if the stator voltage is assumed as the reference direction and all quantities are transferred to the stator side, the voltage and current relationship between the rotor-side and the stator-side are,

$$\overline{I'_r} = -\frac{X_s}{X_m} I_{s\_\mathrm{Re}} + j \cdot sign(s) \cdot \Big(-\frac{U_{s\_\mathrm{Re}}}{X_m} - \frac{X_s}{X_m} I_{s\_\mathrm{Im}}\Big) \quad (2)$$

$$\overline{U'_r} = s \cdot \Big(\frac{X_r}{X_m} U_{s\_\mathrm{Re}} + \frac{\sigma X_r X_s}{X_m} I_{s\_\mathrm{Im}}\Big) - j \cdot (sign(s)) \cdot \Big(s \frac{\sigma X_r X_s}{X_m} I_{s\_\mathrm{Re}}\Big) \quad (3)$$

where X_s, X_m and X_r denote the stator reactance, the magnetizing reactance and the rotor reactance, respectively. σ is the leakage coefficient, defined as $(X_sX_r\text{-}X_m^2)/X_sX_r$. s is the slip value of the induction generator. Moreover, the sign function *sign(s)* means if s is positive, its value becomes 1. Alternatively, if s is negative, its value becomes -1.

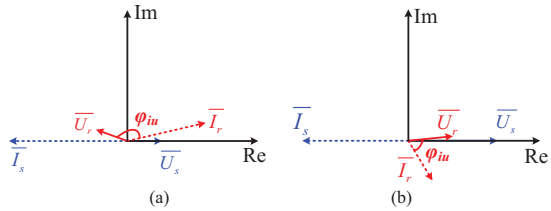

Fig. 3. Phasor diagram of the stator voltage, stator current and rotor voltage, rotor current. (a) Super-synchronous mode; (b) Sub-synchronous mode.

According to (2) and (3), the phasor diagram of the stator voltage, stator current and rotor voltage, rotor current is then shown in Fig. 3. In the super-synchronous mode, the rotor voltage is almost in an opposite phase in respect to the stator voltage, as the slip value is negative. Moreover, the rotor current is almost lagging the rotor voltage 180º, which indicates that the DFIG provides the active power through the

This article has been accepted for publication in a future issue of this journal, but has not been fully edited. Content may change prior to final publication. Citation information: DOI 10.1109/TIE.2014.2359911, IEEE Transactions on Industrial Electronics

rotor-side, and the RSC also supplies the excitation energy for the induction generator. In the sub-synchronous mode, the rotor current is lagging the rotor voltage less than 90º, implying that the RSC provides both the active power and the reactive power to the induction generator.

For the GSC, if a single inductance is used as filter as shown in Fig. 4, by definition of the grid voltage as the reference, the voltage and current relationship between the grid and the converter output are,

$$\overline{I_g} = I_{g\_\mathrm{Re}} + jI_{g\_\mathrm{Im}} \tag{4}$$

$$\overline{U_C} = U_{g\_\mathrm{Re}} - X_g \cdot I_{g\_\mathrm{Im}} + j(-X_g \cdot I_{g\_\mathrm{Re}}) \tag{5}$$

where X_g denotes the filter reactance. The phasor diagram of the grid-side converter voltage and current is shown in Fig. 5.

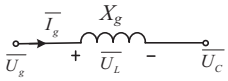

Fig. 4. One phase L filter of the grid-side converter in phasor diagram.

The switching loss in each power device P_{sw} can be calculated as,

$$P_{sw} = \frac{U_{dc}}{U_{dc}^*} \cdot f \cdot \left(\sum_{n=1}^{N} (E_{on}(|i_a(n)|) + E_{off}(|i_a(n)|)) + \sum_{n=1}^{N} E_{rr}(|i_a(n)|)\right) \tag{6}$$

Similarly as (1), the first term is the switching loss for the IGBT T_{sw}, and the second term is the switching loss for the freewheeling diode D_{sw}. E_{on} and E_{off} are the turn-on and the turn-off energy dissipated by the IGBT, and E_{rr} is the reverse-recovery energy dissipated by the diode, which are normally tested by the manufacturer at certain DC-link voltage U_{dc}^*. It is assumed that the switching energy is proportional to the actual DC-link voltage U_{dc}.

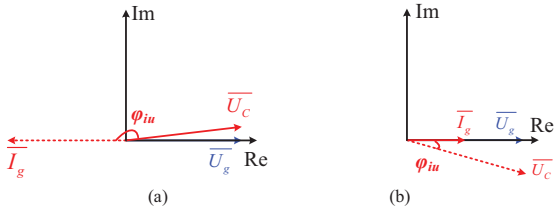

Fig. 5. Phasor diagram of the grid-side converter output voltage and current. (a) Super-synchronous mode; (b) Sub-synchronous mode.

A 2 MW wind turbine system is used as a case study, and its parameters are listed in Appendix. With the aid of the conventional vector control, the maximum power point tracking is used for the active power reference. If no reactive power compensation is taken into account, the loss breakdown of each power device can be analytically evaluated in terms of the RSC and the GSC, as shown in Fig. 6.

B. Thermal cycling of power device

Thermal impedance that decides the junction temperature of the power device usually consists of the thermal parameters of the power module itself (from junction to baseplate or case), and Thermal Integrate Material (TIM) as well as the cooling method, as shown in Fig. 7.

Generally, the thermal time constant of a typical air cooling system is from dozens of seconds to hundreds of seconds for MW-level power converter, while the maximum thermal time constant of the power device is hundreds of milliseconds. On the other hand, the maximum fundamental period of the power converters output current is only one second, which implies that the thermal cycling caused by the air cooling can almost be neglected [26], [27]. As a result, for the steady-state power cycle analysis, the thermal model of the cooling method will only affect the mean junction temperature, but not disturb the junction temperature fluctuation.

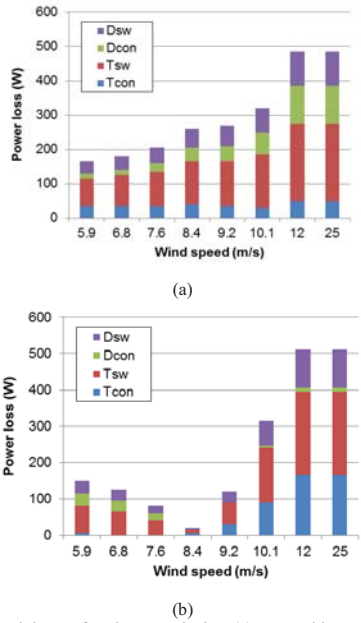

Fig. 6. Loss breakdown of each power device. (a) Rotor-side converter; (b) Grid-side converter.

As the mean junction temperature T_{jm} and the junction temperature fluctuation dT_j are commonly regarded as the two most important reliability assessment indicators, the formulae of them are [28],

$$T_{jm\_T/D} = P \cdot \sum_{i=1}^{4} R_{thjc\_T/D(i)} + P \cdot \sum_{j=1}^{3} R_{thca\_(j)} + T_a \tag{7}$$

$$dT_{j\_T/D} = 2P \cdot \sum_{i=1}^{4} R_{thjc\_T/D(i)} \cdot \frac{(1 - e^{-\frac{t_{on}}{\tau_{thjc\_T/D(i)}}})^2}{1 - e^{-\frac{t_p}{\tau_{thjc\_T/D(i)}}}} \tag{8}$$

In (7), R_{thjc} is the thermal resistance from the junction to case of the power module, R_{thca} is the thermal resistance of the

This article has been accepted for publication in a future issue of this journal, but has not been fully edited. Content may change prior to final publication. Citation information: DOI 10.1109/TIE.2014.2359911, IEEE Transactions on Industrial Electronics

air cooling, in which subscripts T and D denote the IGBT and the freewheeling diode, whereas subscripts i and j denote four-layer and three-layer Foster structure for power module and air cooling, respectively. P is the power loss of each power semiconductor, and T_a is the ambient temperature. In (8), t_{on} denotes the on-state time within each fundamental period of current at the steady-state operation, t_p denotes the fundamental period of the current, τ denotes the each Foster layer's thermal time constant.

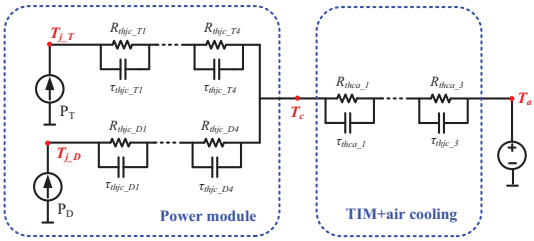

Fig. 7. Thermal model of power semiconductor for power cycles induced by the fundamental frequency.

C. Estimated lifetime based on annual wind profile

Power cycling test is defined that the power components are actively heated up by the losses in the semiconductor and cooled down again with the aid of cooling system. This test can detect the thermo-mechanical stress between the layers with different thermal expansion coefficients, in which the connection between the chip and Direct Bonded Copper (DBC) and bond wire connection seems to be the most frequent failure mechanisms [14], [15], [26].

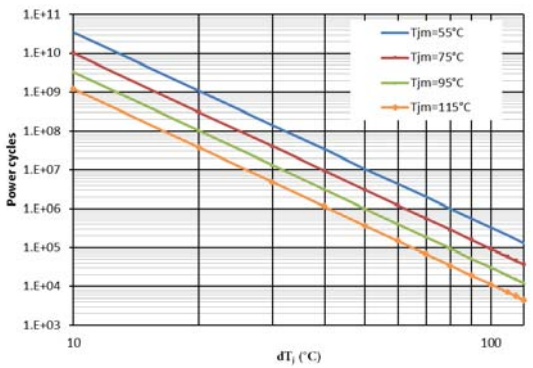

Fig. 8. Example of fitting power cycles curve versus the mean junction temperature and the junction temperature fluctuation according to Coffin-Mansion model [16].

In order to accelerate the testing, the introduced current almost equals the rated current of the power semiconductor, and the time cycling is normally between some seconds to dozens of seconds. The values of the power cycles can be obtained at higher junction temperature fluctuations, and then the values at lower temperature variation can be extrapolated by the Coffin-Mansion equation [16]. Based on the simplified assumption of the uniform failure mechanism over the entire temperature range, the B10 lifetime (10% of sample components fail if power cycles reach the B10 value) is shown in Fig. 8 with various mean junction temperatures and various junction temperature fluctuations.

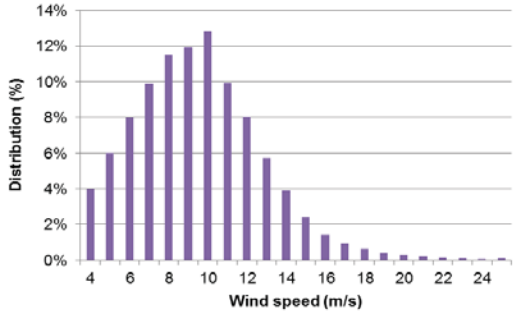

Fig. 9. Class I annual wind profile according to IEC standard [33], [34].

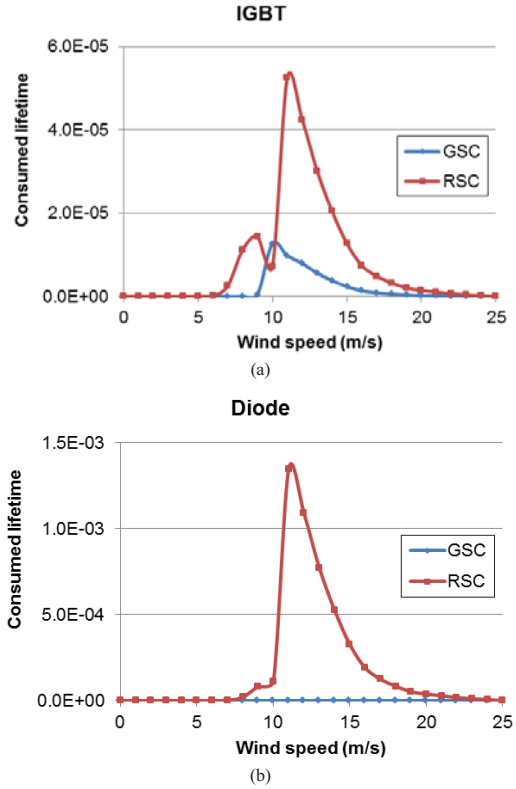

Fig. 10. Consumed lifetime of the switching semiconductors in the back-to-back power converters at each wind speed if the reactive power is zero. (a) IGBT; (b) Diode.

Note: GSC denotes the grid-side converter, and RSC denotes the rotor-side converter.

Based on (7) and (8), as well as Fig. 6, the steady-state mean junction temperature and junction temperature

This article has been accepted for publication in a future issue of this journal, but has not been fully edited. Content may change prior to final publication. Citation information: DOI 10.1109/TIE.2014.2359911, IEEE Transactions on Industrial Electronics

fluctuation can be calculated at each individual wind speed. Together with a Class I annual wind speed distribution shown in Fig. 9, in which the velocity increment is 1 m/s, the individual B10 power cycles can be obtained from the cut-in wind speed of 4 m/s to the cut-off wind speed of 25 m/s. Besides, it is worth to mention the rated wind speed of 11 m/s.

The lifetime consumed per year of the IGBT and freewheeling diode inside the BTB power converters at each wind speed can be calculated as,

$$CL_m = D_m \cdot \frac{365 \cdot 24 \cdot 3600 \cdot f_m}{N_m} \tag{9}$$

where D is the annual percentage of every wind speed, f is the fundamental frequency of the output current, and N is the power cycles consistent with Fig. 8. Subscript m denotes the various wind speed from the cut-in to the cut-off wind speed.

The lifetime consumed per year of the IGBT and freewheeling diode are thus shown in Fig. 10(a) and Fig. 10(b). For the RSC, it can be seen that the diode dominates the lifetime compared to the IGBT, while for the GSC, it is the IGBT that has much less lifetime expectancy. Moreover, the lifespan of the RSC is much shorter than the GSC.

According to the Miner's rule [17], [19], [29], the total consumed lifetime per year can then be estimated by,

$$CL = \sum_{m=4}^{25} CL_m \tag{10}$$

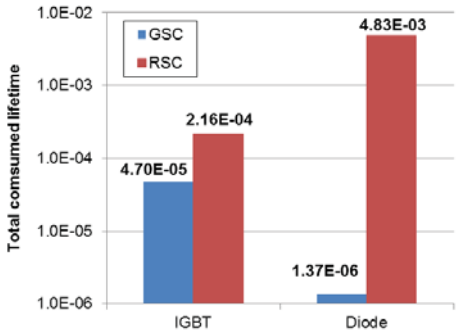

Fig. 11.Total consumed lifetime between the rotor-side converter and the grid-side converter.

A comparison of the total consumed lifetime between the RSC and the GSC is shown in Fig. 11. It is noted that the lifetime of the BTB power converters becomes very unbalanced, in which the lifetime of the GSC only consumes 1/100 of the RSC. Moreover, due to the orders of magnitude difference between the IGBT and the diode in respect to the total consumed lifetime, for simplicity, the thermal performance of the diode is only focused to estimate the RSC lifetime, while only the IGBT is focused to analyze the lifespan for the GSC.

III. Lifetime Reduction to Support Modern Grid Codes

As the wind farms are normally located at the remote areas, stricter grid codes are issued in order to guarantee a stable grid voltage. This section will firstly describe a modern grid code, and then address the additional stress of the power device in respect to the reactive power injection.

A. Modern grid codes

As shown in Fig. 12, the most representative grid code in respect to the reactive power regulation is the E.ON requirement for grid connections [30]. If the active power is above 20%, up to 30% of the under-excited reactive power and 40% of the over-excited reactive power are expected to be supported. For the DFIG configuration, it is worth to note that the under-excited reactive power denotes reactive power absorbed from the grid by the DFIG. Alternatively, the over-excited reactive power denotes the reactive power injected to the grid by the DFIG.

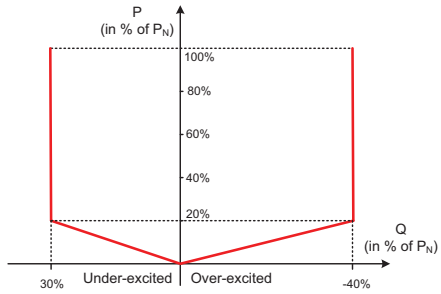

Fig. 12. Reactive power support stated in the German grid code [30].

B. Reactive power stress on BTB power converters

For the RSC, as illustrated in (2) and (3), the rotor current and the rotor voltage of the DFIG is closely related to the generated active power by the wind energy, as well as the reactive power exchange between the DFIG and the grid required by the transmission system operator. Similarly, for the GSC, it can be seen from (4) and (5) that the converter current and its interfacing voltage also depend on the active power and reactive power. As a result, the supportive reactive current introduces additional current stress to the power device as well as the voltage stress in DC-link voltage for both the RSC and the GSC [27]. As these two factors are tightly linked to the loss dissipation of the power semiconductor, the effects of the reactive power injection on the current and voltage stress of the power device are shown in Fig. 13(a) and Fig. 13(b), respectively, where the wind speeds 12 m/s, 8.4 m/s and5.9 m/s indicate the super-synchronous mode, synchronous mode and sub-synchronous mode of the DFIG operation.

For the GSC, the modulation index almost reaches 1.0 at three typical wind speeds when there is no reactive power exchange between the DFIG and the grid. The synchronous mode has the relatively minimum value due to the very small slip power through the power converter. Moreover, the over-excited reactive power stresses the DC-link voltage significantly, while the under-excited reactive power reliefs,

This article has been accepted for publication in a future issue of this journal, but has not been fully edited. Content may change prior to final publication. Citation information: DOI 10.1109/TIE.2014.2359911, IEEE Transactions on Industrial Electronics

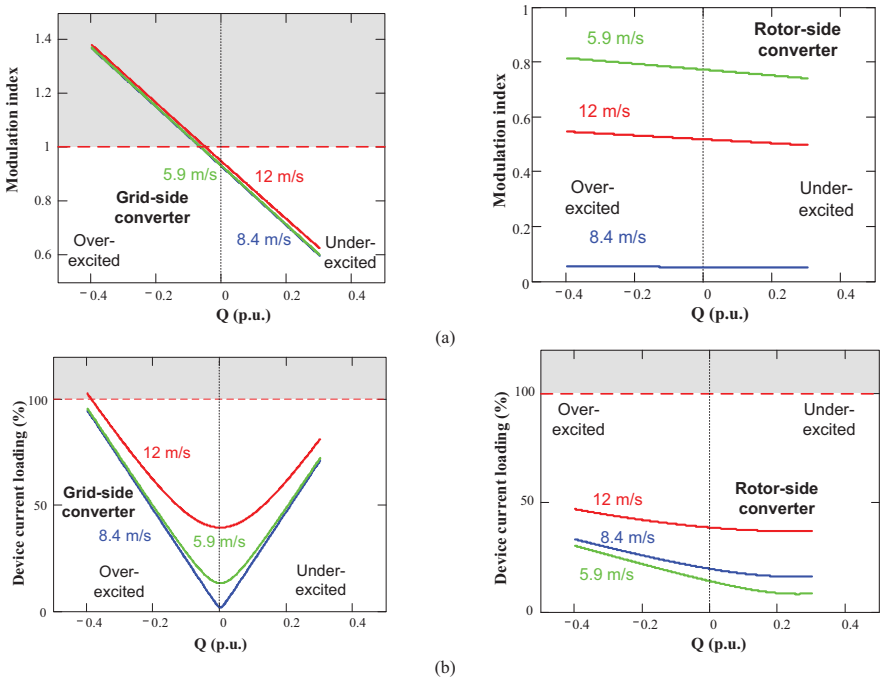

Fig. 13. Effects of the reactive power injection on the current and voltage stress of the power device. (a) Modulation index; (b) Device current loading.

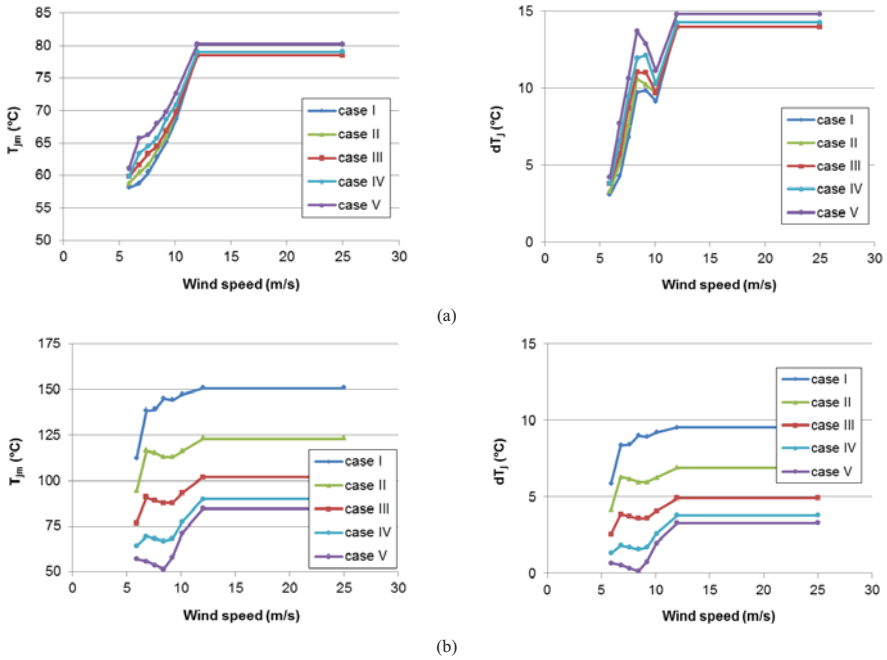

Fig. 14. Thermal profile of the most stressed power semiconductor in terms of the mean junction temperature and the junction temperature fluctuation, where the reactive power is provided with various compensation strategies. (a) Diode in the rotor-side converter; (b) IGBT in the grid-side converter.

This article has been accepted for publication in a future issue of this journal, but has not been fully edited. Content may change prior to final publication. Citation information: DOI 10.1109/TIE.2014.2359911, IEEE Transactions on Industrial Electronics

because the over-excited or the under-excited reactive power introduces the same or opposite direction of voltage drop through the filter inductance in respect to the grid voltage as shown in Fig. 5. Furthermore, either the over-excited or under-excited reactive power considerably increases the current loading of the device.

For the RSC, as illustrated in (2) and (3), the rotor voltage is jointly decided by the stator and rotor winding ratio and slip value of the generator. As a result, the modulation index at different wind speeds are found in Fig. 13(a), in which the highest slip value causes the highest modulation index. In respect to the device loading of the RSC, the situation is also better than the GSC in the case of the reactive power injection. It is interesting to note that under-excited reactive power injection reduces the current stress of the power device, as under this circumstance, the excitation energy actually is supported by the grid. Because of the ratio between the stator winding and rotor winding of the induction generator, the variation of the current in each power device is also smaller than in the GSC. Above all, it is more effective to support the reactive power from the RSC compared to the GSC.

IV. Joint Reactive Power Compensation from BTB Power Converter

As previously mentioned, the RSC and the GSC both have the abilities to support reactive power injection. This section will evaluate the effects of the reactive power flow between the GSC and the RSC seen from the lifetime and reliable operation point of view.

A. Different strategies for joint reactive power compensation

As the over-modulation affects the dynamic performance in the power electronics converter [31], [32], the different control strategies are all realized within the linear modulation range. As shown in Fig. 13, only the over-excited reactive power increases the current stress of the power device in the RSC, thus it will reduce the lifetime of the RSC. Different load sharing for the over-excited reactive power between the RSC and the GSC can be achieved by Table I, where the DC-voltage varies according to the linear modulation range of the GSC.

TABLE I

DIFFERENT STRATEGIES FOR JOINT REACTIVE POWER COMPENSATION

	RSC (pu)	GSC (pu)	U_{dc} (V)
Case I	0	-0.4	1500
Case II	-0.1	-0.3	1350
Case III	-0.2	-0.2	1200
Case IV	-0.3	-0.1	1100
Case V	-0.4	0	1050

Note: It is assumed that 0.4 pu over-excited reactive power is needed according to the grid codes [30].

B. Thermal behavior of the power semiconductor

According to (2) and (4), the different amounts of over-excited reactive power between the RSC and the GSC can be independently expressed by imaginary part of the stator current and the GSC output current. As a result, the conduction loss and the switching loss of the IGBT and the diode can be calculated. Moreover, substituting the loss information into (7) and (8), the most stressed power semiconductors for the BTB power converters (i.e. the freewheeling diode of the RSC and the IGBT of the GSC) are shown in Fig. 14(a) and Fig. 14(b).

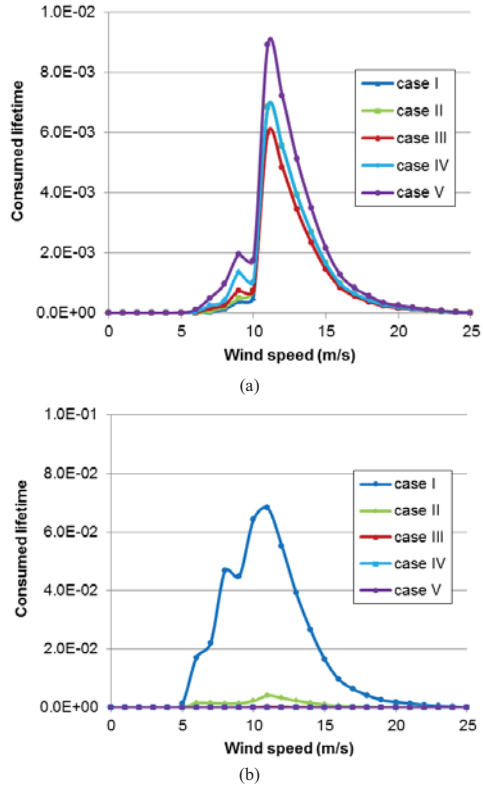

Fig. 15. Consumed lifetime of the most stressed power semiconductor at each wind speed. (a) Rotor-side converter; (b) Grid-side converter.

In Fig. 14(a), it can be seen that the mean junction temperature and the junction temperature fluctuation change insignificantly among all the compensation strategies. Meanwhile, the diode has the worst thermal behavior in Case V (reactive power fully compensated from the RSC), but has the best thermal performance in Case I (reactive power fully compensated from the GSC). In Fig. 14(b), the thermal performance of the IGBT in the GSC at different compensation strategies varies a lot. The worst situation is Case I (reactive power is fully supported by the GSC), in which the mean junction temperature almost reaches 150 ºC.

This article has been accepted for publication in a future issue of this journal, but has not been fully edited. Content may change prior to final publication. Citation information: DOI 10.1109/TIE.2014.2359911, IEEE Transactions on Industrial Electronics

C. Lifetime trade-off between GSC and RSC

With the thermal profile of the most stressed power semiconductor shown in Fig. 14, as well as the fundamental frequency of the power converter output current and the annual wind speed distribution, the lifetime consumed per year of the individual wind speed is shown in Fig. 15. If the wind speed is above the rated value, it is obvious that the wind speed at 11 m/s has the highest consumed lifetime of the RSC. One of the reasons is that, as the rated wind speed is 11 m/s, the wind speed at 11 m/s has the highest percentage above the rated wind speed as shown in Fig. 9. The other factor is the same thermal performance above the rated wind speed as shown in Fig. 14(a). However, if the wind speed is below the rated value, although the 8 m/s wind speed (synchronous operation of the DFIG) hardly contains the highest percentage as shown in Fig. 9, it actually consumes the majority lifetime among the wind speeds below the rated value, owing to the fact that the synchronous operation has the largest junction temperature fluctuation below the rated wind speed as shown in Fig. 14(a). Moreover, the smaller amount of reactive power it injects from the RSC, the smaller consumed lifetime it can obtain.

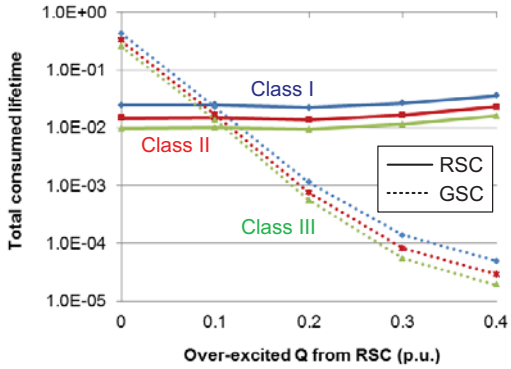

Fig. 16. Total consumed lifetime among the different compensation strategies, in which the various wind classes are also taken into account.

Note: a. The solid line indicates the diode of the rotor-side converter, and the dot line indicates the IGBT of the grid-side converter. b. Color blue, red and green indicate the wind Class I, Class II and Class III, respectively.

For the GSC, the lifetime consumed per year of the individual wind speed changes significantly with different compensation strategies. For instance, the highest consumed lifetime at 11 m/s moves from the worst 6.82E-2 in Case I to the best 1.42E-05 in Case V, which implies that the nearly 5000 times difference between them can easily induce the significant variation of the GSC lifetime.

The total consumed lifetime for the five combined reactive power strategies from the GSC and the RSC are shown in Fig. 16 using log scale, in which three wind classes are also considered. According to the IEC standard [33], [34], the mean wind speed of the Class I, Class II and Class III are 10 m/s, 8.5 m/s and 7.5 m/s, respectively. In the case of the wind Class I, the total consumed lifetime almost stays constant in a log-scale at different compensation schemes from the RSC point of view, while for the GSC, the total consumed lifetime varies significantly. Moreover, it can be seen that the most balanced lifetime between the RSC and the GSC appears in Case II, in which 0.1 pu over-excited reactive power is supported by the RSC and 0.3 pu is provided by the GSC. It is evident that the total consumed lifetime of the RSC can be optimized from 3.59E-2 (Case V) to 2.50E-2 (Case II), which implies 1.5 times enhanced lifespan. For different wind classes, the tendencies are almost consistent with the Class I wind.

V. Experimental Results

In order to validate the equations and control strategies, a down-scale 7.5 kW test system has been built and is shown in Fig. 17. The DFIG is externally driven by a prime motor, and the power electronic converters are linked to the grid through an LCL filter. Two 5.5 kW Danfoss motor drives are used for the GSC and the RSC, both of which are controlled by the implementation of dSPACE 1006. Due to the fact that the junction temperature of the power semiconductor is not easy to be measured, the experimental results are conducted through the electrical characteristics of the DFIG system.

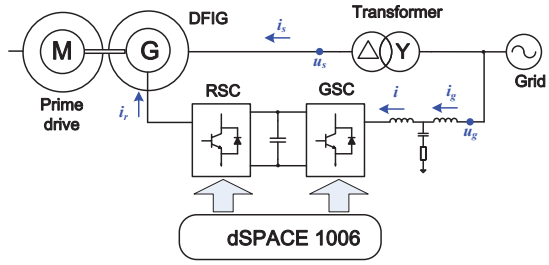

Fig. 17. Setup of the 7.5 kW DFIG system test rig.

With the parameters of the test system summarized in Appendix, the reactive power influence on the current and voltage stress of the BTB power converters are analytically calculated as shown in Fig. 18. It is noted that the tendency of the 7.5 kW DFIG system is similar to the 2 MW system as shown in Fig. 13 in terms of the modulation index as well as the current amplitude. Moreover, as the LCL filter significantly reduces the total inductance of the grid filter compared to the pure L structure filter, the DC-link of the test rig is set at 650 V and this value is high enough to supply 0.4 pu over-excited reactive power even from the GSC as shown in Fig. 18(a). Rotor speeds at 1050 rpm, 1470 rpm and 1800 rpm are selected for the sub-synchronous, synchronous and super-synchronous operations, whose produced active power are 1 kW, 3 kW and 5 kW, respectively. Then the modulation index and current amplitude can be tested at various amounts of the reactive power requirement.

As the loss of the induction generator can hardly be neglected in the 7.5 kW DFIG, an additional current is introduced in the BTB power converters to compensate the generator loss. As shown in Fig. 18(b), if no reactive power is

This article has been accepted for publication in a future issue of this journal, but has not been fully edited. Content may change prior to final publication. Citation information: DOI 10.1109/TIE.2014.2359911, IEEE Transactions on Industrial Electronics

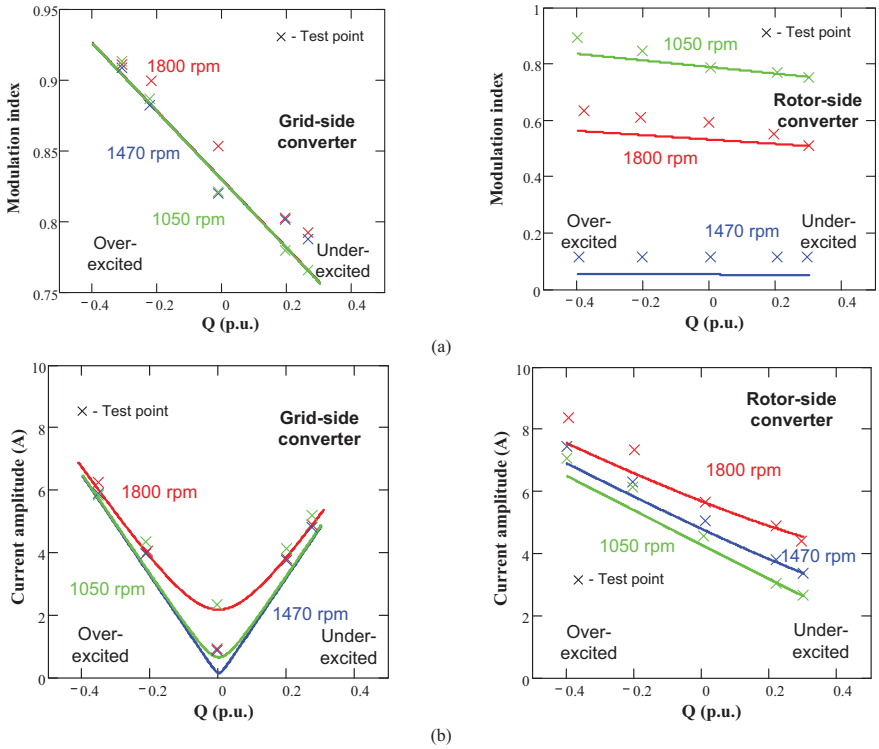

Fig. 18. Experimental validation of the reactive power influence on current and voltage stress of the back-to-back power converters. (a) Modulation index; (b) Device current loading.

Note: Active power references are 5 kW, 3 kW and 1 kW in the cases of the rotor speeds are 1800 rpm, 1470 rpm and 1050 rpm, respectively.

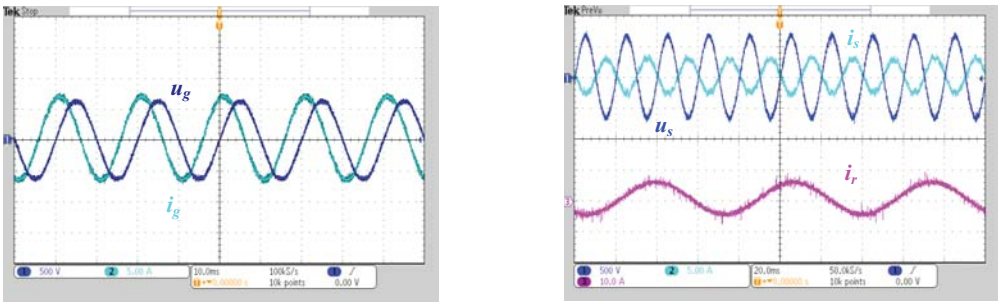

Fig. 19. Experimental result of the DFIG test rig at the sub-synchronous speed of 1050 rpm if the 0.4 pu over-excited reactive power is fully injected by the grid-side converter. (a) Grid current in respect to the grid voltage; (b) Stator current and rotor current in respect to the stator voltage.

taken into account, the test result of the GSC is higher than the theoretical value at the sub-synchronous mode, while the current amplitude is a little lower than theoretical value at the super-synchronous mode. However, for the RSC, if no reactive power injection is considered, the tested rotor current amplitude is similar to the theoretical value because the active current component is rather small compared to the excitation current. Moreover, the tendencies of modulation index and current amplitude of the BTB power converters are consistent with the analytical values. Above all, it is concluded there is a good correlation between theory and experiment if the various amounts of the reactive power are taken into account.

Assuming the DFIG operates in the sub-synchronous mode at the 1050 rpm with 1 kW active power, the full amount of the over-excited reactive power 3 kVar can be provided by either the GSC or the RSC. As shown in Fig. 19, if the

This article has been accepted for publication in a future issue of this journal, but has not been fully edited. Content may change prior to final publication. Citation information: DOI 10.1109/TIE.2014.2359911, IEEE Transactions on Industrial Electronics

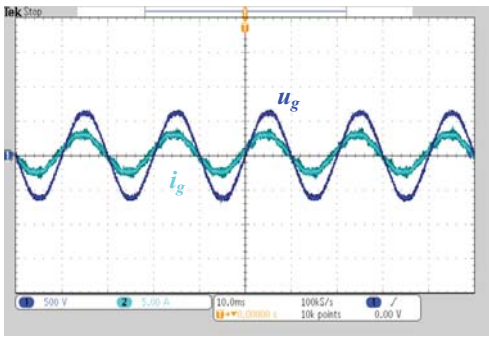

(a)

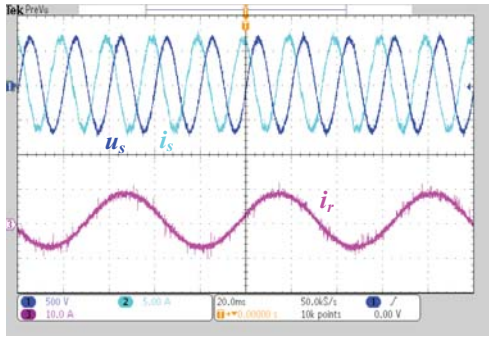

(b)

Fig. 20. Experimental result of the DFIG test rig at the sub-synchronous speed of 1050 rpm if the 0.4 pu over-excited reactive power is fully injected by the rotor-side converter. (a) Grid current in respect to the grid voltage; (b) Stator current and rotor current in respect to the stator voltage.

reactive power compensation is fully provided by the GSC, the active current component could be rather small compared to the reactive current component due to the slip power flowing through. As a result, the GSC current is almost leading the grid voltage 90 degree. For the RSC, as the DFIG injects the power to the grid, the stator current and the stator voltage are almost reverse as expected.

Fig. 20 shows the case when the 0.4 pu over-excited reactive power is completely supported by the RSC. The GSC current is exactly in phase with the grid voltage, while the stator current is leading the stator voltage 90 degree due to the dominating reactive current component.

VI. CONCLUSION

In this paper, the consumed lifetime of the grid-side converter and the rotor-side converter in a DFIG system is firstly compared based on a typical annual wind profile. If there is no reactive power exchange between the DFIG and the grid, the grid-side converter has more than 100 times lifetime compared to the rotor-side converter due to their various control objectives and various fundamental frequencies of the output current.

The influence of the reactive power support required in the modern grid codes is also evaluated for the back-to-back power converters in terms of the modulation index and the current loading of the each device. It is found that the reactive power compensation from the rotor-side converter is more effective than the support from the grid-side converter. Moreover, it can also be seen that the over-excited reactive power significantly reduces the lifetime of the rotor-side converter.

By introducing an optimized reactive power flow between the grid-side converter and the rotor-side converter, the lifetime trade-off can be achieved, thus they have more balanced lifetime. It is concluded that, depending on the specific power converter design, the most appropriate reactive power division between the grid-side converter and the rotor-side converter can enhance the lifetime 1.5 times compared to the case that the reactive power is fully provided through the rotor-side converter. Furthermore, in order to enhance the reliability, a proper asymmetrical design of the back-to-back power converters as well as the chip re-design of the power device could also have a promising potential in design of the wind power converter.

APPENDIX

PARAMETERS FOR A 2 MW AND 7.5 KW DFIG

DFIGs		
Rated power P_n [kW]	2000	7.5
Phase peak voltage U_{sn} [V]	563	311
Stator resistance R_s [mΩ/pu]	1.69/0.007	440/0.023
Stator leakage inductance L_{ls} [mH/pu]	0.04/0.050	3.44/0.056
Rotor resistance R_r [mΩ/pu]	1.52/0.006	640/0.033
Rotor leakage inductance L_{lr} [mH/pu]	0.06/0.085	5.16/0.085
Magnetizing inductance L_m [mH/pu]	2.91/3.840	79.30/1.294
Turns ratio N_s/N_r	0.369	0.336
Power converters		
Rated power [kW]	400	5
DC-link voltage U_{dc} [V/pu]	1050/1.522	650/1.711
Switching frequency f_s [kHz]	2	5
Grid filters		
Boost inductance [mH/pu]	0.5/0.132	18/0.039*

"*" indicates the total inductance of the LCL filter, including both the grid-side inductor and the converter-side inductor.

REFERENCES

[1] "World wind energy association – 2013 half-year report". (Available at: http://www.wwindea.org/home/index.php).

[2] Y. Li, L. Luo, C. Rehtanz, C. Wang, and S. Ruberg, "Simulation of the electromagnetic response characteristic of an inductively filtered HVDC converter transformer using field-circuit coupling," *IEEE Trans. Ind. Electron.* , vol. 59, no. 11, pp. 4020-4031, Nov. 2012.

[3] F. Blaabjerg, Z. Chen, and S. B. Kjaer, "Power electronics as efficient interface in dispersed power generation systems," *IEEE Trans. Power Electron.*, vol. 19, no. 5, pp. 1184-1194, Sep. 2004.

[4] J. M. Carrasco, L. G. Franquelo, J. T. Bialasiewicz, E. Galvan, R. C. P. Guisado, Ma. A. M. Prats, J. I. Leon, and N. Moreno-Alfonso, "Power-electronic systems for the grid integration of renewable energy sources: a survey," *IEEE Trans. Ind. Electron.*, vol. 53, no. 4, pp. 1002-1016, Jun. 2006.

[5] J. M. Guerrero, F. Blaabjerg, T. Zhelev, K. Hemmes, E. Monmasson, S. Jemei, M. P. Comech, R. Granadino, and J. I. Frau, "Distributed generation: toward a new energy paradigm," *IEEE Ind. Electron. Mag.*, vol. 4, no. 1, pp. 52-64, Mar. 2010.

[6] M. Liserre, R. Cardenas, M. Molinas, and J. Rodriguez, "Overview of multi-MW wind turbines and wind parks," *IEEE Trans. Ind. Electron.*, vol. 58, no. 4, pp. 1081-1095, Apr. 2011.

[7] B. Hahn, M. Durstewitz, and K. Rohrig "Reliability of wind turbines - Experience of 15 years with 1500 WTs," *Wind Energy: Proceedings of the Euromech Colloquium*, pp. 329-332, Springer-Verlag, Berlin.

[8] ZVEL, Handbook for robustness validation of automotive electrical/electronic modules, Jun. 2008.

[9] D. Hirschmann, D. Tissen, S. Schroder, and R.W. De Doncker, "Inverter design for hybrid electrical vehicles considering mission profiles," *in Proc. of IEEE Conference Vehicle Power and Propulsion 2005,* pp. 1-6, 2005.

[10] C. Busca, R. Teodorescu, F. Blaabjerg, S. Munk-Nielsen, L. Helle, T. Abeyasekera, and P. Rodriguez, "An overview of the reliability prediction related aspects of high power IGBTs in wind power applications," *Microelectronics Reliability*, vol. 51, no. 9-11, pp. 1903-1907, 2011.

[11] S. Yang, A. Bryant, P. Mawby, D. Xiang, L. Ran, and P. Tavner, "An industry-based survey of reliability in power electronic converters," *IEEE Trans. Ind. Appl.*, vol. 47, no. 3, pp. 1441-1451, May-June 2011.

[12] F. Richardeau, and T. T. L. Pham, "Reliability calculation of multilevel converters: theory and applications," *IEEE Trans. Ind. Electron.*, vol. 60, no. 10, pp. 4225-4233, Oct. 2013.

[13] H. Behjati, and A. Davoudi, "Reliability analysis framework for structural redundancy in power semiconductors," *IEEE Trans. Ind. Electron.,* vol. 60, no. 10, pp. 4376-4386, Oct. 2013.

[14] ABB Application Note, Load-cycling capability of HiPaks, 2004.

[15] A. Wintrich, U. Nicolai, and T. Reimann, "Semikron Application Manual," p. 128, 2011.

[16] U. Scheuermann, and R. Schmidt, "A new lifetime model for advanced power modules with sintered chips and optimized Al wire bonds", *in Proc. of PCIM 2013*, pp. 810-813, 2013.

[17] K. Ma, M. Liserre, F. Blaabjerg, and T. Kerekes, "Thermal loading and lifetime estimation for power device considering mission profiles in wind power converter," *IEEE Trans. Power Electron.,* IEEE early access.

[18] D. Weiss, and H. Eckel, "Fundamental frequency and mission profile wearout of IGBT in DFIG converters for windpower", *in Proc. of EPE 2013*, pp. 1-6, 2013.

[19] H. Wang, M. Liserre, and F. Blaabjerg, "Toward reliable power electronics: challenges, design tools, and opportunities," *IEEE Ind. Electron. Mag.*, vol. 7, no. 2, pp. 17-26, Jun. 2013.

[20] H. Wang, D. Zhou, and F. Blaabjerg, "A reliability-oriented design method for power electronic converters," *in Proc. of APEC 2013*, pp. 2921-2928, 2013.

[21] B. Cezar Rabelo, W. Hofmann, J. L. da Silva, R. G. de Oliveira, and S. R. Silva, "Reactive power control design in doubly fed induction generators for wind turbines," *IEEE Trans. Ind. Electron.*, vol. 56, no. 10, pp. 4154-4162, Oct. 2009.

[22] D. P. Bagarty, and D. Kastha, "Reactive power allocation for loss minimization in a stand-alone variable speed constant frequency double output induction generator," *IET Power Electronics*, vol. 6, no. 5, pp. 851-861, May 2013.

[23] T. B. Soeiro, and J. W. Kolar, "Analysis of high-efficiency three-phase two- and three-level unidirectional hybrid rectifiers," *IEEE Trans. Ind. Electron.*, vol. 60, no. 9, pp. 3589-3601, Sep. 2013.

[24] D. Zhou, F. Blaabjerg, M. Lau, and M. Tonnes, "Thermal analysis of multi-MW two-level wind power converter," *in Proc. of IECON 2012*, pp. 5862-5868, 2012.

[25] K. Zhou, and D. Wang, "Relationship between space-vector modulation and three-phase carrier-based PWM: a comprehensive analysis," *IEEE Trans. Ind. Electron.*, vol. 49, no. 1, pp. 186-196, Feb. 2002.

[26] D. Zhou, F. Blaabjerg, M. Lau, and M. Tonnes, "Thermal cycling overview of multi-megawatt two-level wind power converter at full grid code operation," *IEEJ Journal of Industry Applications*, vol. 2, no. 4, pp. 173-182, Jul. 2013.

[27] M. Marz, and P. Nance, "Thermal modeling of power-electronic system". (Available at: http://www.infineon.com/)

[28] D. Zhou, F. Blaabjerg, M. Lau, and M. Tonnes, "Thermal profile analysis of doubly-fed induction generator based wind power converter with air and liquid cooling methods," *in Proc. of EPE 2013*, pp.1-10, 2013.

[29] M. A. Miner, "Cumulative damage in fatigue," *Journal of Applied Mechanics*, no. 12, A159-A164, 1945.

[30] E.ON-Netz. Requirements for offshore grid connections, Apr. 2008.

[31] D. Zhou, F. Blaabjerg, M. Lau, and M. Tonnes, "Thermal behavior optimization in multi-MW wind power converter by reactive power circulation," *IEEE Trans. Ind. Appl.*, vol. 50, no. 1, pp. 433-440, Jan. 2014.

[32] S. Busquets-Monge, R. Maheshwari, and S. Munk-Nielsen, "Over-modulation of n-level three-leg DC–AC diode-clamped converters with comprehensive capacitor voltage balance," *IEEE Trans. Ind. Electron.*, vol. 60, no. 5, pp. 1872-1883, May 2013.

[33] "Wind turbines – part I: design requirements", IEC 61400-1, 3rd edition.

[34] Vestas website (Available at: http://www.vestas.com/en/wind-power-plants/wind-project-planning/siting/wind-classes.aspx?action=3#/vestas-univers).

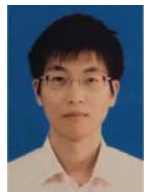

Dao Zhou (S'12) received the B.Sc. in electrical engineering from Beijing Jiaotong University, Beijing, China, in 2007, and the M. Sc. in power electronics from Zhejiang University, Hangzhou, China, in 2010. From 2012, he is pursuing the Ph.D degree in the Department of Energy Technology, Aalborg University, Aalborg, Denmark.

His research interests include two-level power electronics converters and their application in wind power generation systems.

Frede Blaabjerg (S'86-M'88-SM'97-F'03) was with ABB-Scandia, Randers, Denmark, from 1987 to 1988. From 1988 to 1992, he was a PhD student with Aalborg University, Aalborg, Denmark. He became an Assistant Professor in 1992, an Associate Professor in 1996, and a Full Professor of power electronics and drives in 1998. His current research interests include power electronics and its applications such as in wind turbines, PV systems, reliability, harmonics and adjustable speed drives.

He has received 15 IEEE Prize Paper Awards, the IEEE PELS

Distinguished Service Award in 2009, the EPE-PEMC Council Award in 2010, the IEEE William E. Newell Power Electronics Award 2014 and the Villum Kann Rasmussen Research Award 2014. He was an Editor-in-Chief of the IEEE TRANSACTIONS ON POWER ELECTRONICS from 2006 to 2012. He has been Distinguished Lecturer for the IEEE Power Electronics Society from 2005 to 2007 and for the IEEE Industry Applications Society from 2010 to 2011.

Mogens Lau received the M.Sc. in Electrical engineering from Aalborg University, Aalborg, Denmark, in 1999. He worked as development engineer, project manager and line manager within power electronics at leading companies like Siemens, Danfoss, Grundfoss and Vestas. Currently, he is the working with Siemens Wind Power A/S in Brande, Denmark.

Michael Tonnes received the M.Sc. EE degree from Aalborg University, Denmark in 1987, and the Ph.D. degree from the Institute of Energy Technology in 1990.

He was employed by Danfoss in 1987 to perform the Ph.D work within auto-tuning and automatic control of non-linear electrical machines and worked within the technology area of Motor Controls. Michael worked in US in Danfoss High Power Drives for the period 1996-98 and had various management positions within electronic businesses. At present he is Senior Director of R&D at Danfoss Silicon Power GmbH with base in Flensburg, Germany.

He is author and co-author on a number of articles within auto-tuning, motor controls and power electronics in general and holds several patents within the field motor controls and power electronics.

[A.7] D. Zhou, F. Blaabjerg, T. Franke, M. Tonnes, M. Lau, "Reduced cost of reactive power in doubly-fed induction generator wind turbine system with optimized grid filter," *in Proc. of ECCE 2014*, pp. 1490-1499, 2014.

Reduced Cost of Reactive Power in Doubly Fed Induction Generator Wind Turbine System with Optimized Grid Filter

Dao Zhou, Frede Blaabjerg
Department of Energy Technology
Aalborg University
Aalborg, Denmark
zda@et.aau.dk; fbl@et.aau.dk

Toke Franke, Michael Tonnes

Danfoss Silicon Power GmbH
Flensburg, Germany
toke.franke@danfoss.com; michael.tonnes@danfoss.com

Mogens Lau
Siemens Wind Power A/S
Brande, Denmark
mogens.lau@siemens.com

***Abstract*—The modern grid requirement has caused that the wind power system behaves more like conventional rotating generators and it is able to support certain amount of the reactive power. For a typical doubly-fed induction generator wind turbine system, the reactive power can be supported either through the rotor-side converter or the grid-side converter. This paper firstly compares the current ripples and supportive reactive power ranges between the conventional L and optimized LCL filter, if the reactive power is injected from the grid-side converter. Then, the loss distribution is evaluated both for the generator and the wind power converter in terms of the reactive power done by the rotor-side converter or the grid-side converter with various grid filters. Afterwards, the annual energy loss is also estimated based on yearly wind profile. Finally, experimental results of the loss distribution are performed in a down-scaled DFIG system. It is concluded that over-excited reactive power injected from the grid-side converter has lower energy loss per year compared to the over-excited reactive power covered by the rotor-side converter. Furthermore, it is also found that the annual energy loss could even become lower with the optimized filter and thereby more energy production for the wind turbine.**

I. INTRODUCTION

The voltage-source converter is widely used as an interface for the renewable energy systems before they are linked to the grid like in the photovoltaic and wind power system cases, with its advantages in fully control of dc-link voltage, active and reactive power as well as power factor [1]-[3]. A grid filter is normally introduced to avoid the PWM carrier and side-band voltage harmonics coupling to the grid that can disturb other sensitive loads or equipment. For the MW-level wind power converter, due to the quite low switching frequency of the power switching devices (usually several kilo-Hertz), a simple filter inductor consequently becomes bulky, expensive and it may also bring poorer dynamics into the system [4]-[6].

In order to fulfill the modern grid codes [7]-[9], the wind turbine system is currently required to behave more like a traditional power source (e.g. synchronous generator), which implies that the wind turbine system should have the capability of reactive power support. Due to the doubly-fed mechanism of the Doubly-Fed Induction Generator (DFIG) based wind turbine system, the reactive power can be supported either by the Grid-Side Converter (GSC) or the Rotor-Side Converter (RSC). If the reactive power is provided by the GSC, in case of the constant dc-link voltage, the modulation index is closely related to the filter inductance, and it will increase very fast to over-modulation, especially when over-excited reactive power is needed [10]. There are two ways to deal with this issue – increase the dc-link voltage, which gives higher switching loss and power rating, or design an optimized grid filter.

Besides, if a small amount of reactive power is demanded by the transmission system operator, it is also of interest to compare the loss of the whole DFIG system, as the reactive power supported by the GSC only affects the loss of the GSC, while the reactive provided by the RSC not only influences the loss of the RSC, but also the loss of the generator itself. Then, the annual energy loss of the wind turbine system and cost of the reactive power can be calculated based on the annual wind profile at different compensation schemes.

The structure of the paper is organized as the following. Section II addresses the function of the grid filter in terms of the grid current ripple and the reactive power range. Then the LCL filter design procedure and the characteristic comparison between the L filter and the LCL filter is discussed in Section III. The loss model and loss distribution

978-1-4799-5776-7/14/$31.00 ©2014 IEEE

of the DFIG model in the case of over-excited reactive power injection is followed in Section IV. According to an annual wind profile, Section V discusses the energy loss per year. Finally, after the loss distribution of different parts of the DFIG system is measured on a 7.5 kW test rig in Section VI, some concluding remarks are drawn in Section VII.

II. Functions of Grid Filter

One of the most popular concepts in the mainstream wind power system market is the DFIG configuration as shown in Fig. 1. Except for the advantage that the back-to-back power converter takes up only the slip power of the DFIG, this configuration has two possibilities to deliver the demanded reactive power, either from the generator's stator Q_s controlled by the RSC or from the GSC Q_g [10]. The control of the back-to-back power converter is described in [11].

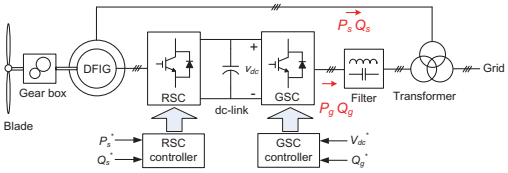

Fig. 1. Typical DFIG configuration in a wind turbine system (GSC: Grid-Side Converter, RSC: Rotor-Side Converter).

As recommended in IEEE 519-1992, harmonics higher than 35th should be explicitly limited [12]. If a simple L filter is assumed to be used, the current ripple amplitude is jointly decided by the dc-link voltage, the switching frequency and inductance value [13]. For a typical 2 MW DFIG based wind turbine system, the main parameters of which are listed in TABLE I, the relationship between the current ripple and the loading is shown in Fig. 2(a). It is noted that as expected the higher inductance is, the lower switching current ripple will be.

TABLE I

Basic Parameters of a 2 MW DFIG System

Rated power P_s	2 MW
Range of DFIG rotor speed n_r	1050 – 1800 rpm
Line frequency f_l	50 Hz
Rated line voltage amplitude U_{gm}	563 V
DC-link voltage U_{dc}	1050 V
Switching frequency f_s	2 kHz

As aforementioned, the value of the filter inductance also affects the modulation index. Fig. 2(b) indicates the relationship between the dc-link voltage and the reactive power (the fully modulation index is assumed). In order to fulfill the reactive power range stated in E.ON Netz [7], the DFIG system should cover up to 0.4 pu Over-Excited (OE) and 0.3 pu Under-Excited (UE) reactive power in respect to the generator power rating. As the pu value is normally defined by the power rating of the induction generator, the used pu value in Fig. 2(b) becomes 2.0 pu OE and 1.5 pu UE reactive power in respect to the GSC, which is five times higher than the pu value seen from the induction generator due to the rated slip power through the GSC. It can be seen that the minimum dc-link voltage increases considerably with higher inductance if the OE reactive power is needed. On the other hand, the higher inductance results in a lower switching ripple. Thus, it is a trade-off procedure and if the inductance is e.g. selected at 0.1 pu, in which the current ripple will be 40% at the rated power due to the low switching frequency. However, for the DFIG system shown in Fig. 1, the final current ripple of the grid side is calculated as the sum of the stator current and the GSC current. Generally, the stator current is much higher than the GSC current, which implies that 40% current ripple at the GSC is acceptable and it is used as the design criteria.

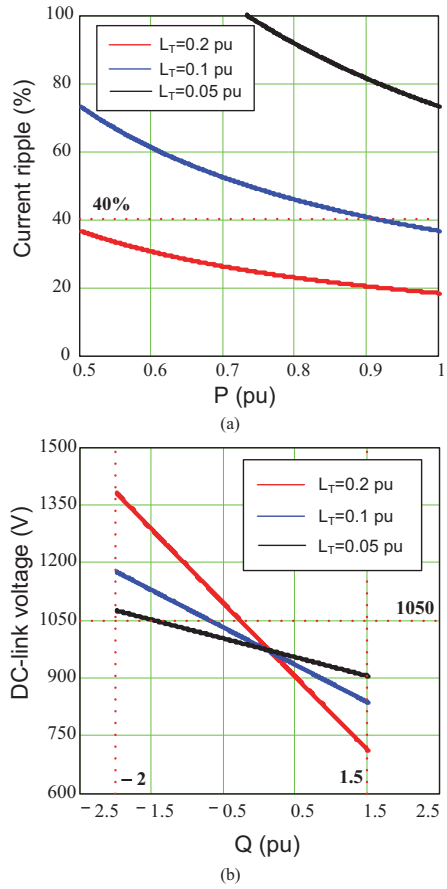

Fig. 2. Influence of grid filter inductance on the GSC performance. (a) Current ripple rate; (b) Reactive power range.

III. Characteristic Comparison of an L and LCL Filter

The equivalent single-phase GSC with an LCL filter is shown in Fig. 3, which typically has no additional sensors compared to the conventional L filter configuration. Although the different positions of the voltage and current sensors may have their own advantages [13], the current sensors on the converter side is chosen, because it can be designed to protect the power semiconductor and it is commonly used in industrial application.

A. Design procedure of LCL filter

As shown in Fig. 3, L_c is the converter side inductance, L_f is the grid side inductance, and C_f is the capacitor bank, which is connected to a damping resistance R_d. The converter current and the grid current are represented by i and i_g. Moreover, the voltage of the converter output and the point of common coupling are represented by v_i, v_g, respectively.

A step-by-step design procedure for LCL filter is described in [3]. This design is focused on that the total inductance of the LCL filter is able to reduce to half compared to the L filter but with the similar current ripple at the grid side. Afterwards, a proper inductance sharing into L_c (0.025 pu) and L_g (0.025 pu) is realized in order to achieve the desired current ripple reduction. The capacitance value (0.1 pu) is then determined by the absorbed reactive power at the rated conditions, in which the resonant frequency becomes 1.35 kHz (67.5% of f_{sw}). The passive damping is inevitably designed to overcome the resonant problem, where its power dissipation is also taken into account [3], [13]-[15]. The used filter parameters are summarized in TABLE II.

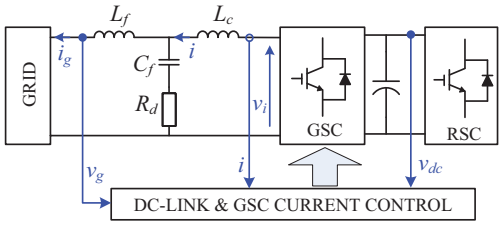

Fig. 3. Equivalent single-phase grid-side converter with LCL filter.

TABLE II

L and LCL Filter Parameters

L filter	Filter inductor L_l	500 μH
LCL filter	Converter-side inductor L_c	125 μH
	Grid-side inductor L_f	125 μH
	Filter capacitor C_f	220 μF
	Damping R_d	0.5 mΩ

B. Characteristic comparison between L and LCL filter

If the transfer function of the PI current controller, the modulation technique as well as some delays introduced by the digital control are considered, the open-loop Bode plots of the L and the LCL filter from the GSC current reference to the line current is then shown in Fig. 4. It is clear that the magnitude and phase characteristic between the L and LCL filter are exactly the same at lower frequency, if the PI parameter used in the current controller is under proper design. It is also noted that the smaller magnitude of the LCL filter appears at the switching frequency compared to the L filter. Moreover, the damping of the LCL filter has a better performance compared to the L filter above the switching frequency as expected.

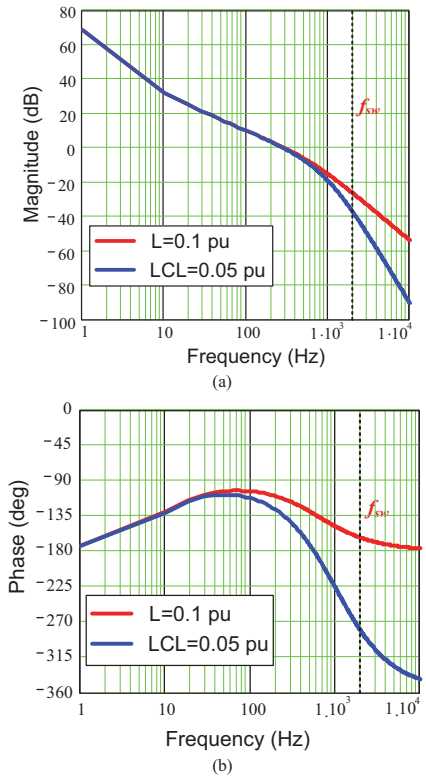

Fig. 4. Bode plot comparison between pure L filter (0.1 pu) and designed LCL filter (0.05 pu). (a) Magnitude diagram; (b) Phase diagram.

IV. Loss Breakdown of DFIG System

The reactive power injection basically consists of the OE reactive power and the UE reactive power. As analyzed in [16], the specific OE reactive power injection decreases the efficiency of the DFIG system. Consequently, only this kind of reactive power operation is in focus in this paper.

A. Loss model of DFIG system

As shown in Fig. 1, the common-adopted methodology to compensate the reactive power is from the stator of the induction generator, due to the fact that it introduces a small increase of the rotor-side current because of the winding ratio between the stator and the rotor of the DFIG [17]. However, this approach not only affects the loss of the RSC, but also imposes the loss of the DFIG itself.

Loss dissipation inside the induction generator generally consists of the copper loss and iron loss as shown in Fig. 5 [18]. If the stator voltage oriented control is applied, the stator-side active power P_s and reactive power Q_s are independently in line with the stator d-axis current i_{sd} and q-axis current i_{sq}. Due to the flux equation existing in the DFIG, the relationship between the rotor and stator current under d-axis and q-axis are,

$$\begin{cases} i'_{rd} = -\dfrac{L_{ls}+L_m}{L_m} i_{sd} \\ i'_{rq} = -\dfrac{U_{sm}}{\omega_1 \cdot L_m} - \dfrac{L_{ls}+L_m}{L_m} i_{sq} \end{cases} \tag{1}$$

where L_{ls} and L_m denote the stator leakage inductance and the magnetizing inductance, U_{gm} denotes the rated grid phase-voltage, and ω_1 is the fundamental electrical angular frequency.

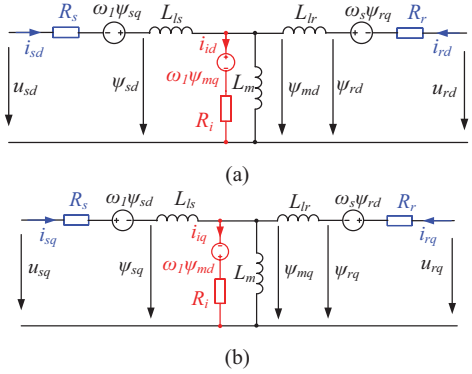

Fig. 5. DFIG equivalent circuit considering copper loss and iron loss. (a) d-axis circuit; (b) q-axis circuit.

The copper loss P_{cu} is resistive losses occurring in the winding coils and can be calculated using the equivalent d-q axis circuit stator resistance R_s and rotor resistance R_r as shown in Fig. 5,

$$P_{cu} = \frac{3}{2} \cdot [(i_{sd}^2 + i_{sq}^2) \cdot R_s + (i_{rd}^2 + i_{rq}^2) \cdot R_r] \tag{2}$$

where i_s and i_r denote the stator current and the rotor current, and the subscript d and q denote the value at d-axis and q-axis circuit, respectively. It can be seen that the copper loss of the induction generator is jointly dependent on the stator active power and reactive power.

Generally, the iron loss is produced by the flux change, and it consists of eddy current loss and hysteresis loss, both of which are tightly connected with the operation frequency and flux density [18]. This method needs to know the empirical formula in advance, and the calculation is normally done according to the Finite Element Method (FEM). Alternatively, iron losses can be estimated from the electrical point of view [19], [20]. In other words, it can be expressed by the equivalent iron resistance R_i in parallel with the magnetizing inductance as shown in Fig. 5.

The voltage equations for the additional iron resistor are,

$$\begin{cases} R_i \cdot i_{id} = \dfrac{d\psi_{md}}{dt} - \omega_1 \cdot \psi_{mq} \\ R_i \cdot i_{iq} = \dfrac{d\psi_{mq}}{dt} + \omega_1 \cdot \psi_{md} \end{cases} \tag{3}$$

where i_i is the equivalent iron loss current, ψ_m is the magnetizing flux. Moreover, with the aid of the relationship between the stator flux and magnetizing flux,

$$\begin{cases} \psi_{md} = \psi_{sd} - L_{ls} \cdot i_{sd} \\ \psi_{mq} = \psi_{sq} - L_{ls} \cdot i_{sq} \end{cases} \tag{4}$$

where ψ_s denotes the stator flux, L_{ls} denotes the stator leakage inductance.

Due to the stator voltage orientation, ψ_{md} is nearly zero, and ψ_{mq} is a constant value because of the stiff grid with the constant voltage and constant frequency. Substituting (4) into (3), the iron current can be deduced,

$$\begin{cases} i_{id} = \dfrac{\omega_1 L_{ls}}{R_i} \cdot i_{sq} + \dfrac{U_{gm}}{R_i} \\ i_{iq} = -\dfrac{\omega_1 L_{ls}}{R_i} \cdot i_{sd} \end{cases} \tag{5}$$

According to (5), it is noted that the d-axis iron loss current depends on the reactive power Q_s, while the q-axis iron loss current is related with the active power P_s. As a consequence, the iron loss P_{fe} can be calculated as,

$$P_{fe} = \frac{3}{2} \cdot [(i_{id}^2 + i_{iq}^2) \cdot R_i] \tag{6}$$

In respect to the losses of the power converter of the DFIG system, it is well described in [16]. If the reactive power is provided by the RSC, the loss model of the generator (copper loss and iron loss) and the RSC (conduction loss and switching loss both in the IGBT and the freewheeling diode) is shown in Fig. 6(a). It is evident that if the references of the active power, reactive power and slip

are known in advance, together with the information of the generator and power switching devices, each type of the losses can be analytically calculated.

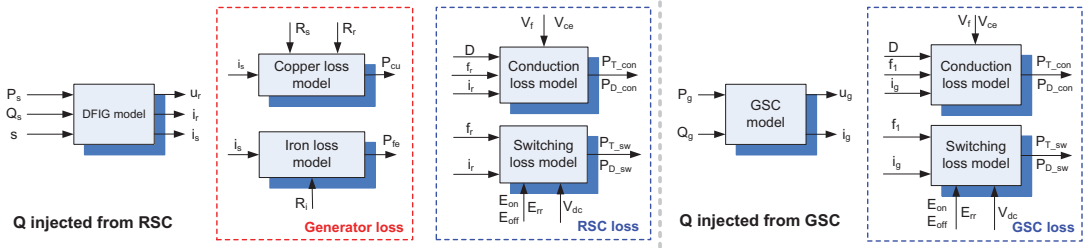

(a) (b)

Fig. 6. Framework of power loss estimation. (a) Reactive power is injected by the RSC; (b) Reactive power is injected by the GSC.

With the aid from the GSC, another approach may be realized to compensate the reactive power, which stresses the GSC and affects the loss of the GSC and the filter. Compared with the GSC losses, the grid filter loss is small enough [21], and it is simply calculated by its parasitic Equivalent Series Resistance (ESR). Similarly, as the conduction loss and switching loss of the IGBT and the diode are analytically solved, thus the GSC loss can be calculated as shown in Fig. 6(b).

B. Loss breakdown of DFIG system

The loss distribution of the whole DFIG system is firstly evaluated at the normal operation (NOR), i.e. no reactive power is exchanged between the DFIG system and the grid. Then, the loss distribution is given in case of the OE reactive power is fully from the RSC (OE_RSC) or the GSC. As the type of the grid filter only influences the loading of the GSC, it can be further divided by L filter (OE_L_GSC) and LCL filter (OE_LCL_GSC). The above cases are summarized in TABLE III. It is worth to mention that the dc-link voltage can be different at various compensation schemes which is consistent with Fig. 2(b). It can be seen that the OE_L_GSC has a higher dc voltage than the OE_LCL_GSC, due to the higher total inductance of the filter.

TABLE III

CASES FOR NORMAL OPERATION AND OVER-EXCITED REACTIVE POWER INJECTION

	Q_s (pu)	Q_g (pu)	U_{dc} (V)
NOR	0	0	1050
OE_RSC	0.4	0	1050
OE_L_GSC	0	0.4	1250
OE_LCL_GSC	0	0.4	1100

The loss breakdown at the rated power of the four cases in terms of the DFIG, the RSC and the GSC is then shown in Fig. 7. In respect to the generator loss, together with the parameters of the DFIG listed in TABLE IV, it can be seen that the generator losses (especially copper losses) increase only in the OE_L_RSC compared to the NOR in Fig. 7(a), because the reactive power injection by the RSC changes the generator's stator and rotor current amplitude. In respect to the RSC losses, it also increases considerably in the OE_L_RSC. Moreover, the power loss (especially the switching loss) increases slightly in OE_L_GSC and OE_LCL_GSC compared to NOR operation, since the dc-link voltage becomes higher. For the GSC losses, OE_L_RSC stays the same with the NOR operation. However, if the reactive power is supported by the GSC, both the conduction losses and the switching losses increase significantly because of the dominating reactive current, and it also becomes three times higher than in the case that the reactive power is injected by the RSC. The tendency of the grid filter loss is similar to the GSC because of the same current through them. It is noted that if the OE reactive power is compensated from the GSC, the LCL filter consumes lower power loss due to the smaller ESR compared to the pure L filter. Besides, compared with the loss of the DFIG and the power converter, the loss dissipated in the DFIG is dominant.

TABLE IV

2 MW GENERATOR AND BACK-TO-BACK POWER CONVERTER

Generator	Rated power P_s	2 MW
	Rated line voltage U_{sm}	563 V
	Stator leakage inductance L_{ls}	0.050 pu
	Rotor leakage inductance L_{lr}	0.085 pu
	Magnetizing inductance L_m	3.840 pu
	Stator resistance R_s	0.007 pu
	Rotor resistance R_r	0.006 pu
	Equivalent iron loss resistance R_i	99.853 pu
	Ration of stator and rotor winding	0.369
Power converters	Used power module	1 kA/1.7 kV
	Grid-side converter	Single
	Rotor-side converter	Two in parallel

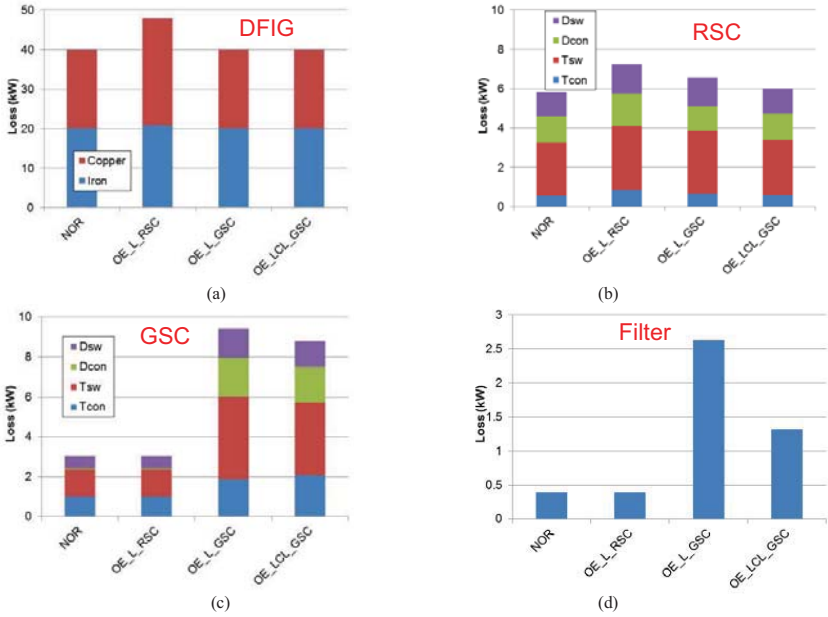

Fig. 7. Loss breakdown at rated wind speed (11 m/s) with various reactive power compensation schemes. (a) DFIG itself; (b) Rotor-side converter; (c) Grid-side converter; (d) Grid filter.

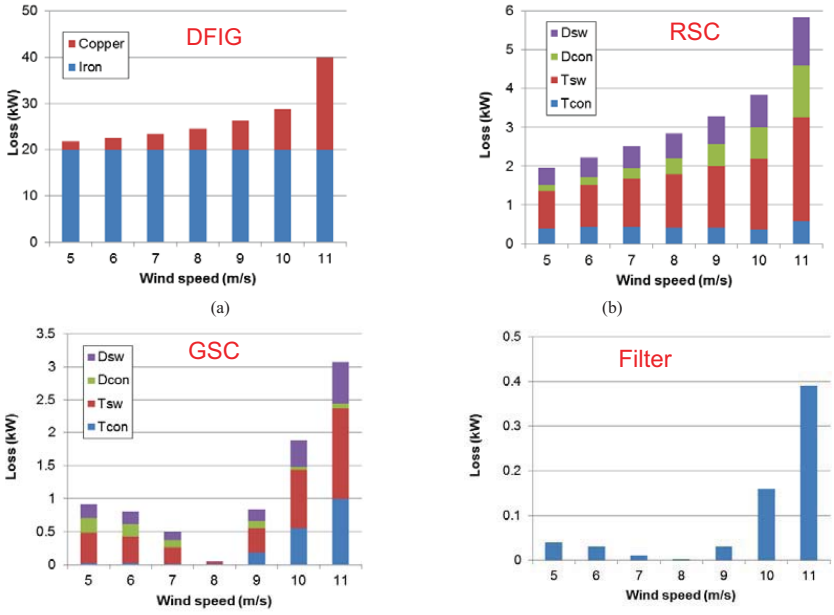

Fig. 8. Loss breakdown at normal operation (NOR) with different wind speeds. (a) DFIG itself; (b) Rotor-side converter; (c) Grid-side converter, (d) Grid filter.

From another perspective - if no reactive power is required, the power loss of various parts in the DFIG system at different wind speeds are shown in Fig. 8 (assuming that after 11 m/s wind turbine is operating at full load). In Fig. 8(a), it is noted that the iron loss stays almost constant at various wind speed, while the copper loss changes dynamically. For the RSC losses shown in Fig. 8(b), it increases with the higher wind speed. In respect to the GSC losses at different wind speeds, it can also be seen that the power loss becomes low at 8 m/s, which is regarded as the synchronous operation as shown in Fig. 8(c). The loss of the grid filter is much smaller than the GSC as shown in Fig. 8(d).

V. Energy Loss Based on Annual Wind Profile

Based on the power loss model and the loss distribution with various amounts of reactive power described in Section IV, this section further estimates the energy loss and cost of reactive power according to an annual wind profile.

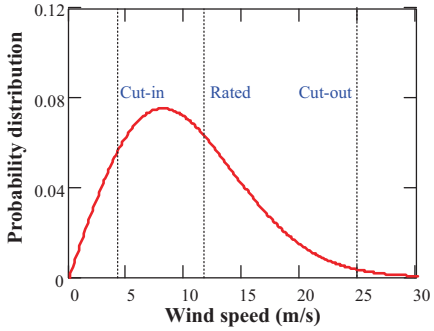

Fig. 9. Class I annual wind distribution defined by IEC standard [22].

The annual wind of Weibull distribution according to the IEC standard - Class I [22], [23] with the mean wind speed 10 m/s is shown in Fig. 9. As each loss (kW) at various wind speeds can be calculated by a wind speed step of 1 m/s as shown in Fig. 8, as well as the yearly wind speed distribution (hours), the annual loss of energy can be calculated. It is worth to mention that the annual loss of energy is only concerned from the cut-in to the rated wind speed, because if the wind speed is higher than rated value, it is assumed that the power loss dissipated (loss of energy production) in the DFIG system can be compensated by the mechanical power from the wind turbine blades.

The annual energy loss of the DFIG system at various operation modes is shown in Fig. 10(a). It is evident that the energy consumed by the induction generator is much higher than in the back-to-back power converter. Moreover, it can be seen that, although the OE reactive power compensation from the GSC significantly imposes the loading of the GSC itself and its filter, the OE_LCL_GSC still has the lowest loss of energy, while the OE_RSC consumes the highest energy loss, as the OE reactive power compensated from the RSC further increases the loss of the DFIG.

It is also an interesting perspective to express the annual energy loss in terms of the percentage over the yearly produced energy, which is accumulated from the cut-in until the cut-off wind speed. As shown in Fig. 10(b), under the assumption that the OE reactive power is required all year around, the worst case is the OE_RSC that takes up 2.05% annual energy, while the best situation is achieved by the OE_LCL_GSC 1.98%, which implies 3.73% energy saving per year.

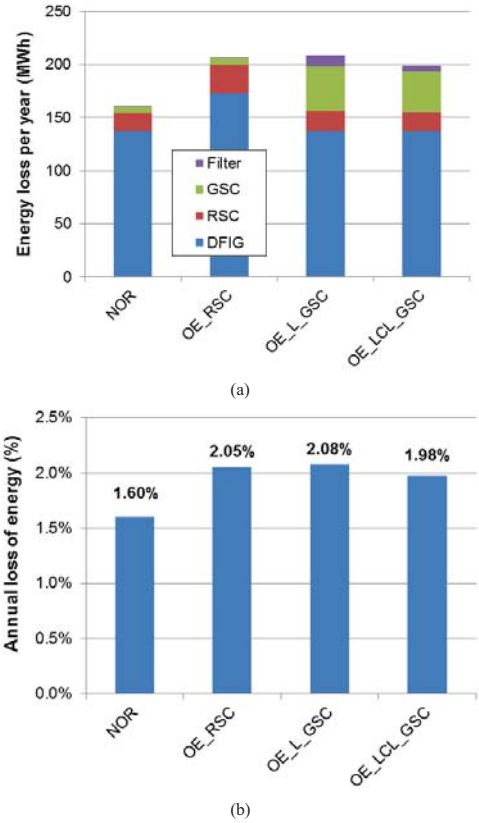

Fig. 10. Annual loss of energy in normal operation and if the OE reactive power is required all year around. (a) Energy loss per year (MWh); (b) Annual loss of energy (%).

VI. Experimental Verification of Loss Dissipation

In order to validate the loss dissipation of the DFIG system at different reactive power compensation methods, a down-scaled 7.5 kW test rig is built up and shown in Fig. 11. The DFIG is externally driven by a prime motor, and two 5.5 kW Danfoss motor drives are used for the GSC and the RSC, both of which are controlled with dSPACE 1006 controllers. Besides, the LCL filter is employed as the grid filter, whose

capacitor branch can be bypassed to realize the L type filter. The important parameters of the test setup are summarized in TABLE V. It is noted that, as the rated rotor speed is 1800 rpm, the pu value of the grid filter is calculated based on the slip power of the DFIG.

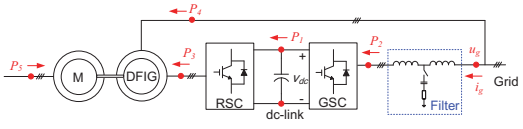

Fig. 11. Setup of 7.5 kW DFIG test rig.

TABLE V

7.5 KW GENERATOR AND 5.5 KW BACK-TO-BACK POWER CONVERTER

Generator	Rated power	7.5 kW
	Rated line voltage	380 V
	Stator leakage inductance	0.056 pu
	Rotor leakage inductance	0.084 pu
	Magnetizing inductance	1.294 pu
	Stator resistance	0.022 pu
	Rotor resistance	0.033 pu
	Equivalent iron loss resistance	35.734 pu
	Ratio of stator and rotor winding	0.336
Power converters	Rated power	5.5 kW
	Grid-side converter rated current	10 A
	Rotor-side converter rated current	10 A
	Switching frequency	5 kHz
Grid filters	L type	
	Interface inductance L_l	5.9% pu
	LCL type	
	Converter-side inductor L_c	3.6% pu
	Grid-side inductor L_f	2.3% pu
	Filter capacitor C_f	20.0% pu
	Damping R_d	13.4% pu

In the condition that the full power of the DFIG 7.5 kW is realized at 1800 rpm, 0.4 pu reactive power according to the grid codes is compensated from the GSC, the current injecting to the grid from the back-to-back power converter is compared with the LCL and L filter as shown in Fig. 12. It is noted that the fundamental currents of the L and the LCL filter both are 4.2 A, and the currents are leading the grid voltage 90 degree, as the majority of which belongs to the reactive component. Furthermore, the maximum value of the harmonic spectrum around the switching frequency is 105 mA with the L filter, which is much higher than the LCL filter 25 mA.

The loss dissipation of the various parts in the down-scaled DFIG system is monitored by Yokogawa Power Analyzer WT3000. The loss of the DFIG itself, the RSC, the GSC and the grid filter are tested separately and they are shown in Fig. 13, in which four conditions are taken into account consistent with Fig. 8. It is worth to mention that the dc-link used in the above four cases is 600 V, 600 V, 750 V and 650 V, respectively. In respect to the loss of the DFIG itself and the RSC, it consumes the highest in the case that the reactive power is compensated from the RSC. However, regarding the GSC, the reactive power supported by the GSC with the L filter leads to the highest power loss. Although the loss consumed in the DFIG actually contains both the DFIG loss and the prime motor loss, the loss dissipation is still much higher compared to the power electronic converters. The loss distribution of various parts is quite similar as analyzed in Fig. 8. The experimental result of total loss dissipation in the DFIG system at 1800 rpm is then shown in Fig. 14.

VII. CONCLUSION

This paper has firstly studied the influence of the grid filter inductance on the current ripple and the reactive power range for a DFIG wind turbine system. Then, an optimized LCL filter design is achieved with half value of the total inductance compared to the pure L-filter.

Due to the existence of the two possibilities to generate the demanded reactive power for the DFIG system – controlled by the rotor-side converter and controlled by the grid-side converter, each of them is analyzed in terms of the DFIG loss and the power converter loss. It is concluded that although the compensation from the grid-side converter significantly increases the power loss of the grid-side converter itself, it will still have lower total loss dissipation of the whole DFIG system, as the compensation approach by the rotor-side converter will impose the DFIG loss as well as the rotor-side converter loss.

Based on a typical annual wind speed distribution, the loss of energy per year is finally discussed. It can be seen that the injection of reactive power is actually not free-of-charge. Assuming the cost the offshore wind power is 0.2 Euro/kWh, compared with the normal operation of 1.60% annual energy loss (32,200 Euro), if the over-excited reactive power is injected by the rotor-side converter, it will increase to 2.05% annual energy loss (41,300 Euro) when the reactive power is needed all year around. On the other hand, if the grid filter is properly designed and the over-excited reactive power is supported by the grid-side converter, the annual energy loss becomes 1.98% (39,700 Euro), which implies 3.73% (1,500 Euro) energy saving per year compared to the over-excited reactive done with the rotor-side converter.

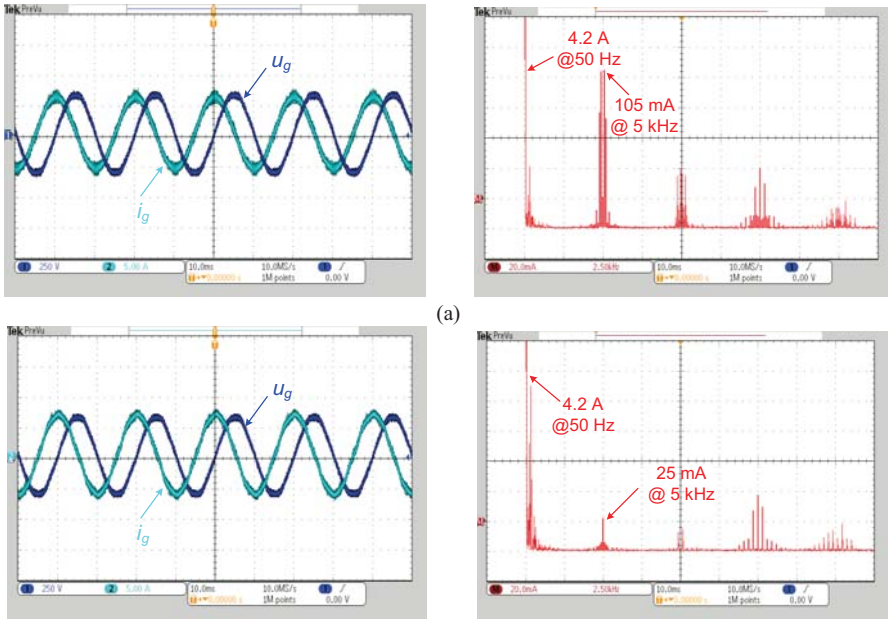

Fig. 12. Waveform and the harmonic of the grid current. (a) L filter; (b) LCL filter.

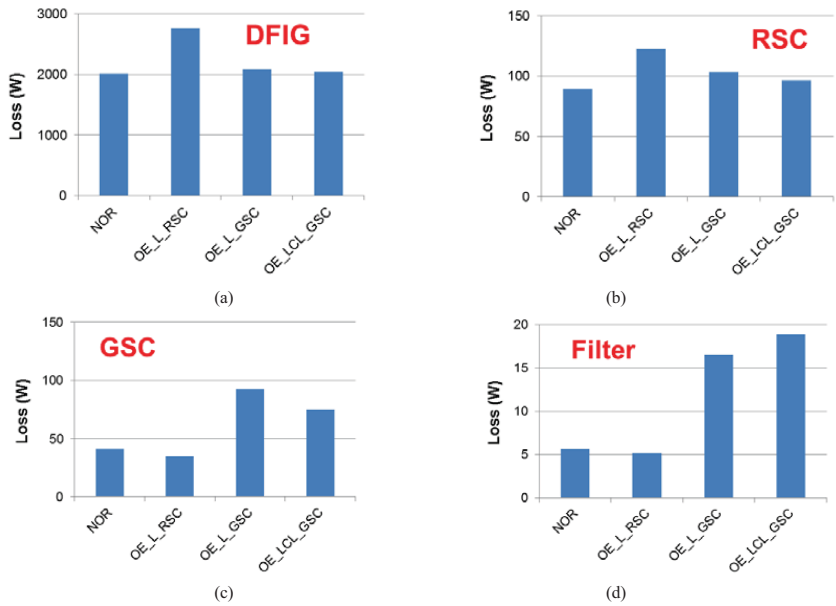

Fig. 13. Measured loss dissipation in the DFIG system at 1800 rpm in case of the normal operation and the various reactive power compensation schemes. (a) DFIG itself; (b) Rotor-side converter; (c) Grid-side converter; (d) Grid filter.

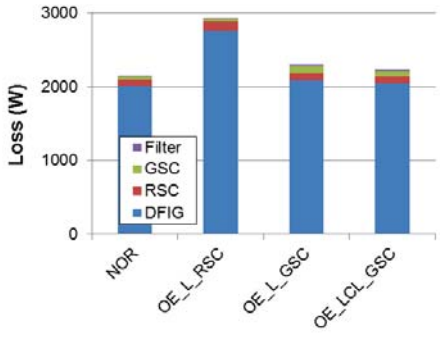

Fig. 14. Experimental result of total loss dissipation in the DFIG system at 1800 rpm in case of the normal operation and the various reactive power compensation schemes.

REFERENCES

[1] A. A. Rockhill, M. Liserre, R. Teodorescu, P. Rodriguez, "Grid-filter design for a multi-megawatt medium-voltage voltage-source inverter," *IEEE Trans. Industrial Electronics*, vol. 58, no. 4, pp. 1205-1217, Apr. 2011.

[2] M. Liserre, F. Blaabjerg, A. Dell'Aquila, "Step-by-step design procedure for a grid-connected three-phase PWM voltage source converter," *International Journal of Electronics*, 91(8), pp. 445-460, Jan. 2004.

[3] M. Liserre, F. Blaabjerg, S. Hansen, "Design and control of an LCL-filter-based three-phase active rectifier," *IEEE Trans. Industry Applications*, vol. 41, no. 5, pp. 1281-1291, Sep. 2005.

[4] Z. Chen, J. M. Guerrero, F. Blaabjerg, "A review of the state of the art of power electronics for wind turbines," *IEEE Trans. Power Electronics*, vol. 24, no. 8, pp. 1859-1875, Aug. 2009.

[5] F. Blaabjerg, Z. Chen, S. B. Kjaer, "Power electronics as efficient interface in dispersed power generation systems," *IEEE Trans. Power Electronics*, vol. 19, no. 5, pp. 1184- 1194, Sep. 2004.

[6] M. Liserre, R. Cardenas, M. Molinas, J. Rodriguez, "Overview of multi-MW wind turbines and wind parks," *IEEE Trans. Industrial Electronics*, vol. 58, no. 4, pp. 1081-1095, Apr. 2011.

[7] E.ON-Netz. Requirements for offshore grid connections, Apr. 2008.

[8] M. Tsili, S. Papathanassiou, "A review of grid code technical requirements for wind farms," *IET on Renewable Power Generation*, vol. 3, no. 3, pp. 308-332, Sep. 2009.

[9] A. Camacho, M. Castilla, J. Miret, R. Guzman, A. Borrell, "Reactive power control for distributed generation power plants to comply with voltage limits during grid faults," *IEEE Trans. on Power Electronics*, IEEE early access.

[10] D. Zhou, F. Blaabjerg, M. Lau, M. Tonnes, "Thermal behavior optimization in multi-MW wind power converter by reactive power circulation," *IEEE Trans. Industry Applications*, vol. 50, no. 1, pp. 433-440, Jan. 2014.

[11] S. Muller, M. Deicke, R. W. De Doncker, "Doubly fed induction generator systems for wind turbines," *IEEE Industry Applications Magazine*, vol. 8, no. 3, pp. 26-33, May 2002.

[12] A. Nagel, R. W. De Doncker, "Systematic design of EMI-filters for power converters," *in Proc. of IAS 2000*, pp. 2523-2525, 2000.

[13] R. Teodorescu, M. Liserre, P. Rodriguez, *Grid Converters for Photovoltaic and Wind Power Systems.* Hoboken, NJ, USA: Wiley, 2011.

[14] R. Pena-Alzola, M. Liserre, F. Blaabjerg, R. Sebastian, J. Dannehl, F. W. Fuchs, "Analysis of the passive damping losses in LCL-filter-based grid converters," *IEEE Trans. on Power Electronics*, vol. 28, no. 6, pp. 2642-2646, Jun. 2013.

[15] W. Wu, Y. He, T. Tang, F. Blaabjerg, "A new design method for the passive damped LCL and LLCL Filter-based single-phase grid-tied inverter," *IEEE Trans. on Industrial Electronics*, vol. 60, no. 10, pp. 4339-4350, Oct. 2013.

[16] D. Zhou, F. Blaabjerg, M. Lau, M. Tonnes, "Thermal cycling overview of multi-megawatt two-level wind power converter at full grid code operation," *IEEJ Journal of Industry Applications*, vol. 2, no. 4, pp. 173-182, Jul. 2013.

[17] S. Engelhardt, I. Erlich, C. Feltes, J. Kretschmann, F. Shewarega, "Reactive power capability of wind turbines based on doubly fed induction generators," *IEEE Trans. Energy Conversion*, vol. 26, no. 1, pp. 364-372, Mar. 2011.

[18] R. Takahashi, H. Ichita, J. Tamura, M. Kimura, M. Ichinose, M. Futami, K. Ide, "Efficiency calculation of wind turbine generation system with doubly-fed induction generator," *in Proc. of International Conference on Electrical Machines (ICEM) 2010*, pp. 1-4, 2010.

[19] S. Wee, M. Shin, D. Hyun, "Stator-flux-oriented control of induction motor considering iron loss," *IEEE Trans. on Industrial Electronics*, vol. 48, no. 3, pp. 602-608, Jun. 2001.

[20] A. G. Abo-Khalil, H. Park, D. Lee, "Loss minimization control for doubly-fed induction generators in variable speed wind turbines," *in Proc. of IECON 2007*, pp. 1109-1114, 2007.

[21] C. Sintamarean, F. Blaabjerg, H. Wang, "Comprehensive evaluation on efficiency and thermal loading of associated Si and SiC based PV inverter applications," *in Proc. of IECON 2013*, pp. 555-560, 2013.

[22] Wind turbines – part I: design requirements", IEC 61400-1, 3rd edition.

[23] Vestas website (Available at: http://www.vestas.com/en/wind-power-plants/wind-project-planning/siting/wind-classes.aspx?action=3#/vestas-univers).

[A.8] D. Zhou, F. Blaabjerg, T. Franke, M. Tonnes, M. Lau, " Reliability and energy loss in full-scale wind power converter considering grid codes and wind classes," *in Proc. of ECCE 2014*, pp. 3067-3074, 2014.

Reliability and Energy Loss in Full-scale Wind Power Converter Considering Grid Codes and Wind Classes

Dao Zhou, Frede Blaabjerg
Department of Energy Technology
Aalborg University
Aalborg, Denmark
zda@et.aau.dk; fbl@et.aau.dk

Toke Franke, Michael Tonnes
Danfoss Silicon Power GmbH
Flensburg, Germany
toke.franke@danfoss.com; michael.tonnes@danfoss.com

Mogens Lau
Siemens Wind Power A/S
Brande, Denmark
mogens.lau@siemens.com

***Abstract*—With the increasing penetration of the wind power, reliable operation and cost-effective wind energy production are of more and more importance. As one of the promising configurations, the cost on reliability and production losses of permanent-magnet synchronous generator based full-scale wind power converter is studied considering the grid code with reactive power production as well as the annual wind profile. Regarding the reliability, it is found that either the Over-Excited (OE) or the Under-Excited (UE) reactive power injection threatens the lifespan under all wind classes. Meanwhile, if the specific designed wind turbine system operates at different wind classes, it can be seen that higher wind class level results in lower lifetime of the power converter. In respect to the cost of the reactive power, either the OE or the UE reactive power increases the energy loss per year significantly if they are provided all year around, in which the OE reactive power injection even has a worse scenario. Moreover, it is also concluded that in order to realize an energy loss saving of the wind turbine system, the constant power factor control strategy is more preferred compared to an extreme reactive power injection.**

I. INTRODUCTION

With the increasing penetration of wind power during recent decades, reliable operation and cost-effective wind energy production are of more and more importance [1]-[3]. Due to the fact that the wind turbine system is required to behave like a conventional synchronous generator (including the capability of the active power and the reactive power) and to overcome the Low Voltage Ride-Through (LVRT), the Permanent-Magnet Synchronous Generator (PMSG) based configuration might become attractive seen from the wind turbine manufacturers [4], since the employed power electronic converter can handle the full-scale of generator power and decouple the grid and the generator.

Another tendency of the wind power development is the popularity of the offshore wind farms, which pushes the wind turbine system to operate with reliable and cost-effective performance. Reliability and robustness of the system are closely related to its mission profile - the representation of all relevant conditions that the system will be exposed to in all of its intended application throughout its entire life cycle [5]. Then the failure may happen during the violation of the strength and stress analysis, in which the stressor factors may be due to the environmental loads (like thermal, mechanical, humidity, etc.), or the functional loads (such as usage profiles, electrical operation). Among the stressors distribution, the thermal cycling accounts for more than a half of the failure probability [5]. On the basis of the universal approach of power semiconductor device reliability assessment stated in [6]-[8], the lifespan of the vulnerable power electronic converter is focused on in terms of thermal cycling caused by the alternative current with one fundamental period.

Widely use of the renewable energy tightly relies on the Levelized Cost Of Electricity (LCOE), whose value is expected to be lower than the traditional fossil energy by the end of the 2030 according to a German report [9]. As studied in [10], [11], the higher lifespan of the renewable energy plant or the higher annual energy production makes the LCOE decrease. Moreover, the produced energy per year of a typical PV plant is not only connected to the site environment (e.g. solar irradiance and ambient temperature), but also limited by the power conversion technology and the commands from the Transmission System Operator (TSO). Consequently, for wind power application, it is necessary to evaluate and analyze the effects of reactive power injection on the energy loss, which will be focused on in this paper.

The structure of this paper is organized as follows. A typical 2 MW PMSG system and the analytical approach to

978-1-4799-5776-7/14/$31.00 ©2014 IEEE

predict the power loss of power switching device are addressed in Section II. Then Section III focuses on the lifetime estimation of the power device seen from the thermal cycling point of view with various reactive power injections and various wind classes. Section IV discusses the annual energy production according to annual wind profile, and addresses the cost of energy loss regarding the various operational modes to inject reactive power. Finally, concluding remarks are drawn in Section V.

II. Loss Calculation of Power Device

A. Configuration of PMSG System

As the TSO recently tightens the LVRT capability of renewable energy system, a PMSG based wind turbine system with full-scale power converter is more widely employed due to its advantage of full power controllability [12]. The back-to-back power converter consists of the generator-side converter and the grid-side converter as shown in Fig. 1. For the generator-side converter, it keeps the rotor speed of the PMSG operating at the Maximum Power Point Traction (MPPT) and the transfers the active power from the wind to the grid. For the grid-side converter, it is designed not only for constant dc-link voltage, but also to provide the full amount of the reactive power required by the TSO. As only the grid-side converter is responsible to react to the grid code requirements, this part is mainly focused in this paper. A popular low-voltage 2 MW PMSG system is selected for a case study, and the parameters of the system are listed in TABLE I [13].

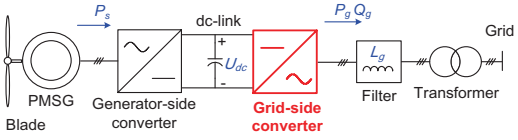

Fig. 1. Configuration of the full-scale power converter based permanent-magnet synchronous generator wind turbine system.

TABLE I

Basic Parameters of 2 MW PMSG System

Rated power P_g	2 MW
Rated line voltage amplitude U_{gm}	563 V
Rated loading current amplitude I_{gm}	2368 A
DC-link voltage U_{dc}	1.1 kV
Grid filter inductance L_g	0.15 mH (0.2 pu)
Line frequency f_1	50 Hz
Switching frequency f_s	2 kHz
Power modules inside grid-side converter leg	1 kA/1.7 kV; four parallel
Cut-in wind speed	4 m/s
Rated wind speed	12 m/s
Cut-out wind speed	25 m/s

B. Derterming Factors of Power Device Loading

If a simple inductor L_g is introduced as the grid filter shown in Fig. 2(a), Fig. 2(b) indicates that the amplitude of the converter output voltage u_c and output current i_g and displacement angle between them φ_{iu} can be expressed in terms of the active power P_g and reactive power Q_g [14],

$$i_g = \sqrt{\left(\frac{P_g}{1.5U_{gm}}\right)^2 + \left(\frac{Q_g}{-1.5U_{gm}}\right)^2} \quad (1)$$

$$u_c = \sqrt{\left(U_{gm} - \frac{X_g \cdot Q_g}{1.5U_{gm}}\right)^2 + \left(-\frac{X_g \cdot P_g}{1.5U_{gm}}\right)^2} \quad (2)$$

$$\varphi_{iu} = a\tan\left(\frac{Q_g}{P_g}\right) - a\tan\left(\frac{X_g \cdot P_g / 1.5U_{gm}}{U_{gm} - X_g \cdot Q_g / 1.5U_{gm}}\right) \quad (3)$$

where X_g denotes the grid filter reactance at the line frequency f_1. It is noted that for the grid-tied converter, the current stress of the power device is determined by the produced active power and reactive power as illustrated in (1), while the voltage stress of the power device, as stated in (2), is not only related to the above mentioned active and reactive power, but also linked to the value of the grid filter inductor.

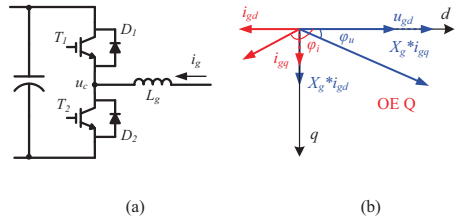

Fig. 2. Illustration of the grid-side converter. (a) One leg of the three-phase grid-tied converter; (b) Converter output current and voltage in d-q axis.

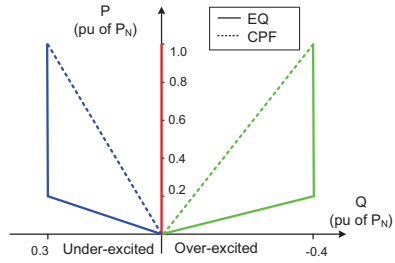

Fig. 3. Supportive reactive power range of modern wind power system stated in German grid codes [15].
Note: EQ denotes operation mode of the extreme reactive power injection and CPF denotes operation mode of the constant power factor.

It is well-known that reactive power is preferred for LVRT in order to rebuild the normal grid voltage for modern renewable energy system. Nevertheless, many pioneering countries of wind energy production (like Germany,

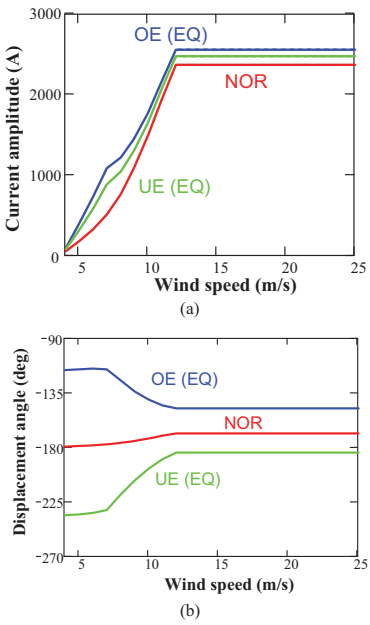

Fig. 4. Reactive power effects on power device loading. (a) Current amplitude versus wind speed; (b) Displacement angle versus wind speed.

Denmark, UK, etc.) have issued grid codes that during normal operation, the reactive power capacity is also defined. As shown in Fig. 3, one of the strictest grid requirements is established by German TSO, in which up to 40% Over-Excited (OE) and 30% Under-Excited (UE) reactive power is delivered if the produced active power is above 20%. Due to different control objectives – various amounts of reactive power injection for either the Extreme Reactive Power (EQ) or the Constant Power Factor (CPF) can be implemented. In the case of the CPF operation, the power factor of the OE reactive power injection is slightly smaller than the UE reactive power injection. Moreover, the whole supportive range of the reactive power is enveloped by the EQ operation.

According to a 2 MW wind turbine power curve [16], together with the reactive power requirement shown in Fig. 3, the envelope of the grid converter current amplitude and the displacement angle is calculated and shown in Fig. 4(a) and Fig. 4(b) from the cut-in 4 m/s until the cut-out 25 m/s, in which the maximum range of the reactive power as well as the no reactive power exchange (NOR) are taken into account. It is noted either the current amplitude or the displacement angle become constant if the wind speed reaches the rated 12 m/s. Moreover, the introduction of either the OE or the UE reactive power imposes additional current stress, which is consistent with (1). Another turning point occurs in the case of the reactive power compensation during the increase of the wind speed because the produced active power gets 0.2 pu at such wind speed. In respect to the displacement angle, the dominant reactive current at lower wind speed forces the converter current almost leading or lagging 90 degree compared to the converter voltage. However, at the higher wind speed, the converter current and voltage are nearly in opposite phase as the component of active current takes up the majority of the total current.

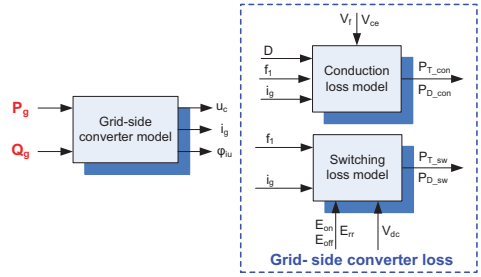

Fig. 5. Framework of power semiconductor loss evaluation in terms of the conduction loss and the switching loss.

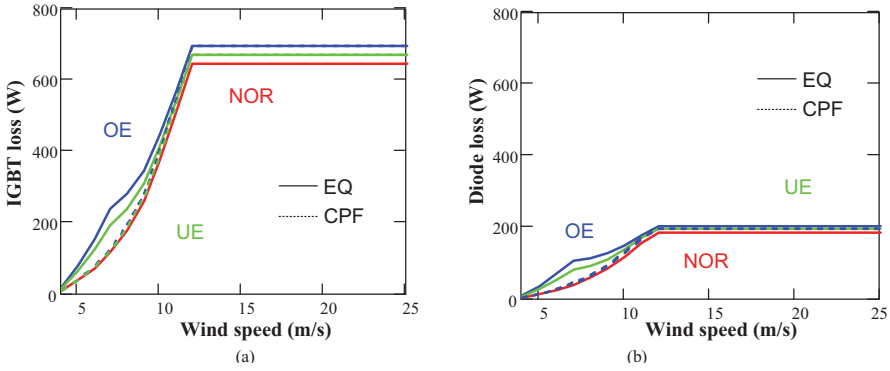

Fig. 6. Loss profile of power semiconductor. (a) IGBT loss; (b) Diode loss.

C. Calculation of Conduction Loss and Switching Loss

Because the change of reactive power alters the current loading of the power device, it is worth to translate this information further into the power dissipation of the power device. In fact, the loss dissipation of the power semiconductor has been studied a lot [17]-[19]. One of them is the physical model of power device during dynamic operation to see the different parasitic parameters influence [18]. Another popular approach, which mainly depends on the test data from power device manufacturer, the loss information during each switching pattern and conduction period could be calculated according to the datasheet, and the power loss is then accumulated by every switching pattern within the whole fundamental period of the loading current [19].

As shown in Fig. 5, the loss evaluation in this paper is based on the second approach – according the grid-side converter model as well as the conduction loss model and the switching loss model of the power device. Using conventional symmetrical space vector modulation [17], the power dissipation of the IGBT and the freewheeling diode can then analytically be calculated as shown in Fig. 6(a) and Fig. 6(b), respectively. It can be seen that the loading of the IGBT is heavier than the diode due to the direction of the active power flow. Furthermore, the loss in the case of the EQ and the CPF reactive power injection are both taken into account.

III. Operational Modes and Wind Classes Effects on Reliability

As the cost on maintenance in offshore wind farm is high, it pushes to the much higher lifespan of the entire wind turbine system. This section will address the impacts of the reactive power on power device reliability with various wind profiles and different operation modes.

A. Methods for Reliability Analysis

Thermal cycling of the junction temperature is caused by the cycling of power losses and it causes mechanical stress between joined materials with different expansion coefficients [6], [8]. Based on the previously mentioned loss evaluation method, the universal procedure of lifetime estimation is shown in Fig. 7. The mean junction temperature T_{jm} and the junction temperature variation of the most stressed dT_j of the power semiconductor can be obtained with the aid of Foster structure thermal model [7] as well as the total IGBT loss P_T and diode loss P_D. Then, together with the on-state time of the loading current within one cycle frequency t_{on}, which is the half value of the fundamental period [20], the power cycles can be calculated according to e.g. Coffin-Manson lifetime model [7]. Afterwards, the concept of the Consumed Lifetime (*CL*) is introduced,

$$\mathrm{CL_i} = \mathrm{D_i} \cdot \frac{365 \cdot 24 \cdot 3600 \cdot \mathrm{f_l}}{\mathrm{N_i}} \tag{4}$$

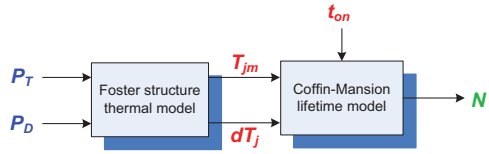

Fig. 7. Framework to estimate the power cycles of power semiconductor.

where subscript *i* denotes a certain wind speed from cut-in to cut-out, *D* denotes the wind speed probability of yearly wind speed, and *N* denotes the power cycles calculated by Fig. 7. CL_i denotes the power cycles consumed per year for the wind speed *i*.

Assuming that the damage accumulates linearly, the Miner's rule [7], [8] is applied in order to calculate the Total Consumed Lifetime (TCL),

$$\mathrm{TCL} = \sum_{\mathrm{i=4}}^{25} \mathrm{CL_i} \tag{5}$$

Due to the fact that the active power is fed into the grid through the grid-side converter, the IGBT is more stressed compared to the freewheeling diode as shown in Fig. 6. Consequently, for this specific power module, the reliability assessment of the grid-side converter only concerns about the IGBT chips.

B. Various Wind Classes

There are two common used density distributions of the wind speed – Weibull function and Rayleigh function. This paper applies for the Weibull distribution [21], which is characterized by a shape parameter of 2. As shown in Fig. 8, three scale parameters are used to represent various IEC wind class I, II and III [22], whose average wind speeds are 10 m/s, 8.5 m/s and 7.5 m/s, respectively. With the cut-in, rated and cut-out wind speed listed in TABLE I, four regions of wind distribution can be categorized.

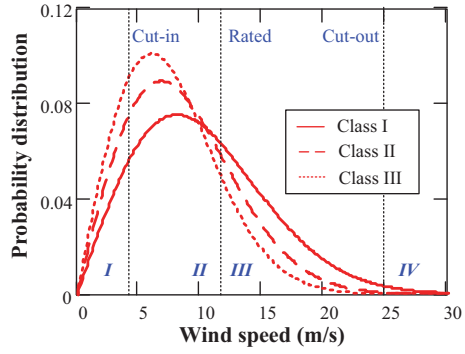

Fig. 8. Annual wind distribution with different wind classes defined by IEC standard [22].

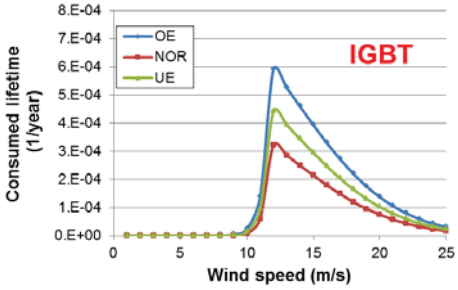

(a)

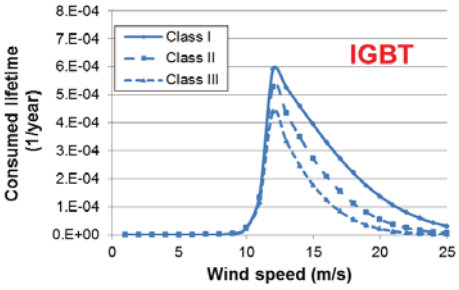

(b)

Fig. 9. Consumed lifetime of the IGBT at different wind speeds. (a) Various types of reactive power injection at Class I wind profile; (b) Various annual wind profile in the case of over-excited reactive power injection.

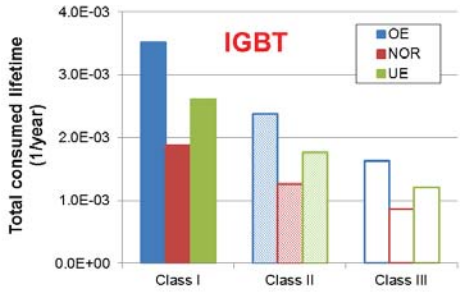

Fig. 10. Total consumed lifetime of the IGBT with various reactive types and various wind classes.

Applying the Class I wind profile as a case study, the consumed lifetime of the IGBT in various types of reactive power injections is shown in Fig. 9(a). It is evident that either the OE or the UE reactive power injection has higher CL compared to the NOR operation. Moreover, it can be seen that, as each wind speed above rated value has the same power cycles, the CL becomes changing consistent with the varying wind speed distribution shown in region III of Fig. 8. Furthermore, it is noted that the wind speed region below cut-in (region I in Fig. 8) and above cut-off wind speed (region IV in Fig. 8) have no contribution to the lifetime consumption.

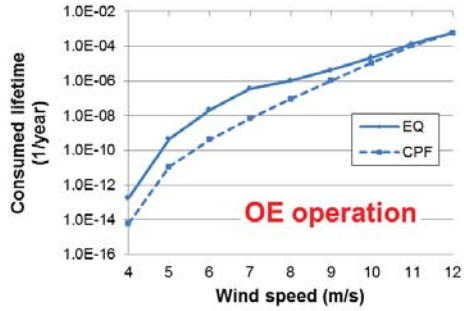

(a)

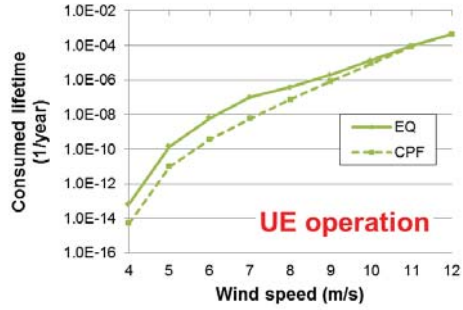

(b)

Fig. 11. Lifetime estimation with different operation modes according to Class I wind profile. (a) Over-excited reactive power injection; (b) Under-excited reactive power injection.

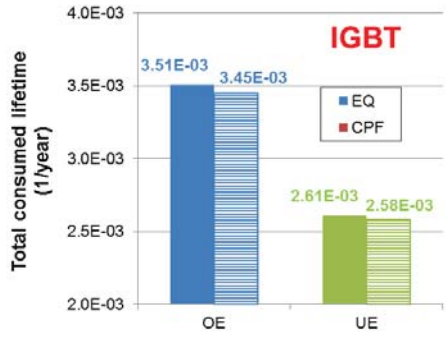

Fig. 12. Total consumed lifetime comparison with different operation modes.

As the OE reactive power has the most severe stress, this situation is used to further compare the effects of different wind profiles on the CL as shown in Fig. 9(b). Since the class I has the highest probability for region III wind speed, the CL of the class I wind profile is highest from the rated speed until the cut-out speed, followed by class II and class III wind profile.

As summarized in Fig. 10, for various types of reactive power injection, regardless of the class level of the wind profile, the OE reactive power injection reduces the lifetime most. In respect to various wind classes, it is noted that the higher class the wind level is, the lower lifetime of the power converter could be.

C. Operation modes of Reactive Power Injection

The effects of various operation modes on the lifetime consumption will be investigated. As shown in Fig. 3, the difference between the EQ and the CPF mainly lies in the wind speed region II from the cut-in to rated wind speed. Using Class I wind profile as a case study, a slight difference of the CL can be found both in the OE operation and the UE operation, as shown in Fig. 11(a) and Fig. 11(b). Consequently, a very small difference appears in the TCL shown in Fig. 12.

IV. Operatinal Modes and Wind Classes Effects on Energy Loss

With the increasing wind power proportion of the total energy production, the cost-effective operation to achieve the lower cost per kWh is preferred. This section is going to analyze the impacts of reactive power on the cost of energy.

A. Important concepts

As the entire loss of the grid-side converter is affected by various amounts of reactive power (either the types of the reactive power or the operation modes), together with the yearly wind speed distribution, the Energy Loss Per Year (ELPY – unit: MWh) can be predicted,

$$\mathrm{ELPY} = \sum_{i=4}^{12} \mathrm{P}_{\mathrm{GSC(n)}} \cdot \mathrm{T}_{\mathrm{(n)}} \tag{6}$$

where the P_{GSC} denotes the total power loss of the grid-side converter, including the total loss of IGBT switch and diode. T denotes the wind speed distribution as shown in Fig. 8. Subscript n denotes the wind speed. It is worth to mention that the ELPY is only of interest from the cut-in to the rated wind speed, because if the wind speed is higher than the rated value, it is assumed that the power loss dissipated in the PMSG system can be compensated from the mechanical power from the wind turbine blades.

The Annual Energy Production (AEP) from wind energy can also be obtained with the aid of the produced power P_g and the annual wind speed distribution T.

$$\mathrm{AEP} = \sum_{i=4}^{25} \mathrm{P}_{\mathrm{g(n)}} \cdot \mathrm{T}_{\mathrm{(n)}} \tag{7}$$

In respect to the AEP, the concerned wind speed is from the cut-in to cut-out wind speed.

The Annual Loss Of Energy (ALOE – unit: %) is achieved by dividing the ELPY from the AEP.

$$\mathrm{ALOE} = \frac{\mathrm{ELPY}}{\mathrm{AEP}} \cdot 100\% \tag{8}$$

As a result, Fig. 13 graphically shows the framework to predict the cost of energy loss in terms of the ELPY, AEP and ALOE.

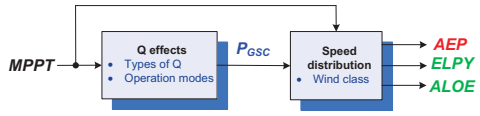

Fig. 13. Framework to predict the cost of energy loss in respect to the reactive power requirement from grid codes.

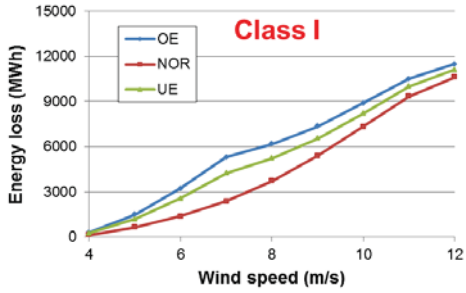

(a)

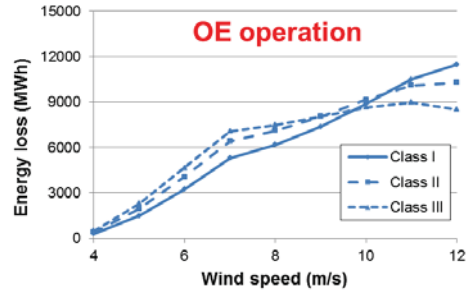

(b)

Fig. 14. Energy loss from cut-in to rated wind speed. (a) Various types of reactive power at Class I wind profile; (b) Various wind classes in case of OE reactive power.

B. Various Wind Classes

Taking Class I wind profile for example, the energy loss of the grid-side converter is shown in Fig. 14(a) at various types of reactive power injection. It is noted that only the

difference between the cut-in and rated wind speed is taken into account. Due to the fact that the OE reactive power imposes the energy loss most, this kind of the reactive power injection is then considered at various wind profiles. As shown in Fig. 14(b), it can be seen that the shape of the energy loss at each wind speed is consistent with the wind distribution in Fig. 8 at this specific strategy of the reactive power injection.

By adding the energy loss of the individual wind speed together, the ELPY is shown Fig. 15(a), in which either the UE or the OE reactive power injection increases the ELPY at all kinds of the wind classes. Moreover, regardless of reactive power type, it is interesting to see that all kinds of wind classes have almost similar EPLY. Due to the calculated AEP for each wind class, the ALOE is shown in Fig. 15(b). It is evident that the higher wind class is, the lower ALOE will be, because a higher wind class actually yields larger amount of the AEP. Besides, the highest ALOE 0.89 % appears at Class III, if the OE reactive power is injected all year around.

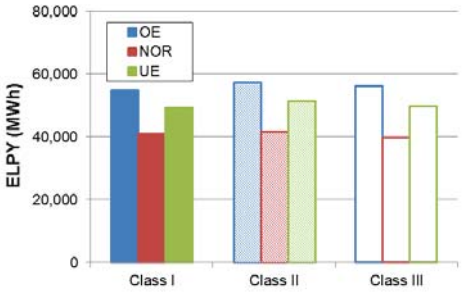

(a)

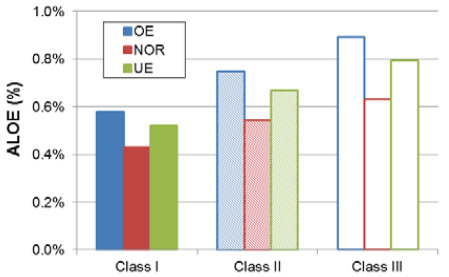

(b)

Fig. 15. Cost of energy with different wind classes. (a) Energy Loss Per Year (ELPY); (b) Annual Loss Of Energy (ALOE).

C. *Operation modes of Reactive Power Injection*

In respect to the operation modes at wind Class I, the EQ and the CPF reactive power injection is accordingly compared. As shown in Fig. 16, regardless the OE or UE reactive power, the CPF operation mode is more cost-effective than the EQ operation mode, as the consumed energy is less in the CPF mode.

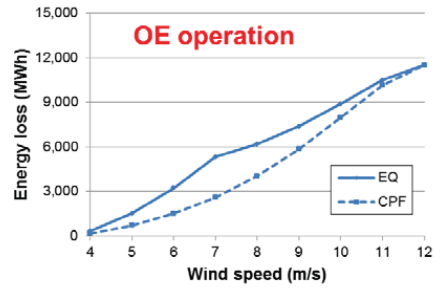

(a)

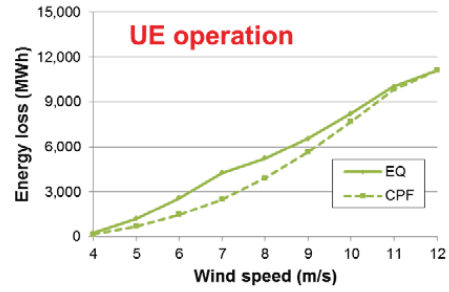

(b)

Fig. 16. Influence of the different operational modes on energy loss for a 2 MW wind turbine. (a) Over-excited reactive power injection; (b) Under-excited reactive power injection.

Consequently, as shown in Fig. 17(a), the CPF control scheme saves considerable energy either in the OE reactive power or the UE reactive power injection. According to Fig. 17(b), the ALOE reduce from 0.58% to 0.47% if the operation mode switches from the EQ to the CPF operation, implying 19.0% energy saving for the CPF compared to the EQ if the OE reactive power is required all year around. It is also applied to the UE reactive power injection, 13.5% energy saving can be obtained, if the control scheme changes from the EQ operation to the CPF operation.

V. CONCLUSION

This paper addresses a universal method to evaluate the loss dissipation inside the power switching device of wind power converter taking into account a number of operational modes. It is clear that the loss breakdown of the power device is jointly dependent on the active power reference from the MPPT algorithm and the required reactive power reference from the TSO. If the reactive power is injected according to the German grid codes, the cost on reliability and loss production are then evaluated in terms of various wind classes and operation modes.

In respect to reliability, it can be seen that either the OE or the UE reactive power significantly reduces the lifetime - the OE reactive power has the worst scenario. If different mission profiles are taken into consideration, it is concluded that higher wind class level has shorter lifespan of the power converter. Meanwhile, it is evident that a small difference of the total consumed lifetime occurs with various operational modes – the extreme reactive power and the constant power factor control strategies.

Regarding the energy loss, the introduction of the reactive power, either the OE reactive power or the UE reactive power, considerably imposes the energy loss per year, in which the OE reactive power has the worst scenario. However, when the different wind profiles are taken into account, similar energy loss per year is unexpectedly observed. Moreover, it is found that the constant power factor control scheme is preferred due to its energy saving at 19.0% and 13.5%, if the OE and the UE reactive power are provided all year around.

REFERENCES

[1] F. Blaabjerg, K. Ma, "Future on power electronics for wind turbine systems," *IEEE Journal of Emerging and Selected Topics in Power Electronics*, vol. 1, no. 3, pp. 139-152, Sept. 2013.

[2] H. Polinder, J. A. Ferreira, B. B. Jensen, A. B. Abrahamsen, K. Atallah, R. A. McMahon, "Trends in wind turbine generator systems," *IEEE Journal of Emerging and Selected Topics in Power Electronics*, vol. 1, no. 3, pp. 174-185, Sept. 2013.

[3] H. Wang, M. Liserre, F. Blaabjerg, P. Rimmen, J. Jacobsen, T. Kvisgaard, J. Landkildehus, "Transitioning to physics-of-failure as a reliability driver in power electronics," *IEEE Journal of Emerging and Selected Topics in Power Electronics*, vol. 2, no. 1, pp. 97-114, Mar. 2014.

[4] M. Liserre, R. Cardenas, M. Molinas, J. Rodriguez, "Overview of multi-MW wind turbines and wind parks," *IEEE Trans. Industrial Electronics*, vol. 58, no. 4, pp. 1081-1095, Apr. 2011.

[5] "ZVEI - Handbook for robustness validation of automotive electrical/electronic modules," Jun. 2013.

[6] ABB Application Note, Load-cycling capability of HiPaks, 2004.

[7] K. Ma, M. Liserre, F. Blaabjerg, T. Kerekes, "Thermal loading and lifetime estimation for power device considering mission profiles in wind power converter," *IEEE Trans. on Power Electronics*, IEEE Early Access.

[8] L. Wei, R. J. Kerkman, R .A. Lukaszewski, H. Lu, Z. Yuan, "Analysis of IGBT power cycling capabilities used in doubly fed induction generator wind power system," *IEEE Trans. on Industry Applications*, vol. 47, no. 4, pp. 1794-1801, Jul. 2011.

[9] C. Kost, J. Mayer, J. Thomsen, Levelized cost of electricity renewable energy technologies. (website: www.ise.fraunhofer.de)

[10] E. Koutroulis, F. Blaabjerg, "Design optimization of transformerless grid-connected PV inverters including reliability," *IEEE Trans. on Power Electronics*, vol. 28, no. 1, pp. 325-335, Jan. 2013.

[11] X. Yu, A. M. Khambadkone, "Reliability analysis and cost optimization of parallel-inverter system," *IEEE Trans. on Industrial Electronics*, vol. 59, no. 10, pp. 3881-3889, Oct. 2012.

[12] J. Dai, D. Xu, B. Wu, "A novel control scheme for current-source-converter-based PMSG wind energy conversion systems," *IEEE Trans .on Power Electronics*, vol. 24, no. 4, pp. 963-972, Apr. 2009.

[13] D. Zhou, F. Blaabjerg, M. Lau, M. Tonnes, "Thermal analysis of multi-MW two-level wind power converter," *in Proc. of IECON 2012*, pp. 5862-5868, 2012.

[14] D. Zhou, F. Blaabjerg, M. Lau, M. Tonnes, "Thermal behavior optimization in multi-MW wind power converter by reactive power circulation," *IEEE Trans. on Industry Applications*, vol. 50, no. 1, pp. 433-440, Jan. 2014.

[15] E.ON-Netz. Requirements for offshore grid connections, Apr. 2008.

[16] Vestas, V-90 wind turbine. (Website: http://www.vestas.com).

[17] J. W. Kolar, H. Ertl, Franz C. Zach, "Influence of the modulation method on the conduction and switching losses of a PWM converter system," *IEEE Trans. on Industry Applications*, vol. 27, no. 6, pp. 1063-1075, Nov. 1991.

[18] Y. Ren, M. Xu, J. Zhou, F. C. Lee, "Analytical loss model of power MOSFET," *IEEE Trans. on Power Electronics*, vol. 21, no. 2, pp. 310-319, Mar. 2006.

[19] B. Backlund, R. Schnell, U. Schlapbach, R. Fischer, E. Tsyplakov, "Applying IGBTs", ABB Application Note, Apr. 2009.

[20] D. Zhou, F. Blaabjerg, M. Lau, M. Tonnes, "Thermal profile analysis of doubly-fed induction generator based wind power converter with air and liquid cooling methods," *in Proc. of EPE 2013*, pp. 1-10, 2013.

[21] The Swiss wind power data website. (Website: http://wind-data.ch/tools/weibull.php)

[22] Wind turbines – part I: design requirements", IEC 61400-1, 3rd edition.

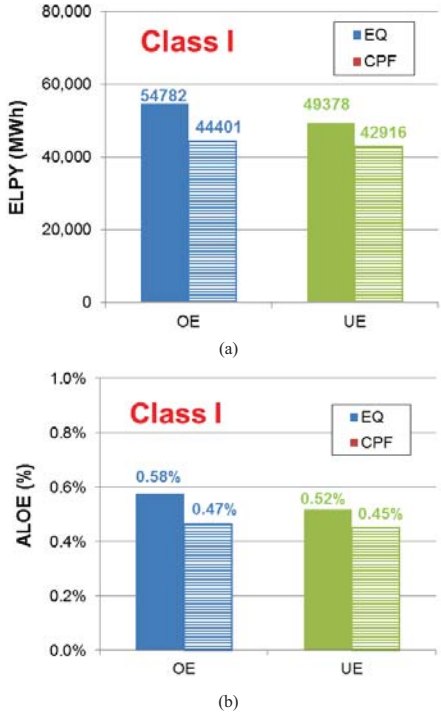

Fig. 17. Energy loss per year with different operation mode under wind Class I. (a) Energy Loss Per Year (ELPY); (b) Annual Loss Of Energy (ALOE).

[A.9] D. Zhou, F. Blaabjerg, "Thermal behavior of doubly-fed Induction generator wind turbine system during balanced grid fault," *in Proc. of APEC 2014*, pp. 3076-3083, 2014.

Thermal Behavior of Doubly-Fed Induction Generator Wind Turbine System during Balanced Grid Fault

Dao Zhou, Frede Blaabjerg
Department of Energy Technology
Aalborg University
Aalborg, Denmark
zda@et.aau.dk, fbl@et.aau.dk

Mogens Lau, Michael Tonnes
Danfoss Silicon Power GmbH
Flensburg, Germany
mogens.lau@danfoss.com, michael.tonnes@danfoss.com

Abstract— Ride-through capabilities of the doubly-fed induction generator (DFIG) during grid fault have been studied a lot. However, the thermal performance of the power device during this transient period is seldom investigated. In this paper, the dynamic model for the DFIG and the influence of the rotor current to the damping time of the stator flux and rotor terminal voltage during the symmetrical grid fault is firstly evaluated. Then, the theoretical analysis for the safety operation area of the power device is given in terms of the various voltage dips and various rotor speeds, in which simulation results are used to verify. Finally, the power loss and the thermal profile are shown at the transient period of the DFIG. It is concluded that, in order to guarantee the same damping time of the stator flux, the serious voltage dip results in the higher power losses as well as the junction temperature fluctuation, and may even damage the rotor converter, if the design is not considered carefully.

I. Introduction

The penetration of wind power is expected to achieve 20% of the total electricity production by 2020 in Europe [1]. Because of the noise emission, footprint limitation and richer wind energy, the wind turbines are moving from onshore to offshore. Meanwhile, the lifetime of the wind turbine system are inversely prolonged to 20-25 years under such uncertain and harsh environment, whose mission profile leads to a faster fatigue and might give a higher failure rate. As the most vulnerable power electronic component, more and more efforts have been recently devoted to the reliable behavior of the power semiconductor due to the increased cost and time for repair after failures [2]-[5]. It is widely accepted that the thermal profile of the power semiconductor is an important indicator of the lifetime and it has an influence on the reliable operation. The power cycle number to failure is quite relevant to the junction temperature fluctuation as well as the mean junction temperature [6]-[10].

The Doubly-Fed Induction Generator (DFIG) is a widely used configuration for wind turbines above 1 MW. It provides the advantage of variable speed operation and four-quadrant active and reactive power capabilities using the converter rated for only a small fraction (20%-30%) of the rated power. However, on detecting a grid fault, the generator unit is usually disconnected to protect the vulnerable rotor converter. In the recent years, this has been achieved by so-called crowbar. As the penetration of wind power continues to increase, more wind turbines are required to ride through the grid faults, and to contribute to the system stability after the fault clearance. Researchers are addressing this issue from several points of view. For instance, the study described in [11], [12] analyzes the intrinsic in the DFIG during the grid fault and proposes its dynamic model. Many control strategies are suggested to support the DFIG to ride through the grid fault without the crowbar or with the enable time of the crowbar as soon as possible [13]-[17]. The thermal behavior of the power devices during grid fault is evaluated for both the permanent magnet synchronous generator based full-scale power converter and the DFIG based partial-scale power converter at steady-state operation [18], [19].

This paper focuses on the transient thermal behavior of the DFIG wind turbine system during the balanced grid fault, in order to identify critical issues which can cause lifetime reduction. Section II is a brief introduction to the dynamics of the DFIG model, and then the influence of rotor current on the stator flux damping and the rotor terminal voltage is analyzed in section III. The safety operation area of the traditional demagnetizing control is theoretically studied and verified by the simulation in section IV. The power loss and thermal profile of the switching power device is shown in Section V. Finally, conclusions are drawn in the last section.

II. Dynamic DFIG Model under Grid Fault

A lot of references have discussed the modeling of DFIG under grid faults [11]-[17]. If the stator reference frame, static to the stator winding, is introduced, assuming the rotor variables are all transferred to the stator-side, the voltage equation of the generator's stator and rotor can be expressed as follows,

$$\boldsymbol{u}_s = R_s \boldsymbol{i}_s + \frac{d}{dt}\boldsymbol{\psi}_s \tag{1}$$

$$\boldsymbol{u}_r = R_r \boldsymbol{i}_r + \frac{d}{dt}\boldsymbol{\psi}_r - j\omega_m \boldsymbol{\psi}_r \tag{2}$$

where $\boldsymbol{u}$, $\boldsymbol{i}$ and $\boldsymbol{\psi}$ are the space vector of voltage, current and flux of the induction generator, respectively. R denotes the generator's intrinsic resistance, and ω_m denotes the rotor angular frequency. The subscripts s and r denote stator quantities and rotor quantities. The additional third term in (2)

978-1-4799-2325-0/14/$31.00 ©2014 IEEE

represents the compensation transforming from the rotor reference frame to the stator reference frame, where the rotor reference frame rotates correspondingly at rotor speed with respect to the stator winding.

Similarly, with the aid of the stator reference frame, the stator flux $\boldsymbol{\psi}_s$ and rotor flux $\boldsymbol{\psi}_r$ equations are given by,

$$\boldsymbol{\psi}_s = L_s \boldsymbol{i}_s + L_m \boldsymbol{i}_r \tag{3}$$

$$\boldsymbol{\psi}_r = L_m \boldsymbol{i}_s + L_r \boldsymbol{i}_r \tag{4}$$

where L_m is the magnetizing inductance, and L is the self-inductance of stator-side and the rotor-side of the DFIG.

In normal operation, the space vector of stator flux rotates at slip speed ω_r with respect to the rotor winding, which is the product of the slip s and the synchronous angular speed ω_s. However, during a balanced full-dip grid voltage fault, the dc component of the stator flux appears, and the stator flux no longer rotates but freezes with the respect to the stator winding. As a result, the stator flux is rotating at speed ω_m with respect to rotor winding. In the case of a balanced partial-dip grid voltage fault, the stator flux can consequently be expressed as a sum of a forced flux $\boldsymbol{\psi}_{sf}$ and a natural flux $\boldsymbol{\psi}_{sn}$ [7],

$$\boldsymbol{\psi}_s = \boldsymbol{\psi}_{sf} + \boldsymbol{\psi}_{sn} \tag{5}$$

According to the superposition principle, the dynamic model of the DFIG is thus depicted in terms of two independent circuits: the forced machine model and the natural machine model. For the forced machine shown in Fig. 1(a), it stands for the steady-state operation of the DFIG, where the stator of the induction generator connects to the remaining grid voltage (p is the voltage dip level), and no transient stator flux is considered. On the other hand, the natural machine shown in Fig. 1(b) is used for a transient period, whose stator is short-circuited, and an initial natural flux exists in the stator. In order to investigate the dynamic response of the DFIG under grid fault, only the natural machine is focused in the following.

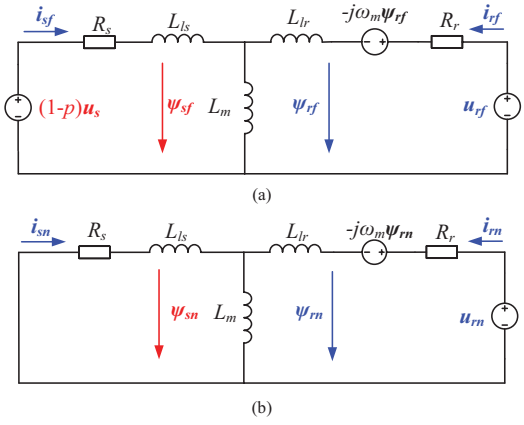

Fig. 1. Dynamic model of the DFIG under a balanced grid fault. (a) Forced machine model; (b) Natural machine model.

III. Influence of Rotor Current Under DFIG Natural Model

DFIG based wind turbine generators shown in Fig. 2 are susceptible to grid-side low voltage or short-circuit due to the presence of the power electronics converter on the rotor-side. If a three-phase voltage sag happens on the grid-side, as aforementioned, a dc component of stator natural flux emerges immediately, which induces a considerably increase of electromagnetic force (EMF). The rotor current thus increases substantially without proper protection, and may even damage the rotor converter. Moreover, the existence of stator natural flux prevents the rotor converter to provide the reactive power injection. As a consequence, the damping time of the stator flux and analysis of rotor voltage are two important aspects in case of grid faults. However, in normal operation, the rotor converter is designed to adjust the active power and the reactive power of the stator side through the controllability of the rotor current. This section will investigate the effect of the rotor current on DFIG's natural flux evolution and induced rotor voltage.

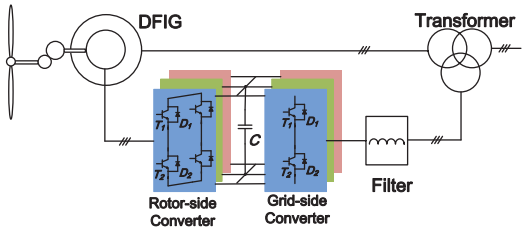

Fig. 2. Configuration of the wind turbine system equipped with DFIG.

A. Natural flux evolution

According to Fig. 1(b), as no stator voltage in the natural machine model is taken into account, expressing the relationship between the stator flux and the rotor current through (1) and (3) yields,

$$\frac{d}{dt}\boldsymbol{\psi}_{sn} = -\frac{R_s}{L_s}\boldsymbol{\psi}_{sn} + \frac{R_s}{L_s}L_m \boldsymbol{i}_{rn} \tag{6}$$

where the subscript n indicates the variables in natural machine model. If the rotor side is open-circuit, from the first term, it is inferred that the natural flux is exponentially decaying with the DFIG's own time constant, whose value is quite large, up to 1 to 1.5 seconds for a MW generator [12]. If no counter-action is adopted, the transient period remains for several seconds, which is unfortunately a violation with the fast response of the reactive power defined in the recent grid codes [20], [21].

The second term denotes the influence of rotor current in the evolution of the stator flux. Depending on the phase angle between the rotor current and the natural flux, the damping could be either accelerated or decelerated. For instance, if the rotor converter injects a current in phase with the natural flux, the damping of the stator flux will be slowed down, and might even be canceled out or become negative. Under this

specific situation, the natural flux will not disappear, but rather increase until the rotor converter goes out of control.

The opposite situation happens if a crowbar is connected to the rotor. The crowbar is a protection against the grid faults that allows a low resistance across the rotor windings. The connection of the crowbar generates the circulation of large current through the rotor windings and stator windings. Since the rotor current is almost in opposite phase to the natural flux, the flux damping will be accelerated. However, this hardware solution is hardly helpful in injecting reactive power, and inevitably increases the cost of the system.

B. Voltage at rotor terminals

Based on (3) and (4), the rotor flux can be represented in terms of the stator flux and rotor current by eliminating the stator current. If the rotor reference frame is introduced, the previous expression of the rotor voltage in (2) can be transformed as the following,

$$\boldsymbol{u}_{rn}^{r} = (R_r + \sigma L_r \frac{d}{dt})\boldsymbol{i}_{rn}^{r} + \frac{L_m}{L_s}\frac{d}{dt}\boldsymbol{\psi}_{sn}^{r} \tag{7}$$

where the superscript r denotes the rotor reference frame, and σ denotes the leakage inductance coefficient $\sigma=1-L_m^2/L_sL_r$. It is observed that the first term of the expression is the voltage drop in the rotor resistance and in the transitory rotor inductance, and the second term of the expression is the EMF induced by the stator flux in rotor windings. If (6) is deduced under the rotor reference frame, (7) can be further simplified as [22],

$$\boldsymbol{u}_{rn}^{r} \approx (R_r + R_s)\boldsymbol{i}_{rn}^{r} - j\sigma\omega_m L_r \boldsymbol{i}_{rn}^{r} - j\omega_m \boldsymbol{\psi}_{sn}^{r} \tag{8}$$

Viewed from the rotor, the DFIG behaves as EMF $\boldsymbol{e}_{rn}$ induced by the stator natural flux, in series with rotor and stator resistance as well as the transitory inductance of the machine. The equivalent circuit of the machine is thus depicted in Fig. 3. In order to guarantee the current controllability, the rotor converter should be sized to generate a voltage at least larger than the EMF.

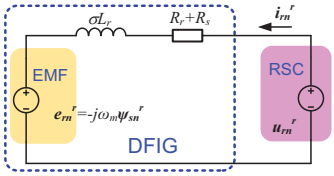

Fig. 3. Equivalent machine model in viewpoint of the rotor.

IV. Control for Grid Fault Ride-through Operation

Xiang *et. al* [11] proposed the demagnetizing control technique to protect the rotor converter against the grid faults without a crowbar or with a crowbar active time as short as possible [12]. In this section, the demagnetizing control scheme will briefly be described. Then the Safety Operation Area (SOA) will be theoretically analyzed in terms of various voltage dip levels and various rotor speeds. After that, the SOA is verified by simulation results.

A. Demagnetizing current influence to stator flux

The basic idea of the demagnetizing current is to introduce a rotor current opposite to the stator flux,

$$\boldsymbol{i}_{rn} = -k\boldsymbol{\psi}_{sn} \tag{9}$$

Substituting (9) into (6), the evolution of the stator flux is then obtained,

$$\frac{d}{dt}\boldsymbol{\psi}_{sn} = -(\frac{R_s}{L_s} + \frac{R_s}{L_s}L_m k)\boldsymbol{\psi}_{sn} \tag{10}$$

The stator flux is exponentially decaying with the certain time constant,

$$\tau_s = \frac{L_s}{R_s(1+kL_m)} \tag{11}$$

It shows that the introduction of the demagnetizing current will accelerate the decaying of the natural flux.

B. Demagnetizing current effects on rotor voltage

Consider that the generator operates under normal operation until a symmetrical voltage dip occurs at a given moment $t=0$. The space vector of the grid voltage is,

$$\boldsymbol{u}_s = \begin{cases} U_s e^{j\omega_s t} & t \le 0 \\ (1-p)U_s e^{j\omega_s t} & t > 0 \end{cases} \tag{12}$$

where U_s denotes the amplitude of the grid voltage.

Neglecting the insignificant voltage drop through the stator resistance, the stator flux after the grid fault can be obtained,

$$\boldsymbol{\psi}_s = -j(\frac{(1-p)U_s}{\omega_s}e^{j\omega_s t} + \frac{pU_s}{\omega_s}e^{-\frac{t}{\tau_s}}) \tag{13}$$

The first term can be regarded as stator forced flux $\boldsymbol{\psi}_{sf}$, still rotating with synchronous angular speed. The second term is the stator natural flux $\boldsymbol{\psi}_{sn}$, static with stator winding. The amplitudes of these two kinds of stator flux are dictated by the voltage dip level.

Assuming the grid voltage is the reference vector, Fig. 4 graphically shows the space vector diagram of the rotor voltage. The stator flux $\boldsymbol{\psi}_{sn}$ is lagging the stator voltage $\boldsymbol{u}_s$ 90 degree, and the rotor current $\boldsymbol{i}_{rn}$ is opposite to the stator flux.

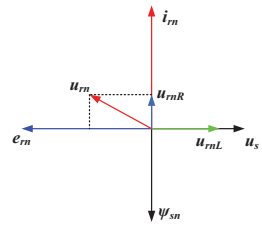

Fig. 4. Space vector diagram for rotor voltage under stator reference frame.

According to (8), the voltage drop $\boldsymbol{u}_{rnR}$ through the resistance and $\boldsymbol{u}_{rnL}$ transitory inductance is in phase of rotor current and lagging the current 90 degree, respectively.

Moreover, the EMF e_{rn} is lagging the stator flux 90 degree. It is noted that, besides the acceleration of damping stator flux, the demagnetizing control normally has an advantage to reduce the rotor voltage as well.

C. Analysis of safety operation area

The rotor converter usually employs the IGBT module as a semiconductor switching device. Its continuous current rating is determined by the steady-state current, while during the transient period the over-current may occur. Generally speaking, the maximum current switched by the power device can be the peak pulse rating, as long as the junction temperature is still permissible and the *V-I* switching trajectory is within the SOA. The pulse current rating of an IGBT module is typically two times of the continuous current rating. As mentioned before, the stator natural flux induces the overcurrent and overvoltage in the rotor converter during a balanced grid fault. From (8) and (13), the EMF is jointly decided by the voltage dip level and rotor speed. Therefore, it is interesting to investigate the SOA of the rotor converter in terms of various voltage dip levels and various rotor speeds, in which the instantaneous rotor current is constrained below 2.0 pu., while the rotor converter dc-link voltage is also maintained below the device voltage rating.

A 2 MW DFIG wind turbine is used for the case study, whose parameters are given in Appendix. Because of a low-voltage system, a common 1 kA/1.7 kV power module from leading manufacturer is selected. Based on (8), the relationship between the rotor voltage and the rotor current at different voltage dips is shown in Fig. 5, in which the rotor speed is set at 1800 rpm. It can be seen that, if the rotor is open-circuit, the higher dip level causes the higher EMF viewed from rotor side. Besides, the demagnetizing current reduces the rotor voltage, and even brings the rotor converter back to SOA with a proper amount of the demagnetizing current. Due to partial-scale feature compared to the generator, the rotor converter will be destroyed by serious voltage dip, e.g. when the dip level reaches 0.8 pu.

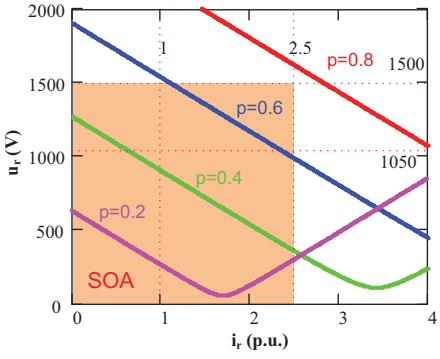

Fig. 5. Voltage amplitude at rotor terminal versus rotor current with various grid voltage dips at rotor speed 1800 rpm, where p is the voltage dip.

During the grid fault, the demagnetizing current injection results in an even higher rotor speed [11]. The rotor speed is assumed to be 1950 rpm in comparison with the maximum normal speed 1800 rpm. Fig. 6 shows the relationship between the rotor voltage and the rotor current at different rotor speeds when the voltage dip is 0.8 pu. It is noted that the higher rotor speed also induces higher EMF of the rotor, and the rotor converter is able to ride through the grid fault easier at lower rotor speed.

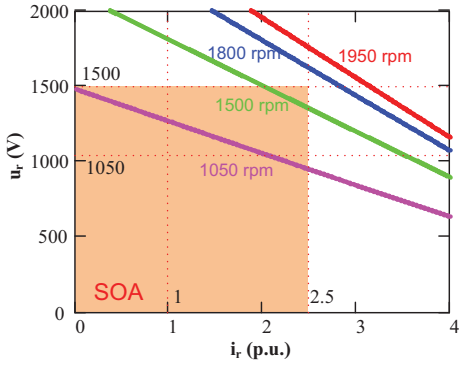

Fig. 6. Voltage amplitude at rotor terminal versus rotor current with various rotor speeds at the voltage dip: p=0.8.

D. Simulation validation

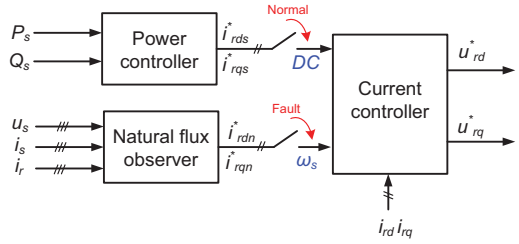

Fig. 7. Control diagram for rotor converter during normal operation and grid fault condition.

The control scheme for the rotor converter is shown in Fig. 7, where the control objective is switched from the active power and the reactive power to the demagnetization of the stator transient flux if the grid fault happens. The rotor reference current is obtained through a natural flux observer, due to its dc component viewed from the stator-side, the rotor reference current becomes a grid angular frequency ω_s viewed from the rotor side. However, in normal operation, the rotor reference current is a dc component viewed from the rotor side. As a result, the actual frequency of the rotor current in the case of the grid fault is the rotor speed, while in normal operation the frequency of the rotor current becomes the slip speed.

The wind turbine is required to start injecting reactive power in about 500 ms to 600 ms from the beginning of the fault, complying with the latest grid code requirement [20], [21]. The damping time for the stator flux is consequently set at 180 ms. As shown in Fig. 8, the stator flux returns to normal within around 600 ms, which is consistent with the above

damping time design. Furthermore, the stator current may reach up to 3 pu, and it has two frequencies during the transient period: the dc component and the grid frequency as illustrated in (13).

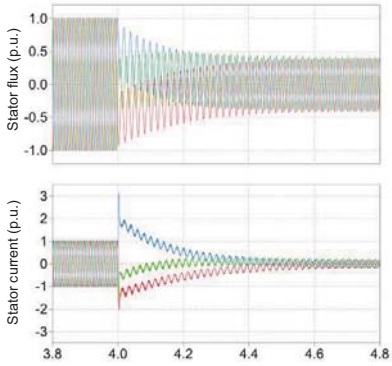

Fig. 8. Damping time of natural flux (e. g. rotor speed at 1800 rpm and voltage dip at 0.6).

The rotor voltage and the rotor current are then shown in Fig. 9 with the different voltage dip levels. In order to verify the evaluation in Fig. 5, four various dip levels are independently simulated. In Fig. 9(a) and Fig. 9(b), the rotor converter can survive through the grid fault. In Fig. 9(d), as the rotor voltage is higher than 1500 V, it excesses the linear modulation index and the rotor converter loses the control of the rotor current. The above phenomena agree with the analysis in Fig. 5. However, in Fig. 9(c), in case of the voltage dip at 0.6 pu, the simulation shows that the rotor side converter operates out of the SOA during the fault ride-through period. It is due to the error introduced by the control gain.

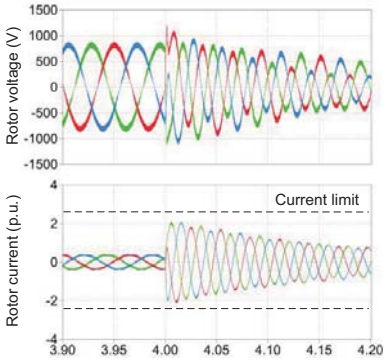

Fig. 10. Simulation of SOA vs. rotor speed in case of dip level at 0.8 and rotor speed at 1050 rpm.

Fig. 10 shows the simulation of SOA versus rotor speed in the case of the voltage dip at 0.8 pu, and the rotor speed at 1050 rpm. Compared with the simulation in Fig. 9(d), it is obvious that if the rotor speed is reduced, it is possible for the rotor converter to ride through the same serious voltage dip.

V. Thermal Behavior of Power Device

As the demagnetizing control introduces the various rotor current as well as the rotor voltage at different voltage dips and rotor speeds, this section will analyze the power loss distribution and the thermal cycling of power device in the case of a balanced grid fault.

A. Power loss distribution

The power loss model, consisting of the conduction losses and switching losses, can be referred to [23], [24]. Based on the on-state voltage drop and switching energy against the load current and the DC-link voltage provided by the manufacturers, the conduction losses and switching losses are accumulated by every switching cycle within one fundamental frequency. The simulation of the power loss has been obtained with the use of PLECS blockset in Simulink [25].

According to Fig. 9, it is noted that the current of the rotor in the three phases becomes extremely unbalanced. Moreover, as the current is exponential decaying, the maximum current through the power modules in the upper and lower of the same bridge is also different. Fig. 11 shows power loss distribution of the most stressed power device at different grid voltage dips, and Fig. 11(a) and Fig. 11(b) are the situations for the rotor speed at 1800 rpm and 1050 rpm, respectively.

In the case of the rotor speed at 1800 rpm from Fig. 11(a), during the normal operation, it is noted that the conduction loss are mainly consumed by the diode compared to the IGBT because of its power flow direction in the super-synchronous mode. However, it is the IGBT that dissipates higher switching loss due to the fact that the turn-on and turn-off energy in the IGBT has larger value than the reverse recovery energy in the diode according to the manufacturer's datasheet. With the increase of the voltage dip level, the natural stator flux becomes higher. In order to guarantee the same damping time of the stator flux, the initial rotor current becomes higher, which causes the increasing power loss.

In the case of the rotor speed at 1050 rpm from Fig. 11(b), due to the maximum power point tracking, the generated power is much lower than the rotor speed at 1800 rpm in the normal operation. Therefore, the power devices are considerably less stressed. Moreover, in the sub-synchronous mode, the direction of the active power through the rotor converter is also reverse, which implies that the IGBT consumes higher conduction loss. Similarly, the more serious voltage dip, the heavier the power device is loading. Furthermore, at the same grid dip 0.8, the power loss at rotor speed 1800 rpm is higher than the case at 1050 rpm, which agrees with the rotor current and voltage characteristic shown in Fig. 9(d) and Fig. 10.

B. Thermal cycling

The thermal model of the power devices, including the IGBT and the freewheeling diode are shown in Fig. 12 in the form of the power module, the thermal grease and the heat-sink. The electrical analogies representing thermal variables are used, in which the power dissipation in the IGBT and the

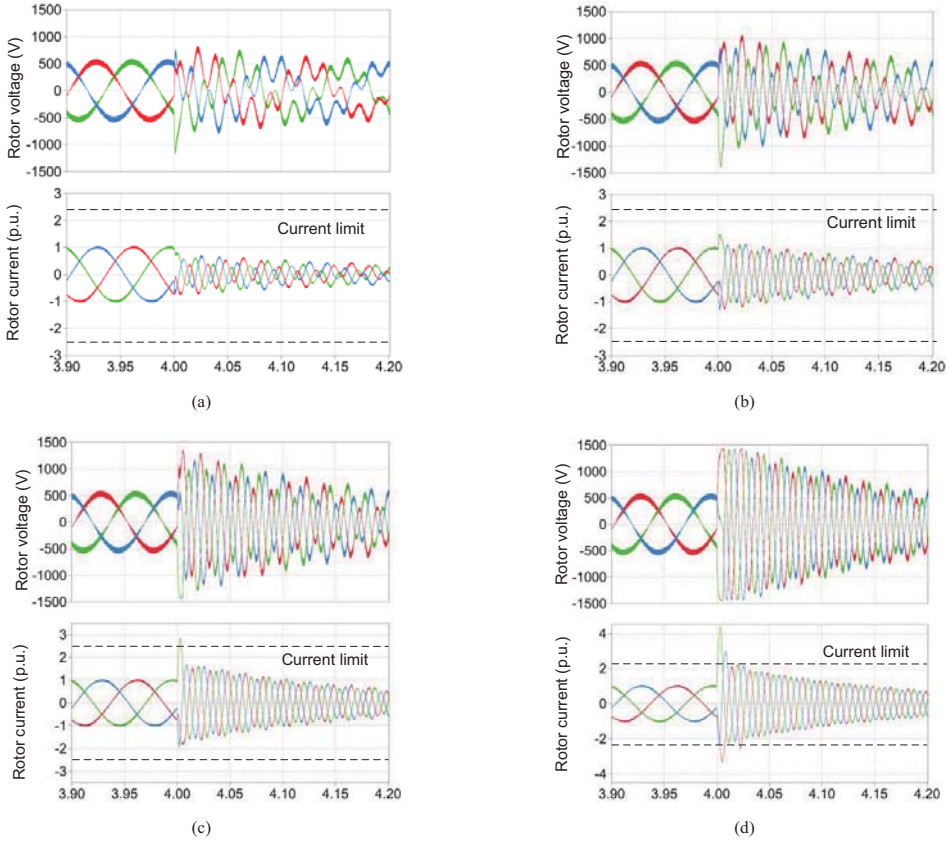

Fig. 9. Simulation of safety operation area vs. dip level in case of rotor speed=1800 rpm at different voltage dips. (a) p=0.2; (b) p=0.4; (c) p=0.6; (d) p=0.8.

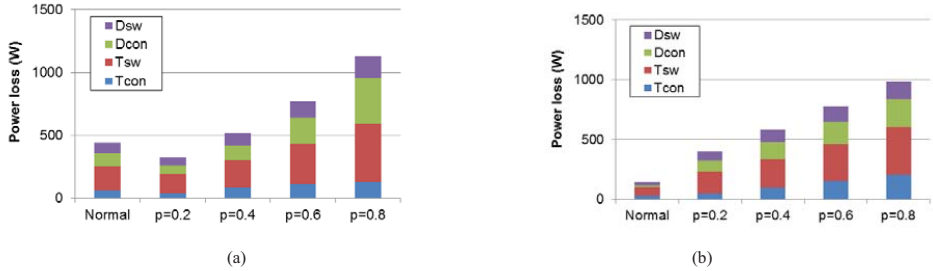

Fig. 11. Power loss distribution at different grid voltage for the rotor-side converter. (a) Rotor speed at1800 rpm; (b) Rotor speed at 1050 rpm.

diode are expressed as current source, the voltage source stand for constant temperature levels, and RC elements are used to signify the thermal impedance.

The thermal impedance from junction to case is modeled as a four-layer Foster RC network, whose values are normally provided by the manufacturer's datasheet. As the Foster structure requires the constant temperature at the terminal, the thermal capacitance of the thermal grease and cooling methods are considered infinite high, which is consequently represented by a controllable voltage source updated by the instantaneous power losses. Meanwhile, the ambient temperature is set to 50 ºC as an indication of the worst case.

Based on the thermal model shown in Fig. 12, the thermal performance of the power device can be simulated again by

PLECS. The simulation of the junction temperature is shown in Fig. 13, where the balanced grid fault to 0.2 pu occurs at the time instant t=4 s.

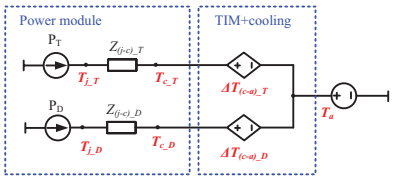

Fig. 12. Thermal model of the power switching device.

Note: TIM stands for Thermal Interface Material.

In case of the rotor speed at 1800 rpm from Fig. 13(a), during the normal operation, the mean junction temperature for the IGBT is higher than the diode, but the junction temperature fluctuation of the diode is higher. If the grid fault happens, the fundamental frequency of the thermal cycling switches from the slip frequency to the rotor speed frequency. Moreover, the switching power device, especially the diode is much more stressed, where the highest junction temperature reach 110 ºC and the junction temperature fluctuation changes from 12.8 ºC to 42.0 ºC.

In the case of the rotor speed at 1050 rpm in Fig. 13(c), the power device is much less stressed in normal operation, which is consistent with the power loss profile shown in the Fig. 11(b). Moreover, the IGBT has a higher mean junction temperature and the junction temperature fluctuation. When the grid fault happens, both the IGBT and the diode become more loaded, and they are more equally heated. The maximum junction temperature fluctuation of the diode changes from 2.3 ºC to 18.4 ºC.

As shown in Fig. 13(b), in which the rotor speed becomes 1500 rpm, the maximum thermal cycling of change from 10.9 ºC in normal operation to 29.3 ºC during the grid faults.

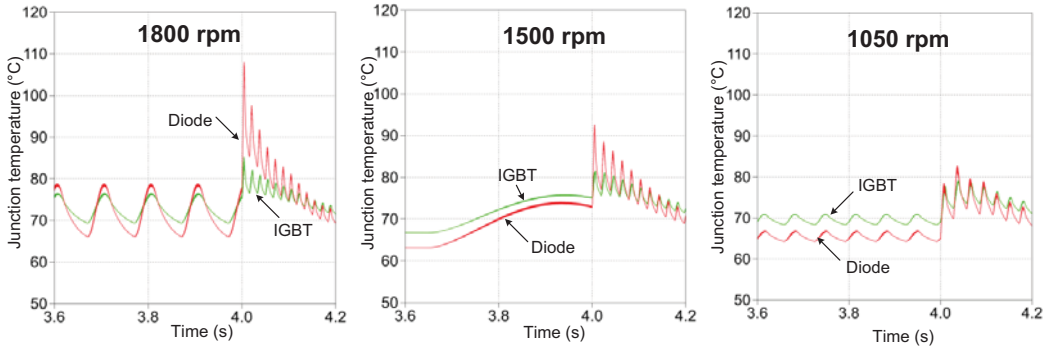

(a) (b) (c)

Fig. 13. Simulation of the junction temperature if the voltage becomes 0.2 pu. (a) Rotor speed at 1800 rpm; (b) Rotor speed at 1500 rpm; (c) Rotor speed at 1050 rpm.

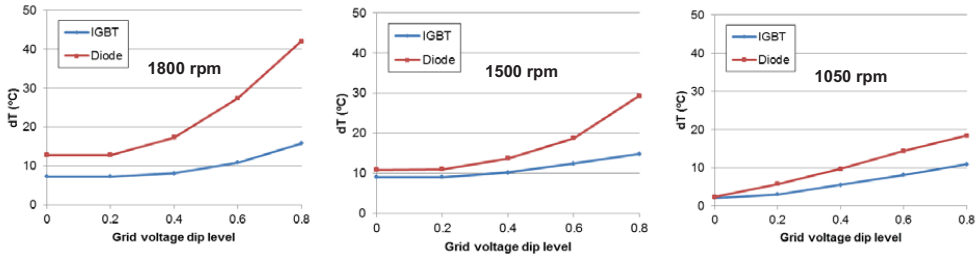

(a) (b) (c)

Fig. 14. Junction temperature fluctuation at different grid voltage dip levels. (a) Rotor speed at 1800 rpm; (b) Rotor speed at 1500 rpm; (c) Rotor speed at 1050 rpm.

In order to evaluate the thermal profile of the power device at different voltage dip levels, Fig. 14 summarizes the junction temperature for the maximum and minimum rotor speeds from the normal operation to the balanced grid fault the voltage dip up to 0.8 pu. At the maximum rotor speed seen from the Fig. 14(a), the shallow voltage dip does not change the value of the junction temperature fluctuation due to the smaller demagnetizing current. If the dip level increases, the junction

temperature fluctuation in the diode has much higher value than the IGBT. Fig. 14(c) shows the situation at the rotor speed 1050 rpm, it is noted that the more voltage dips, the more serious the power device is loaded. As shown in Fig. 14(b), the case that rotor speed becomes 1500 rpm is also investigated.

VI. Conclusion

This paper has studied the impact of rotor current on the stator flux damping time and the rotor terminal voltage for the DFIG in the case of the balanced grid fault.

The safety operation area of the rotor converter by demagnetizing control is theoretically analyzed in terms of the various grid voltage dips and the various rotor speeds. In order to guarantee the same damping time of the stator flux, the simulation also verifies the above safety operation area.

The power loss and thermal behavior are then evaluated for the transient period during balanced grid fault. It is concluded that the serious voltage dip results in higher power losses as well as the junction temperature fluctuation, and may even damage the rotor converter, if the design is not considered carefully.

Appendix

Parameters for a 2 MW DFIG

Ratings: P_n = 2.0 MW, U_s = 563V (phase amplitude), four pole

Turns ratio: $N_s/N_r = 0.369$

Stator resistance: $R_s = 1.688\ \text{m}\Omega$

Stator leakage inductance: $L_s = 0.038$ mH

Rotor resistance: $R_r' = 1.524\ \text{m}\Omega$

Rotor leakage inductance: $L_r' = 0.064$ mH

Magnetizing inductance: $L_m = 2.91$ mH

References

[1] European Commission Climate Action, "*The EU climate and energy package*," Mar. 2007.

[2] F. Blaabjerg, Z. Chen, S. B. Kjaer, "Power electronics as efficient interface in dispersed power generation systems," *IEEE Trans. on Power Electronics*, vol. 19, no. 5, pp. 1184-1194, Sep. 2004.

[3] F. Blaabjerg, K. Ma, D. Zhou, "Power electronics and reliability in renewable energy systems," *in Proc. of ISIE 2012*, pp. 19-30, May. 2012.

[4] S. Yang, A. Bryant, P. Mawby, D. Xiang, L. Ran, P. Tavner, "An industrial-based survey of reliability in power electronic converters," *IEEE Trans. on Industrial Applications*, vol. 47, no. 3, pp. 1441-1451, May. 2011.

[5] H. Polinder, J. A. Ferreira, B. B. Jensen, A. B. Abrahamsen, K. Atallah, R. A. McMahon, "Trends in Wind Turbine Generator Systems," *IEEE Journal of Emerging and Selected Topics in Power Electronics*, vol. 1, no. 3, pp. 174-185, Sep. 2013.

[6] A. Wintrich, U. Nicolai, W. Tursky, T. Reimann, "*Application manual power semiconductors*," Semikron international GmbH, Nuremburg, 2011.

[7] ZVEL, Handbook for robustness validation of automotive electrical/electronic modules, Jun. 2008.

[8] F. Richardeau, T. T. L. Pham, "Reliability calculation of multilevel converters: theory and applications," *IEEE Trans. on Industrial Electronics*, vol. 60, no. 10, pp. 4225-4233, Oct. 2013.

[9] H. Behjati, A. Davoudi, "Reliability analysis framework for structural redundancy in power semiconductors," *IEEE Trans. on Industrial Electronics*, vol. 60, no. 10, pp. 4376-4386, Oct. 2013.

[10] ABB Application Note, Load-cycling capability of HiPaks, 2004

[11] D. Xiang, L. Ran, P. J. Tavner, S. Yang, "Control of a doubly fed induction generator in a wind turbine during grid fault ride-through,", *IEEE Trans. on Energy Conversion*, vol. 21, no. 3, pp. 652-662, Sep. 2006.

[12] J. Lopez, E. Gubia, E. Olea, J. Ruiz, L. Marroyo, "Ride through of wind turbines with doubly fed induction generator under symmetrical voltage dips," *IEEE Trans. on Industrial Electronics*, vol. 56, no. 10, pp. 4246-4254, Oct. 2009.

[13] W. Chen, D. Xu, M. Chen, F. Blaabjerg, "Comparison of current control strategies for DFIG under symmetrical grid voltage dips," *in Proc. of IECON 2013*, pp. 1540-1545, Nov. 2013.

[14] J. Liang, W. Qiao, R.G. Harley, "Feed-forward transient current control for low voltage ride-through enhancement of DFIG wind turbines", *IEEE Trans. on Energy Conversion*, vol. 25, no. 3, pp. 836-843, Sep. 2010.

[15] F. K. A. Lima, A. Luna, P. Rodriguez, E. H. Watanabe, F. Blaabjerg, "Rotor voltage dynamics in the doubly fed induction generator during grid faults", *IEEE Trans. on Power Electronics*, vol. 25, no. 1, pp. 118-130, Jan. 2010.

[16] R. Cardenas, R. Pena, S. Alepuz, G. Asher, "Overview of control systems for the operation of DFIGs in wind energy applications," *IEEE Trans. on Industrial Electronics*, vol. 60, no. 7, pp. 2776-2798, July 2013.

[17] S. Xiao, G. Yang, H. Zhou, H. Geng, "An LVRT control strategy based on flux linkage tracking for DFIG-based WECS," *IEEE Trans. on Industrial Electronics*, vol. 60, no. 7, pp. 2820-2832, July 2013.

[18] K. Ma, F. Blaabjerg, M. Liserre, "Operation and thermal loading of three-neutral-point-clamped wind power converter under various grid faults," *in Proc. of ECCE 2012*, pp. 2410-2418, 2012.

[19] D. Zhou, F. Blaabjerg, M. Lau, M. Tonnes, "Thermal analysis of two-level wind power converter under symmetrical grid fault," *in Proc. of IECON 2013*, pp. 1902-1907, Nov. 2013.

[20] E.ON-Netz. *Requirements for offshore grid connections*, Apr. 2008.

[21] M. Tsili, S. Papathanassiou, "A review of grid code technical requirements for wind farms," *IET on Renewable Power Generation*, vol. 3, no. 3, pp. 308-332, Sep. 2009.

[22] G. Abad, J. Lopez, M. Rodriguez, L. Marroyo, G. Iwanski, *Doubly fed induction machine-modeling and control for wind energy generation.* Piscataway, NJ: IEEE Press, 2011, pp. 265-302.

[23] D. Zhou, F. Blaabjerg, M. Lau, M. Tonnes, "Thermal analysis of multi-MW two-level wind power converter," *in Proc. of IECON 2012*, pp.5862-5868, Oct. 2012.

[24] D. Zhou, F. Blaabjerg, M. Lau, M. Tonnes, "Thermal cycling overview of multi-metawatt two-level wind power converter at full grid code operation," *IEEJ Journal of Industry Applications*, vol. 2, no. 4, pp. 173-182, Jul. 2013.

[25] User manual of PLECS blockset version 3.2.7 March 2011. (Available: http://www.plexim.com/files/plecsmanual.pdf

[A.10] D. Zhou, F. Blaabjerg, "Dynamic thermal analysis of DFIG rotor-side converter during balanced grid fault," *in Proc. of ECCE 2014*, pp. 3097-3103, 2014.

Thermal Behavior of Doubly-Fed Induction Generator Wind Turbine System during Balanced Grid Fault

Dao Zhou, Frede Blaabjerg
Department of Energy Technology
Aalborg University
Aalborg, Denmark
zda@et.aau.dk, fbl@et.aau.dk

Mogens Lau, Michael Tonnes
Danfoss Silicon Power GmbH
Flensburg, Germany
mogens.lau@danfoss.com, michael.tonnes@danfoss.com

Abstract— Ride-through capabilities of the doubly-fed induction generator (DFIG) during grid fault have been studied a lot. However, the thermal performance of the power device during this transient period is seldom investigated. In this paper, the dynamic model for the DFIG and the influence of the rotor current to the damping time of the stator flux and rotor terminal voltage during the symmetrical grid fault is firstly evaluated. Then, the theoretical analysis for the safety operation area of the power device is given in terms of the various voltage dips and various rotor speeds, in which simulation results are used to verify. Finally, the power loss and the thermal profile are shown at the transient period of the DFIG. It is concluded that, in order to guarantee the same damping time of the stator flux, the serious voltage dip results in the higher power losses as well as the junction temperature fluctuation, and may even damage the rotor converter, if the design is not considered carefully.

I. Introduction

The penetration of wind power is expected to achieve 20% of the total electricity production by 2020 in Europe [1]. Because of the noise emission, footprint limitation and richer wind energy, the wind turbines are moving from onshore to offshore. Meanwhile, the lifetime of the wind turbine system are inversely prolonged to 20-25 years under such uncertain and harsh environment, whose mission profile leads to a faster fatigue and might give a higher failure rate. As the most vulnerable power electronic component, more and more efforts have been recently devoted to the reliable behavior of the power semiconductor due to the increased cost and time for repair after failures [2]-[5]. It is widely accepted that the thermal profile of the power semiconductor is an important indicator of the lifetime and it has an influence on the reliable operation. The power cycle number to failure is quite relevant to the junction temperature fluctuation as well as the mean junction temperature [6]-[10].

The Doubly-Fed Induction Generator (DFIG) is a widely used configuration for wind turbines above 1 MW. It provides the advantage of variable speed operation and four-quadrant active and reactive power capabilities using the converter rated for only a small fraction (20%-30%) of the rated power. However, on detecting a grid fault, the generator unit is usually disconnected to protect the vulnerable rotor converter. In the recent years, this has been achieved by so-called crowbar. As the penetration of wind power continues to increase, more wind turbines are required to ride through the grid faults, and to contribute to the system stability after the fault clearance. Researchers are addressing this issue from several points of view. For instance, the study described in [11], [12] analyzes the intrinsic in the DFIG during the grid fault and proposes its dynamic model. Many control strategies are suggested to support the DFIG to ride through the grid fault without the crowbar or with the enable time of the crowbar as soon as possible [13]-[17]. The thermal behavior of the power devices during grid fault is evaluated for both the permanent magnet synchronous generator based full-scale power converter and the DFIG based partial-scale power converter at steady-state operation [18], [19].

This paper focuses on the transient thermal behavior of the DFIG wind turbine system during the balanced grid fault, in order to identify critical issues which can cause lifetime reduction. Section II is a brief introduction to the dynamics of the DFIG model, and then the influence of rotor current on the stator flux damping and the rotor terminal voltage is analyzed in section III. The safety operation area of the traditional demagnetizing control is theoretically studied and verified by the simulation in section IV. The power loss and thermal profile of the switching power device is shown in Section V. Finally, conclusions are drawn in the last section.

II. Dynamic DFIG Model under Grid Fault

A lot of references have discussed the modeling of DFIG under grid faults [11]-[17]. If the stator reference frame, static to the stator winding, is introduced, assuming the rotor variables are all transferred to the stator-side, the voltage equation of the generator's stator and rotor can be expressed as follows,

$$\boldsymbol{u}_s = R_s \boldsymbol{i}_s + \frac{d}{dt}\boldsymbol{\psi}_s \tag{1}$$

$$\boldsymbol{u}_r = R_r \boldsymbol{i}_r + \frac{d}{dt}\boldsymbol{\psi}_r - j\omega_m \boldsymbol{\psi}_r \tag{2}$$

where $\boldsymbol{u}$, $\boldsymbol{i}$ and $\boldsymbol{\psi}$ are the space vector of voltage, current and flux of the induction generator, respectively. R denotes the generator's intrinsic resistance, and ω_m denotes the rotor angular frequency. The subscripts s and r denote stator quantities and rotor quantities. The additional third term in (2)

978-1-4799-2325-0/14/$31.00 ©2014 IEEE

represents the compensation transforming from the rotor reference frame to the stator reference frame, where the rotor reference frame rotates correspondingly at rotor speed with respect to the stator winding.

Similarly, with the aid of the stator reference frame, the stator flux $\boldsymbol{\psi}_s$ and rotor flux $\boldsymbol{\psi}_r$ equations are given by,

$$\boldsymbol{\psi}_s = L_s \boldsymbol{i}_s + L_m \boldsymbol{i}_r \tag{3}$$

$$\boldsymbol{\psi}_r = L_m \boldsymbol{i}_s + L_r \boldsymbol{i}_r \tag{4}$$

where L_m is the magnetizing inductance, and L is the self-inductance of stator-side and the rotor-side of the DFIG.

In normal operation, the space vector of stator flux rotates at slip speed ω_r with respect to the rotor winding, which is the product of the slip s and the synchronous angular speed ω_s. However, during a balanced full-dip grid voltage fault, the dc component of the stator flux appears, and the stator flux no longer rotates but freezes with the respect to the stator winding. As a result, the stator flux is rotating at speed ω_m with respect to rotor winding. In the case of a balanced partial-dip grid voltage fault, the stator flux can consequently be expressed as a sum of a forced flux $\boldsymbol{\psi}_{sf}$ and a natural flux $\boldsymbol{\psi}_{sn}$ [7],

$$\boldsymbol{\psi}_s = \boldsymbol{\psi}_{sf} + \boldsymbol{\psi}_{sn} \tag{5}$$

According to the superposition principle, the dynamic model of the DFIG is thus depicted in terms of two independent circuits: the forced machine model and the natural machine model. For the forced machine shown in Fig. 1(a), it stands for the steady-state operation of the DFIG, where the stator of the induction generator connects to the remaining grid voltage (p is the voltage dip level), and no transient stator flux is considered. On the other hand, the natural machine shown in Fig. 1(b) is used for a transient period, whose stator is short-circuited, and an initial natural flux exists in the stator. In order to investigate the dynamic response of the DFIG under grid fault, only the natural machine is focused in the following.

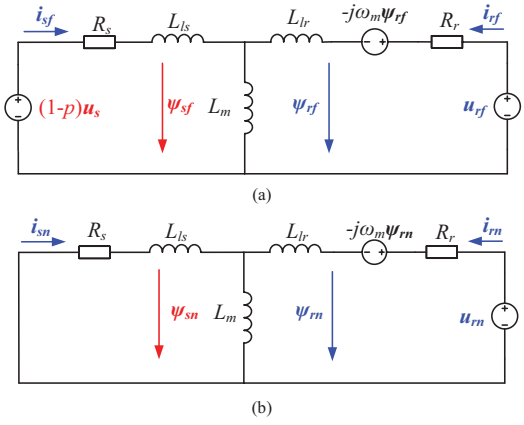

Fig. 1. Dynamic model of the DFIG under a balanced grid fault. (a) Forced machine model; (b) Natural machine model.

III. Influence of Rotor Current Under DFIG Natural Model

DFIG based wind turbine generators shown in Fig. 2 are susceptible to grid-side low voltage or short-circuit due to the presence of the power electronics converter on the rotor-side. If a three-phase voltage sag happens on the grid-side, as aforementioned, a dc component of stator natural flux emerges immediately, which induces a considerably increase of electromagnetic force (EMF). The rotor current thus increases substantially without proper protection, and may even damage the rotor converter. Moreover, the existence of stator natural flux prevents the rotor converter to provide the reactive power injection. As a consequence, the damping time of the stator flux and analysis of rotor voltage are two important aspects in case of grid faults. However, in normal operation, the rotor converter is designed to adjust the active power and the reactive power of the stator side through the controllability of the rotor current. This section will investigate the effect of the rotor current on DFIG's natural flux evolution and induced rotor voltage.

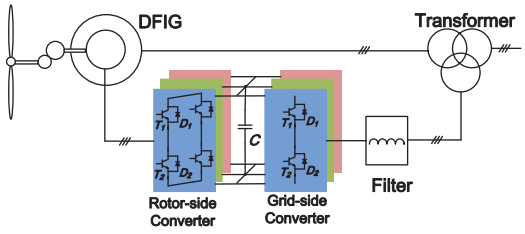

Fig. 2. Configuration of the wind turbine system equipped with DFIG.

A. Natural flux evolution

According to Fig. 1(b), as no stator voltage in the natural machine model is taken into account, expressing the relationship between the stator flux and the rotor current through (1) and (3) yields,

$$\frac{d}{dt}\boldsymbol{\psi}_{sn} = -\frac{R_s}{L_s}\boldsymbol{\psi}_{sn} + \frac{R_s}{L_s}L_m \boldsymbol{i}_{rn} \tag{6}$$

where the subscript n indicates the variables in natural machine model. If the rotor side is open-circuit, from the first term, it is inferred that the natural flux is exponentially decaying with the DFIG's own time constant, whose value is quite large, up to 1 to 1.5 seconds for a MW generator [12]. If no counter-action is adopted, the transient period remains for several seconds, which is unfortunately a violation with the fast response of the reactive power defined in the recent grid codes [20], [21].

The second term denotes the influence of rotor current in the evolution of the stator flux. Depending on the phase angle between the rotor current and the natural flux, the damping could be either accelerated or decelerated. For instance, if the rotor converter injects a current in phase with the natural flux, the damping of the stator flux will be slowed down, and might even be canceled out or become negative. Under this

specific situation, the natural flux will not disappear, but rather increase until the rotor converter goes out of control.

The opposite situation happens if a crowbar is connected to the rotor. The crowbar is a protection against the grid faults that allows a low resistance across the rotor windings. The connection of the crowbar generates the circulation of large current through the rotor windings and stator windings. Since the rotor current is almost in opposite phase to the natural flux, the flux damping will be accelerated. However, this hardware solution is hardly helpful in injecting reactive power, and inevitably increases the cost of the system.

B. Voltage at rotor terminals

Based on (3) and (4), the rotor flux can be represented in terms of the stator flux and rotor current by eliminating the stator current. If the rotor reference frame is introduced, the previous expression of the rotor voltage in (2) can be transformed as the following,

$$\boldsymbol{u}_{rn}^{r} = (R_r + \sigma L_r \frac{d}{dt})\boldsymbol{i}_{rn}^{r} + \frac{L_m}{L_s}\frac{d}{dt}\boldsymbol{\psi}_{sn}^{r} \tag{7}$$

where the superscript r denotes the rotor reference frame, and σ denotes the leakage inductance coefficient $\sigma=1-L_m^2/L_sL_r$. It is observed that the first term of the expression is the voltage drop in the rotor resistance and in the transitory rotor inductance, and the second term of the expression is the EMF induced by the stator flux in rotor windings. If (6) is deduced under the rotor reference frame, (7) can be further simplified as [22],

$$\boldsymbol{u}_{rn}^{r} \approx (R_r + R_s)\boldsymbol{i}_{rn}^{r} - j\sigma\omega_m L_r \boldsymbol{i}_{rn}^{r} - j\omega_m \boldsymbol{\psi}_{sn}^{r} \tag{8}$$

Viewed from the rotor, the DFIG behaves as EMF $\boldsymbol{e}_{rn}$ induced by the stator natural flux, in series with rotor and stator resistance as well as the transitory inductance of the machine. The equivalent circuit of the machine is thus depicted in Fig. 3. In order to guarantee the current controllability, the rotor converter should be sized to generate a voltage at least larger than the EMF.

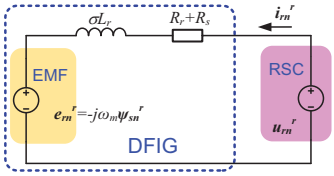

Fig. 3. Equivalent machine model in viewpoint of the rotor.

IV. Control for Grid Fault Ride-through Operation

Xiang *et. al* [11] proposed the demagnetizing control technique to protect the rotor converter against the grid faults without a crowbar or with a crowbar active time as short as possible [12]. In this section, the demagnetizing control scheme will briefly be described. Then the Safety Operation Area (SOA) will be theoretically analyzed in terms of various voltage dip levels and various rotor speeds. After that, the SOA is verified by simulation results.

A. Demagnetizing current influence to stator flux

The basic idea of the demagnetizing current is to introduce a rotor current opposite to the stator flux,

$$\boldsymbol{i}_{rn} = -k\boldsymbol{\psi}_{sn} \tag{9}$$

Substituting (9) into (6), the evolution of the stator flux is then obtained,

$$\frac{d}{dt}\boldsymbol{\psi}_{sn} = -(\frac{R_s}{L_s} + \frac{R_s}{L_s}L_m k)\boldsymbol{\psi}_{sn} \tag{10}$$

The stator flux is exponentially decaying with the certain time constant,

$$\tau_s = \frac{L_s}{R_s(1+kL_m)} \tag{11}$$

It shows that the introduction of the demagnetizing current will accelerate the decaying of the natural flux.

B. Demagnetizing current effects on rotor voltage

Consider that the generator operates under normal operation until a symmetrical voltage dip occurs at a given moment $t=0$. The space vector of the grid voltage is,

$$\boldsymbol{u}_s = \begin{cases} U_s e^{j\omega_s t} & t \le 0 \\ (1-p)U_s e^{j\omega_s t} & t > 0 \end{cases} \tag{12}$$

where U_s denotes the amplitude of the grid voltage.

Neglecting the insignificant voltage drop through the stator resistance, the stator flux after the grid fault can be obtained,

$$\boldsymbol{\psi}_s = -j(\frac{(1-p)U_s}{\omega_s}e^{j\omega_s t} + \frac{pU_s}{\omega_s}e^{-\frac{t}{\tau_s}}) \tag{13}$$

The first term can be regarded as stator forced flux $\boldsymbol{\psi}_{sf}$, still rotating with synchronous angular speed. The second term is the stator natural flux $\boldsymbol{\psi}_{sn}$, static with stator winding. The amplitudes of these two kinds of stator flux are dictated by the voltage dip level.

Assuming the grid voltage is the reference vector, Fig. 4 graphically shows the space vector diagram of the rotor voltage. The stator flux $\boldsymbol{\psi}_{sn}$ is lagging the stator voltage $\boldsymbol{u}_s$ 90 degree, and the rotor current $\boldsymbol{i}_{rn}$ is opposite to the stator flux.

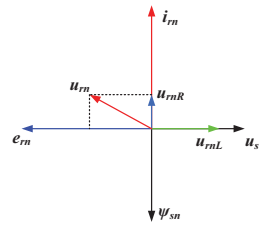

Fig. 4. Space vector diagram for rotor voltage under stator reference frame.

According to (8), the voltage drop $\boldsymbol{u}_{rnR}$ through the resistance and $\boldsymbol{u}_{rnL}$ transitory inductance is in phase of rotor current and lagging the current 90 degree, respectively.

Moreover, the EMF e_{rn} is lagging the stator flux 90 degree. It is noted that, besides the acceleration of damping stator flux, the demagnetizing control normally has an advantage to reduce the rotor voltage as well.

C. Analysis of safety operation area

The rotor converter usually employs the IGBT module as a semiconductor switching device. Its continuous current rating is determined by the steady-state current, while during the transient period the over-current may occur. Generally speaking, the maximum current switched by the power device can be the peak pulse rating, as long as the junction temperature is still permissible and the *V-I* switching trajectory is within the SOA. The pulse current rating of an IGBT module is typically two times of the continuous current rating. As mentioned before, the stator natural flux induces the overcurrent and overvoltage in the rotor converter during a balanced grid fault. From (8) and (13), the EMF is jointly decided by the voltage dip level and rotor speed. Therefore, it is interesting to investigate the SOA of the rotor converter in terms of various voltage dip levels and various rotor speeds, in which the instantaneous rotor current is constrained below 2.0 pu., while the rotor converter dc-link voltage is also maintained below the device voltage rating.

A 2 MW DFIG wind turbine is used for the case study, whose parameters are given in Appendix. Because of a low-voltage system, a common 1 kA/1.7 kV power module from leading manufacturer is selected. Based on (8), the relationship between the rotor voltage and the rotor current at different voltage dips is shown in Fig. 5, in which the rotor speed is set at 1800 rpm. It can be seen that, if the rotor is open-circuit, the higher dip level causes the higher EMF viewed from rotor side. Besides, the demagnetizing current reduces the rotor voltage, and even brings the rotor converter back to SOA with a proper amount of the demagnetizing current. Due to partial-scale feature compared to the generator, the rotor converter will be destroyed by serious voltage dip, e.g. when the dip level reaches 0.8 pu.

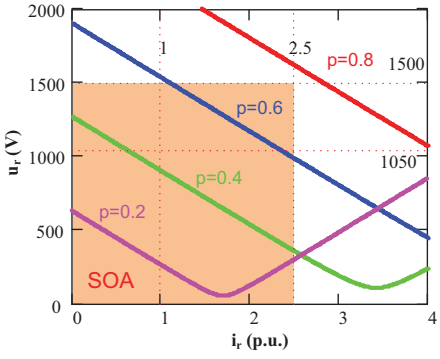

Fig. 5. Voltage amplitude at rotor terminal versus rotor current with various grid voltage dips at rotor speed 1800 rpm, where p is the voltage dip.

During the grid fault, the demagnetizing current injection results in an even higher rotor speed [11]. The rotor speed is assumed to be 1950 rpm in comparison with the maximum normal speed 1800 rpm. Fig. 6 shows the relationship between the rotor voltage and the rotor current at different rotor speeds when the voltage dip is 0.8 pu. It is noted that the higher rotor speed also induces higher EMF of the rotor, and the rotor converter is able to ride through the grid fault easier at lower rotor speed.

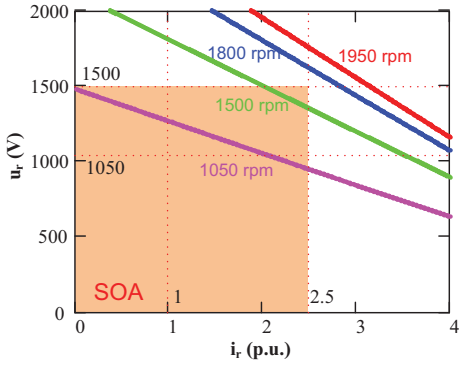

Fig. 6. Voltage amplitude at rotor terminal versus rotor current with various rotor speeds at the voltage dip: p=0.8.

D. Simulation validation

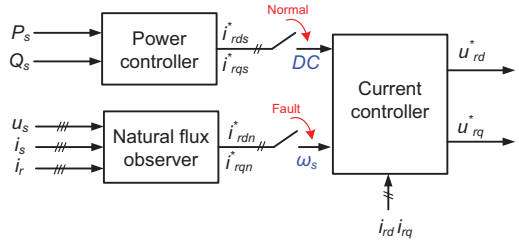

Fig. 7. Control diagram for rotor converter during normal operation and grid fault condition.

The control scheme for the rotor converter is shown in Fig. 7, where the control objective is switched from the active power and the reactive power to the demagnetization of the stator transient flux if the grid fault happens. The rotor reference current is obtained through a natural flux observer, due to its dc component viewed from the stator-side, the rotor reference current becomes a grid angular frequency ω_s viewed from the rotor side. However, in normal operation, the rotor reference current is a dc component viewed from the rotor side. As a result, the actual frequency of the rotor current in the case of the grid fault is the rotor speed, while in normal operation the frequency of the rotor current becomes the slip speed.

The wind turbine is required to start injecting reactive power in about 500 ms to 600 ms from the beginning of the fault, complying with the latest grid code requirement [20], [21]. The damping time for the stator flux is consequently set at 180 ms. As shown in Fig. 8, the stator flux returns to normal within around 600 ms, which is consistent with the above

damping time design. Furthermore, the stator current may reach up to 3 pu, and it has two frequencies during the transient period: the dc component and the grid frequency as illustrated in (13).

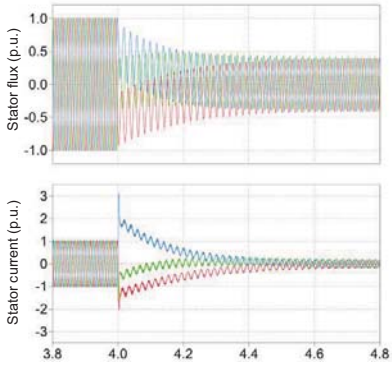

Fig. 8. Damping time of natural flux (e. g. rotor speed at 1800 rpm and voltage dip at 0.6).

The rotor voltage and the rotor current are then shown in Fig. 9 with the different voltage dip levels. In order to verify the evaluation in Fig. 5, four various dip levels are independently simulated. In Fig. 9(a) and Fig. 9(b), the rotor converter can survive through the grid fault. In Fig. 9(d), as the rotor voltage is higher than 1500 V, it excesses the linear modulation index and the rotor converter loses the control of the rotor current. The above phenomena agree with the analysis in Fig. 5. However, in Fig. 9(c), in case of the voltage dip at 0.6 pu, the simulation shows that the rotor side converter operates out of the SOA during the fault ride-through period. It is due to the error introduced by the control gain.

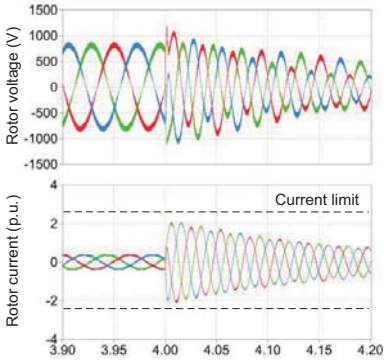

Fig. 10. Simulation of SOA vs. rotor speed in case of dip level at 0.8 and rotor speed at 1050 rpm.

Fig. 10 shows the simulation of SOA versus rotor speed in the case of the voltage dip at 0.8 pu, and the rotor speed at 1050 rpm. Compared with the simulation in Fig. 9(d), it is obvious that if the rotor speed is reduced, it is possible for the rotor converter to ride through the same serious voltage dip.

V. Thermal Behavior of Power Device

As the demagnetizing control introduces the various rotor current as well as the rotor voltage at different voltage dips and rotor speeds, this section will analyze the power loss distribution and the thermal cycling of power device in the case of a balanced grid fault.

A. Power loss distribution

The power loss model, consisting of the conduction losses and switching losses, can be referred to [23], [24]. Based on the on-state voltage drop and switching energy against the load current and the DC-link voltage provided by the manufacturers, the conduction losses and switching losses are accumulated by every switching cycle within one fundamental frequency. The simulation of the power loss has been obtained with the use of PLECS blockset in Simulink [25].

According to Fig. 9, it is noted that the current of the rotor in the three phases becomes extremely unbalanced. Moreover, as the current is exponential decaying, the maximum current through the power modules in the upper and lower of the same bridge is also different. Fig. 11 shows power loss distribution of the most stressed power device at different grid voltage dips, and Fig. 11(a) and Fig. 11(b) are the situations for the rotor speed at 1800 rpm and 1050 rpm, respectively.

In the case of the rotor speed at 1800 rpm from Fig. 11(a), during the normal operation, it is noted that the conduction loss are mainly consumed by the diode compared to the IGBT because of its power flow direction in the super-synchronous mode. However, it is the IGBT that dissipates higher switching loss due to the fact that the turn-on and turn-off energy in the IGBT has larger value than the reverse recovery energy in the diode according to the manufacturer's datasheet. With the increase of the voltage dip level, the natural stator flux becomes higher. In order to guarantee the same damping time of the stator flux, the initial rotor current becomes higher, which causes the increasing power loss.

In the case of the rotor speed at 1050 rpm from Fig. 11(b), due to the maximum power point tracking, the generated power is much lower than the rotor speed at 1800 rpm in the normal operation. Therefore, the power devices are considerably less stressed. Moreover, in the sub-synchronous mode, the direction of the active power through the rotor converter is also reverse, which implies that the IGBT consumes higher conduction loss. Similarly, the more serious voltage dip, the heavier the power device is loading. Furthermore, at the same grid dip 0.8, the power loss at rotor speed 1800 rpm is higher than the case at 1050 rpm, which agrees with the rotor current and voltage characteristic shown in Fig. 9(d) and Fig. 10.

B. Thermal cycling

The thermal model of the power devices, including the IGBT and the freewheeling diode are shown in Fig. 12 in the form of the power module, the thermal grease and the heat-sink. The electrical analogies representing thermal variables are used, in which the power dissipation in the IGBT and the

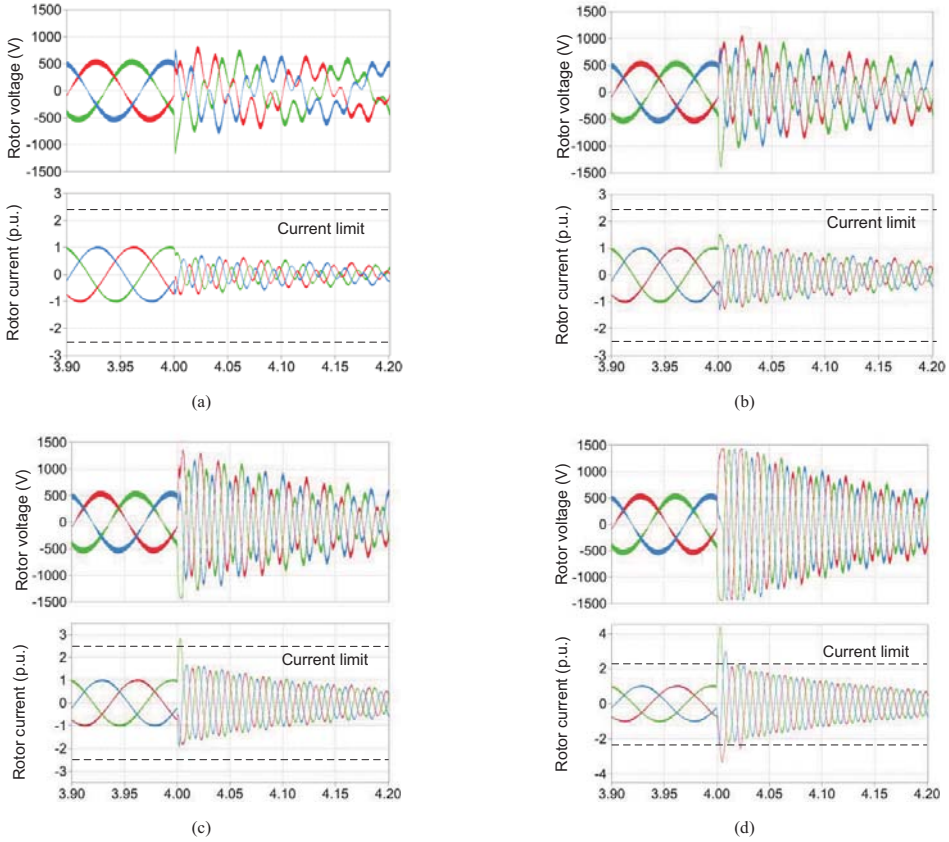

Fig. 9. Simulation of safety operation area vs. dip level in case of rotor speed=1800 rpm at different voltage dips. (a) p=0.2; (b) p=0.4; (c) p=0.6; (d) p=0.8.

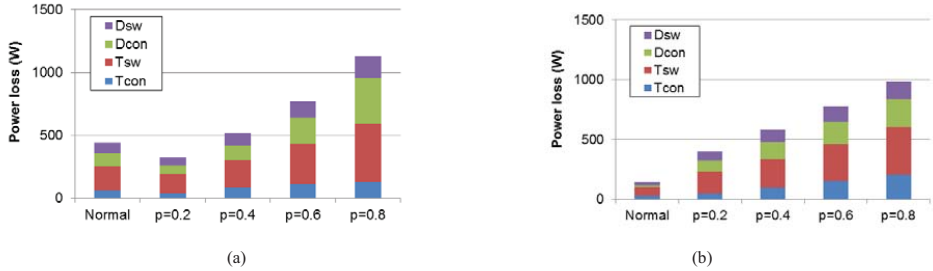

Fig. 11. Power loss distribution at different grid voltage for the rotor-side converter. (a) Rotor speed at1800 rpm; (b) Rotor speed at 1050 rpm.

diode are expressed as current source, the voltage source stand for constant temperature levels, and RC elements are used to signify the thermal impedance.

The thermal impedance from junction to case is modeled as a four-layer Foster RC network, whose values are normally provided by the manufacturer's datasheet. As the Foster structure requires the constant temperature at the terminal, the thermal capacitance of the thermal grease and cooling methods are considered infinite high, which is consequently represented by a controllable voltage source updated by the instantaneous power losses. Meanwhile, the ambient temperature is set to 50 ºC as an indication of the worst case.

Based on the thermal model shown in Fig. 12, the thermal performance of the power device can be simulated again by

PLECS. The simulation of the junction temperature is shown in Fig. 13, where the balanced grid fault to 0.2 pu occurs at the time instant t=4 s.

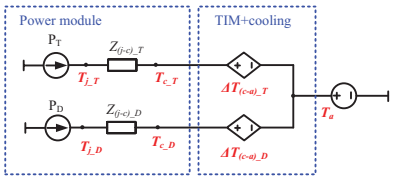

Fig. 12. Thermal model of the power switching device.

Note: TIM stands for Thermal Interface Material.

In case of the rotor speed at 1800 rpm from Fig. 13(a), during the normal operation, the mean junction temperature for the IGBT is higher than the diode, but the junction temperature fluctuation of the diode is higher. If the grid fault happens, the fundamental frequency of the thermal cycling switches from the slip frequency to the rotor speed frequency. Moreover, the switching power device, especially the diode is much more stressed, where the highest junction temperature reach 110 ºC and the junction temperature fluctuation changes from 12.8 ºC to 42.0 ºC.

In the case of the rotor speed at 1050 rpm in Fig. 13(c), the power device is much less stressed in normal operation, which is consistent with the power loss profile shown in the Fig. 11(b). Moreover, the IGBT has a higher mean junction temperature and the junction temperature fluctuation. When the grid fault happens, both the IGBT and the diode become more loaded, and they are more equally heated. The maximum junction temperature fluctuation of the diode changes from 2.3 ºC to 18.4 ºC.

As shown in Fig. 13(b), in which the rotor speed becomes 1500 rpm, the maximum thermal cycling of change from 10.9 ºC in normal operation to 29.3 ºC during the grid faults.

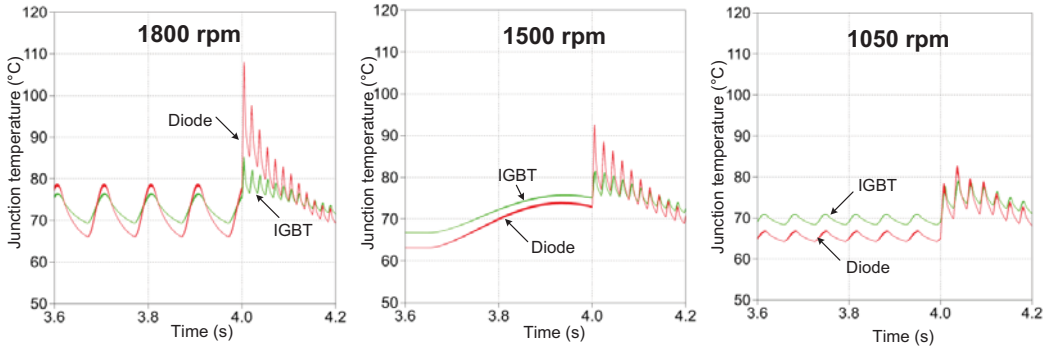

(a) (b) (c)

Fig. 13. Simulation of the junction temperature if the voltage becomes 0.2 pu. (a) Rotor speed at 1800 rpm; (b) Rotor speed at 1500 rpm; (c) Rotor speed at 1050 rpm.

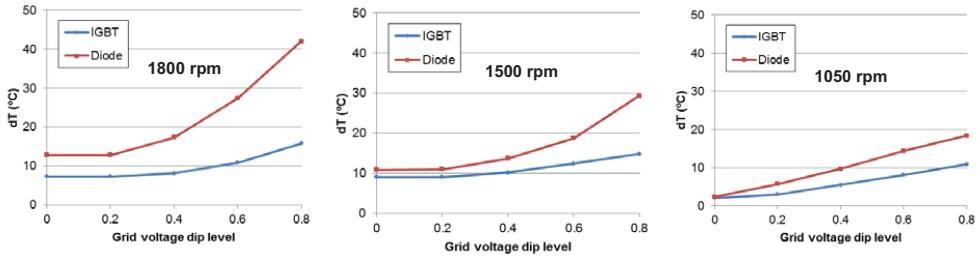

(a) (b) (c)

Fig. 14. Junction temperature fluctuation at different grid voltage dip levels. (a) Rotor speed at 1800 rpm; (b) Rotor speed at 1500 rpm; (c) Rotor speed at 1050 rpm.

In order to evaluate the thermal profile of the power device at different voltage dip levels, Fig. 14 summarizes the junction temperature for the maximum and minimum rotor speeds from the normal operation to the balanced grid fault the voltage dip up to 0.8 pu. At the maximum rotor speed seen from the Fig. 14(a), the shallow voltage dip does not change the value of the junction temperature fluctuation due to the smaller demagnetizing current. If the dip level increases, the junction

temperature fluctuation in the diode has much higher value than the IGBT. Fig. 14(c) shows the situation at the rotor speed 1050 rpm, it is noted that the more voltage dips, the more serious the power device is loaded. As shown in Fig. 14(b), the case that rotor speed becomes 1500 rpm is also investigated.

VI. Conclusion

This paper has studied the impact of rotor current on the stator flux damping time and the rotor terminal voltage for the DFIG in the case of the balanced grid fault.

The safety operation area of the rotor converter by demagnetizing control is theoretically analyzed in terms of the various grid voltage dips and the various rotor speeds. In order to guarantee the same damping time of the stator flux, the simulation also verifies the above safety operation area.

The power loss and thermal behavior are then evaluated for the transient period during balanced grid fault. It is concluded that the serious voltage dip results in higher power losses as well as the junction temperature fluctuation, and may even damage the rotor converter, if the design is not considered carefully.

Appendix

Parameters for a 2 MW DFIG

Ratings: P_n = 2.0 MW, U_s = 563V (phase amplitude), four pole

Turns ratio: $N_s/N_r = 0.369$

Stator resistance: $R_s = 1.688\ \text{m}\Omega$

Stator leakage inductance: $L_s = 0.038$ mH

Rotor resistance: $R_r' = 1.524\ \text{m}\Omega$

Rotor leakage inductance: $L_r' = 0.064$ mH

Magnetizing inductance: $L_m = 2.91$ mH

References

[1] European Commission Climate Action, "*The EU climate and energy package*," Mar. 2007.

[2] F. Blaabjerg, Z. Chen, S. B. Kjaer, "Power electronics as efficient interface in dispersed power generation systems," *IEEE Trans. on Power Electronics*, vol. 19, no. 5, pp. 1184-1194, Sep. 2004.

[3] F. Blaabjerg, K. Ma, D. Zhou, "Power electronics and reliability in renewable energy systems," *in Proc. of ISIE 2012*, pp. 19-30, May. 2012.

[4] S. Yang, A. Bryant, P. Mawby, D. Xiang, L. Ran, P. Tavner, "An industrial-based survey of reliability in power electronic converters," *IEEE Trans. on Industrial Applications*, vol. 47, no. 3, pp. 1441-1451, May. 2011.

[5] H. Polinder, J. A. Ferreira, B. B. Jensen, A. B. Abrahamsen, K. Atallah, R. A. McMahon, "Trends in Wind Turbine Generator Systems," *IEEE Journal of Emerging and Selected Topics in Power Electronics*, vol. 1, no. 3, pp. 174-185, Sep. 2013.

[6] A. Wintrich, U. Nicolai, W. Tursky, T. Reimann, "*Application manual power semiconductors*," Semikron international GmbH, Nuremburg, 2011.

[7] ZVEL, Handbook for robustness validation of automotive electrical/electronic modules, Jun. 2008.

[8] F. Richardeau, T. T. L. Pham, "Reliability calculation of multilevel converters: theory and applications," *IEEE Trans. on Industrial Electronics*, vol. 60, no. 10, pp. 4225-4233, Oct. 2013.

[9] H. Behjati, A. Davoudi, "Reliability analysis framework for structural redundancy in power semiconductors," *IEEE Trans. on Industrial Electronics*, vol. 60, no. 10, pp. 4376-4386, Oct. 2013.

[10] ABB Application Note, Load-cycling capability of HiPaks, 2004

[11] D. Xiang, L. Ran, P. J. Tavner, S. Yang, "Control of a doubly fed induction generator in a wind turbine during grid fault ride-through,", *IEEE Trans. on Energy Conversion*, vol. 21, no. 3, pp. 652-662, Sep. 2006.

[12] J. Lopez, E. Gubia, E. Olea, J. Ruiz, L. Marroyo, "Ride through of wind turbines with doubly fed induction generator under symmetrical voltage dips," *IEEE Trans. on Industrial Electronics*, vol. 56, no. 10, pp. 4246-4254, Oct. 2009.

[13] W. Chen, D. Xu, M. Chen, F. Blaabjerg, "Comparison of current control strategies for DFIG under symmetrical grid voltage dips," *in Proc. of IECON 2013*, pp. 1540-1545, Nov. 2013.

[14] J. Liang, W. Qiao, R.G. Harley, "Feed-forward transient current control for low voltage ride-through enhancement of DFIG wind turbines", *IEEE Trans. on Energy Conversion*, vol. 25, no. 3, pp. 836-843, Sep. 2010.

[15] F. K. A. Lima, A. Luna, P. Rodriguez, E. H. Watanabe, F. Blaabjerg, "Rotor voltage dynamics in the doubly fed induction generator during grid faults", *IEEE Trans. on Power Electronics*, vol. 25, no. 1, pp. 118-130, Jan. 2010.

[16] R. Cardenas, R. Pena, S. Alepuz, G. Asher, "Overview of control systems for the operation of DFIGs in wind energy applications," *IEEE Trans. on Industrial Electronics*, vol. 60, no. 7, pp. 2776-2798, July 2013.

[17] S. Xiao, G. Yang, H. Zhou, H. Geng, "An LVRT control strategy based on flux linkage tracking for DFIG-based WECS," *IEEE Trans. on Industrial Electronics*, vol. 60, no. 7, pp. 2820-2832, July 2013.

[18] K. Ma, F. Blaabjerg, M. Liserre, "Operation and thermal loading of three-neutral-point-clamped wind power converter under various grid faults," *in Proc. of ECCE 2012*, pp. 2410-2418, 2012.

[19] D. Zhou, F. Blaabjerg, M. Lau, M. Tonnes, "Thermal analysis of two-level wind power converter under symmetrical grid fault," *in Proc. of IECON 2013*, pp. 1902-1907, Nov. 2013.

[20] E.ON-Netz. *Requirements for offshore grid connections*, Apr. 2008.

[21] M. Tsili, S. Papathanassiou, "A review of grid code technical requirements for wind farms," *IET on Renewable Power Generation*, vol. 3, no. 3, pp. 308-332, Sep. 2009.

[22] G. Abad, J. Lopez, M. Rodriguez, L. Marroyo, G. Iwanski, *Doubly fed induction machine-modeling and control for wind energy generation.* Piscataway, NJ: IEEE Press, 2011, pp. 265-302.

[23] D. Zhou, F. Blaabjerg, M. Lau, M. Tonnes, "Thermal analysis of multi-MW two-level wind power converter," *in Proc. of IECON 2012*, pp.5862-5868, Oct. 2012.

[24] D. Zhou, F. Blaabjerg, M. Lau, M. Tonnes, "Thermal cycling overview of multi-metawatt two-level wind power converter at full grid code operation," *IEEJ Journal of Industry Applications*, vol. 2, no. 4, pp. 173-182, Jul. 2013.

[25] User manual of PLECS blockset version 3.2.7 March 2011. (Available: http://www.plexim.com/files/plecsmanual.pdf